

# **Contributions to induction thermography inspection and automated view planning**



**Mondragon  
Unibertsitatea**

**Beñat Urtasun Marco**

Supervisor: Dr. Imanol Andonegui

Dr. Luka Eciolaza

Dr. Eider Gorostegui

Department of Electronics and Computer Science

Mondragon Goi Eskola Politeknikoa

Mondragon Unibertsitatea

Mondragon University

This dissertation is submitted for the degree of

*Doctor of Philosophy*

January 2024



A mi madre...





# **Declaration**

Beñat Urtasun Marco  
January 2024



## **Acknowledgements**

Esta tesis ha sido desarrollada en el de termografía de Lortek S.Coop. en colaboración con el departamento de automatización y robótica de la universidad de Mondragon. El autor está especialmente agradecido por a Lortek S.Coop., por haber hecho posible esta tesis.

Una vez terminada la tesis, llega el momento de dar las gracias a todas las personas que me han ayudado a llegar a este punto. Me gustaría empezar dando las gracias a Imanol Andonegui por confiar en mí y brindar un apoyo tanto a nivel técnico como personal. Quiero dar las gracias de especial manera Eider Gorostegui por haberme dado la posibilidad de desarrollar mis ideas en el departamento de termografía de Lortek, además de sus animos constantes, y facilidades para hacer cualquier prueba. Quiero agradecer también a otras personas sin las que no habría sido posible realizar gran parte del trabajo debido a las incontables horas dedicadas a etiquetar imágenes, además de brindar apoyo en el laboratorio, como Pablo López y Jon Mata. Y a Fran Huertos y Pedro Alvarez por haber posibilitado su desarrollo hasta su forma final.

Quiero dar las gracias a mi padre que ha tenido que levantarme el ánimo en más de una ocasión, y, especialmente a mi madre que siempre creyó en mi, y que se fue durante el transcurso, sabiendo que algún día se la dedicaría.

This thesis has been developed in the field of thermography at Lortek S.Coop., in collaboration with the Department of Automation and Robotics at Mondragon University. The author is particularly grateful to Lortek S.Coop. for making this thesis possible.

Upon completing the thesis, it is time to express gratitude to all the people who have helped me reach this point. I would like to begin by thanking Imanol Andonegui for trusting in me and providing both technical and personal support.

I want to express special thanks to Eider Gorostegui for giving me the opportunity to develop my ideas in the thermography department at Lortek, in addition to her constant encouragement and facilitation of any tests. I also want to thank other individuals without whom a significant portion of the work would not have been possible due to countless hours

dedicated to labeling images and providing support in the laboratory, such as Pablo López and Jon Mata. And to Fran Huertos and Pedro Alvarez to enable its completion in its final form.

I want to thank my father, who has had to lift my spirits on more than one occasion, and especially my mother, who always believed in me and passed away, knowing that someday I would dedicate it to her.

## **Abstract**

The non-destructive inspection industry faces challenges in automating processes quickly to meet growing demands. Techniques like active thermography and 3D measurements encounter difficulties in contexts requiring reduced inspection times, leading to time and resource-intensive automation. Induction thermography, focused on surface integrity inspection, is sensitive to system position, requiring multiple thermographies and extending inspection times inspecting defects with unknown orientation. The automation of surface inspection on complex geometries involves prolonged timelines and expert resources. The thesis addresses these both challenges by proposing enhancements in induction thermography, including a multi-directional system and a continuous scanning method. It also introduces a system for generating robot inspection trajectories on arbitrary geometries, significantly reducing planning time without human intervention.



# Table of contents

<b>List of figures</b>	<b>xv</b>
<b>List of tables</b>	<b>xix</b>
<b>Nomenclature</b>	<b>xxi</b>
<b>1 State of the art</b>	<b>5</b>
1.1 Destructive testing . . . . .	5
1.2 Conventional non-destructive testing . . . . .	6
1.2.1 Liquid penetrant testing . . . . .	6
1.2.2 Magnetic particles inspection . . . . .	7
1.2.3 Eddy currents inspection . . . . .	8
1.2.4 Ultrasonic testing . . . . .	9
1.3 Thermography . . . . .	9
1.3.1 Thermography as a non destructive testing . . . . .	10
1.3.2 Infrared detectors . . . . .	12
1.3.3 Optically excited thermography . . . . .	13
1.3.4 Induction thermography . . . . .	18
1.3.5 Other active thermography techniques . . . . .	21
1.3.6 Processing techniques . . . . .	22
1.4 Quantitative analysis and probability of detection . . . . .	26
1.4.1 Precision and recall . . . . .	26
1.4.2 Hit and miss - POD . . . . .	26
1.4.3 A VS $\hat{A}$ - POD . . . . .	27
1.5 View planning . . . . .	28
1.5.1 Motivation . . . . .	29
1.5.2 Generic view-planning algorithm . . . . .	29
1.5.3 View planning system . . . . .	30

1.5.4	Data structures . . . . .	33
1.5.5	Model-based view planning . . . . .	35
1.5.6	Next-best-view . . . . .	37
<b>2</b>	<b>Phase shifted imaging on multi-directional thermography</b>	<b>41</b>
2.1	Introduction . . . . .	41
2.1.1	Related works . . . . .	42
2.1.2	Contributions . . . . .	43
2.2	Methods . . . . .	44
2.2.1	A multi-directional induction thermography system . . . . .	44
2.2.2	Preliminary experiments on notches . . . . .	46
2.2.3	Thermo-inductive phase-shifting . . . . .	49
2.2.4	Phase-shifted optical flow . . . . .	50
2.2.5	Rotation vector field convolution . . . . .	51
2.3	Results . . . . .	51
2.3.1	Experimental measurements on different materials . . . . .	51
2.3.2	POD on Inconel 718 and Haynes 282 with TIG welds . . . . .	53
2.4	Conclusions . . . . .	55
<b>3</b>	<b>Quadratic inductor</b>	<b>63</b>
3.1	Introduction . . . . .	63
3.2	Methods . . . . .	64
3.2.1	Inductor description . . . . .	64
3.2.2	Setup . . . . .	67
3.3	Results . . . . .	68
3.3.1	Notched samples . . . . .	68
3.3.2	Natural cracks . . . . .	71
3.4	Conclusions . . . . .	78
<b>4</b>	<b>Dynamic multi-directional induction thermography</b>	<b>79</b>
4.1	Introduction . . . . .	79
4.1.1	Motivation . . . . .	79
4.1.2	Related works . . . . .	80
4.2	Outline . . . . .	81
4.3	Methods . . . . .	82
4.3.1	Setup . . . . .	83
4.3.2	Synchronized pseudo-static multi-directional thermography . . . . .	83



---

4.3.3	Thermal drift compensation . . . . .	85
4.3.4	Temporal compression . . . . .	86
4.4	Results . . . . .	87
4.4.1	Quantitative evaluation criteria . . . . .	88
4.4.2	Quantitative analysis . . . . .	88
4.5	Discussion . . . . .	108
4.6	Conclusions . . . . .	108
<b>5</b>	<b>Sparse model-based view planning for complex geometries</b>	<b>111</b>
5.1	Introduction . . . . .	111
5.1.1	Motivation . . . . .	112
5.1.2	Related work . . . . .	112
5.1.3	VPP combinatorial formulation . . . . .	115
5.1.4	Contributions . . . . .	116
5.2	Methods . . . . .	117
5.2.1	Surface point sampling . . . . .	118
5.2.2	Visibility calculation . . . . .	118
5.2.3	Robot accessibility testing . . . . .	127
5.2.4	Inspection time optimization . . . . .	127
5.3	Experiments and results . . . . .	130
5.3.1	Synthetic view-planning . . . . .	131
5.3.2	Real tests . . . . .	133
5.4	Discussion . . . . .	137
5.5	Conclusions . . . . .	138
<b>6</b>	<b>Conclusions</b>	<b>141</b>
	<b>References</b>	<b>143</b>



# List of figures

1.1	Liquid penetrant inspection. . . . .	7
1.2	Magnetic particle example. . . . .	8
1.3	Steady-state heat conduction through solid. (a) Linear heat conduction as thermal resistance. (b) Two materials with a perfect thermal interface. (c) Cracked block. . . . .	10
1.4	Optically excited thermography. . . . .	14
1.5	Laser line scanning thermography. . . . .	17
1.6	Induction thermography scheme. . . . .	18
1.7	Induction thermography process diagram. . . . .	21
1.8	Thermography tensor representation. . . . .	23
1.9	Binocular vision . . . . .	32
2.1	Phase-shifted induction thermography processing pipeline. . . . .	44
2.2	Tetra-pole inductor. . . . .	46
2.3	Multi-directional induction thermography system setup. . . . .	47
2.4	Multi-directional thermogram. . . . .	48
2.5	Directional phase images on notches. . . . .	57
2.6	Directional Phase contrasts. . . . .	58
2.7	Thermo-inductive phase-shifting . . . . .	58
2.8	Normalized phase-shifted interpolation. . . . .	58
2.9	Phase-shifted optical flow. . . . .	59
2.10	Motion field potential functions. . . . .	59
2.11	Modified fluorescent penetrant inspection TIG Inconel weld. . . . .	59
2.12	Multi-directional DFT in TIG Haynes weld. . . . .	60
2.13	Phase-shifted optical flow vorticity signal profiles. . . . .	60
2.14	Clustered cracks association examples. . . . .	61
2.15	Hit/Miss Probability of Detection. . . . .	61
2.16	Natural weld crack detection. . . . .	62

3.1	Quadratic inductor. . . . .	64
3.2	Schematic diagram for coils in opposite sides. . . . .	65
3.3	Magnetic field direction of two opposing coils. . . . .	65
3.4	Quadratic inductor states. . . . .	67
3.5	Experimental setup. . . . .	68
3.6	Quadratic inductor on notches. . . . .	70
3.7	Notches phase contrast and SNR as a function of relative orientation of magnetic field and crack, $\Psi$ . . . . .	71
3.8	Natural cracks samples. . . . .	72
3.9	Quadratic inductor on steel mooring chain. . . . .	73
3.10	Quadratic inductor on TIG welded hayness sample. . . . .	74
3.11	Steel mooring chain, SNR (dB) and delta phase ( $^{\circ}$ ) with multiple induction combinations . . . . .	76
3.12	Haynes TIG welded probe, SNR (dB) and delta phase ( $^{\circ}$ ) with multiple induction combinations . . . . .	77
4.1	Dynamic multi-directional induction thermography system. . . . .	82
4.2	Dynamic multi-directional induction thermography processing setup. . . . .	83
4.3	Multi-directional thermo-inductive square wave modulation. . . . .	84
4.4	Pseudo-static synchronized thermograms. . . . .	84
4.5	Pseudo-static synchronized thermograms. . . . .	85
4.6	Pseudo-static synchronized thermograms. . . . .	85
4.7	Thermal drift compensation. . . . .	86
4.8	Average oscillating components. . . . .	86
4.9	Samples with natural cracks. . . . .	87
4.10	Registered forged bolt. . . . .	89
4.11	Steel screw FFT Magnitude. . . . .	91
4.12	Steel screw FFT Phase. . . . .	91
4.13	Steel screw Standard deviation, cooling thermogram. . . . .	92
4.14	Steel screw Skewness, cooling thermogram. . . . .	92
4.15	Steel screw Kurtosis, cooling thermogram. . . . .	93
4.16	Steel screw Delta temperature. . . . .	93
4.17	Steel screw PCA component 1. . . . .	94
4.18	Steel screw PCA component 2. . . . .	94
4.19	Steel screw PCT component 1. . . . .	95
4.20	Steel screw PCT component 2. . . . .	95
4.21	Steel screw RPCA low rank, temporal L2 norm. . . . .	96

---

4.22	Steel screw RPCA sparse, temporal L2 norm. . . . .	96
4.23	Steel screw TSR first derivative fitted to cooling thermogram, showing frame corresponding to 25% time of cooling frame. . . . .	97
4.24	Steel screw TSR second derivative derivative fitted to cooling thermogram, showing frame corresponding to 25% time of cooling frame. . . . .	97
4.25	Registered Steel billet. . . . .	99
4.26	Steel billet FFT Magnitude. . . . .	101
4.27	Steel billet FFT Phase. . . . .	101
4.28	Steel billet Standard deviation, cooling thermogram.. . . .	102
4.29	Steel billet Skewness, cooling thermogram.. . . .	102
4.30	Steel billet Kurtosis, cooling thermogram.. . . .	103
4.31	Steel billet Delta temperature. . . . .	103
4.32	Steel billet PCA component 1. . . . .	104
4.33	Steel billet PCA component 2. . . . .	104
4.34	Steel billet PCT component 1. . . . .	105
4.35	Steel billet PCT component 2. . . . .	105
4.36	Steel billet RPCA low rank, temporal L2 norm. . . . .	106
4.37	Steel billet RPCA sparse, temporal L2 norm.. . . .	106
4.38	Steel billet TSR first derivative fitted to cooling thermogram, showing frame corresponding to 25% time of cooling frame. . . . .	107
4.39	Steel billet TSR second derivative fitted to cooling thermogram, showing frame corresponding to 25% time of cooling frame. . . . .	107
5.1	Visibility as a bipartite graph. . . . .	116
5.2	System overview. . . . .	117
5.3	Visibility evaluation. . . . .	119
5.4	Camera sampling. . . . .	121
5.5	Optical axes grid parameters in SE(3). . . . .	122
5.6	Hierarchical binning of optical axes. . . . .	123
5.7	Local axes adjacency. . . . .	124
5.8	Sparse visibility bipartite graph with extrapolated edges. . . . .	125
5.9	Scan sequencing. . . . .	130
5.10	Synthetic coverage sequence. . . . .	131
5.11	Robotic 3D inspection setup. . . . .	134
5.12	Synthetic scan VS real clouds. . . . .	135
5.13	Evaluated coverage sequence and displacement errors. . . . .	136
5.14	Reconstructed model. . . . .	137



# List of tables

2.1	Magnetic field orientations as a function of the activation of the coils. . . .	46
2.2	Experimental parameters . . . . .	48
2.3	Hit/Miss Probability of Detection summary. . . . .	56
3.1	Natural crack recall, hayness sample. . . . .	75
4.1	Forged bolt SNR . . . . .	89
4.2	Steel billet SNR . . . . .	99
5.1	Gocator 3520 view-frustum parameters. . . . .	119
5.2	Synthetic VPP comparison. . . . .	132
5.3	Robot view-planning parameters. . . . .	134





# Nomenclature

## Acronyms / Abbreviations

AABB Axis aligned bounding box

AUC Area under curve

AUV Autonomous underwater vehicle

BSP Binary space partitioning

CDBN Convolutional deep belief network

CDF Cumulative density function

CFRP Carbon fiber reinforced polymer

CI Confidence interval

CNN Convolutional neural network

CRS Compressed row sparse

CTSP Clustered travelling salesman problem

DFT Discrete Fourier Transform

DIT Dynamic induction thermography

ECI Eddy current inspection

ECT Eddy current thermography

EDM Electrical Discharge Machining

EL Electro-luminescence

FFT	Fast Fourier Transform
FK	Forward kinematics
FMT	Frequency modulated thermography
FPA	Focal plane array
FWHM	Full width at half maximum
GFRP	Glass fiber reinforced polymer
GRASP	Greedy randomized adaptive search procedures
HOS	Higer order derivatives
IK	Inverse kinematics
IT	Induction thermography
LPT	Liquid penetrant testing
LST	Line scan thermography
LT	Lockin thermography
MDP	Markovian decision process
MFT	Multi-frequency Thermography
MLP	Multi-layer-perceptron
MPI	Magnetic particle inspection
MSE	Mean square error
NBV	Next best view
NDE	Non destructive evaluation
OBB	Oriented bounding box
OD	Optical density
OF	Optical flow
PCA	Principal component analysis

---

PCT	Principal component thermography
POD-HM	Hit miss probability of detection
POD	Probability of detection
PT	Pulse thermography
RL	Reinforced learning
RPCA	Robust principal component analysis
RTSP	Robot travelling salesman problem
SAU	Self-attention unit
SCP	Set cover problem
SDF	Signed distance function
SIB	Semi-infinite body
SIT	Static induction thermography
SNR	Signal-to-noise ratio
SST	Spot scan thermography
TDC	Thermal drift compensation
TIG	Tungsten inert gas
TSP	Travelling salesman problem
TSR	Thermal signal reconstruction
UAV	Unmanned aerial vehicle
UGV	Unmanned ground vehicle
UT	Ultrasonic testing
VPP	View planning problem



# Introduction

## Motivation

The growth in the industry of non-destructive inspection techniques and dimensional control presents continuous challenges in which these processes are expected to be automated on a shorter time span and meet increasingly demanding requirements.

In particular, surface integrity induction thermography is a technique that allows localized heating in surface and subsurface defects, which can be detected with an infrared camera. In this sense, defect detection is highly sensitive to the relative position of conventional induction systems which ultimately requires multiple thermographies rotating the induction system for cracks with unknown defect orientations, thereby extending inspection times.

On the other hand, the automation of surface inspection itself may be an aspect that requires experts for the inspection of complex geometries, leading to a lengthy automation process spending many resources.

As this is a dual problem linked to the requirements of the inspection technique and automation itself, a series of issues affecting induction thermography and the procedural automation of dimensional inspection have been addressed in this thesis.

This thesis deals with this problem by making contributions in the field of induction thermography that enhance the technique with systems allowing multi-directional inspection. To achieve this, a new inductor design, a multi-directional induction system capable of generating thermographies equivalent to the rotation of the system, and a new method enabling continuous multi-directional scanning of the surface of the pieces to be inspected have been proposed.

The second aspect aimed at improving the automation of inspections involves the development of a system that generates robot inspection trajectories for dimensional inspection with a 3D scanner on arbitrary geometries. This system has several improvements over classical systems, enabling a reduction in robot planning time from hours to just over a second, without any human intervention.

## Contributions

Considering the context of this thesis, the contributions are aimed at improving the induction thermography, and the automated 3D inspection planning.

Induction thermography is an inspection technique which is able to identify superficial and subsuperficial defects, but in many cases, the identification of cracks depends on the relative orientation of the crack regarding the magnetic field generated by the induction system. In this scenario, a novel multi-directional induction thermography scheme has been presented, which is able to induce a magnetic field on four directions, inducing eddy currents with varying distributions which are mostly affected by the presence of defects. This results in varying thermal responses of each directional thermography, which exhibit an new feature that has not been previously described, consisting on the apparent rotating motion of the typical defect pattern on thermal phase-image. As a result, the thermal response associated to the defects can also be determined by the variation of the thermal response as a function of the magnetic field orientation, which effectively increase the available information for data mining and detection on induction thermography. This novel induction thermography scheme and a novel processing method exploiting this rotating feature of defects has been presented. It generates a heat map of the most probable locations of defects. The quantification of this method has been evaluated with a probability of detection (POD) in two sets of samples, with more than 400 cracks combined, comparing the proposed technique to the manual labelling of phase images, yielding an improved detection. This can be explained taking into account that some crack patterns not visible on a the separated phase images, but its rotational motion yield a significant signal. This multi-directional induction system employs an existing tetra-pole inductor which can be used in this manner, but the resulting thermal distribution is mainly concentrated on the proximity of the coils which is not optimal for induction thermography. To address this problem, a novel inductor has been proposed inducing a more uniformly directional magnetic field allowing for greater coverage and and its usage on multidirectional schemes. Another problem which has been addressed in this thesis is the detection of cracks with unknown directions on a scan thermography. Scan thermography enables the continuous inspection of a surface without having to stop the recording throughout the whole inspection. The novel method introduces a new system for dynamic thermographic inspections, alternating the orientation of the magnetic field while the system is moving regarding the surface. To enable the extrapolation of existing thermal processing methods, a novel a normalized space-time fusion has been proposed. This novel method reduces inspection times, avoiding any thermographic dead time associated with coverage movement and inductor physical rotation.

These contributions are focused on the induction thermography itself, considering the automation and path planning for complete coverage of the inspected part as another process. Taking into account that this aspect of the automation is a lengthy process, requiring many resources, a procedural 3D inspection robotic path-planning for arbitrary geometries has been proposed with multiple contributions over existing methods aimed at improving the runtime of the planning and inspection itself. This procedural inspection system, or view planning, incorporates algorithmic improvements that reduce the search space through combinatorial clustering, and enhancements in the dual optimization of robot inspection time and capture pose selection, demonstrating effectiveness in field tests with complex geometries and a 12-axis kinematic chain.

## Structure

The structure of the thesis starts with a literature review (chapter 1) of inspection techniques, with an emphasis on thermography and specifically on induction thermography, as well as the view planning problem (VPP). From Chapter 2 to Chapter 5 thermography issues are dealt, while the last chapter, Chapter 6, tackles a general procedure for the definition of an optimized surface inspection. It is a completely general chapter, that can be applied to thermography as well as other inspection techniques like vision.

- Chapter 2 presents a new multi-directional induction system for induction thermography. This system allows the generation of directional thermographies, exhibiting a rotation pattern, which has not been observed previously, that has led to the development of a novel processing method, demonstrating a higher detection probability compared to separate analysis. This system, in turn, enables an inspection equivalent to rotating the inspection system, thereby reducing the automation process.
- Chapter 3 details the development of a new type of inductor that induces a more uniformly directional magnetic field than conventional alternatives with a fixed magnetic field. This allows for greater coverage and facilitates the use of multidirectional schemes, as the one proposed in the previous chapter.
- Chapter 4 introduces a new system for dynamic thermographic inspections, alternating the orientation of the magnetic field simultaneously. A space-time fusion is applied, generating a set of processable directional thermographies with conventional thermographic algorithms. This further reduces inspection times, avoiding any thermographic dead time associated with coverage movement and system rotation.

- Chapter 5 presents a new system for planning the 3D robotic inspection trajectory of arbitrary geometries. It incorporates algorithmic improvements that reduce the search space through combinatorial clustering. Additionally, it includes enhancements in dual optimization of robot inspection time and capture pose selection, demonstrating effectiveness in field tests with complex geometries and a 12-axis kinematic chain.



# Chapter 1

## State of the art

In this section, a set of techniques most commonly employed for inspection is listed with the aim of identifying dimensional and/or structural defects on the surfaces of interest. The techniques are described along with their underlying physical principles, as well as the limitations and challenges associated to its industrialization.

The structure is based on the type of techniques, starting with destructive inspection methods followed by non-destructive ones. Non-destructive techniques are further categorized into three blocks: sec. 1.1 conventional non-destructive methods, sec. 1.2 visual and geometric methods, sec. 1.3 those based on active and passive thermography. Sec. 1.4 deals with Probability of detection analysis, a procedure to help to quantify the confidence in the ability of a testing technique to detect defects of different sizes reliably. Finally, sec. 1.5 contextualizes all the View Planing procedure.

### 1.1 Destructive testing

In this section, various use cases of the main destructive inspection methods employed in the industry are presented, along with the most common defects associated with each of the mentioned materials. These techniques are often considered the "golden standard" for determining mechanical properties and detecting defects in many cases.

One notable approach involves the use of residual stress tests, such as drilling a series of holes, where stress is measured using a strain gauge [1]. In the case of welded joints, the appearance of any defect can alter the internal distribution of these stresses, attributed to factors such as burn-through, lack of fusion, lack of penetration, and slag in arc welding. Laser welding, on the other hand, commonly exhibits defects such as marginal oxidation incisions, undercuts, depressions, induced porosity, solidification cracking associated with excessive tensile strain stress, blowouts, and underfills, among other types of defects.

For common composite materials like Carbon Fiber Reinforced Plastic (CFRP) or Glass Fiber Reinforced Plastic (GFRP), the use of tensile and fatigue tests is widespread due to the numerous defects associated with their manufacturing and life cycle, such as delamination, external impact, barely visible impact damage (BVID), interlaminar disbonds, porosities, or matrix cracking. Considering another common process like forging, tensile [2] or fatigue [3] tests allow the determination of certain properties of the resulting pieces. In this context, common defects are often associated with unfilled sections, cold shuts, scale pits resulting from improper surface cleaning, misalignments of the dies, flaking associated with abrupt cooling, and surface cracking, among others. Furthermore, casting processes can yield various defects such as gas porosity, improper shrinkage, mold defects, among others, which can impact their properties. Compressive testing [4] in this context reveals the material's behavior under a compressive load.

In the case of joining different materials, the use of special adhesives is common, benefiting from the majority of the listed techniques [5]. Additionally, peel tests, as in Mondon et al. [6], are often conducted, and their results can indicate defects present in the adhesive, such as porosity, voids, poor curing, and improper thickness, among others.

## **1.2 Conventional non-destructive testing**

In this section, various non-destructive techniques are outlined, often conforming to international standards and demonstrating decades of use in the industry.

### **1.2.1 Liquid penetrant testing**

Liquid penetrant testing (LPT), is a conventional non-destructive technique (NDT) employed for the detection of surface defects mainly on non-ferromagnetic materials. It consists on the application of a low-viscosity fluorescent liquid that permeates the cavities of surface cracks after a specified time, as determined by the standard which depend on the capillarity, viscosity, and surface tension of the liquid. Subsequently, excess liquid is removed, and a developer is applied, causing the impregnated liquid to emerge from the cracks, facilitating their identification under ultraviolet light.

This method is capable of detecting various discontinuities, including fatigue cracks, shrinkage cracks, porosity, laps, and seams. It also provides an indication of a lack of bonding between joined metals.

However, this process has certain drawbacks. The impregnation time is on the order of minutes, it is not applicable to porous materials, and the repeatability of the process

depends on the skill and conditions of the inspector. Additionally, it requires prior cleaning, a temperature range between 4 and 50 °C, and the use of consumables that may cause skin irritation [7] and eye damage due to ultraviolet radiation.

Figure 1.1 displays a TIG welded Hayness samples used on this thesis subjected to LPT, (a) after the application of the developer imaged with a  $7 \mu\text{m}/\text{px}$  resolution Leica microscope on a TIG weld of a Hayness sample and (b) the same sample under white light on the visible spectrum.

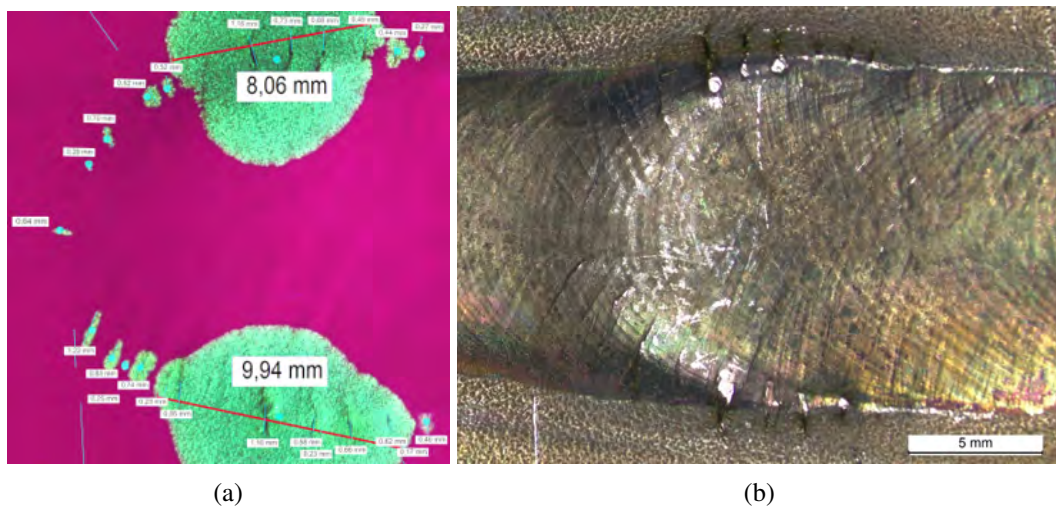


Fig. 1.1 TIG welded Hayness 282 sample with multiple concentric cracks (a) under UV light after the developer application of a LPI, and (b) visible with white light.

### 1.2.2 Magnetic particles inspection

Magnetic Particle Inspection (MPI) is a NDT method used to detect surface and near-surface defects in ferromagnetic materials. The magnetization of a cracked surface covered by magnetic particles suspended in a liquid or dry powder form, provokes its accumulation in the proximity of the discontinuities where the flux leakage of the magnetic field is higher. Considering that the magnetic field disturbance depends on the relative orientation of the cracks, it is necessary to repeat the test in at least three directions with a  $45^\circ$  separation. Under these conditions, the localized concentration of the particles can be clearly identified with ultraviolet light. The inspection of coated materials or subsurface defects with a depth of 2 mm in some cases are the main benefits compared to LPI in ferromagnetic materials. Automated MPI systems are available, but most of the drawbacks of LPI remain. Fig. 1.2 displays an example of a magnetic particle inspection (MPI), with a mooring chain fragment under UV light (a), and the corresponding photograph (b).

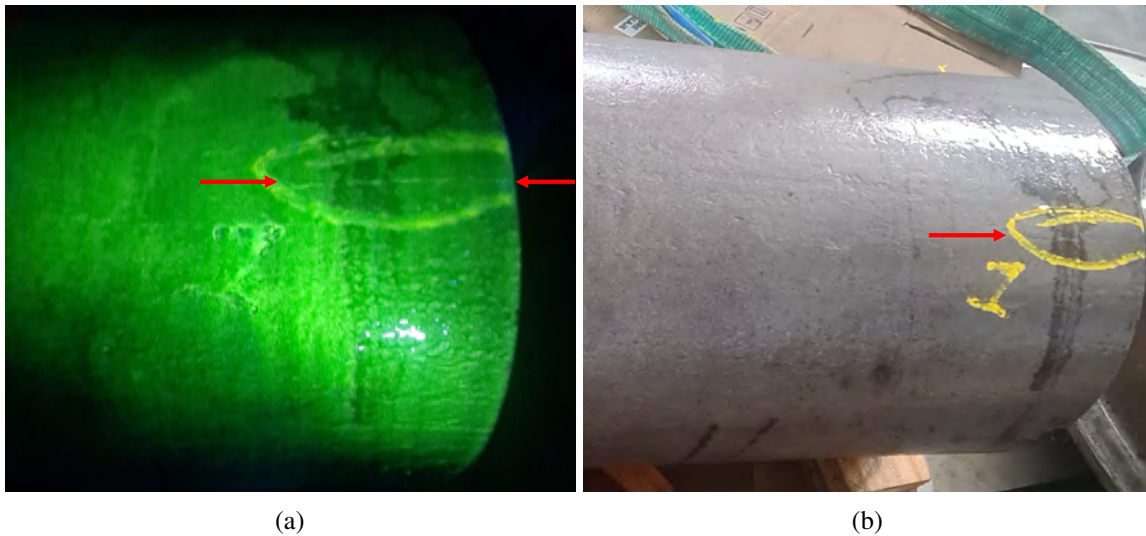


Fig. 1.2 Magnetic particle example. (a) MPI fluorescent image of the same sample. (b) Photo of a mooring chain fragment.

### 1.2.3 Eddy currents inspection

Eddy current inspection (ECI) is based on the perturbation of Eddy currents around defects. This technique relies on two coils, a primary which generates a magnetic field near the surface, inducing Eddy currents, and a secondary which is induced by the electric field of those currents. The induction frequency of the primary coil conditions the depth at which the Eddy currents are induced, but in most commercial probes, it operates with a frequency range between 1 and 2 kHz.

The alterations in these currents correlate with the voltage measured by a secondary coil, which depends on the electrical conductivity, magnetic permeability, geometry, and material. The correlation between the current induced by the primary coil and measured on the secondary is consistent in the absence of defects, but it is important to note that the induced currents are tangential to the coil's center, which can affect crack detection depending on its relative position. Both coils are typically assembled on the same probe which is swept through the inspected surface, and the alteration of the induced voltage of the secondary coil associated to a defect is instantaneous which makes this technique suitable for online inspection and monitoring.

Another advantage is it does not require cleaning the surface and it is applicable at high temperatures, also allowing measurement of other material properties such as tensile strength [8]. Furthermore, it is noteworthy that, depending on the material's skin depth, the technique can have a detection capability of several millimeters in depth. However, it can only be

applied to conductive materials which are mainly orthogonal to surface, and the variations in magnetic permeability and surface uniformity complicate signal interpretation, as seen in welding scenarios. Additionally, it's worth mentioning that the inspection area coverage can be increased with a coil array. Nevertheless, in this scenario the signal interpretation becomes more complex, and the setup time for inspection is longer.

### 1.2.4 Ultrasonic testing

Ultrasonic testing (UT), is one of the most widely used techniques [9] applicable to a variety of materials. Ultrasonic waves propagate through a material until they encounter a medium discontinuity, such as air, at which point they reflect back to the source. Analysis of these reflections allows for the measurement of depth and, in some cases, triangulation of their position.

An ultrasonic transducer captures this signal, coupled to the material using a couplant, such as water or oil, to improve signal transmission. The signal can be received either through reflection if the probe is close to the emitter or through attenuation if it is separated. The emitter typically operates in the range of 0.5 to 15 MHz.

Another possible improvement is the employment of angle beam probes can also be employed, allowing the waves to propagate at an angle different from the normal, enabling the detection of inclined cracks and providing other advantages. Furthermore immersion of the component can act as a couplant. The use of multiple piezoelectric crystals that transmit and receive independently at different times allows the coverage of a higher area, while at the same time it enables the creation of constructive interference in the wavefronts which enables the beam to be focused on a wider range of depths and incident angles. Another option involves employing a pulsed laser for non-contact vibration generation, which is then captured using a laser doppler vibrometer. It's important to note that the detection of deep defects depend considerably on the geometry of the component, often requiring customized processing for each specific case.

## 1.3 Thermography

This section provides a concise overview of various active thermography techniques, [10] with a particular emphasis on induction thermography.

Initially, a brief introduction of the thermography as non destructive testing is exposed, followed by a short overview of the most common infrared detectors. Subsequently a description of the prevalent heating sources and excitation modalities commonly employed in

active thermography is shown. And lastly, a succinct overview is provided for the processing algorithms commonly utilized.

### 1.3.1 Thermography as a non destructive testing

In the presence of any temperature difference between two media, there is a thermal transfer that can occur through convection, radiation, or conduction. It is the latter that, in most cases, enables the use of thermography as a non-destructive inspection method. The fact that thermal conductivity varies in the presence of internal inhomogeneities or cracks compared to the surrounding material causes a localized temperature difference.

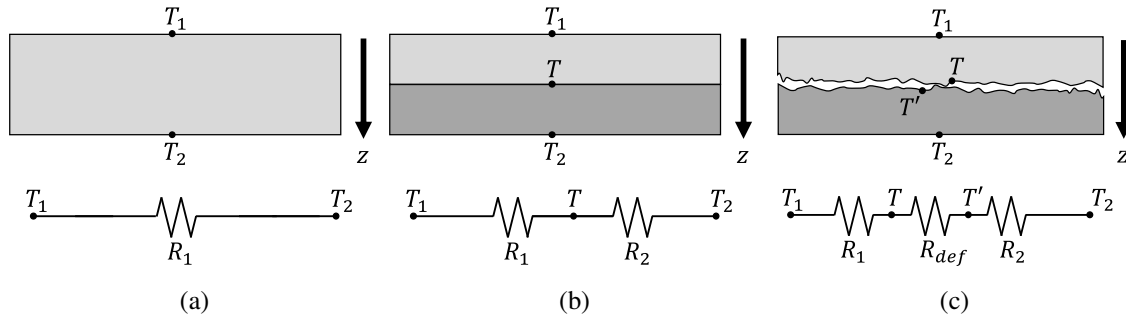


Fig. 1.3 Steady-state heat conduction through solid. (a) Linear heat conduction as thermal resistance. (b) Two materials with a perfect thermal interface. (c) Cracked block.

Given a solid block with thickness  $L$  as an example, as depicted in Figure 1.3a, with two opposite faces along the  $z$ -axis at different temperatures  $T_1$  and  $T_2$ , the amount of lost energy  $q$  is:

$$q = \frac{T_1 - T_2}{z} \lambda = \frac{T_1 - T_2}{R_{th} A} [W] \text{ with } R_{th} = \frac{z}{\lambda A} [K/W] \quad (1.1)$$

where,  $\lambda [W/mK]$  is the thermal conductivity,  $R_{th} [K/W]$  is thermal resistance, and  $A$  is the area. In this scenario, the temperature variation is linear along  $z$ , allowing the establishment of a steady-state analogy with the laws of electricity. In this context, the perfect union of two materials in one dimension acts as a pair of thermal resistances in series as shown in fig. 1.3b. Thus, the presence of any cavity or inhomogeneity in the material can be interpreted as the presence of an intermediate resistance, leading to a noticeable temperature difference, as shown in fig. 1.3c.

The transient three dimensional heat diffusion is typically integrated with the Fourier heat conduction equation, which considers an external heat source  $Q^H$ , by integrating the

temperature of the following expression:

$$\frac{\partial T}{\partial t} = \alpha \nabla^2 T + \frac{Q^H}{\rho c} \quad (1.2)$$

where  $\alpha = \frac{\kappa}{\rho c}$  [ $m^2/s$ ] is the thermal diffusivity,  $\kappa$  [ $W/(mK)$ ] is the thermal conductivity,  $\rho$  [ $kg/m^3$ ] is the density,  $c$  [ $J/(kgK)$ ] is the thermal capacity, and  $\nabla^2 T = \left( \frac{\partial^2 T}{\partial x^2} + \frac{\partial^2 T}{\partial y^2} + \frac{\partial^2 T}{\partial z^2} \right)$  is the Laplacian of temperature.

The recording of thermal diffusion in the absence of any external heating is referred to as passive thermography. Another aspect to consider is that the thermal radiation  $q_{rd}$  perceived by the camera depends on the absolute temperature  $T$  and emissivity  $\varepsilon$  as stated by the Stefan-Boltzmann (SB) law,

$$q_{rd} = \varepsilon \sigma_{SB} T^4 \quad (1.3)$$

, with  $\sigma_{SB}$  being the SB constant. On certain occasions, the variation in emissivity itself allows the presence of contamination from other materials without any thermal variation, such as the detection of slag present in molten metal in various steelmaking processes [11]. But in most cases, some form of thermal variation associated with an external source must be present to measure temperature differences associated to defects, such as the in-situ thermographic inspection of wind turbine blades, which is preferably conducted during sunrise or sunset [12], with temperature differences of up to 20°C depending on the side exposed to the sun. This allows for the detection of deeper defects. Many examples of passive thermography rely on pre-existing heating, such as the inspection of transformers [13], thermal leakage in facades [14], as well as the inherent heating in manufacturing processes like TIG welding [15] or friction stir welding [16], among others. Considering that passive thermography does not have the ability to exercise a control over the thermal propagation and its interaction with defects, meticulous consideration becomes imperative when selecting optimal capture conditions, cameras, and filters.

In many instances, manufacturing processes do not generate any residual heating, as observed in the manual formation of laminated composites, commonly employed in the aeronautic sector which are commonly required to comply with strict regulations regarding surface integrity. Conversely, the underlying thermal variations of some processes such the welded joining of steel, hinder any signal attributable to small defects.

Therefore, the direct control of the thermal excitation enables the optimization of the inspection to a broader range of defects and materials.

In the following section, a brief review of the most common focal plane arrays (FPA) present in infrared cameras will be presented (sec. 1.3.2). The subsequent three sections



discuss various thermal sources along with their respective modulation methods. Starting with thermo-optical excitation sources (sec. 1.3.3), which are prevalent in many use cases and employ most of the excitation modalities, they are going to be presented in the first place. Afterwards the induction thermography (sec. 1.3.4) is covered with a in more detail. And lastly, other active thermography methods are briefly reviewed (sec. 1.3.5).

And the final section addresses the thermographic processing methods that enable the extraction and data mining of the signals associated with defects (sec. 1.3.6).

### 1.3.2 Infrared detectors

An overview is presented of the most common infrared detectors focusing on the focal plane arrays (FPA) found in the majority of commercial thermographic cameras that rely on the thermal or photonic detection. FPA [17, 18] sensors are commonly used in this technique to measure the temperature over a certain area to detect the presence of defects. Although these sensors are capable of detecting infrared radiation, which is evidently correlated with temperature, they present a series of challenges that hinder the precise determination of temperature. Some of those problems which are common for all these sensor, are intrinsic to the thermographic system, which include the vignetting effect, nonuniform spectral response, nonlinear response within the dynamic range of the instrument, mechanical vibrations from external actuators used for scanning, vibrations from cooling systems, restricted depth of field associated to the wide aperture of the lenses required to increase the thermal signal, as well as the Narcissus effect where the detector perceives its reflection in the optics, among other factors. It is important to highlight that the calibration procedures commonly employed to estimate the temperature from the raw sensor readings are not discussed here.

#### Thermal detectors

The most widely available and affordable sensors are based on the transduction of the thermal radiation using a bolometer [19]. A bolometer is a resistive sensor that exhibits linear changes in conductivity in response to small temperature variation, it is composed by a heat absorber adhered to a sensitive layer. The arrays of monolithic microbolometers which are micromachined in silicon have typically a sensitive layer made out of vanadium oxide (VOx) or amorphous silicon with a small thermal capacity to enable a fast thermal response [20]. The pixel pitch of each microbolometer are on the order of the microns which allow for high resolution sensors. They can have a broadband sensitivity range and are able to operate at room temperature with sensitivities of ranging from 20 to 40mK depending on the sensor pixel pitch.



### Photonic detectors

These sensors are based on the excitation of the incident photons, which are mainly categorized in two groups, photovoltaic and photoconductive sensors [21]. They typically require an active cooling to 90K or lower temperatures to avoid the dark currents, [22]. Considering that these sensors directly absorb the projected photons, without any heating of the device itself, they exhibit a reduced latency and higher sensitivities of up to 10 mK compared to a bolometer.

However, their applicability is limited to a narrow wavelength range, determined by the materials used. Typically, these materials include indium antimonide (InSb) with a wavelength range of 3-5  $\mu\text{m}$ , mercury cadmium telluride (MCT) with ranges of 3-5  $\mu\text{m}$  and 8-12  $\mu\text{m}$ , or lead sulfide (PbS) up to 3  $\mu\text{m}$  [21]. Commercial cameras employing these sensors are more expensive compared to the cameras employing microbolometers, and the required cooling results in a heavier device which limits the scope of their practical applications.

### 1.3.3 Optically excited thermography

There are many sources to optically heat a surface by projecting a light, associated with different types of sources. Whether it's with a lamp, with a pulsed heating with a very short full width at half maximum (FWHM) pulse ranging from 0.1 to 50 ms, or an extended heating covering a specific area. Laser sources are also common to project a point or line that scans the surface to be inspected.

The following sections will cover the most common excitation modalities used with these light sources to heat the surface for an active thermography non-destructive evaluation.

#### Pulsed and step heating thermography

One of the most commonly used sources for thermographic excitation involves the use of tungsten halogen lamps or similar alternatives that project light onto the surface. This projection can cover either a static area [10], a line [23] or a point [10]. Additionally, there is the option of capturing temperature from the same side as the projector, i.e., by reflection, or alternatively by transmission.

The typical setup is illustrated in fig. 1.4, which comprises two lamps heating the surface and an infrared camera measuring the temperature. Both are synchronized and controlled by a signal generator, with a PC recording and processing the thermography.

One of the most common methods to induce thermal excitation is to induce an instantaneous heating, ideally modeled as a Dirac delta function, on a semi-infinite body (SIB) with

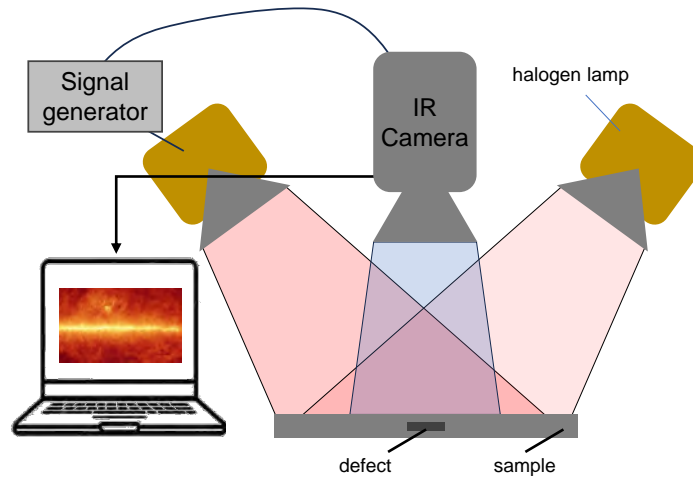


Fig. 1.4 Optically excited thermography.

depth along  $z$  axis. The model presented by [24] introduces an analytical function for the thermal evolution at the surface as a function of depth, as shown in the following expression:

$$T_{sib}(z, t) = \frac{Q}{\lambda} \sqrt{\frac{\kappa}{\pi t}} \exp\left(-\frac{z^2}{4\kappa t}\right) \quad (1.4)$$

Here,  $Q$  is the amount of energy,  $\lambda$  [ $\frac{W}{mK}$ ] is the thermal conductivity,  $\kappa$  [ $m^2/s$ ] is the thermal diffusivity, and time is referenced after the pulse. Considering the temperature at the surface ( $z = 0$ ) on a logarithmic scale in time and temperature, it results in the following expression:

$$\ln(T_{sib}(z = 0, t)) = -\frac{1}{2} \ln t + \ln\left(\frac{Q}{\lambda} \sqrt{\frac{\kappa}{\pi}}\right) \quad (1.5)$$

Equation 1.5 has a slope of  $-1/2$  in the early moments after cooling. This has led to the development of various processing methods that identify any subsurface anomaly in relation to the variation with respect to that slope [10].

Although the diffusion speed of an instantaneous pulse is very fast, the amount of energy that penetrates the material may be limited based on depth. Furthermore, the amount of energy projected in a pulse is reduced, so the energy penetration ratio up to a certain depth may be insufficient to discern a temperature variation associated with deep defects. Additionally, the use of high-power flashes may be limited in certain situations due to their volume, cost and electrical source. Therefore, extended heating, or Step Heat Thermography, is a viable solution in many cases [25, 26].

### Lockin thermography

Another typical excitation modality employing halogen tungsten lamps and induction thermography, among other excitation sources, consists on the periodic heating with a fixed frequency sinusoidal wave, first described by Carlomagno and Berardi [27] and later developed by Busse [28] among others. It is based on the dispersion of highly attenuated thermal waves inside the material which is a phenomenon first described by J. Fourier [29]. The thermographic system is coupled to a thermal wave source which yields a periodical transfer of heat at the surface (depth  $z=0$ ), which is modelled describing the temperature decay in one dimension, as a function of the depth  $z$  and starting temperature  $T_0$ , with the following expression from [28],

$$T(z,t) = T_0 e^{-z/\mu} \cos\left(\frac{2\pi z}{\lambda} - 2\pi f t\right) = T_0 e^{-z/\mu} \cos(\phi(z) - 2\pi f t) \quad (1.6)$$

Here,  $\mu$  is the thermal diffusion length as,

$$\mu = \sqrt{\frac{\kappa}{\rho c \pi f}} = \sqrt{\frac{\alpha}{\pi f}} \quad (1.7)$$

, with  $\kappa$  being the thermal conductivity,  $\rho$  the density and  $c$  the specific and  $\alpha = \frac{\kappa}{\rho c}$  the thermal diffusivity. The resulting thermal wavelength is  $\lambda = 2\pi\mu$  with a propagation speed of the waves  $v = \lambda f = 2\sqrt{\pi f \alpha}$ .

Considering eq. 1.6, the phase can be expressed as a direct function of the depth and thermal diffusion length:

$$\phi(z) = \frac{2\pi z}{\lambda} = \frac{z}{\mu} \quad (1.8)$$

Taking into account that  $\mu$  is inversely proportional to the square root of the modulation frequency, the higher the modulation, the shallower the propagation would be, and on the contrary, the lower frequencies will reach higher depths but at a slower pace.

It is worth considering that the propagated thermal wave inside the object is reflected when it reaches inhomogeneities, creating an oscillating interference pattern which is clearly reflected on the frequency domain of the thermogram as a variation in the phase and amplitude, compared to a sound area.

Subsequently, the details of the different processing techniques will be outlined, many of which assume that the sample is thermally on a steady-state. In this regard, Breitenstein et al. [30] proposes a decomposition of the thermogram as the sum of a linear, continuous, and oscillatory component. The latter has a waveform similar to that of the steady state,

allowing for the cancellation of thermal variation between pulses. This, in turn, decreases the amplitude and phase image distortions.

It is also possible to continuously integrate the thermal signal to generate both the real and imaginary component referenced to a square-wave with the same modulation frequency, which makes this technique feasible for continuous online scanning and defect monitorization on electronic devices [30].

Another aspect to consider is that the heat source must be calibrated to ensure a proportional energy regarding the modulation, as well as a uniform radiation across the entire surface [10].

### **Frequency modulated thermography**

Other excitation methods recur to a frequency modulated thermography (FMT) [31], enhancing the depth estimation on CFRP flat bottom holes, employing both a time-domain Hilbert transform as well as a FFT for the analysis of the thermography. Mulaveesala et al. [32] and D'Accardi [33] reported a multi-frequency thermography system (MFT), modulating the activation of the lamps using two superimposed square-wave signals with two different frequencies to inspect a CFRP sample. Betta et al. [34] discussed the frequency modulated thermography on an induction thermography system, employing both a multi-tone modulation signal based on the summation of a discrete set of sinusoidal signals, as well as a chirp signal which continuously increases the frequency. Their results shows an increased SNR in both FMT modes, compared to a single frequency excitation, as well as the partial dimensional extraction of defects, which can be explained by the varying thermal diffusion lengths associated to the modulation frequency.

### **Line and spot scan thermography**

Most of the thermal diffusion associated with the projection of light onto a surface spreads primarily along the surface normal. This makes it ideal for detecting defects parallel to the surface at the expense of reducing the capability to detect defects normal to it [10].

In this regard, the scanning of a point or point from a laser or halogen source provokes a lateral thermal propagation that is disrupted by the presence of any type of defect, enabling the generation of thermal gradients that interfere with the plane perpendicular to the surface. As a result, spot scan thermography (SST) [35] and line scan thermography (LST) [36] use a laser enabling the emission of coherent light with a uniform optical density (OD) compared to an halogen lamp projected on a line.

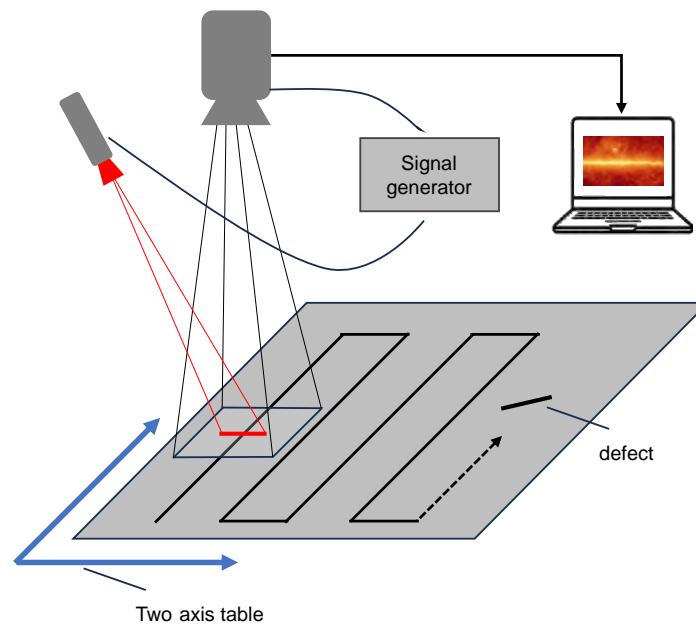


Fig. 1.5 Laser line scanning thermography, with the inspected surface on a 2 axis table, moving on a raster pattern relative to the camera and laser line controlled by a signal generator and a PC retrieving the infrared video.

A common scheme of LST employing a laser is shown in fig. 1.5, covering the surface with a planar raster trajectory.

The thermal response associated with a defect can be identified by both the change in the heating pattern of the scanned area and a sharp temperature variation, with the "Thermal barrier" effect [37, 38] being a common example for detecting cracks perpendicular to the plane.

Another aspect to consider is that the relative motion between the camera and the surface, requires a robust registration to common reference to be inspected. This is done to generate a pseudo-static thermal sequence with thermograms of each point associated with a common temporal reference.

Several laser-based systems have been demonstrated, projecting a point [35] and a line [36], with some systems scanning a large composite surface with the laser and camera mounted on a robot [39], as well as the employment of laser arrays for a rapid inspection [40]. Additionally, there are alternative laser excitation modalities employing lock-in modulation of the intensity [41, 37], which are able to generate a thermal wavefield, enhancing the detectability of cracks, irrespective of the presence of arbitrary surface patterns.

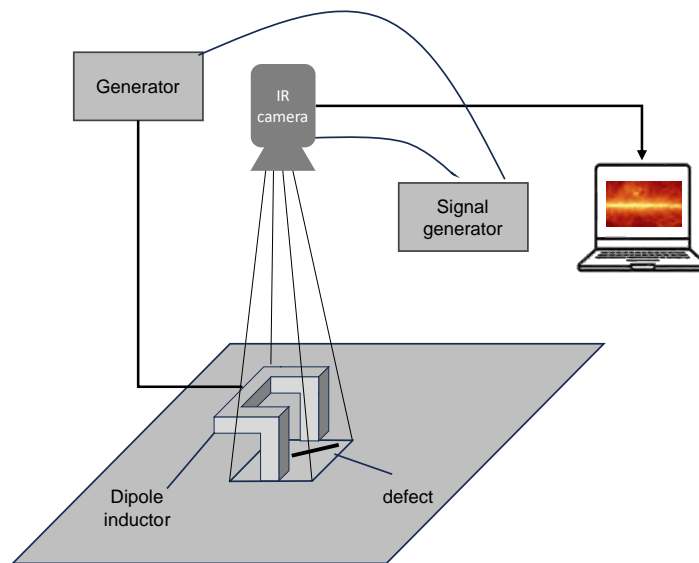


Fig. 1.6 Induction thermography, employing a dipole inductor powered by generator with a window for direct sight from IR camera.

### 1.3.4 Induction thermography

As previously exposed for the case of Eddy currents testing (ECT), the induced currents interact with defects, generating a measurable local electric field with a probe. In the case of induction thermography, an alternating magnetic field is induced with an inductor located next to the surface, causing superficial and subsuperficial heating captured by the FPA of an infrared camera.

Induction thermography (IT) uses a probe comprised of a coiled conductive piece of wire close to a test surface to generate Eddy currents. In essence, exciting a time varying current on the coil to generate a magnetic field, with a frequency ranging from 10 to 500 kHz. In the proximity to the test surface, the magnetic field interacts with the test part inducing Eddy currents running opposite to the currents in the probe. Fig. 1.6 displays an induction thermography setup with dipole inductor next to the inspected surface with an opening to enable the direct line of sight of infrared camera.

This intense magnetic field, rapidly magnetizes and demagnetizes the surface. In the presence of any abrupt change in magnetic permeability, as is the case with material inhomogeneities or sudden variations in geometry, a the magnetic field is partially leaked [42]. This is primarily due to magnetostrictive moved dislocations associated with internal friction damping [43], which ultimately results in a localized heating. The alternating magnetic field also produces a field of Eddy currents orthogonal to it, due to the electromotive force exerted on the free electrons of the material as the magnetic flux changes. The density of the Eddy

current field  $J$  decreases exponentially with respect to the depth  $z$ , following

$$J = J_s e^{-\frac{(1+j)z}{\delta}} \quad (1.9)$$

, where  $J_s$  is the surface density and  $\delta$  is the skin depth. The skin depth represents the depth at which  $J$  decreases to  $J_s/e$  and is defined as  $\delta = (\pi\mu_0\mu_r\sigma f)^{-1/2}$ , where  $\sigma$  is the electrical conductivity,  $\mu_0$  is the magnetic permeability in a vacuum, and  $\mu_r$  is the relative permeability. On the other hand, induced currents are affected by abrupt changes in conductivity and magnetic permeability, which may be associated with the defects. Thus, the presence of a crack that interrupts the currents will cause them to deviate around it, creating zones with higher and lower current density.

The non-zero resistivity of the material produces Joule heating radiation and in particular, test-parts discontinuities, such as cracks produce a noticeable change in the radiated heating distribution. Taking into account that the current flows through a material with a certain resistance  $R$ , Joule heating will occur, which can be approximated with the following expression for a linear conductor

$$Q^H [W] = I^2 R t \quad (1.10)$$

, where  $I$  is the current,  $t$  is the time. The resistance can be described as  $R = L/(\sigma S)$ , where  $L$  is the length of the conductor,  $S$  is its cross-section area, and  $\sigma$  is the electrical conductivity. The electrical conductivity at a temperature  $T$  can be approximated with respect to a conductivity  $\sigma_0$  measured at another temperature  $T_0$  with the following expression  $\sigma = \sigma_0(1 + \alpha(T - T_0))^{-1}$ , where  $\alpha$  is the temperature coefficient of resistivity. This current can be expressed in terms of density as  $I = J_s S$ , where  $S$  is the cross-section area through which it flows.

Considering the above, the terms of Joule heating can be substituted in terms of  $J$ . Thus,

$$Q^H = (J_s S)^2 \frac{L}{\sigma S} t = \frac{J_s^2}{\sigma} V t \quad (1.11)$$

where the volume is  $V = L S$ , and  $\sigma$  is the electrical conductivity. Considering this expression per unit time and volume, we have  $Q^H = \frac{J_s^2}{\sigma}$ , exposing that any variation in both terms will cause a variation in local instantaneous heating, making it particularly sensitive to the aforementioned defects.

The resulting heat associated to both phenomena can be estimated, assuming the principle of energy conservation and the Fourier heat equation, resulting in the temperature  $T(x, y, z, t)$ , which can be modeled by integrating eq. 1.2, with  $Q^H$  being the sum of the

instantaneous heat of both phenomena,  $\alpha$  thermal diffusivity,  $\kappa$  thermal capacity, and  $\nabla^2 T$  the Laplacian of temperature.

Although the heating from both phenomena may overlap, the relative contribution of each one can vary significantly, as in the case of ferro-magnetic materials where induced currents predominate. In any case, the set of externally controllable factors can be optimized to enhance thermal interference from cracks. This optimization may involve varying the intensity and shape of the field with respect to the surface, as well as the frequency.

Thus, the inductor, its relative placement and the employed generator are key factors in this type of thermographic inspection. Note that there is already a large literature focused on identifying the optimum parameter definition in the IT technique, i.e. finding the most suitable lock-in regimes considering the skin depth, the thermal penetration depth, and the crack dimensions to be detected [44–46]. These studies are mostly based on extensive empirical analysis from both laboratory and field investigations of faults and advanced diagnosis applications.

Undoubtedly, the results and conclusions of such investigations are of particular interest for current induction thermographic inspection applications, however, the detection of these cracks is strongly conditioned by the relative orientation between the crack and the direction of the magnetic field produced by the inductor, which can be a non-predictable variable.

Using a custom inductor, such as single coil [47], a dipole [48] or a Helmholtz coil pair [49, 50] which are composed of two coils, produces a fixed magnetic field with a predominant direction. This limits the resulting thermal disparity in the vicinity of the cracks in certain configurations. The magnitude of this effect is minimized when both the direction of the crack and the resulting Eddy currents associated to the magnetic field are aligned [51, 45, 52]. The reliable detection of the cracks, regardless of its orientation is indeed one of the main challenges of IT. There is though a very limited number of studies dedicated to overcoming this critical drawback in IT, indeed the majority of modern induction systems stem from functional old designs that have been subsequently optimized to enhance induction heating, have been inherited from welding and thermal treatment applications [53, 54], and thus the generated magnetic field shows a unique direction in most cases. This limitation of the inductor can be overcome by scanning the area considering different orientations relative to the inductor. This rotation would require an external intervention such as a robot gripper but it also increases the inspection time, its cost and makes it more complex. Angle-independent thermo-inductive system have been previously demonstrated, employing a pair of Helmholtz coils disposed in an orthogonal manner containing the inspected part, resulting in a varying magnetic field orientation derived from the vector addition associated to an induction frequency differential [50] with two generators. The required containment of



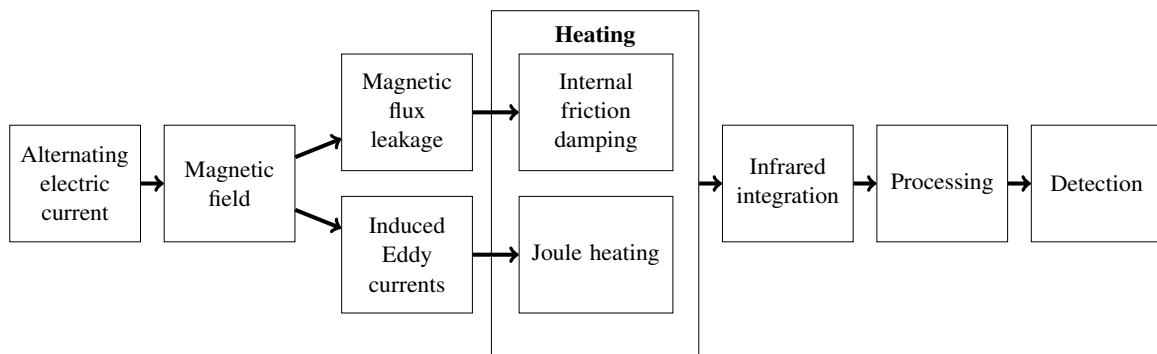


Fig. 1.7 Induction thermography process diagram.

the part limits the potential use-cases of the system to small parts. Other approaches have resorted to the circular polarization of the Eddy currents employing a tetra-pole inductor [55, 56] which generates a rotating magnetic field.

Fig. 1.7 summarizes the induction thermography process, considering both phenomena and subsequent diffusion which is measured by an infrared camera.

### 1.3.5 Other active thermography techniques

In addition to the previously mentioned heat sources, there are many alternatives with a wide range of applications. However, these will not be explored with the same level of depth as they are out of the core of this thesis.

**Microwave** Microwave Thermography (MWT) is a technique based on the heating associated to an electromagnetic wave on 1 to 30 GHz spectrum, enabling homogeneous volumetric heating, with absorption rates varying according to the material and defects present. Considering that radiation absorption is largely dependent on electrical conductivity, Levesque et al. [57] proposed a system in the 1990s for detecting inserts in glass-epoxy using a microwave-emitting parabolic antenna, allowing partial estimation of their depth and dimensions. Sakagami et al. [58] proposed another system inspecting a concrete block with artificial cavities by recording cooling after heating the surface with a 2.4 GHz microwave oven and shielding the remaining faces. The cavities do not exhibit significant heating compared to the rest of the block, but the infiltration of water enables a localized heating due to their high microwave radiation absorption rate. Qaddoumi et al. [59] proposed a system comprised of an open-ended rectangular waveguide probe radiating microwaves on the X-band (8.2–12.4 GHz) and K-band (18–26.5 GHz) to inspect the corrosion of coated metallic samples below the paint considering the varying rate of absorption associated to rust.

**Electro-luminescence** Another possible alternative consist on the electro-luminescent effect by reverse biasing a solar cell. This allows for the direct visualization of the state of the solar cells based on infrared emission [60].

**Thermosonics** The usage of an ultrasonic wave propagating on the workpiece to generate heat captured by an infrared camera is known as vibro-thermography or thermosonics. It entails the inducing of strong vibrations in a test piece with an ultrasonic pressed against the surface of the test sample, which often yields to the generation of uncontrolled frequency components. As a result, the repeatability of this technique is challenging in many scenarios, as described in the following review Ulmar et al. [61]. An additional consideration is that the induced vibrations may cause ghosting in the IR camera. Despite this, the technique is deemed effective in numerous scenarios, given that acoustic vibrations can penetrate to considerable depths.

**Air heating** Mercer et al. [62] also demonstrated the usage as of forced air to heat or liquid CO<sub>2</sub> to cool a composite sample, enabling the detection of defects. This heat source has also been proven useful for the partial detection of some defects in Lumber [63].

**Thermo-resistive** The usage an electric current to produce Joule heating is also an effective method as demonstrated first by Sakagami et al. [64], yielding a localized contrast on notched steel plates. The thermographic inspection inducing Joule heating of composites containing electrically-conductive aligned carbon nanotubes has also been demonstrated with good results [65].

### 1.3.6 Processing techniques

This section discuss multiple thermographic processing techniques to enable the subsequent detection of defects. These methods usually employ conventional statistical methods or they recur to the transformation of the thermography into the frequency domain, among others. Moreover, they consistently strive to discriminate and isolate the information pertaining to defects from the broader dataset. Prior to the description of the exposed methods, the data representation is detailed in the next section.

### Thermography image representation

The data structure containing the thermography can be defined as a third order tensor  $A_{n_x \times n_y \times n_t}$  with 3 modes or 2d *slices* corresponding for each dimension as shown in fig. 1.8a,

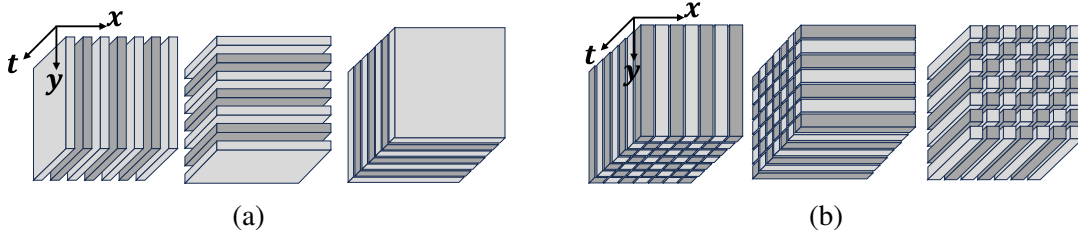


Fig. 1.8 Thermography tensor representation. (a) Slices corresponding to  $x$ ,  $y$  and  $t$  dimensions. (b) Fibers associated to  $x$ ,  $y$  and  $t$  dimensions.

denoted as  $A(i, :, :)$ ,  $A(:, i, :)$  and  $A(:, :, i)$  for the  $x$ ,  $y$  and  $t$  dimensions respectively. The tensor can also be seen as combination of 1D *fibers*, denoted analogously. Note that the thermogram of a single pixel can be referred as a mode-3 fiber,  $A(i, j, :)$  as shown in the right hand side of fig. 1.8b.

## Processing algorithms

**Differential absolute contrast** This is one of the classical methods based on the subtraction of the temperature and a sound area for the entire thermography [10], which can be expressed as  $C(x, y, t) = T(x, y, t) - T_s(t)$ . The thermal contrast can also be computed throughout the whole thermography [66], or its peak [67], and it can additionally be normalized in many ways [68]. These methods are very sensitive to the combined variations on surface emissivity, noise, and the variance of the heating along the surface. Another factor that particularly affects these methods is that a careful selection of the instant  $t$  is necessary, which might vary depending on the depth and shape of each defect.

**Phase thermography** Originally proposed by Maldague [69], it is based on the analysis of the thermography on the frequency domain. Employing the well-known DFT [70]:

$$F(f) = \frac{1}{N} \sum_{n=0}^{N-1} T(t) e^{-j2\pi \frac{fn}{N}} = R(f) + jI(f) \quad (1.12)$$

a set of complex components,  $R(f)$  and  $I(f)$ , for each frequency  $f$  are obtained, which can be expressed in polar form with the amplitude  $A(f) = \sqrt{R(f)^2 + I(f)^2}$  and the phase  $\phi(f) = \text{atan2}(I(f), R(f))$ . In lock-in thermography, it has already been described the relation of the phase image to the depth and thermal diffusion length as described in eq. 1.8. The amplitude is related to the perceived temperature variation. The spectrum of the thermogram typically exhibit an exponential decay of the amplitude after the carrier frequency (or

modulation frequency in lockin), which is one of the main reasons that most of the information is retained by its phase image. This method is also useful on pulsed thermography, based on the assumption that an ideal Dirac delta has an infinite flat spectrum in the frequency domain. Another aspect to consider is that real pulses do not have an infinitesimal FWHM nor a square shape, thus the amplitude of its broad spectrum is not constant. As for lockin thermography, on a thermal steady-state, the carrier frequency of the modulation is the primary harmonic employed for its analysis.

**Thermal signal reconstruction** The thermal signal reconstruction (TSR), originally proposed by Shepard et al. [71], models the exponential temperature decay of pulsed thermography cooling as a logarithmic polynomial in a log-log scale. The logarithm of each thermogram is fitted to the following log-poly  $\ln(T(t)) = \sum_{n=0}^N a_n [\ln(t)]^n$ , using a low-order expansion for the polynomial with 5 to 7 coefficients. This enables a thermogram reconstruction with  $T(t) = \exp(\sum_{n=0}^N a_n (\ln(t))^n)$ , with less noise and enabling the algebraic computation of its polynomial derivatives, as well as its temporal resampling. The time-derivative images are of particular interest, since they can reduce the effect of background artefacts. Its discrete computation from the raw thermogram is very sensible to the noise, and this method enables an increased SNR for small and shallow defects.

**Higher order derivatives** Higher order derivatives (HOS) [72] is a statistical temporal compression technique based on the central statistical moments. Assuming that the cooling of a pulsed thermography has a shape similar to a Weibull distribution, the higher order statistics are very sensitive to the changes of its shape and amplitude. The simplest statistical parameters to evaluate the tendency and variability of a distribution is the mean  $\mu = \frac{1}{N} \sum_n^N t$ , and the variance  $\sigma^2 = \frac{1}{N} \sum_n^N (t - \mu)^2$ . The third and fourth standardized or central statistical moments, named as the skewness and kurtosis represents the relative symmetry and the relative flatness regarding a normal distribution respectively. They are defined as  $M_i = \frac{\mu^i}{\sigma^i}$ , with  $\mu^i = \frac{1}{N} \sum_n^N (t_n - \mu)^i$  and  $\sigma^i = (\frac{1}{N} \sum_n^N (t - \mu)^2)^{\frac{i}{2}}$  and  $i$  being the statistical order. Both the skewness and kurtosis do not represent any physical variable but they are correlated to outliers in the thermogram distribution which is useful for the extraction of additional features and data mining.

**Principal component thermography** The principal component thermography (PCT) exposed by Rajic [73], is based on the singular value decomposition of the thermography. Considering a flattened thermography  $A_{m \times n_t}$ , with  $m = n_x \times n_y$  and  $m > n_t$ , the full SVD decomposition is defined as  $A = UDV^T$ , with  $D_{n_t \times n_t}$  being a diagonal matrix of the principal

components ordered in descending order,  $U_{m \times m}$  and  $V_{t \times t}$  being orthonormal basis. The first  $p$  columns of  $U$  can be statistically associated to a set of plausible undetermined factors related to each pixel/point. Rajic normalized the thermography and preserved the first two columns, or components, with the first one associated to mean and second one correlated with the defects. The discriminative capacity of this method has been reported by many authors, e.g. Griefahn et al. [74] could separate the surface reflections and Sutthaweekul et al. [75] was able to correlate the microwave probe lift-off distance, and both of them were able to discriminate the defects on separate components.

**Principal component analysis** The PCT is a computationally expensive technique for most thermographies, but multiple approximations have been proposed, the first one based on the principal component analysis (PCA) [76], first exposed on a thermography by Marinetti [77], consisting on the projection of the thermography into an orthonormal basis of the temporal scatter matrix of the thermography calculated with the SVD. The temporal scatter matrix of the thermography can be defined as  $S_{n_t \times n_t} = (A_{center})^T (A_{center})$ , with  $A_{center}$  being the flattened thermography subtracting the mean of the thermogram for each point. The orthogonal decomposition of the scatter matrix is  $S = UDV^T$ , and selecting a subset of  $p$  columns of  $U_{t \times t}$  denoted as  $W_{t \times p}$ , the flattened thermography  $A$ , can be projected to a new base with:  $A'_{m \times p} = A_{center} \times W$ . This method can be a good approximation, so long each mean-centered thermogram is roughly equal to the raw thermogram subtracting the mean of each frame.

**Robust principal component analysis** Liang et al. [78], demonstrated a robust SNR with a challenging background on a pulsed induction thermography scenario, using the robust principal component analysis (RPCA), exposed by Candés et al. [79]. It is based on the assumption that the thermography can be decomposed in two components. The first one being a low-rank matrix  $L_0$ , typically associated to a background and a second one related to the outliers  $S_0$  which is correlated to the defects, denoted as  $M = L_0 + S_0$  with  $M$  being the three-way tensor of the thermography. The numerical resolution proposed by Candés uses to a convex optimization, formulating the optimization as  $\min \|L_0\|_* + \lambda S_0$ , subject to  $M = L_0 + S_0$ , with  $\|L_0\|_*$  being the nuclear norm representing the sum of the singular values of  $L_0$ . This results in 2 three-way tensors which can be subsequently processed.

## 1.4 Quantitative analysis and probability of detection

The quantification of the reliability of the the previously discussed inspection techniques can be measured using multiple methods. In this regard, there is a set of accepted methods to estimate the probability of detection (POD) according to sector-specific regulations, as is the case in the aerospace and military industries.

Numerous methods allow for a comparison between techniques, which can statistically weigh all the information extracted from tests with varying degrees of detail. In some cases, these methods also consider the reliability of the comparative result.

In this section, these are presented, starting with the precision/recall ratios on sec. 1.4.1. Subsequently, we will expose the "Hit & miss" probability of detection (HM-POD), as a measure of the flaw size  $a$  on sec. 1.4.2. Finally, a method which compares response  $\hat{a}$  versus flaw size  $a$  1.4.3.

Another aspect to consider, is that these methods are detailed on the MIL-HDBK-1823A standard [80], which is considered the state of the art for conducting POD studies in many industries [81]. A robust implementation of the regression POD algorithms complying to this standard is available in R programming language, developed by Annis [82].

### 1.4.1 Precision and recall

Having a ground truth obtained with a previously validated technique, a set of tests is conducted on the same set of pieces to inspect. In this sense, the result of the evaluated technique yield a certain number of true positives  $TP$ , true negatives  $TN$ , false positives  $FP$ , and false negatives  $FN$ , over a total of defects  $TP + FN$ . The recall [83] is the ratio of true positives defined as:

$$Recall = \frac{TP}{TP + FN} \quad (1.13)$$

On the other hand, it is not desirable for the technique to generate a high number of false positives due to the operational implications it may have. In this way, the precision of the technique is defined as:

$$Precision = \frac{TP}{TP + FP} \quad (1.14)$$

### 1.4.2 Hit and miss - POD

Considering that the probability of detecting a defect is typically proportional to its size, denoted as  $a$ , the previous precision/recall ratios are unable to define a threshold POD as a function of  $a$ , which limits its extrapolation to different scenarios.

In many applications, the appraisal of an inspection technique is typically associated with the bigger defect to miss, and for this reason, the POD is generally expressed as a function of the defect size, defined as an ideal binary step function.

Considering that each crack can be detected or not depending on its size, one could define a threshold at  $a$  corresponding to the desired percentile of the necessary probability of detection. However, given that the density and noise of the distribution are variable, such a threshold may not be accurate in practice.

In a realistic situation, the POD is typically described as an ascending sigmoid function, that can be modelled in many ways. The most accepted HM-POD model to fit the set of binary points associated to the experiments, is the log-logistic distribution [84], written as:

$$POD(a) = \frac{e^{\frac{\pi}{\sqrt{3}}\left(\frac{\ln a - \mu}{\sigma}\right)}}{1 + e^{\frac{\pi}{\sqrt{3}}\left(\frac{\ln a - \mu}{\sigma}\right)}} \quad (1.15)$$

where  $\mu$  and  $\sigma$  are the mean and standard deviation, respectively. In addition, the regression of that model can weight the varying confidence interval (CI) with the likelihood-ratio method [85].

### 1.4.3 A VS $\hat{A}$ - POD

Assuming that the evaluated technique produces a signal instead of a binary result, it becomes possible to fit this signal with respect to the defect size. The method is analogous to the one in the previous section, and although the proportionality of the signal  $\hat{a}$  to the defect size  $a$  is a priori correlated, the function that best fits it does not necessarily have to be an ideal step function or a sigmoid.

Another aspect to consider, is the relation between the underlying signal of the technique might not even follow a monotonic curve compared to the defect size, which can make the final thresholding a very challenging task.

In the case of image-based signal it is very common to compare the signal regarding the background noise, using a Signal to noise ratio (SNR), which is typically defined as:

$$SNR(x, y) = 20 \log_{10} \frac{abs(S(x, y) - \mu_{sound})}{\sigma_{sound}} [dB] \quad (1.16)$$

where  $S(x, y)$  is the value of a certain pixel,  $\mu_{sound}$  and  $\sigma_{sound}$  are the mean and standard deviation of sound area. In this regard, the distribution of  $\hat{a}$  - a might vary according to the use case.

Assuming that this distribution follows a line on a log-log scale, with a standard deviation  $\delta$ , the function is defined as:

$$\hat{a} = \beta_0 + \beta_1 a \quad (1.17)$$

where,  $\beta_0$  and  $\beta_1$  are the offset and slope, respectively.

The regression to model the probability of detecting a higher signal  $Y$ , regarding a certain threshold  $y_{th}$ , can be defined with the following expression:

$$POD(a) = Pr(Y > y_{th}) = 1 - \Phi_{Norm} \left[ \frac{y_{th} - \beta_0 + \beta_1 x}{\delta} \right] \quad (1.18)$$

where,  $\phi_{Norm}$  is the standard normal cumulative density function (CDF),  $x = \log(a)$ , and  $y_{th} = \log(\hat{a}_{th})$  is the signal threshold limit.

Considering that the signal of the same defect might vary depending on some uncontrolled variables of the inspection, multiple regressions can be weighted using the method reported by Meeker et al. [86]. Another aspect to consider is that the conventional least square regression is generally avoided, mainly due to the varying variance along the curve. A weighed likelihood-ratio method [85] enables the estimation of the varying CI on the fitted sigmoid.

## 1.5 View planning

The preceding sections have delved into surface and subsurface inspection methods, with a particular emphasis on active thermography and its applications. However, there has been no discussion of the crucial aspects associated with its automation. In this regard, the inspection of an object or surface of interest typically needs to meet a series of requirements or constraints associated to the employed technology, while ensuring the complete coverage of the surface to be inspected. In an industrial environment, this is often addressed through manual CAD/CAM programs that define these trajectories in a virtual environment, which must then be tested on the actual component to make the necessary corrections associated with any unforeseen deviations from the real environment.

Therefore, the automation of the inspection itself can be a lengthy process that requires expertise in both the inspection technique and automation. Consequently, it has been deemed appropriate to implement a system that procedurally resolves the trajectory generation for a generic inspection process such as 3D surface reconstruction.



This section provides a brief overview of the literature related to the View Planning Problem (VPP) exposed, considering that the goal of this problem is to procedurally automate the surface inspection using an arbitrary system. This section is organized as follows, beginning with a review of the applications that motivate this problem. Subsequently, the two approaches are presented, outlining the associated general flow. Depending on the employed sensor and approach of the problem, multiple data structures related to the spatial representation are required. The following section reviews the View Planning Problem (VPP) using a 3D model of the object or approximate environment, referred to as model-based VPP. Finally, the next-best-view (NBV) is discussed, which determines the next capture pose that yields a higher coverage.

### 1.5.1 Motivation

The purpose of the problem is to plan the positioning of one or multiple sensors with the goal of visualizing a known [87] or unknown surface [88], of an object or scene.

This problem arises in a relatively broad range of applications. Firstly, there may be a need to procedurally automate the inspection of a known or unknown object. Additionally, the objective may involve positioning a network of cameras [89] or static sensors under certain constraints to cover a certain area. In situations where an autonomous robot is available [90], its active guidance for exploration and mapping of an environment constitutes another possible application [91]. In some instances, the total coverage may not always be the objective, such as object recognition [92] or pose estimation [93, 94] of already known objects, where the goal is to find optimal viewpoints that minimize the ambiguity of the task.

In industrial settings, the automation of the inspection process is often carried out by an expert, which can be time and resource-intensive. Furthermore, there may not be an approximate model of the object, which will end up being manually scanned either way. On the other hand, the elements comprising a view-planning system consist of one or multiple sensors, usually positioned by one or more robots, which are detailed in section 1.5.3. The basic VPP systems are described in section 1.5.2.

### 1.5.2 Generic view-planning algorithm

The strategies for solving the problem can vary depending on the goal or available information. For example, it may be the case that there is an approximate model of the object or environment to be explored, allowing for an offline planning, referred to as model-based view-planning problem [95]. In contrast, if no such model is available, an approach called next-best-view (NBV) is employed [88].

The model-based VPP has the advantage of having more information, and it follows a sequential workflow, starting with (1) the sampling of a set of hypothetical capture poses, (2) the simulation of their perception, and lastly (3) a selection of the final subset of capture poses that meets the task requirements. Most of these systems distinguish themselves in the last two steps, considering different criteria for simulation, such as minimizing reflections and uncertainty in 3D measurements [96, 97], or taking into account the energy radiated by a pair of halogens perceived by an infrared camera on a thermographic inspection [98]. The problem formulation varies based on the type of task, so in an inspection object inspection, the main goal consists on maximizing surface coverage, while on the recognition or pose estimation, the aim is to reduce any ambiguity.

If an approximate model of the object is not available, the next-best-view approach is based on an iterative scheme consisting on (1) the selection of one or more poses, (2) path planning, (3) capture, and (4) update of the virtual environment space.

### 1.5.3 View planning system

As mentioned earlier, this system requires at least one sensor and a robot or positioning system. The following briefly outlines the most common types of robots and sensors employed for VPP applications.

#### Robot

In this context, multiple types of stationary robots can be employed, such as CNC 3D Cartesian positioning [99] or robotic arms with various degrees of freedom that allow control over position and orientation [100, 101], some of which employ non-holonomic kinematic chains with overactuated robots to increase their effective workspace and maneuverability [102], as well as the employment of multiple arms [97].

Typically, these robots have a Cartesian workspace limited by the robots joint limits, and an arbitrary Cartesian pose may have a finite subset of configurations or infinite in cases where more than 6 degrees of freedom are needed to reach a position with a specific orientation. In any case, the positioning space of the cameras may be limited not only by the robot but also by external constraints [95]. On the other hand, mobile robots commonly used for active recognition and mapping applications can move through various mediums. Numerous examples of VPP systems employing such robots use unmanned aerial vehicles (UAV) [90, 91], which can explore a known [103, 104] or unknown environment [105, 91], even employing swarms of drones simultaneously [106], as well as recognizing people with infrared cameras in rescue operations [107].

The use of autonomous underwater vehicles (AUV) on a VPP context is also common for inspecting known ship hulls [108], underwater structures [109], or the inspection of known sections of the seabed [110–113].

Other VPP systems employ unmanned ground vehicles (UGV), considering three-dimensional inspection of an interior [114], thermal mapping of an interior for the detection of thermal leaks [115], or inspection of terrain [116].

### Sensors

The set of sensors that can be employed in a view planning problem (VPP) can be very diverse [117], mostly comprising cameras and stereo cameras, profilometers, structured light scanner, infrared cameras, lidars, as well as depth sensors based on multiple cameras.

It is common to use cameras in the visible spectrum [118] or infrared [115, 98] (sec. 1.3.2), and in some instances, the use of hyperspectral cameras allows for the extraction of more information [119]. The visibility can be estimated with a pinhole model, where the incident light ray passes through a focal point and projects onto a plane. Therefore, simulating the visibility of a camera can be based on the path followed by these rays through ray-casting or by projecting the scene onto that plane, as briefly discussed in section 5.2.2.

Given that the majority of VPP applications focus on surface reconstruction, the subsequent paragraphs will outline the prevalent types of 3D scanners employed for this task.

There are various types of depth sensors that allow the generation of point clouds based on different principles. It is possible to use a binocular or stereo vision system, based on the same principle as human vision to infer the distance to an object. In its simplest version with two cameras on the same epipolar plane and parallel orientation of the optical axis, a purely geometric relationship is established between the object's distance from the cameras and its projection in the images captured by them. Using the binocular pinhole model shown in fig. 1.9, with a distance between cameras  $b$  and focal length  $f$ , the orthogonal distance  $z$  of a point  $P \subset \mathbb{R}^3$  can be geometrically calculated in terms of the pixel distance of each camera, the projections of a point  $P$  from both cameras, called disparity  $d = (u_2 - u_1)$ , where  $d = -\frac{fb}{z}$ ,  $z = \frac{fb}{d}$ , with  $u_1$  and  $u_2$  being the distance of the projected point of each camera.

Considering the minimum error as  $\Delta z = \frac{z^2}{fb}$ , the accuracy at long distances is limited by the distance between the cameras and focal distance, making it less suitable in many circumstances. Additionally, the estimation of the disparity of all points present in both images (disparity image) is problematic, as it requires associating the points based on image features. A faster and robust generation of the disparity map can be achieved by employing the basic principle of photogrammetry [120], which considers that the infinite optical ray associated to a pixel can be projected on the other camera sensor plane drawing a line.

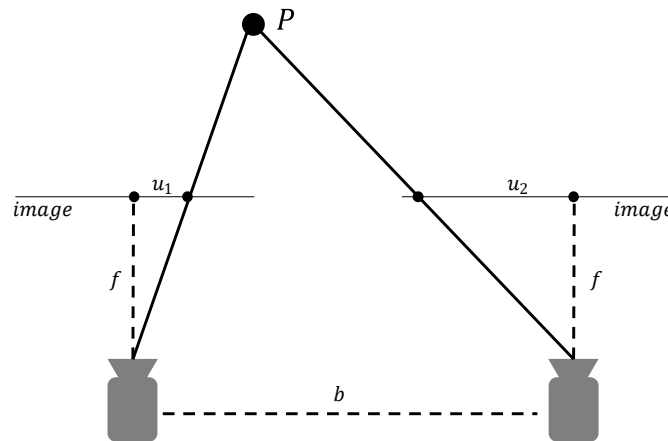


Fig. 1.9 Binocular stereo vision under epipolar constrain.

Considering an epipolar constrain allows the associated line to be parallel to the epipolar plane, accelerating and strengthening the generation of the disparity map. Moreover, it is not always possible to produce a dense disparity map due to the lack of information or lack of visual surface texture of the surface. Hence, stereo systems projecting pseudo-random or similar patterns exist allowing the generation of dense point clouds with a better control of the lighting conditions. This method can be generalized [120, 121] to sets of cameras, where perception can be fused in pairs or sets of cameras to expand the field of view [122].

Alternatively, exploiting the time-of-flight (TOF) of light can be used to estimate distance. In its simplest version, a square-wave light is emitted, and immediately reflected, causing the wave to have a phase shift corresponding to the round-trip time of light based on the distance  $d = c\Delta t / (2n)$ , where  $c$  is the speed of light, and  $n$  is the refractive index of the medium. In this regard, such sensors can have a long range, although their spatial resolution is more limited and depends on the emitted light frequency. Another factor to consider is that the resulting point cloud can have many outliers in the vicinity of edges due to the averaging of TOF of the nearby and distant surface surrounding the edge.

LiDAR is another technology that uses the time-of-flight principle for depth determination, employing a set of infrared laser beams with a circular movement, capturing reflections with point light transducers. These systems can cover large areas, but the resolution is limited by the pulsing frequency and the number of beams. Recently solid-state LiDAR systems have also been demonstrated [123].

On the other hand, the use of a linear laser beam can be captured by a camera, enabling the determination of the position of the impinged surface. In this sense, profilometry can infer the position of the set of points of the laser beam visible by the camera, given its known intrinsic parameters, and the relative extrinsic position of the laser plane with respect to the

camera. There are many models to estimate this set of parameters, with the simplest being to estimate the transformation of the plane, or homography, of the camera sensor relative to the laser plane [124].

### 1.5.4 Data structures

In this section, the most commonly used types of spatial representation are described, both in the capture and planning phases.

Considering the representation of the workspace, it is commonly defined as dynamic tree of objects with relative poses between them, with the global coordinate system being its root. Frameworks like ROS [125] or Gazebo [126] represent the interrelation by breaking down the robot's links, where the kinematic chain is updated or simulated. The effective workspace of the robot also has to consider possible collisions, so it is common for these frameworks to integrate a collision backend, implementing libraries such as FCL [127] or Bullet [128], among others.

Depending on the circumstances, the internal representation of objects and their surfaces may vary, either to represent static three-dimensional information captured by sensors or used by the VPP algorithms and downstream tasks.

#### Point Cloud

The most common raw representation of 3D sensors is simply a collection of points relative to a specific frame. In this sense, they can be structured point clouds in a two-dimensional buffer, or a multi-channel image, or alternatively as an unordered list of points. The points are usually 2 or 3 dimensions, and it is common for them to have more attributes, such as intensity, color, or surface normals, among others.

#### Meshes

It is a set of flat polygons defined by their vertices and mutual interrelation. The interrelation of polygons, or topology, can be implemented or transformed into any of the alternative representations of undirected graphs. The most compact way to define a mesh is with an adjacency list of Cartesian vertices for each polygon. It is common for meshes to have a single type of polygon, with triangles and quadrilaterals being the most used. Additionally, the ordering of vertices in the adjacency list is predefined based on the direction of normals.

## Grids and spatial indexers

Considering that the view-planning problem, as well as the downstream applications such as surface reconstruction commonly use these types of data structures, it is of the utmost importance to have a comprehensive understanding.

As previously stated (sec. 1.5.2), the next-best-view is based on the spatial subdivision of the free, occupied and unknown space which serves as the basis for its decision.

Multiple VPP algorithms, as well as downstream applications use these data structures as the basis for its execution or to reduce the runtime. For instance, the computation of the visibility using a naive ray-casting based on the intersection of geometric primitives [129] scales poorly, as it requires to compute the collision of each ray, regarding all the geometric primitives of the scene. In this scenario, it is desirable to have an efficient traversal of the scene by the ray, to minimize the number of collision evaluation, by skipping the empty space, while avoiding the non-intersecting geometry.

The radial and k-nearest neighbour (knn) search queries are typical functions associated to these data structures, which are commonly used to accelerate the post-processing and segmentation of point clouds, as well as the computation of many radial basis functions for the implicit surface reconstruction to locally [130], or globally [131] sample a signed distance function (SDF) [132]. Another typical use case of the these data structures, is the spatial indexing of the objects [133], or fragments of it [134], to enable a faster discrete or continuous [135], collision evaluation.

The selection of the optimal data structure depends on many factors, such as the type of data that it contains, the queries required, as well as the time to build and update on a dynamic environment. The most common spatial indexing data structures are mainly categorized as a (1) collection of geometric primitives, (2) grids, as well as (3) trees, which typically contain points, polygons and voxels, among other types of data.

**Geometric primitives** The simplest method to perform a high level spatial subdivision consist on enclosing the objects on a bounding primitive, such as axis aligned (AABB) or oriented bounding boxes (OBB), spheres and ellipsoids, among others, enabling a high level collision check, regarding other objects or rays.

**Grids** A uniform grid is one of the simplest spatial indexers to implement with fast access time, and its construction can be implemented in many ways, using k-dimension tensor containing each voxel, or an ordered hash-list of the occupied ones. The fixed resolution means that its size is not optimal to contain spaces with varying density and resolution.

**Trees** The simplest hierarchical space subdivision consists on a kd-tree [136] which iteratively partitions the space in axis aligned planes containing the median or mean of the data. This results on a binary tree with the lower level containing the data itself. Other planar binary partitions, such as the binary space partitioning (BSP) [137] generalizes this idea, allowing an arbitrary orientation and location of the splitting planes. The spatial subdivision can also be extended employing quadtrees [138] which are good for 2D or mostly planar data, as well as Octrees [139], both of which orthogonally subdivide the volume with a uniform spacing for each level, resulting in 4 or 8 nodes per parent respectively. It is also common to label the nodes extending the set of attributes with other kinds of data or labels. Occupancy labels such as free, occupied and unknown space are of special interest for many application such as VPP and dynamic workspace representation. An example of this is the octomap [140], which consists on an octree which fuses the occupancy of multiple sensors with a temporal update rule clamping the occupancy on nodes with a consistent occupancy probability across multiple sensors. This enables a dynamic compression of the graph by pruning the sub-nodes with the same occupancy labels.

### 1.5.5 Model-based view planning

The classical sampling-based VPP, employs an approximate model of the targeted surface, such as the one exposed by Scott [87], starts with the sampling of viewpoints, its subsequent simulation and the final set cover ensuring the maximum coverage. The sampling of the viewpoints starts by decimating [141] or resampling [142] the surface mesh, which yields another mesh with a different distribution and density of the primitives. This mesh is used to sample the surface points by selecting the vertices or the barycenters of the mesh primitives. These points are used to sample a set of a priori ideal viewpoints with a normal incidence angle from a distance corresponding to the maximum optical resolution, which is defined as the center of the depth of field (DOF). Other viewpoint sampling methods such as the one exposed by Jing et al. [103], generates a volume surrounding the object, computed by calculating the perpendicular at the surface points of the object, and adding the minimum and maximum distance of the DOF. This 3D volume is used to randomly sample the origins of the viewpoints, and their orientations is determined with a potential function of the neighbouring surface normals.

The resulting set of viewpoints is then simulated considering the visibility among other factors depending on the use case, resulting in a visibility vector of  $M$  surface points for each viewpoint  $i$ , denoted as  $\vec{A}_i$ . The visibility of the  $N$  viewpoints, regarding  $M$  surface points conforms a visibility matrix,  $\mathbf{A}_{\text{vis}} = (\vec{A}_1, \dots, \vec{A}_N)$ , which can be interpreted as a bipartite graph relating both disjoint sets, as formulated by Tarbox et al. [143]. This data structure, which

can be interpreted as a bipartite graph, enables a combinatorial formulation of the VPP as a Set Cover Problem (SCP), to maximize the coverage of the surface with the minimum number of viewpoints.

The visibility matrix can also consider multiple configurations of the scanning device, as demonstrated by Gronle et al. [99], which modelled multiple focal distances of a confocal microscope as different viewpoints, effectively multiplying the size of the visibility matrix.

Considering that the total area to cover is finite, the likelihood of visualizing the same surface patches increases as the number of viewpoints rises. The diminishing returns of this problem is one aspect of its submodularity associated to the total overlap of the visibility [104]. Therefore the coverage and number of viewpoints are two conflicting objectives which must be approximated in a reasonable time scale. The optimization of the problem has been previously solved employing well-established meta-heuristics such as, greedy [144], linear programming [145], Lagrangian relaxation [146], simulated annealing [147], particle swarm optimization [96], and genetic algorithms [148], among others.

The conventional Greedy Set Cover [144], repeatedly selects the next column (viewpoint) of  $\mathbf{A}_{\text{vis}}$ , which maximizes the coverage of the remaining uncovered points, until the whole set is covered in  $O(\log n)$ , [149]. Its unweighted cost, as well as the deterministic selection criteria, precludes the exploration of alternative solutions, which can be improved with a randomized selection [150].

Another aspect to consider is that its parallelization is able reduce the runtime with a similar solution, so long the problem is subdivided in buckets of maximal near-independent sets [151]. Kava et al. [152] defined the greedy SCP as a markovian decision process (MDP) yielding a combination of probable coverage sequences associated to the cumulative probabilities of each selection branch, and a greedy gain considering the gained coverage, as well as the adjacent boundary of the preselected candidates weighted with a learnt parameter. In this scenario, a reinforced learning (RL) framework was used to learn the weighing parameter showing a performance greater or equal to a greedy SCP, given sufficient learning time.

The set cover yields a set of unordered inspection frames which might be used to position static cameras or generate an inspection trajectory, minimizing the inspection time and considering the kinematic constraints of the robot and camera attached to the robot wrist, by employing a combinatorial optimization known as the Travelling Salesman Problem (TSP). Most of these methods have been tested in simple geometries with typical runtimes on the order of minutes [87, 96, 153, 154].



### 1.5.6 Next-best-view

The NBV is an alternative approach of the same problem which was proposed by Connolly [88], consisting on the iterative selection and capture of the surface represented on a octree occupancy map, considering the occupied, free and unknown or unseen space. The free space is determined by ray-casting from the sensor to the occupied voxels flagging the traversed voxels. It uses two selection heuristics, the first one being a simple sphere sampling which determines the next camera frame with largest number of potential unseen voxels, and a second one focusing on the boundary voxels of occupied and unknown ones. The exploration of the boundaries between unseen and occupied voxel was also exploited by Banta et. al [155], which presents multiple heuristics ranging from coarse to fine integrated on a later stage. It starts with an edge-based sensor placement of the depth image, coinciding with the boundary between occupied and unseen space, followed by the sampling of the centroid of occluded voxel and at a later phase of the scanning it samples cluster of nearby occluded areas.

Kriegel et al. [156] also recurs to the boundary search considering the trend of the surface as well as the occupancy uncertainty. His system is able to autonomously explore the scene with a 3D camera and reconstruct objects with a laser stripe scanner on a higher resolution.

Khalfaoui et al. [157] proposed a selection criteria based on visual information, favoring the surface patches with an unreliable visibility associated to a large incident angle and considering potential occlusions according to the partial occupancy map.

Another method employing visual information proposed by Vasquez et al. [158], proposes a utility function that simultaneously weights for each view-point candidate the potential number of unseen voxels close to occupied ones, a reduced navigation distance, as well as quality metric based on the average incidence angle, promoting rays traversing a larger number of occupied voxels (occlusion). His algorithm also deals with positioning errors by modelling the positioning error as a 0 gaussian mean, on local cartesian window considering the utility function. It recurs to the local sampling of the utility function associated to the chosen viewpoint and convolves the sampled window with a gaussian filter from which the best possible candidate is selected.

Delmerico et al. [159] proposed and tested experimentally multiple volumetric information (VI) metrics for each viewpoint by integrating the information going of each voxel of an octomap. The most relevant VI metrics are (1) an occlusion aware VI being the cumulative occupancy probability of unobserved voxels traversed by all the rays casted from the sensor, an entropy VI based on the occupancy uncertainty of unseen voxel, (3) a rear side voxel VI weighing the visible entropy of unknown voxels which are adjacent to occupied ones, (4) a proximity count VI, weighing the occlusion aware with the minimum distance of an

unseen voxel towards an occupied one. These metrics were also combined with entropy of each voxel, and the experimental results shows that the entropy-based VI metrics effectively reduce the entropy of the overall map (cumulative entropy), but they underperform compared to the rest on a surface reconstruction task. This observation is explained by the fact that all that uncertain voxels end up being rescanned instead of promoting unsee voxels. Note that in this system the potential occlusion is tested by ray-tracing from the viewpoint assuming that unknown voxels are free.

Another aspect considered by Krainin et al. [160] is that in most scenarios the full coverage of an object is impossible due to the surface on which is located. His system relocates the object considering the occlusion of the robot gripper and previous coverage, as well as the self-occlusion of the rest of the robot regarding the scanner. The regrasping for an optimal coverage has also been explored by Kobayashi et al. [97], employing a dual arm robot with hand-over from one arm to the other, considering the followed path on configuration space of the robot.

Wu et al. [161] exposed a Convolutional Deep Belief Network (CDBN) [162] modelling the probability distribution of an occupancy map enabling the synthesis of an extrapolated point cloud from a certain viewpoint, which serves as the basis for recognition as well as NBV planning. Other synthesized methods, recur to a point completion networks [163], to estimate the visibility of the extrapolated cloud by ray-casting on its occupancy voxels, while at the same time weighting the confidence of each point with a parallel network as demonstrated by Wu et al. [164]. Other types of NBV algorithms avoid intermediate cloud extrapolation, such as the one exposed by Zeng et al. [165] which models the information gain of a set of viewpoints, considering the raw point clouds and capture poses demonstrating good generalization capabilities, as well as a fast inference time. The training starts by sampling a set of viewpoints and initializing a null binary selection vector state. It follows an iterative selection of the pose that maximizes the coverage gain and saving a supervised training pair of (1) partial point cloud and selection vector state, along with (2) the coverage gain of the new capture. The process continues up to certain number of iterations, and is repeated on multiple 3D models. The network architecture extracts global features of the partial point cloud by max pooling a vector of point-wise features. The point-wise features, current view-state and global features are concatenated with a self-attention unit (SAU) [166], which is subsequently passed through a multi layer perceptron (MLP) followed by max pooling yielding an estimate of the new binary coverage of each point of the object. The loss function is based on the MSE of the output vector regarding the ground-truth coverage gain. Network ablation study prove that the inclusion of prior feature extraction and merging with SAU enables an improved coverage prediction. Vasquez et al. [167] exposed a deep CNN

predicting the NBV position without any intermediate extrapolation or decision process. His method employed  $32^3$  occupancy grid as input and the determination of the viewpoint orientation is determined geometrically by pointing towards the object center of the partial cloud.



# Chapter 2

## Phase shifted imaging on multi-directional thermography

In this section a novel multi-directional Eddy current thermography (ECT) system is presented generating sets of directional phase images that have been fused with a processing algorithm allowing for an improved probability of detection (POD). This chapter is a modified transcription of a paper published by the author [168].

### 2.1 Introduction

Inhomogeneous electromagnetic Joule heating derived from the diversion of induced Eddy currents provoked by cracks, altering its path around as well as under its bottom, is the principal phenomenon enabling its usage as a non-destructive-evaluation (NDE) technique. Most induction thermography systems employ inductors derived from old designs, optimized for localized heating with a fixed magnetic field direction. This provokes a directional detection blind-spot for surfaces with random crack orientations. In the preliminary experiments we have observed that the pattern associated with the thermal response distribution can be geometrically correlated to the relative orientation of the magnetic field regarding the crack, conforming to a rotating feature that has not been described before. Extracting the apparent motion as an optical flow, with a phase-shifting interpolation of the intermediate orientations, generates a signal that enables a robust segmentation of a wide variety of defects in ferritic and austenitic alloys. Its performance has been evaluated with two ‘Hit/Miss’ POD studies TIG welds Inconel 718 and Haynes 282 alloys. Results show an increased detectability regarding the manual labelling of the defects in the same directional set, employing the same input.

### 2.1.1 Related works

Industrial manufacturing processes such as welding, steel hot rolling or casting are prone to cracks and porosity defects. Yet these defective features act as a stress concentration site which negatively affect the fatigue life and tensile properties of as-built parts. Furthermore, when these faulty parts are subjected to large mechanical forces defects in these components could lead to fatal consequences. Therefore, it is crucial to identify these defective parts through a quality inspection process, on the one hand, to ensure product quality and, on the other hand, to enhance material circularity, requalifying it or reusing it in some other process, i.e., minimizing environmental footprint. The detection of cracks in manufactured metal alloys is conventionally performed with techniques such as the magnetic particle inspection (MPI) and liquid penetrant inspection (LPI).

However, the detectability of cracks using MPI and LPI is limited and depends on the inspector's skill, which reduces the reliability of these techniques. Additionally, these methods require the use of toxic chemicals and may require the removal of the component's coating before inspection, which increases both the manufacturing and inspection times. Moreover, the manual and time-consuming nature of traditional inspection processes does not fit well with modern manufacturing lines. As manufacturing processes have become increasingly automated and faster, inspection processes must keep pace to avoid creating bottlenecks in the production line. In industrial practice, both Eddy current and induction thermography (IT), [69], techniques are commonly used for 100 %-testing of components and for spot checks, though Eddy current testing is limited to relatively simple geometries, fails to find large-scale defects as well as shallow inclined cracks, and does not allow to identify the cracks in thin materials. In this contribution, IT is featured as an interesting alternative to overcome these limitations.

Undoubtedly, the results and conclusions of such investigations are of particular interest for current induction thermographic inspection applications, however, the detection of these cracks is strongly conditioned by the relative orientation between the crack and the direction of the magnetic field produced by the inductor, which is indeed a non-predictable variable.

Using a customary inductor, such as a dipole or a pair of Helmholtz coils which are composed of two coils, produces a fixed magnetic field with a predominant direction. This limits the resulting thermal disparity in the vicinity of the cracks in certain configurations. The magnitude of this effect is minimized when both the direction of the crack and the resulting Eddy currents associated to the magnetic field are aligned [51, 45, 52]. The robust detection of the cracks, regardless of its orientation is indeed one of the main challenges of IT. There is though a very limited number of studies dedicated to overcoming this critical drawback in IT, indeed the majority of modern induction systems stem from functional old

designs that have been subsequently optimized to enhance induction heating, which have been inherited from welding and thermal treatment applications [53, 54], and thus the generated magnetic field shows a unique direction in most cases. This limitation of the inductor can be overcome by scanning the area considering different orientations relative to the inductor. This rotation would require an external intervention such as a robot gripper but it also increases the inspection time, its cost and makes it more complex. Angle-independent thermo-inductive systems have been previously demonstrated, employing a pair of Helmholtz coils disposed in an orthogonal manner containing the inspected part, resulting in a varying magnetic field orientation derived from the vector addition associated to an induction frequency differential [50]. The required containment of the part limits the potential use-cases of the system to small parts. Other approaches have resorted to the circular polarization of the Eddy currents employing a tetra-pole inductor [55, 56] which generates a rotating magnetic field.

### 2.1.2 Contributions

The main contributions of this work lie in:

- the development of a new thermo-inductive modality, based on the generation of a discrete set of thermographies with multiple magnetic field orientations.
- The identification of a new type of rotational feature associated to the tips and narrow points of the cracks and defects, which can be geometrically correlated with the direction of the magnetic field.
- The development of an interpolation method to approximate the intermediate orientations of the magnetic field, while canceling a large part of the noise present in the phase images, which is not affected by the variation of the orientation of the magnetic field.
- The design of a processing algorithm that fuses the directional phase images of the thermography, on a pixel-wise basis, exploiting the apparent motion of the pattern associated to the cracks, which has demonstrated good results in different materials and defect types.
- The rigorous evaluation of the performance for the automatic detection of the cracks, following the MIL-HDBK-1823A standard, in two distinct types of TIG weld defects on Inconel 718 and Haynes 282, with 218 and 337 cracks respectively. Obtaining the a90/95 crack size, that is the crack size that can be detected with 90% probability with a confidence level of 95%. The results demonstrate a probability of detection that is

not dependent on the relative orientation, with an increased detectability regarding the manual identification of the cracks in their respective phase images.

## 2.2 Methods

This section exposes the novel system which is illustrated in fig. 2.1, starting with the generation of (a) directional phase images (sec. 2.2.2) with a switched tetra-pole inductor (sec. 2.2.1), followed by a normalized (b) phase-shifted interpolation (sec. 2.2.3), displaying an apparent rotation of resulting heating around the crack tips, which is (c) estimated with an optical flow (sec. 2.2.4), yielding a vector field concentric to the cracks, which is integrated with a vorticity convolution (d), generating a signal correlated to the center of the cracks (sec. 2.2.5).

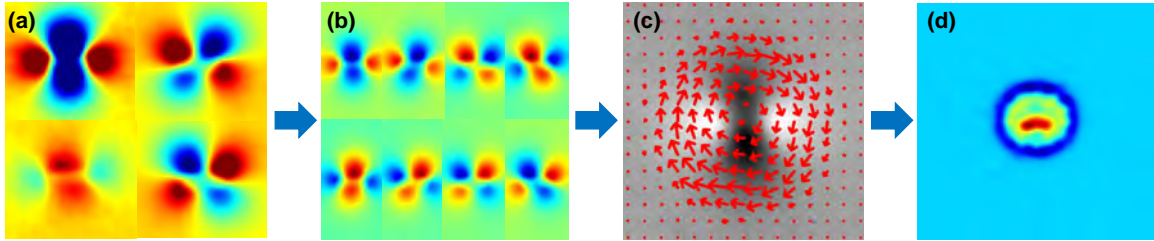


Fig. 2.1 Phase-shifted induction thermography processing pipeline. (a) phase images of each direction, (b) phase-shifted uniform sampling, (c) optical flow motion, (d) vorticity of the vector field.

### 2.2.1 A multi-directional induction thermography system

An inductive thermography inspection system consists of three main components: a wave generator, an infrared camera, and an inductor. During the inspection, the inductor, powered by an alternating current, generates a magnetic field. This magnetic field interacts with the material, inducing Eddy currents beneath the surface. The density distribution of these currents shows an exponential decay as you move away from the surface, decreasing to 1/e (approximately 37%) at the skin depth,  $\delta_{ec}$ . The skin depth is determined by factors such as the material's resistivity  $\rho$ , the frequency of the Eddy currents  $f$ , and the vacuum  $\mu_0$  and relative  $\mu_r$  magnetic permeability, i.e.  $\delta_{ec} = \sqrt{\rho / (\pi f \mu_0 \mu_r)}$ .

The skin effect has implications for thermographic inspections because it affects the depth at which thermal patterns are detected. Higher-frequency currents or fields have shallower skin depths, resulting in more surface-sensitive measurements. Conversely, lower-frequency currents or fields penetrate deeper into the material, allowing for the detection of thermal



patterns at greater depths. Moreover, surface geometry, the isotropy of the material, and the presence of cracks, pores, and sharp edges strongly influence the distribution and path of the Eddy currents and lead to localized Joule heating. This heating causes a localized increase of the emitted infrared radiation, which is typically captured and measured using an infrared camera. While this procedure is widely used, there remains a need for critical analysis of these measurements to accurately assess the presence or absence of defects. Interestingly, the design and configuration of the induction device significantly influence the distribution of the radiated field, thereby presenting additional challenges in the analysis process.

Conventional inductor designs, including dipoles and Helmholtz coils, are commonly constructed with twin or single coils that generate a magnetic field with a fixed direction. Consequently, the induced Eddy currents exhibit a predominant direction aligned with the magnetic field. The interaction between the Eddy currents and the defects is also influenced by the relative orientation of both, potentially causing the currents to flow around or beneath the defects. As previously stated, the presence of defects and the interplay with the Eddy currents have been quantifiably observed in studies, particularly when the crack and the Eddy currents are not parallel. Consequently, conventional inductors face significant limitations in consistently detecting defects in random crack samples. In contrast, a tunable induction system capable of rotating the induced magnetic field overcomes potential directional blind spots. A multidirectional inductor, capable of comprehensive coverage of all crack directions under examination, ensures that all cracks are subjected to the thermal stimulus. This capability becomes particularly important when dealing with complex shapes, irregular geometries, or components with varying thicknesses. With this regard, we devised a new tetra-polar inductor, based on the tetra-polar magnetic yoke reported in [55], though it features the ability to further control the induced magnetic field on it.

The inductor, shown in fig. 2.2, is comprised of 2 pairs of coils,  $C_x$  and  $C_y$ , arranged along the horizontal and vertical sides of a hollow square-shaped ferrite. This configuration allows for the convenient placement of an infrared camera on top, ensuring a direct line of sight and visibility to the inspected surface.

The resulting magnetic field of the 2 dipoles can be expressed as a vector addition in  $\mathbb{R}^2$  as  $\mathbf{B} = \mathbf{B}_x \sin(2\pi f_x + \phi_x) + \mathbf{B}_y \sin(2\pi f_y + \phi_y)$ , where  $B_x$ ,  $B_y$ ,  $f_x$ ,  $f_y$ ,  $\phi_x$  and  $\phi_y$  are the field amplitudes, frequency and phase shifts on the transversal directions, respectively. Thus, by activating or deactivating the coils and reversing their polarity, the tetra-polar inductor can achieve four distinct orientations of the magnetic field, which we will hereafter denote as  $\beta_i$ , where  $i$  is one of the four orientations available using the proposed system. The specific orientations and their corresponding labels are presented in Table 2.1.

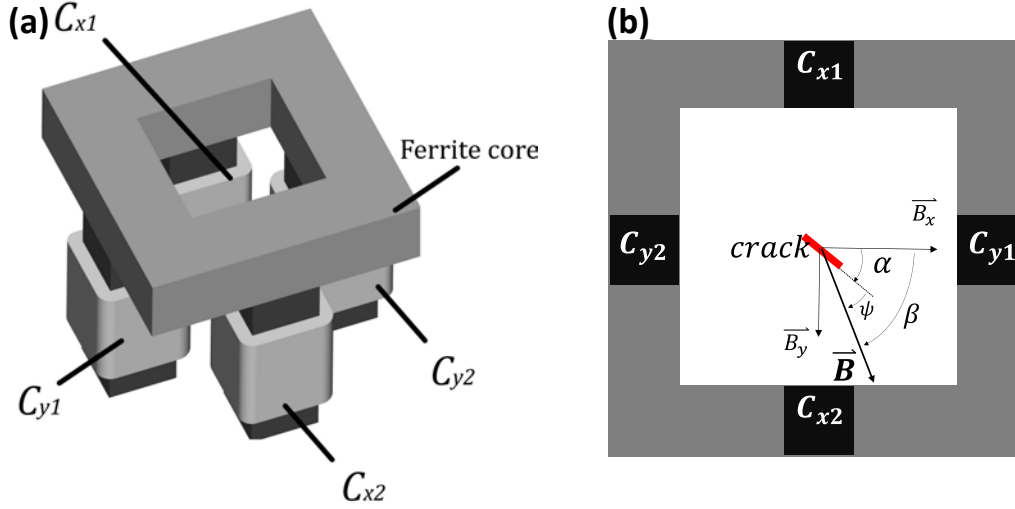


Fig. 2.2 Tetra-pole inductor. (a) a 3D illustration based on [55], with 2 pair of independent coils and (b) is a top view of the inductor defining the relative orientation of the magnetic field,  $\beta$ , and the crack,  $\alpha$ , regarding the inductor, and the angle between both,  $\psi$ .

Table 2.1 Magnetic field orientations as a function of the activation of the coils.

$\beta$	State
$\beta_0$	$V_x \neq 0, V_y = 0$
$\beta_{45}$	$V_x = V_y \neq 0$
$\beta_{90}$	$V_x = 0, V_y \neq 0$
$\beta_{135}$	$V_x = -V_y \neq 0$

The complete experimental setup is shown in Fig. 2.3. It includes a Flir X6541sc infrared camera equipped with a Stirling-cooled 640x512 InSb sensor. This camera is capable of achieving frame rates of 125 Hz at full frame or 4 kHz in windowing mode. The induction generator utilized is the Edevis ITVis 3000 MHF, which has been employed in various scenarios and was developed in [169]. It incorporates a full-bridge inverter circuit with pulse-width modulation, operating within a continuous frequency range of 10 kHz to 60 kHz. And a switching device to alternate between the different states.

## 2.2.2 Preliminary experiments on notches

To demonstrate the multi-directional induction capability of the system, a set of experiments has been carried out to analyze this aspect. Previous research has empirically demonstrated the relation between the thermal response and the relative orientation between the longitudinal direction of the crack and the magnetic field [51, 45, 52].

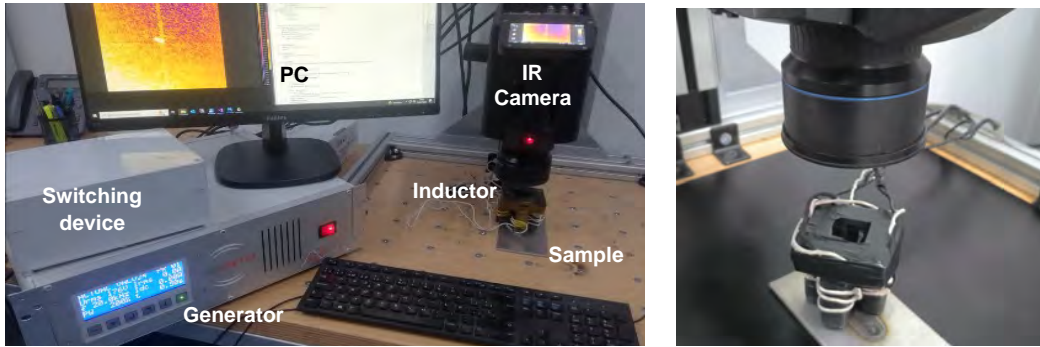


Fig. 2.3 Multi-directional induction thermography system setup. (a) Overall system composed by an induction generator, switching box, PC, IR camera, tetra-pole inductor and a welded sample. (b) A closeup of the camera inductor and welded sample.

This relation can be used to determine if the magnetic field is effectively rotating, by generating a similar thermal response by maintaining the same relative orientation of the magnetic field,  $\beta$ , and the crack,  $\alpha$ , that we denote  $\psi = \alpha - \beta$ , as shown in fig. 2.2b. The thermal radiation is measured by the infrared sensor, which is affected by local emissivity variations, inhomogeneous initial surface temperature, as well as the directional emissivity, among others. The bias introduced by the raw thermal recording is mitigated by selecting the phase image of the carrier frequency of the pulses, associated to the Discrete Fourier Transform (DFT) of the whole thermal recording [69]. Note that in this case, the carrier frequency is typically called lock-in frequency. This results in the most accepted metric to evaluate the thermal response for this type of application, defined as the absolute phase contrast [170], subtracting the local maxima and minima of the pattern, denoted as  $\Delta\phi = \phi_{max} - \phi_{min}$ . To simplify the analysis, two artificial notches have been produced with Electrical Discharge Machining (EDM), with 0.7 mm and 1.3 mm length and the same depth and width of 0.75 mm and 0.1 mm respectively. Note that the notched surface material is Inconel 718, in a sample measuring 4.75 x 80 x 150 mm. The set of experiments combines the 4 discrete orientations of the magnetic field,  $\beta$ , combined with 4 identical rotations of the crack,  $\alpha$ , resulting in 16 measurements for each notch.

The measurements parameters are described in the first line of table 2.2 describing the heating and cooling time of each pulse as a function of the lock-in frequency and duty ratio of a square wave. The switching occurs during the cooling of the third pulse of each  $\beta$  state, enabling the continuous recording of the 4 states, as illustrated in fig. 2.4a, showing a thermogram corresponding to a sound area.

Note that both the inductor and the camera remain stationary for all the measurements, with the same recording and thermo-inductive parameters. Fig. 2.5 shows the experimental

Table 2.2 Experimental parameters describing the recording and thermo-inductive parameters associated to the preliminary test, probability of detection and supplementary samples.

Experiment	$f_{induction}$ kHz	$f_{frame\ rate}$ Hz	$t_{integration}$ ms	PWM %	$f_{lock-in}$ Hz	duty ratio %	pulses per state	resolution mm/px
Preliminary test	20	300	1	50 %	5	50 %	3	0.75
POD	30	220	1	50 %	5	50 %	3	0.75
Forged Crankshaft	50	300	1	55 %	6	50 %	6	0.75
Steel billet	40	300	1	75 %	2.5	50 %	3	0.75
Forged Steel Bolt	40	300	1	70 %	2.5	50 %	3	1.00

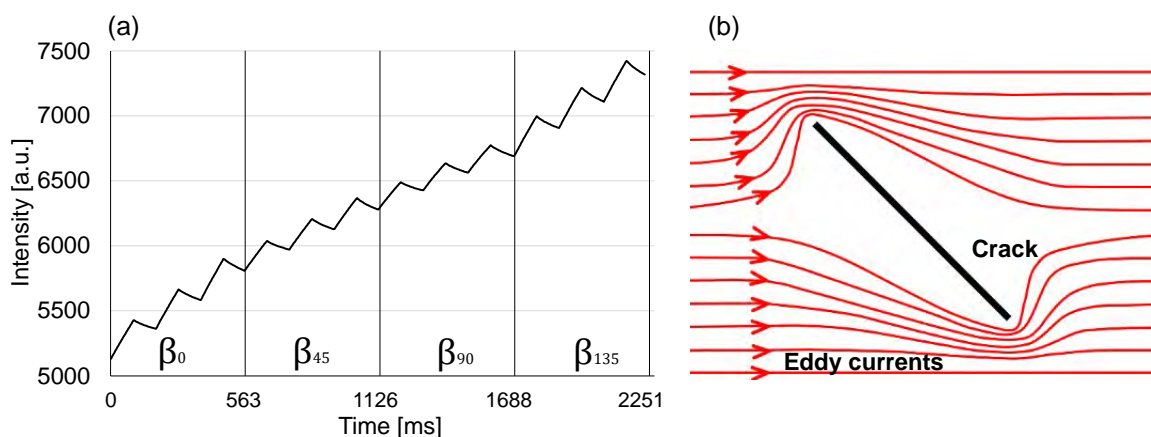


Fig. 2.4 Multi-directional thermogram. (a) Raw IR thermogram of a sound area subjected to a 5 Hz multidirectional square wave induction with 3 pulses per direction, (b) Symbolic Eddy current distribution circumventing oblique crack.

results, with the phase images as a function of  $\alpha$  for each row, and  $\beta$  for each column. The upper left diagonal phase images, with  $\psi = 0^\circ$ , exhibit the same rotated pattern. The last column shows the amplitude with the maximum increase of intensity perceived by the camera in arbitrary intensity units with  $\psi = 0^\circ$ , resulting in the highlighting of the notch. Note that the real cracks won't produce such amplitude images as it will be shown later. The pattern exhibits a localized heat originating from the tips of the notch, associated to a higher Eddy current density. Whereas the middle of the notch displays the opposite trend linked to the diversion Eddy currents under the crack. Fig. 2.6a displays the phase contrast of the whole set as a function of  $\psi$ , with a maximal phase contrast with  $\psi = 0$ . Note the phase contrast is directly correlated to  $\psi$  confirming an equivalent thermal response associated to the direction of the magnetic field.

Another aspect to consider, that has not been previously exposed, is the apparent rotation of the pattern as a function of  $\psi$ . Fig. 2.6b shows the phase image profiles of the 4  $\beta$  states with  $\alpha = 0$ , in the 0.7mm notch, plotting the phase profile of a 0.4mm radius semi-circle

centered in the notch, with  $\theta$  being the counterclockwise angle formed by each point, the center of the notch and the horizontal axis.

The resulting polar profile of each  $\beta$ , resembles a 2Hz sinusoidal wave with a  $\beta$  phase-shift, that can be modelled with the following expression,

$$I(\theta, \beta) = \mu(\theta) + \phi(\alpha, \beta)\cos(2\theta - \alpha - \beta) \quad (2.1)$$

with  $\mu$  representing the average and  $\phi$  the phase contrast as a function of  $\alpha$  and  $\beta$ . Note that the apparent motion limits the precise estimation of the orientation and length of the crack, employing a single  $\beta$ . In this scenario, the apparent rotation of the pattern can be explained by the varying asymmetry of the Eddy current distribution circumventing an oblique crack around its tips, as illustrated in in fig. 2.4b.

### 2.2.3 Thermo-inductive phase-shifting

The shifted polar profiles shown in fig. 2.6b are similar to a wave form phase-shifting. As a result, equation 2.1, can be adapted to the fundamental phase-shifting equation, assuming that the global displacement of the signals is associated to the magnetic field orientation,  $\beta$ , with a phase,  $\gamma$ , the mean,  $\mu$ , the amplitude,  $\phi$ , and the pixel intensity of the  $\beta$  signal,  $I$ , resulting in the following expression.

$$I(x, y, \beta) = \mu(x, y) + \phi(x, y)\cos(\gamma(x, y) + \beta) \quad (2.2)$$

Many methods have been exposed to compute the pixel-wise phase-shifting with predefined shifting sequences [171, 172]. In the current induction scheme shifting sequence, (0, 45, 90, 135), a generalized method, such as the one exposed in [173] has been employed, yielding the global solution, as a function of the pixel intensities.

$$\gamma = \text{atan2} \left( \frac{I_{\beta_{45}} - I_{\beta_{135}}}{I_{\beta_0} - I_{\beta_{90}}} \right) \quad \phi = \frac{1}{2} \sqrt{(I_{\beta_0} - I_{\beta_{90}})^2 + (I_{\beta_{45}} - I_{\beta_{135}})^2} \quad \mu = \frac{1}{4} (I_{\beta_0} + I_{\beta_{45}} + I_{\beta_{90}} + I_{\beta_{135}}) \quad (2.3)$$

The resulting phase-shifted images for the sequence of images for  $\alpha = 0$  are shown in fig. 2.7.

The amplitude,  $\phi$  exhibits an increased signal associated to the pixel-wise variance of the four images, the average,  $\mu$ , is clearly correlated to the image spotting the highest amplitude and the phase-shift,  $\gamma$ , shows a concentric pattern centered in the notch, corresponding to a monotonic variation of the relative orientation of the crack. The resulting model can be effectively used to continuously sample the intermediate  $\beta$  orientations with the expression

(2.2). Another clear benefit is that the subtraction of the mean can reduce the noise. Fig. 2.8 displays on the upper row the 4 original phase images of the 1.3mm notch with  $\alpha = 0$ , and below the uniformly sampled  $\beta$  synthetic images corresponding to the same range subtracting the mean.

### 2.2.4 Phase-shifted optical flow

The normalized rotational motion associated from the phase-shifted interpolation can be effectively described as an invariant feature of the cracks. The apparent motion between two images can be estimated with a method known as the optical flow (OF). The relative translation between two consecutive frames can be defined as  $I(x, y, t) = I(x + \Delta x, y + \Delta y, t + \Delta t)$ , which can be extrapolated to a dense or sparse planar vector field defined on a bounded set  $\mathbb{R}^2$ , as  $\Omega(x, y) = (\Delta x, \Delta y)^T = (u, v)^T$ , with  $u = \frac{\partial x}{\partial t}$ ,  $v = \frac{\partial y}{\partial t}$ . The OF estimation has been resolved in most of the classical OF algorithms recurring to correlation-based methods, such as the seminal work of Horn-Schunck [174], which is based on two assumptions. The first one being a photometric consistency of the moving point formulated as a line constraint or direction, written as,

$$\frac{dI}{dt} = 0 = \frac{\partial I}{\partial x} \frac{\partial x}{\partial t} + \frac{\partial I}{\partial y} \frac{\partial y}{\partial t} + \frac{\partial I}{\partial t} = E_x u + E_y v + E_t \quad (2.4)$$

with  $E_x$ ,  $E_y$  and  $E_t$  being the partial derivatives of the image. The second assumption is a term that enforces the smoothness of the solution by reducing the differences of the local flow, formulated as the minimization of the Laplacian of  $\Omega$ , written as:  $\nabla^2 u = \frac{\partial^2 u}{\partial x^2} + \frac{\partial^2 u}{\partial y^2}$  and  $\nabla^2 v = \frac{\partial^2 v}{\partial x^2} + \frac{\partial^2 v}{\partial y^2}$ .

Other common methods, rely on image pyramids to extrapolate the flow regardless of the scale [175], while modern approaches employ supervised Convolutional Neural Networks showing an improved performance [176]. OF thermographic use-cases have been mainly employed in image stabilization to generate pseudo-static sequences [60], as well as an alternative thermal signal processing [177].

A set of flows have been generated employing the method exposed by Farneback [178], implemented in OpenCV, computing the consecutive synthetic images uniformly sampled with the expression (2.2), subtracting the mean. Considering a rotational motion, the flow direction is a-priori constant which can be averaged to reduce the temporal noise. Fig. 2.9 shows the average flow of 100 images uniformly sampled in the following cyclic range of  $\beta$ ,  $[0, 45, 90, 135, 0)$ , for both notches and  $\alpha = 0$ .

### 2.2.5 Rotation vector field convolution

A fundamental concept of vector calculus, employed in fluid dynamics and electrodynamics among other fields, known as the Helmholtz decomposition, provides a simple solution to the motion analysis of the flow. Based on the assumption that the fluids are typically modelled as irrotational and incompressible, a set of constraints can be established, leading to scalar functions associated to its velocity vector field. Therefore, the optical flow can be decomposed as the summation of two components  $\Omega = \Omega_c + \Omega_r$ , with  $\Omega_c$ , being the incompressible or divergent free component with  $0 = \nabla \cdot \Omega_c$ , and  $\Omega_r$  is the irrotational or curl free component with  $0 = \nabla \times \Omega_r$ .  $\nabla$  denotes the symbolic operator whose components represent the partial derivatives,  $\nabla = (\frac{\partial}{\partial x}, \frac{\partial}{\partial y})$ . The spatial integral of  $\nabla \cdot \Omega = \frac{\partial u}{\partial x} + \frac{\partial v}{\partial y}$  over a region is called the divergence, and its orthogonal complementary,  $\nabla \times \Omega = \frac{\partial u}{\partial y} - \frac{\partial v}{\partial x}$ , is its vorticity.

As a result, the following expressions can approximate the vorticity and divergence, adapted to the optical flow,

$$w_{vort} = \sum_i^m \sum_j^n |\hat{r}_{ij} \times \Omega_{ij}|, \quad w_{div} = \sum_i^m \sum_j^n |\hat{r}_{ij} \cdot \Omega_{ij}| \quad (2.5)$$

with  $\hat{r}_{ij}$  being the local unit vector. Figure 2.10a and b shows the vorticity and the orthogonal cross-sections, and fig. 2.10c and d displays the divergence with its corresponding cross-sections. The maximum vorticity is centered in the crack with a depression surrounding it below the background signal. On the other hand, the divergence does not exhibit a clear convergence to the center of the notch. Considering that the vorticity is correlated to the center of the notch, a simple blob detector implemented in OpenCV, can effectively estimate the location of the cracks. The results will employ the vorticity with a positive truncation.

## 2.3 Results

### 2.3.1 Experimental measurements on different materials

To evaluate the performance of the exposed methods, summarized in fig. 2.1, a set of experiments has been carried out in different components made of different materials and with a diverse set of cracks.

A set of samples with natural cracks arising from the TIG and Laser welding has been characterized with a different set of methods, to enable a subsequent comparison. First, standard LPI inspections have been carried out according to ISO 23277, by a certified



inspector, leading to a partial detection of the cracks, as shown in fig. 2.11a. This procedure involves, among other things, the application of a low-viscosity fluorescent penetrant liquid that impregnates the cavities of the cracks after a certain time defined by the standard, depending on the liquid viscosity, capillarity, as well as surface tension. Subsequent removal of the excess and the final application of a developer causes the remaining penetrant liquid to bleed to the surface, allowing an easier detection. Due to the proximity of the cracks, this last step provokes widespread staining of contiguous cracks, impeding its distinct identification. In other words, the standard LPI inspection does not have enough resolution to individualize and measure the cracks, as shown in fig. 2.11b.

To enable a precise determination of the length and shape of the cracks, the standard procedure has been modified, by excluding the application of the final developer. Under a high intensity UV lamp, the samples are imaged with a  $7 \mu\text{m}/\text{px}$  resolution Leica microscope, revealing the fluorescent liquid internally permeated in the crack, as shown in figure. 2.11c. In a second step, macrographs have been taken with a Leica microscope (Leica DVM6), which has allowed for precise measurements of the length of the cracks (fig. 2.11a) under the same frame.

Fig. 2.12 displays the multi-directional DFT amplitude and phase images of the sample shown in fig 2.11. As can be observed, the directional amplitudes, shown in the first row, do not exhibit clear differences that might increase the available information. Note that some of the isolated cracks can be easily identified but its pattern can be mistakenly associated to common features, such as the natural welding surface texture and superficial scratches, among other patterns. The second row displays the multi-directional phase images, exhibiting the shifted butterfly pattern [179, 52] with a varying overlap of the pattern near the clusters of parallel cracks.

Fig. 2.13a shows the phase-shifted optical flow with an increased amplitude of the flow concentric to the cracks. Fig. 2.13b displays the resulting vorticity with a cross-section traversing a cluster of parallel cracks, plotted in fig. 2.13c. Note that the depression surrounding the cracks enables the distinct identification of the cracks.

Considering the positive results shown in the previous sample, the method has been tested in other samples, and materials with different types of cracks, as shown in fig. 2.16, with the experimental parameters shown in table 2.2, with the first two samples employing same values of the POD.

Note that fig. 2.16a and b display a TIG and laser welds made on an Inconel 718 sample, with the modified LPI procedure in the first column. Fig. 2.16a exhibits a set of cracks with a similar distribution as the one shown in fig. 2.13, but fig. 2.16b has the commonly known “fishbone crack” with a large crack centred along the weld and very small radial cracks.



Fig. 2.16c, d and e, shows a forged steel crankshaft, a steel billet, as well as a forged steel bolt respectively, with a MPI in the first column.

Note that the welded samples exhibit the typical butterfly pattern, resulting in a vorticity that clearly correlates the centre of the cracks. On the other hand, the steel samples have longer cracks, typically associated with lamination or forging defects producing a very different longitudinal pattern. However, its rotational component is clearly visible in the discontinuities and bridges of the cracks. This suggests that the narrow gaps and sharp discontinuities, such as ones present in the bridges of the cracks and the crack-tips, are locally constraining the direction of the Eddy currents, regardless of the predominant magnetic field orientation, thereby altering the local Eddy current density distribution.

### 2.3.2 POD on Inconel 718 and Haynes 282 with TIG welds

In the previous section, a robust establishment of the ground-truth of the defects has been presented and all cracks have been measured. This characterization is necessary for a POD analysis to evaluate the performance of the method presented in this work, relative to existing ones. For the POD analysis, the "Hit and Miss" (HM-POD) model has been employed, following the MIL-HDBK-1823A standard. This procedure is considered the state of the art for conducting POD studies in many industries [81], with a validated implementation in R programming language, used in the current analysis, developed by Annis [82]. The simplest POD analysis can be expressed as the ratio of true positives (TP), regarding the total number of defects, denoted as  $Recall = TP/(TP + FN)$ , with the false negatives (FN), representing the undetected defects. This oversimplified scalar, does not reflect the real detectability related to the size or length of the defects, denoted as  $a$ . In many applications, the appraisal of an inspection technique is typically associated with the bigger defect to miss, and for this reason, the POD is generally expressed as a function of the defect size, defined as an ideal binary step function. In a realistic situation, the POD is typically described as an ascending sigmoid function, that can be modelled in many ways. The most accepted HM-POD model to fit the set of binary points associated to the experiments, is the log-logistic distribution [84], written as:

$$POD(a) = \frac{e^{\frac{\pi}{\sqrt{3}}\left(\frac{\ln a - \mu}{\sigma}\right)}}{1 + e^{\frac{\pi}{\sqrt{3}}\left(\frac{\ln a - \mu}{\sigma}\right)}} \quad (2.6)$$

with  $\mu$  and  $\sigma$  being the mean and standard deviation respectively. Additionally, the regression of that model has an associated uncertainty determined by a confidence interval (CI), typically estimated with the likelihood-ratio method [85].

In this scenario, the natural cracks arising from the TIG and Laser welds have been produced on two types of alloys, namely, Inconel 718 and Haynes 282. Since the materials have different types of cracks, as well as ferromagnetic properties and surface emissivity, affecting the perceived thermal response of the signal, it has been estimated that the POD analysis must be separated in two sets with their own distinct results. A set of 13 samples with 218 cracks for the Inconel case, and 14 samples with 337 cracks for the Haynes case, has been used to conduct both analyses according to [180], stating that a set of 60 cracks is the minimum required. The followed HM-POD, for both Haynes and Inconel sets, has consisted in the following steps.

- An enhanced LPI to establish ground-truth and labelling of the defects and length.
- Phase-shifted induction thermography with a manual labelling of the butterfly pattern present in each phase image.
- The processing algorithm shown in fig. 2.1, with the local maxima search, generating the key points overlaid in the vorticity.
- Alignment and correlation of detected points with the ground-truth.

Note that an added difficulty to the correlation of the detected points is the clustered distribution of some cracks, with a corresponding local maxima plateau covering multiple cracks, as it can be seen in fig. 2.13 and fig. 2.16a. The criteria that have been used to correlate the local maxima of the vorticity and the LPI ground truth has consisted in an association based on its proximity. Fig. 2.14a shows an instance of 3 cracks and one local maxima, coinciding with 2 cracks. Fig. 2.14b spots 2 parallel cracks matched by a set of 3 points. Fig. 2.14c has 3 cracks, with a false negative.

Both the Inconel and Haynes have a set of 4 hit and miss values corresponding to the manual labelling of the butterfly patterns for each direction, a 5<sup>th</sup> one associated to the union of the 4 phase images, and the 6<sup>th</sup> one linked to the phase-shifting. Since the manually labelled mono-directional phase-images are so sensible to the orientation, they generate a hit-miss distribution that is very difficult to reliably fit resulting in very poor results.

To have a fair comparison, the union of the manual labelling of all the directions has been considered to effectively employ the same input as the phase-shifted method. The HM-POD curves are shown in fig. 2.15, with the upper row displaying the Haynes phase-shifted (a), and manual labelling (b). The lower row shows the TIG Inconel 718, with the phase-shifted POD (c) and its associated manual labelling (d). Note that the employed regression model has consisted in the log-logistic function implemented in the software made by Annis [82].

The corresponding results of the analysis are summarized in table 2.3. As it can be observed, the resulting POD analysis in both sets is significantly more robust employing the phase-shifted. It is also worth noting that some of the identified cracks were imperceptible in the static mono-directional phase images, but their rotational component has contributed to its automatic identification.

## 2.4 Conclusions

In this chapter, a novel multi-directional thermo-inductive system has been proposed which is able to generate thermographies with a discrete set of predominant Eddy current directions. The multiple orientations of the Eddy currents generate a varying path around the defect, resulting in a thermal response dependent on a directional component. The 4 directional observations produced by the exposed system enable the detection of cracks with an unknown orientation.

The variation of the phase image pattern, regarding the magnetic field orientation, exhibits a new type of rotating feature that has not been described before. This differentiating feature has motivated the development of a processing technique, inspired by the phase-shifting, based on the integration of the relative motion of the thermal response. This directional thermal response has also been observed in a set of different samples and types of cracks.

Note that the resulting thermal response of the pulses is based on the composition of the current and precedent ones. The separation of both effects could generate an improved thermal contrast, compared to a FFT of the raw thermogram, such as the one employed in this work for simplicity. The superposition of multiple induction modalities, combining discrete or continuous directional and temporal modulations remains an interesting topic, which could potentially yield to complementary information.

The whole processing technique has exploited the rotating motion of the cracks in steel and superalloys such as Inconel 718, and Haynes 282, showing a strong correlation in all the exposed cases. The performance evaluation of this technique has been conducted with a 'Hit/Miss' Probability of Detection model, showing an increased sensitivity regarding the manual labelling of the phase-images butterfly patterns of the cracks. Future works should focus on the generalization of the technique to all types of defects, employing machine learning models, or neural networks, that would be able to carry out a fused training of the set of the discrete set of directional images. Multi-spectral and color-based Convolutional Neural Networks seem like good candidates to generalize the technique to enable an increased sensitivity of the phase-shifted induction thermography. Alternatively, the development of tailor made techniques that would focus on a sparse statistical reduction of the optical

flow, into a set of trainable descriptors would also be a worthwhile option to explore in upcoming iterations. Ultimately, a rigorous physical modelling of the observed phenomena is necessary to further optimize the technique or develop new methods, as well as an eventual extrapolation to other use-cases.

Table 2.3 Hit/Miss Probability of Detection summary of both sets of welds comparing the manual labelling with the exposed method.  $a_{50}$ ,  $a_{90}$  and  $a_{90/95}$  are the minimum lengths providing a probability of detection of 50 %, 90 % and 90 % with a confidence level of 95 %, respectively.

Set	Method	$a_{50}$ <i>mm</i>	$a_{90}$ <i>mm</i>	$a_{90/95}$ <i>mm</i>	nTot	nHits
Haynes 282	Phase-Shift	0.3757	0.7424	0.8545	337	251
Haynes 282	Manual Labelling	0.6252	1.115	1.26	337	192
Inconel 718	Phase-Shift	0.3599	0.5771	0.6656	218	182
Inconel 718	Manual Labelling	0.5184	1.068	1.279	218	148

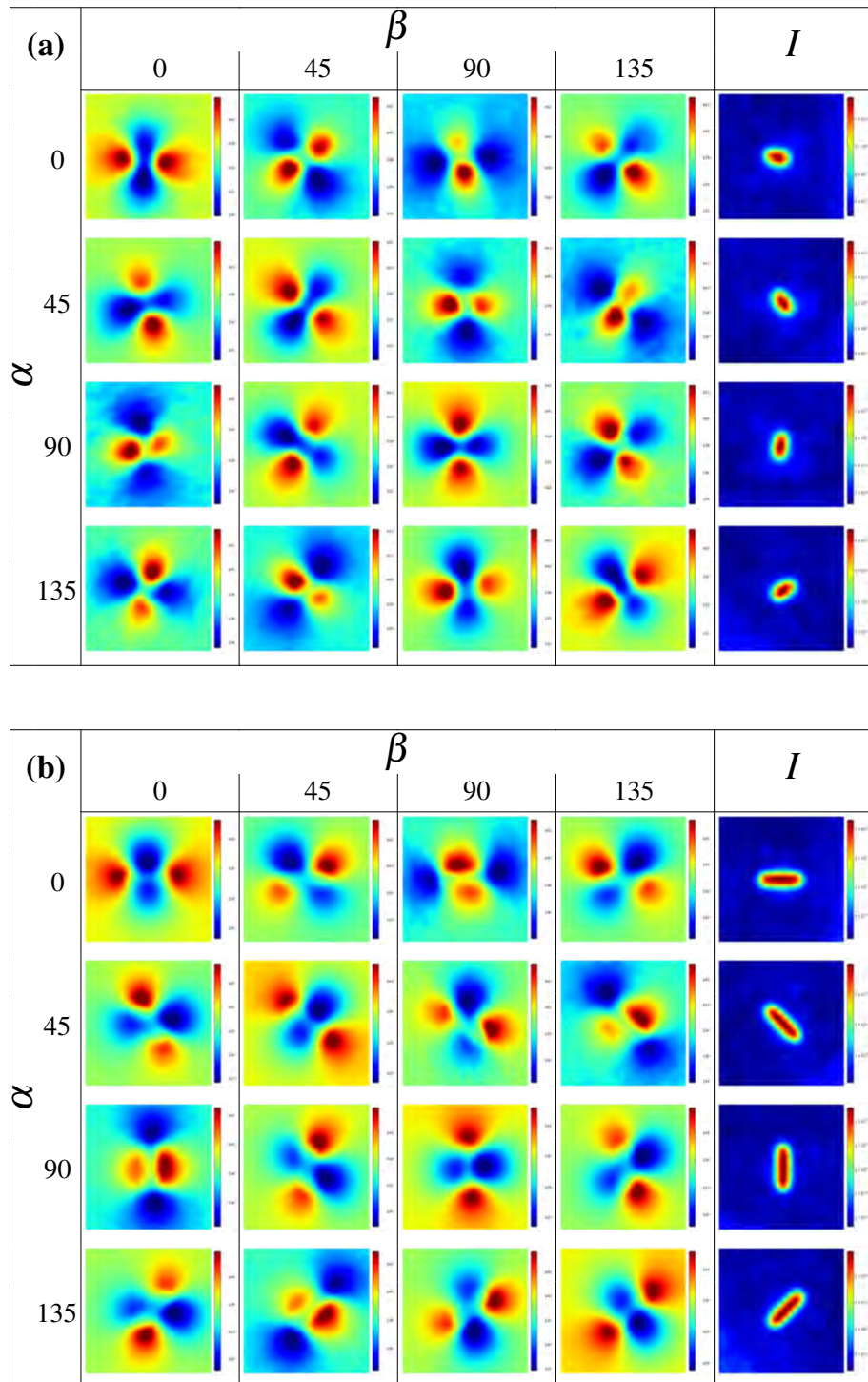


**Fig. 2.5 Phase images on notches, as a function of the magnetic field orientation.** The first four columns shows the phase images in degrees as a function of the direction of  $\beta$  and the last one corresponds to the amplitude of the FFT. The rows displays the notches in different directions,  $\alpha$ . (a) 0.7mm, (b) 1.3mm.

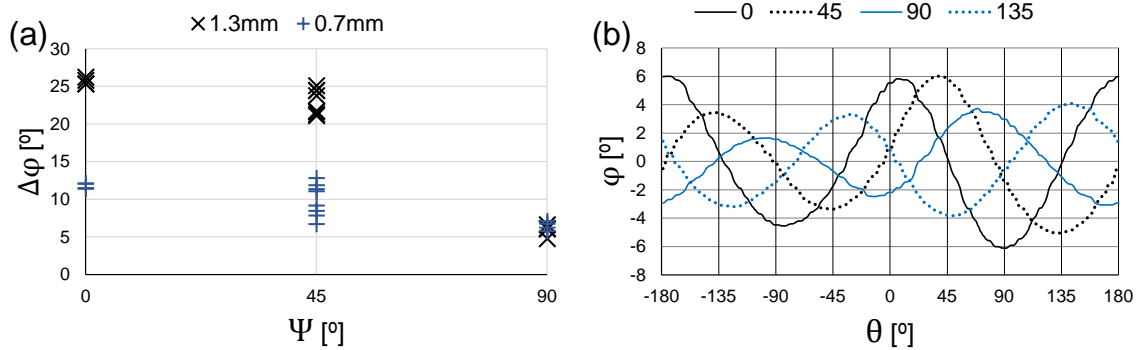


Fig. 2.6 Directional Phase contrasts. (a) Phase Contrast as a function of the relative orientation between the the artificial defect and the magnetic field  $\psi$ , (b) Polar profiles of the phase images centered in the crack with a radius of 0.4 mm, coinciding with phase maximum of the 0.7 mm notch and  $\alpha = 0^\circ$ .

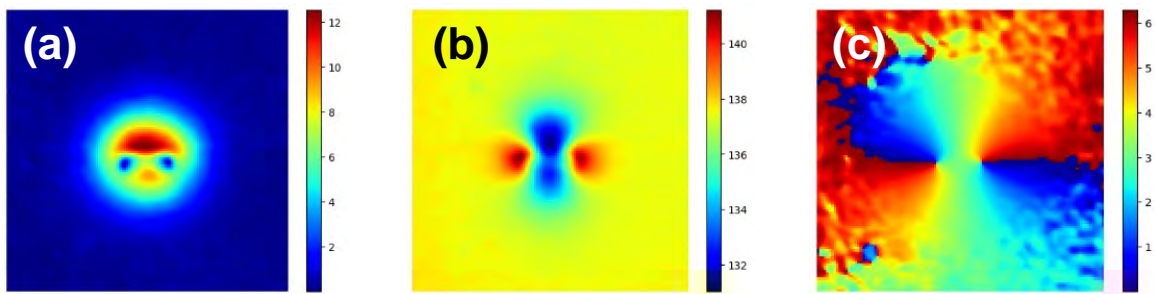


Fig. 2.7 Thermo-inductive phase-shifting. Image corresponding to the parameters of the phase-shifting of the four phase images of the carrier frequency (a)  $\phi$  amplitude [°], (b)  $\mu$  average [°], (c)  $\gamma$  phase-shift [rad].

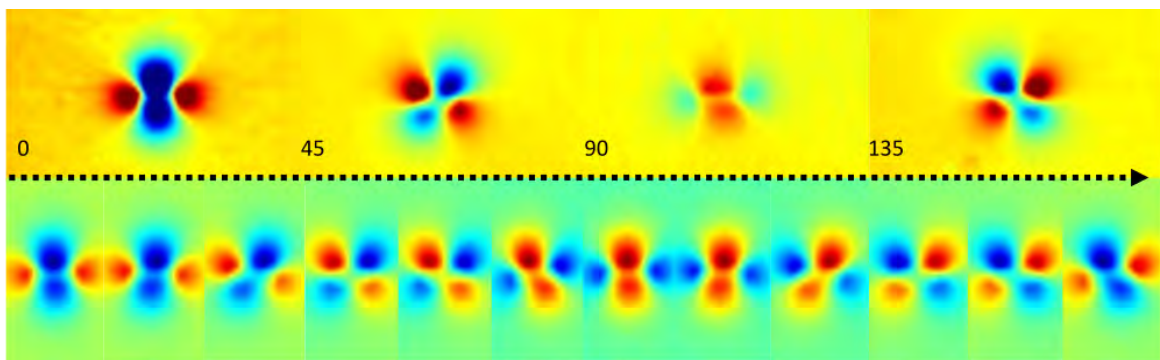


Fig. 2.8 Normalized phase-shifted interpolation. Upper row with the 4 original phase images of the 1.3mm notch with  $\alpha = 0$ , below a sequence of synthetic phase-shifted images with a uniform sampling of  $\beta$  covering the same range.



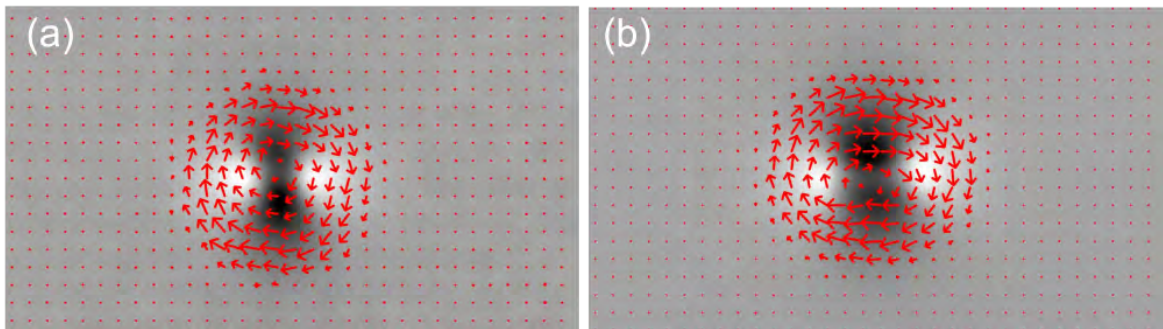


Fig. 2.9 Phase-shifted optical flow average overlaid on top of the first phase image. (a) 0.7 mm, (b) 1.3 mm.

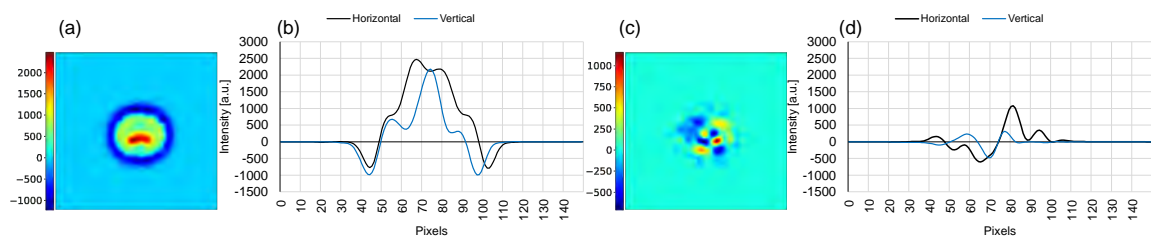


Fig. 2.10 Motion field potential functions. (a) Intensity and orthogonal cross-sections of the vorticity (a, b), and the divergence (c, d).

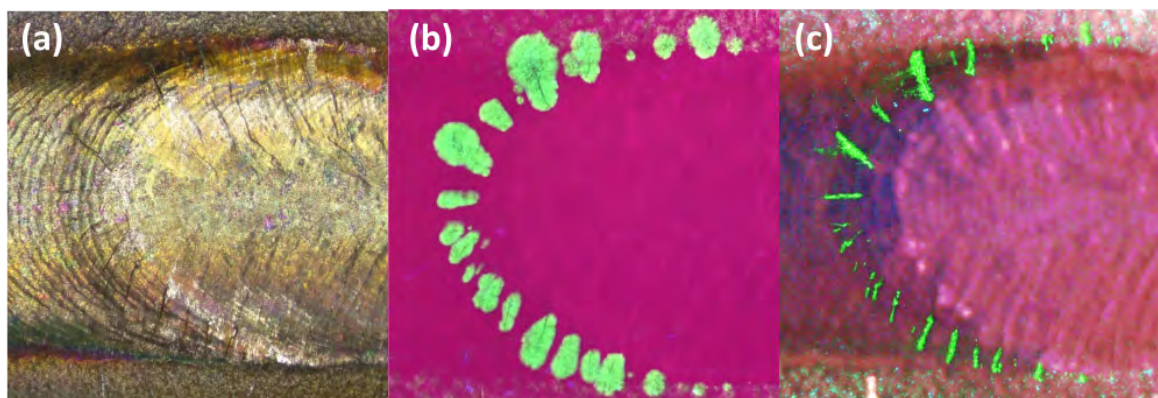


Fig. 2.11 Modified fluorescent penetrant inspection TIG Inconel weld. (a) clean surface, (b) Standard LPI under UV light after the application of a developer, (c) Enhanced LPI under UV light after removing the excess of the fluorescent liquid.

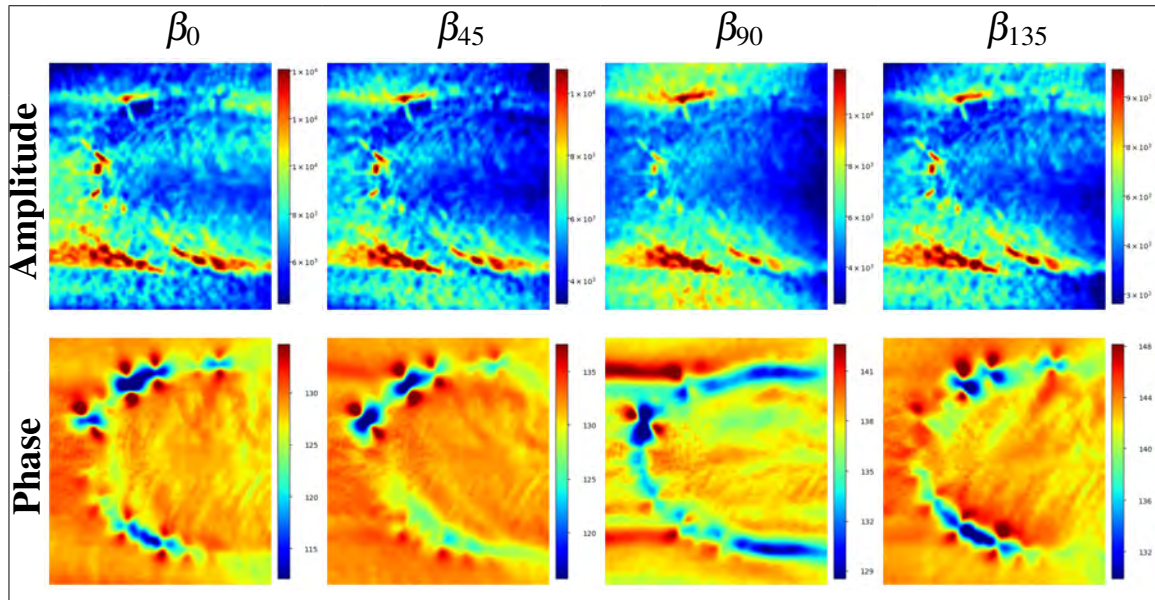


Fig. 2.12 Multi-directional DFT in TIG Haynes weld. Upper and lower row displaying the directional amplitudes in arbitrary units and phases in degrees of the carrier frequency, associated to the four directions,  $\beta$ .

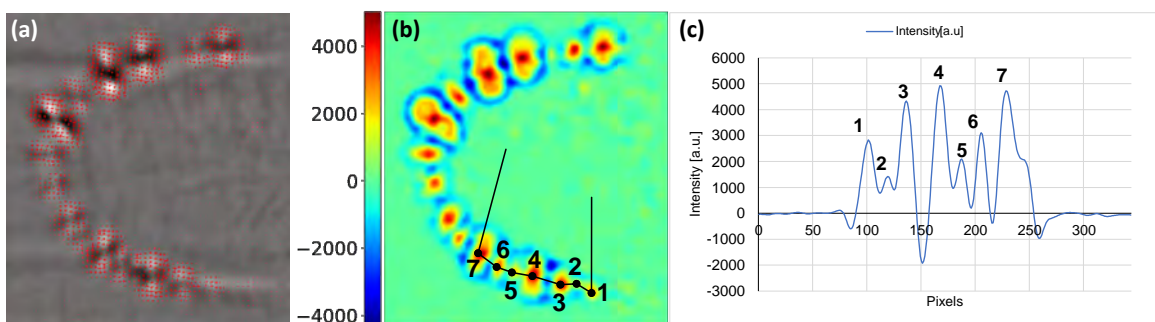


Fig. 2.13 Phase-shifted optical flow vorticity signal profiles. (a) Optical flow of Haynes weld overlaid on top of the phase image, (b) Vorticity, (c) Vorticity profile highlighting the peaks corresponding to the center of the cracks.



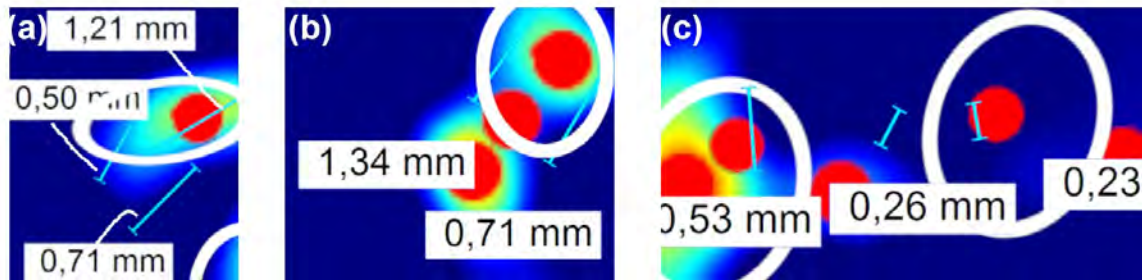


Fig. 2.14 Clustered cracks association examples. Vorticity image fragments displaying an overlay of the real cracks in bright blue and the corresponding size, the detected peak of the vorticity in red, and the association of the crack and the peaks highlighted in white, yielding a number of true and false positives, as well as false negatives. (a)  $Tp=2$ : 0.5, 1.21 mm,  $Fn=1$ : 0.71 mm,  $Fp=0$ , (b)  $Tp=2$ : 1.34, 0.71 mm, (c)  $Tp=2$ : 0.53, 0.23 mm,  $Fp=0$ ,  $Fn=1$ : 0.26 mm,  $Fp=2$ .

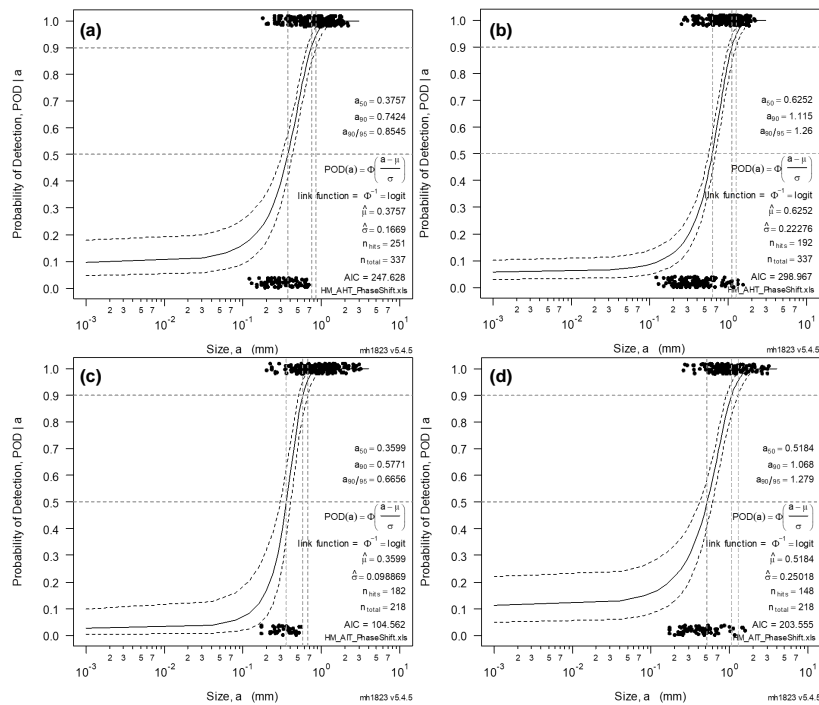


Fig. 2.15 Hit/Miss Probability of Detection. Estimated POD sigmoid with a solid line, and the upper and lower confidence level with a dotted line. Four PODs corresponding to both sets and methods. (a) Haynes Phase-shift, (b) Haynes union manual labelling, (c) Inconel Phase-shift, (d) Inconel union manual labelling.

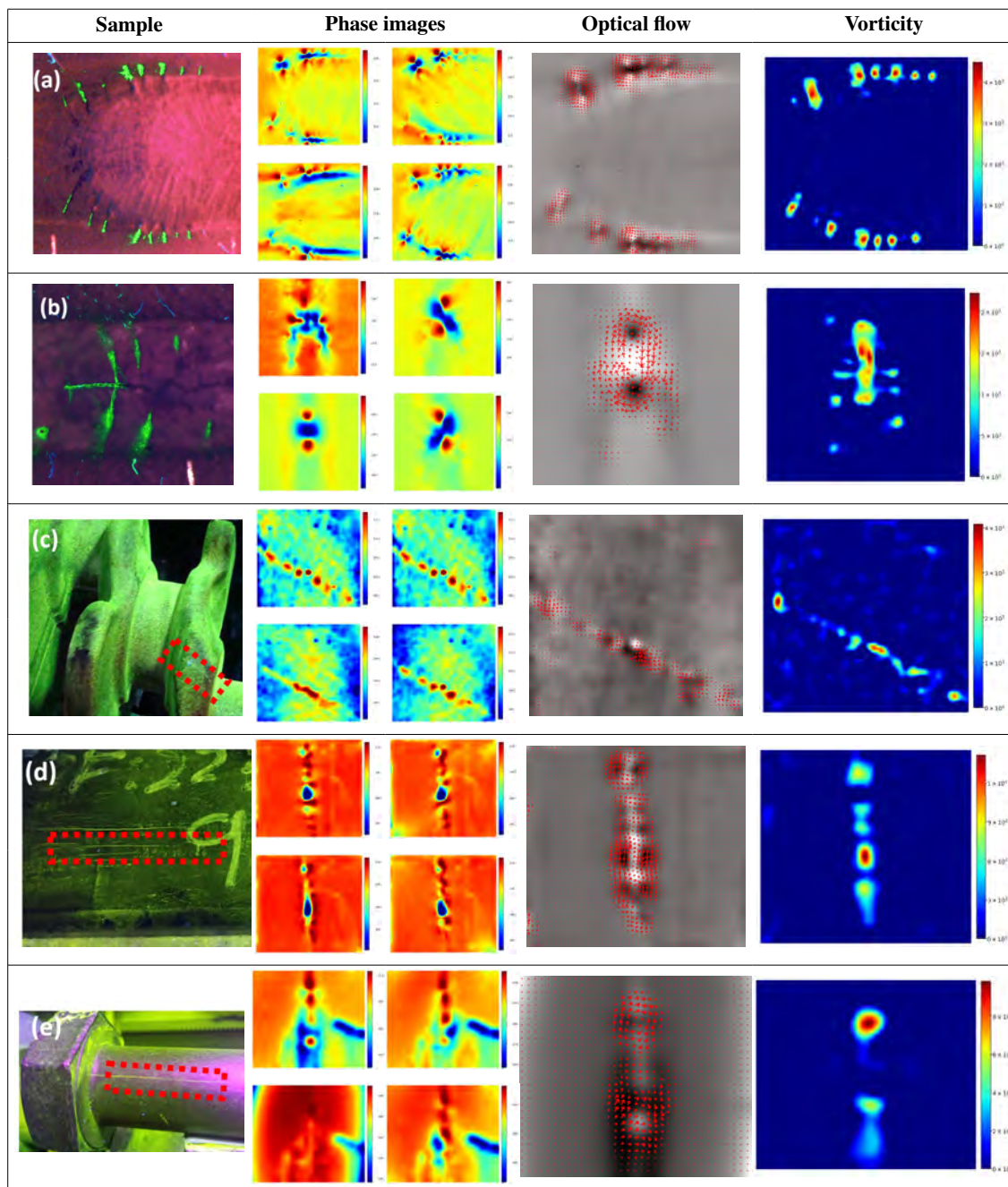


Fig. 2.16 Natural weld crack detection. The first column displays the samples with the enhanced LPI for TIG inconel (a) and a laser inconel 718 (b), and a MPI for (c) forged steel crankshaft, (d) steel billet and (e) forged steel bolt. The remaining columns displays the multi-directional phase images, the optical flow, as well as the vorticity with a positive truncation.

# Chapter 3

## Quadratic inductor

### 3.1 Introduction

The previous chapter exposed a system to generate directional magnetic fields with a tetra-pole inductor, which enables a new type of induction thermography modality. Considering that this novel technique enables a robust detection of the cracks regardless of their orientation, it has been deemed interesting to develop an inductor which is able to induce a more uniform magnetic field. In this chapter, a novel type of inductor is presented, with four coils wound on a hollow parallelepiped core, which is able to generate a magnetic field with multiple orientations, enabling the detection of defects with an arbitrary orientation orthogonal to the inspected surface.

Eddy current thermography (ECT) is a technique consisting on the induction of a magnetic field to generate a superficial ECT (Eddy Current Testing) is a technique that induces a magnetic field to generate superficial heating, allowing the detection of surface and subsurface defects that may cause alterations in the resulting thermal diffusion, captured by an infrared camera.

In this context, the disturbance of thermal diffusion caused by the crack may be influenced by the relative orientation of the defects with respect to the magnetic field, as observed in the literature review. While in many cases, the set of defects may have a predominant orientation, this is not always guaranteed, as seen in the case of crack patterns in the welds of Chapter 2.

There are some inductors, such as the tetra-pole proposed by Yang et al. [181], and the one presented by Li et al. [56], both of which consist of two pairs of coils. These coils individually generate an orthogonal magnetic field between them. In both works, the coils are wound around "legs" that directly contact the surface. Additionally, in both cases, the authors subject both pairs of coils to a 90° phase-shifted waveform.

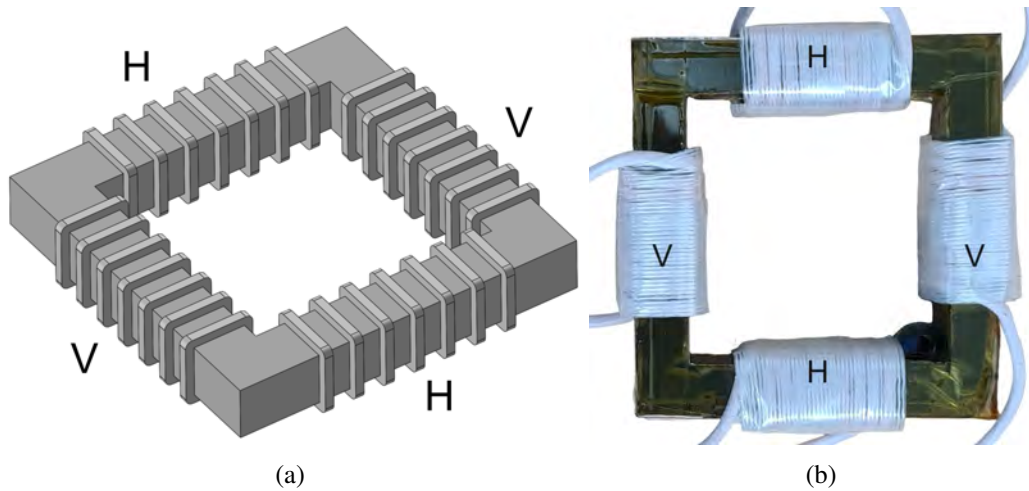


Fig. 3.1 Quadratic inductor. (a) 3D render with labelled coil pairs. (b) Instance used in experiments.

This arrangement allows them to generate a rotating magnetic field, analogous to vertical polarization, with a rotation speed identical to the electrical frequency of the source powering the coils.

In section 3.2, the inductor is described and in section 3.3, the results of the tests are presented.

## 3.2 Methods

In this section a brief description of the proposed inductor is presented, as well as the tested modalities of the results.

### 3.2.1 Inductor description

It is a quadratic inductor with a hollow parallelepiped-shaped core, featuring two pairs of parallel coils labeled  $H$  and  $V$ , on each side. Fig. 3.1a provides a 3D view of the inductor with the four coils, and fig. 3.1b displays one of the manufactured instances based on this design.

Depending on the internal window of the inductor, it can be adapted to different use cases, allowing for a higher magnetic field density or a different inspection area.

Taking into consideration that the distribution of the magnetic field can be influenced by the shape of the coil and the inductor, both of which have a rectangular form in this case, it can be proposed that the magnetic field density is inversely proportional to the square of the

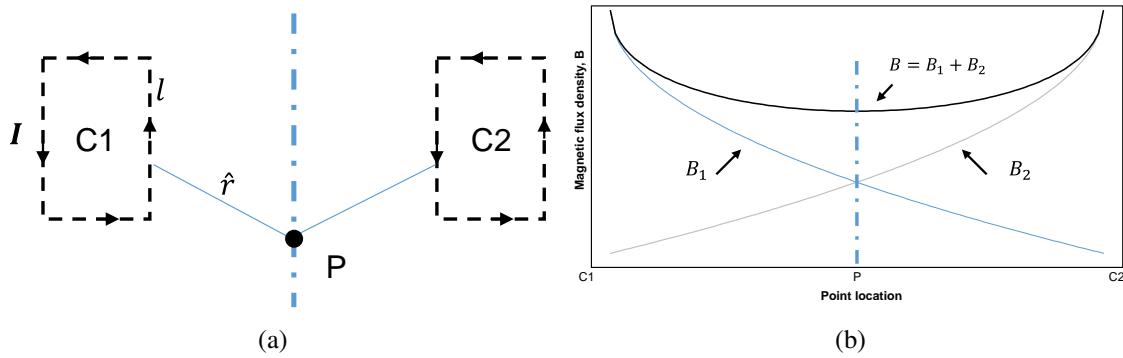


Fig. 3.2 Schematic diagram for coils in opposite sides. (a) Currents of both coils relative to  $P$ , on the surface. (b) Schematic trend of magnetic flux density of both coils.

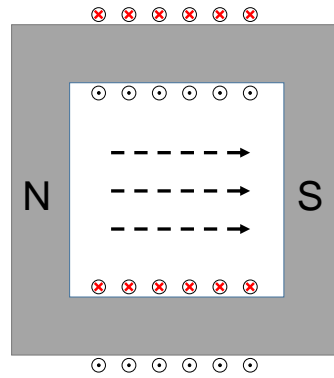


Fig. 3.3 Magnetic field direction of two opposing coils.

distance from the conductor, according to Biot and Savart's theorem, as follows:

$$dB = \frac{\mu}{4\pi} \frac{Idl \times \hat{r}}{r^2} \quad (3.1)$$

Here,  $r$  is the distance,  $\mu$  is the magnetic constant,  $Idl$  is the infinitesimal displacement of the conductor, and  $\hat{r}$  is the unit vector between the evaluated point and the conductor. In this context, the schematic representation of the relationship between the two coils, with a counter-clockwise current, and a point  $P$  located between them is shown in fig. 3.2a. On the other hand, the sum of both magnetic fields can be schematically seen in fig. 3.2b, yielding a higher density of the magnetic flux in the proximity of the coils, with a lower density and variation on the center.

Taking into account the direction of the current and the arrangement of the coils, the predominant direction of the magnetic field at the center of the inductor is parallel to the winding axis of each coil pair, as illustrated in the fig. 3.3.

The simultaneous activation of the two orthogonal pairs of coils can be ideally defined as a vector addition in  $\mathbb{R}^2$  with  $\vec{\mathbf{B}} = \vec{\mathbf{B}}_x + \vec{\mathbf{B}}_y$ , where  $\vec{\mathbf{B}}_x = \vec{i}\phi_x \sin(2\pi f_x t + \theta_x)$  and  $\vec{\mathbf{B}}_y = \vec{j}\phi_y \sin(2\pi f_y t + \theta_y)$ , with  $\phi$ ,  $f$  y  $\theta$  are the field amplitudes, frequency and phase shifts of both pairs of coils respectively.

The resulting magnetic field amplitude is  $|\vec{\mathbf{B}}| = \sqrt{\vec{\mathbf{B}}_x^2 + \vec{\mathbf{B}}_y^2}$  and its orientation or phase is defined as  $\beta = \arctan \frac{\vec{\mathbf{B}}_y}{\vec{\mathbf{B}}_x}$ .

As a result, it is possible to replicate the same scheme of rotational induction as proposed by Yang et al. [181] and Li et al. [56], using the same induction frequency along both axes and an absolute phase difference,  $\Delta\theta = |\theta_x - \theta_y|$ , of  $90^\circ$ . However, in this case, such a possibility has not been experimentally tested. Alternatively, there is the option of using two different induction frequencies that result in a continuous variation of  $\beta$ , analogous to the approach presented by Oswald-Tranta et al. [182]. This induction modality has been tested during the development of the thesis, as a proof of concept, with two generators, yielding thermographies which enables the detection of cracks, regardless of their orientation with a single pulse.

To test the capabilities of this inductor, the selective induction of the coils has been performed yielding four magnetic flux directions, using the same scheme described in Chapter 2. These directions are illustrated in fig. 3.4 considering the currents in each pair of coils in red, and the resulting magnetic flux in dotted lines.



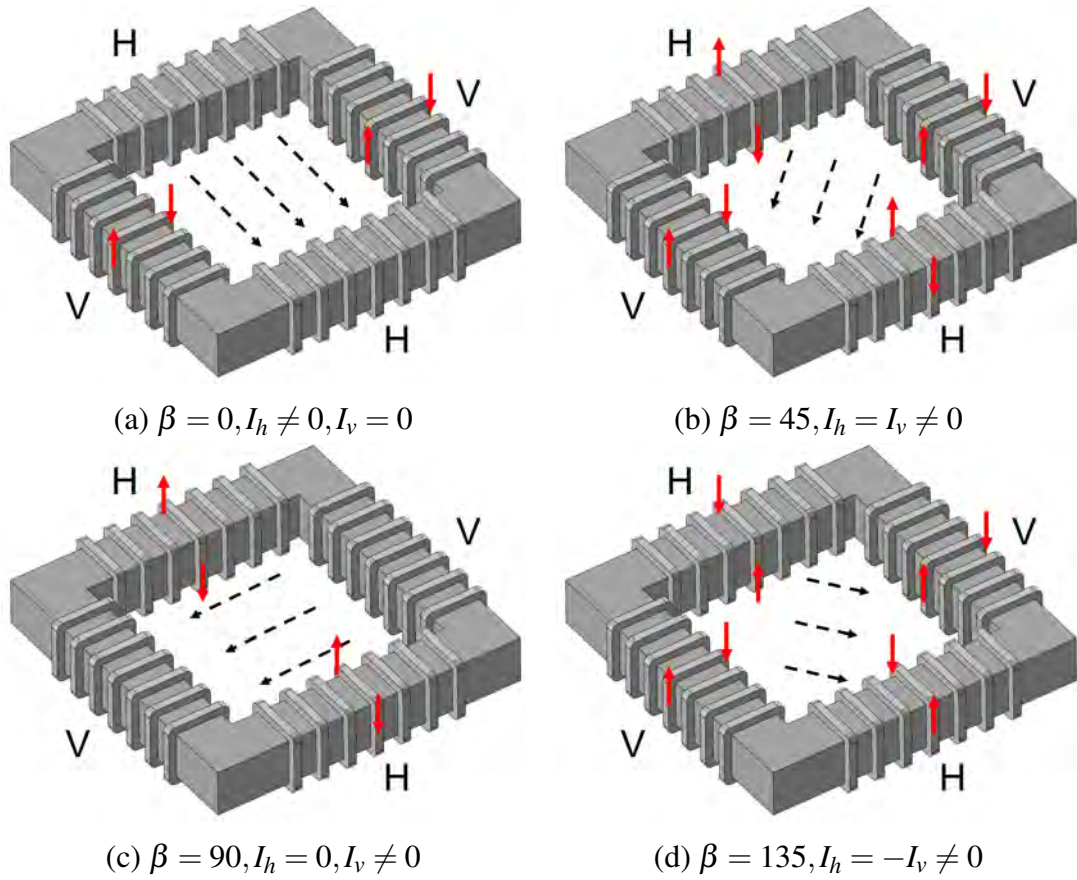


Fig. 3.4 Quadratic inductor states, considering different currents for each pair of coils.

### 3.2.2 Setup

To empirically validate the results achieved using this inductor for non-destructive testing through thermography, the experimental setup depicted in Figure 3.5 has been used afterwards.

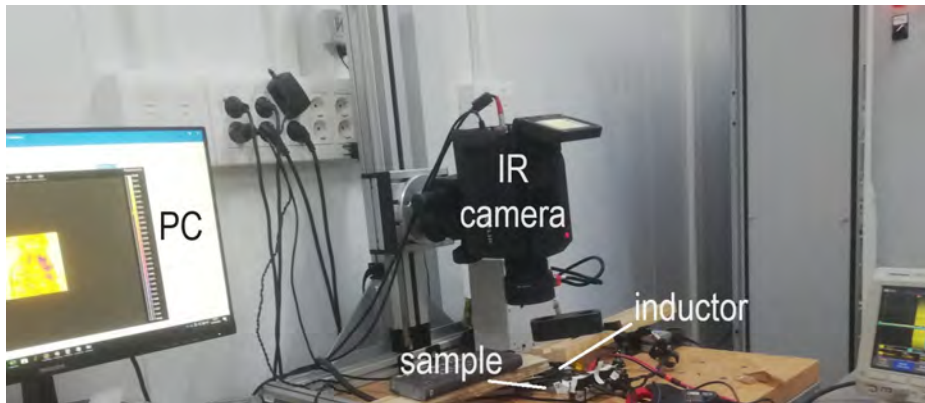


Fig. 3.5 Experimental setup.

It is composed by a Flir X6541sc infrared camera equipped with a Stirling-cooled 640x512 InSb sensor capable of achieving a frame rate of 125 Hz at full frame or 4 kHz in windowing mode. The quadratic inductor is powered by an Edevis ITVis 3000 MHF generator, which incorporates a full-bridge inverter circuit with pulse-width modulation, enabling an induction frequency range from 10 kHz to 60 kHz. The activation of the inductor coils is handled by a switching device, enabling the alteration of the magnetic field orientations of the inductor in 4 different states. The experimental parameters of both notches and natural cracks are: 300Hz framerate, 0.001 integration time, 20kHz induction frequency, 4 square lockin pulses with 5Hz frequency, yielding 0.8s recording time.

## 3.3 Results

In this section a set experiments has been carried out to evaluate the proposed inductor on a set of notched probes and samples with natural cracks.

### 3.3.1 Notched samples

A set of notched samples made out of an austenitic allow used in the aeronautic sector called Inconel 718, has been subjected to multiple induction thermography tests, considering the 4 activation states of the inductor rotating the inductor only in orientations. Two artificial notches have been produced with Electrical Discharge Machining (EDM), with 0.7 mm and 1.3 mm length and the same depth and width of 0.75 mm and 0.1 mm respectively. Note that the notched surface material is Inconel 718, in a sample measuring 4.75 x 80 x 150 mm. The measurements will be analogous to the ones exposed on chapter 2, but in this scenario the inductor will be rotated, instead of the sample. Fig. 3.6 shows the phase images on the first



---

columns for each inductor state  $\beta$ , last column amplitude of  $\beta = 0$ , and the rows correspond to an induction rotating the inductor  $\alpha$  degrees, last columns delta intensity colored in three been to show its distribution.

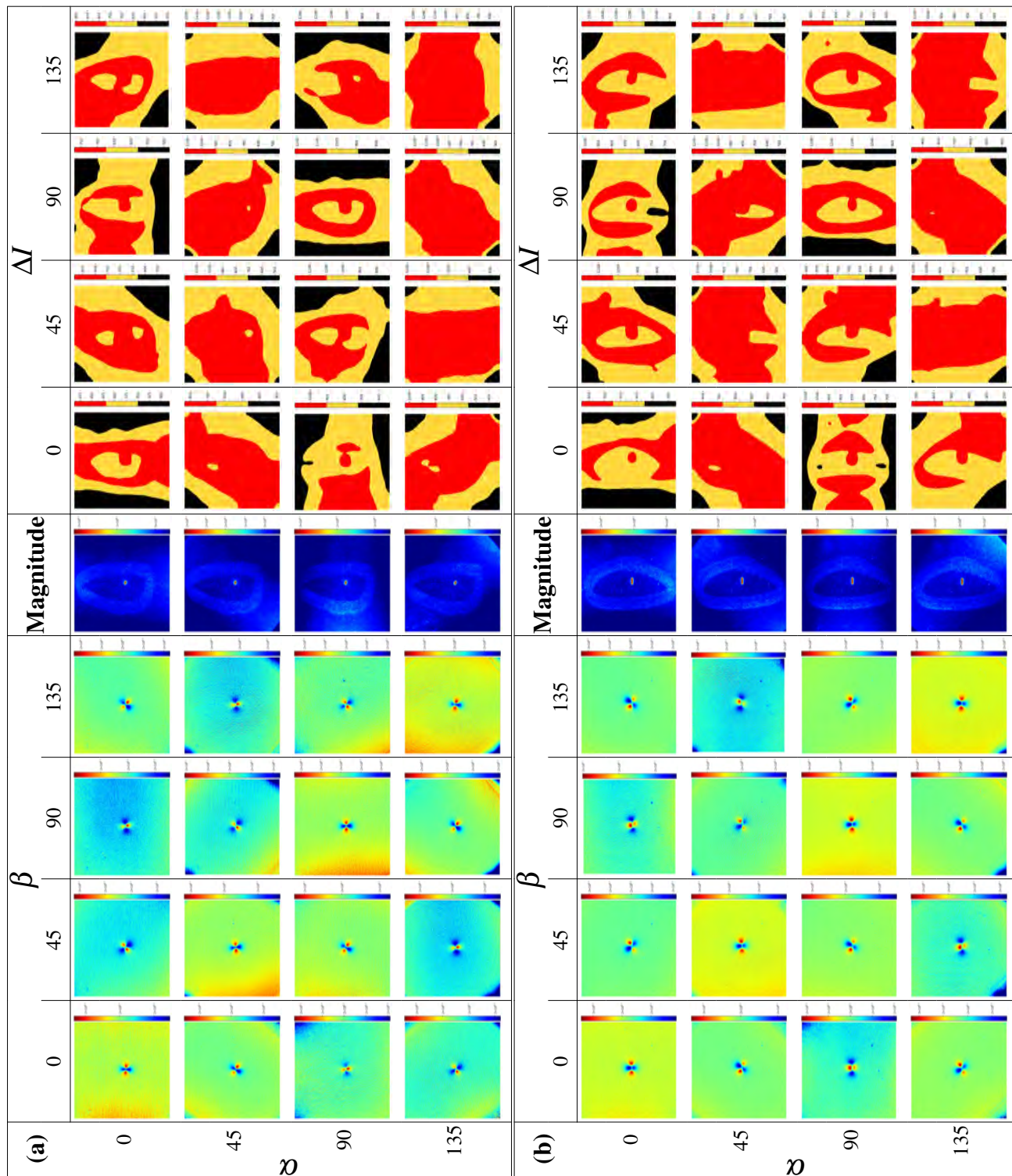


Fig. 3.6 Quadratic inductor on notches, phase images  $\beta$  on the columns, rotating the inductor on the rows  $\alpha$  and the sample and camera remaining stationary, fifth column magnitude  $\beta = 0$ , last column magnitude  $\beta = 0$ , last column delta intensity colored in 3 bins. (a) 0.7mm (b) 1.3mm.

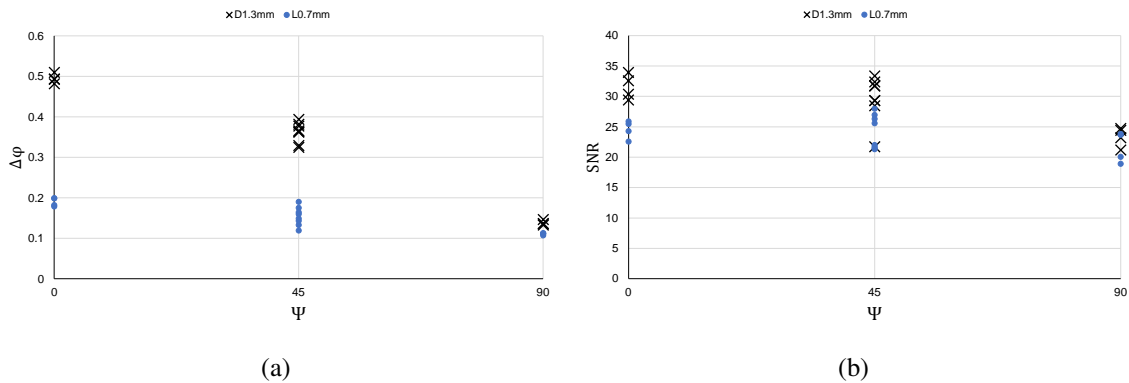


Fig. 3.7 Notches phase contrast and SNR as a function of relative orientation of magnetic field and crack,  $\Psi$ . (a) Delta Phase [rad]. (b) SNR [dB]

The analysis shown in fig. 3.7 quantifies the phase contrasts of the 32 measurements, as well as the SNR employing the following expression  $SNR = 20 \log_{10} \frac{\Delta\varphi}{\sigma}$ , with  $\sigma$  standard deviation of a sound area and  $\varphi$  being the local contrast of the crack tips and crack center. These results are analogous to the ones exposed on the same notches in chapter 2.

The absolute phase contrast and SNR shows a similar trend compared to the tetra-pole inductor exposed in chapter 2.

### 3.3.2 Natural cracks

Two samples have been tested following the same procedure, (1) a cracked fragment of a steel mooring chain, as depicted in fig. 3.8a, and (2) hayness 282 TIG welded sample on fig. 3.8b.

Fig. 3.9 and fig. 3.10 depicts the phase, as well as the magnitude images of the chain fragment and hayness sample, with a rotating butterfly pattern.

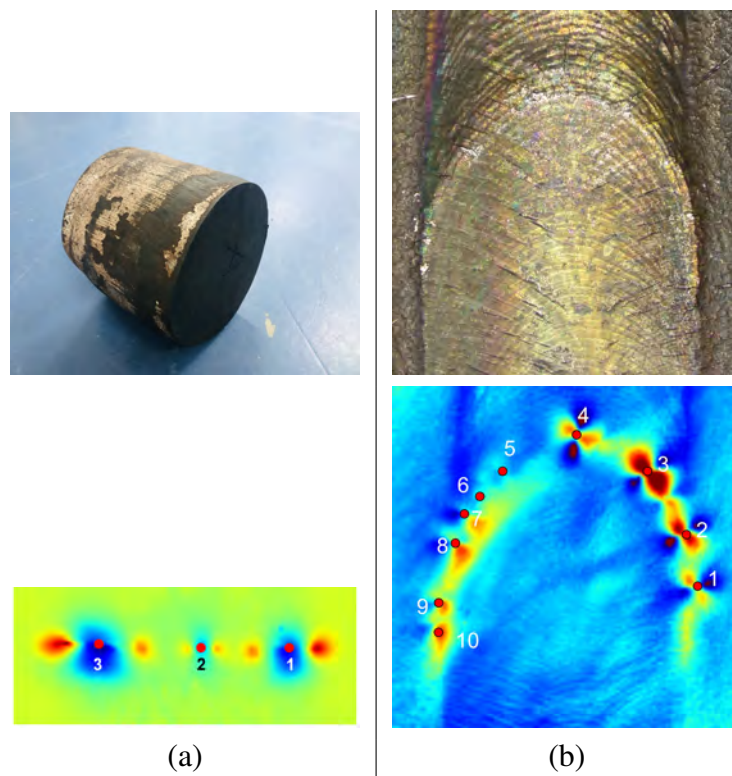


Fig. 3.8 Natural cracks samples. Upper row upper photograph, lower phase image with labelled crack centers. (a) Steel mooring chain fragment. (b) Hayness TIG welded coupon.

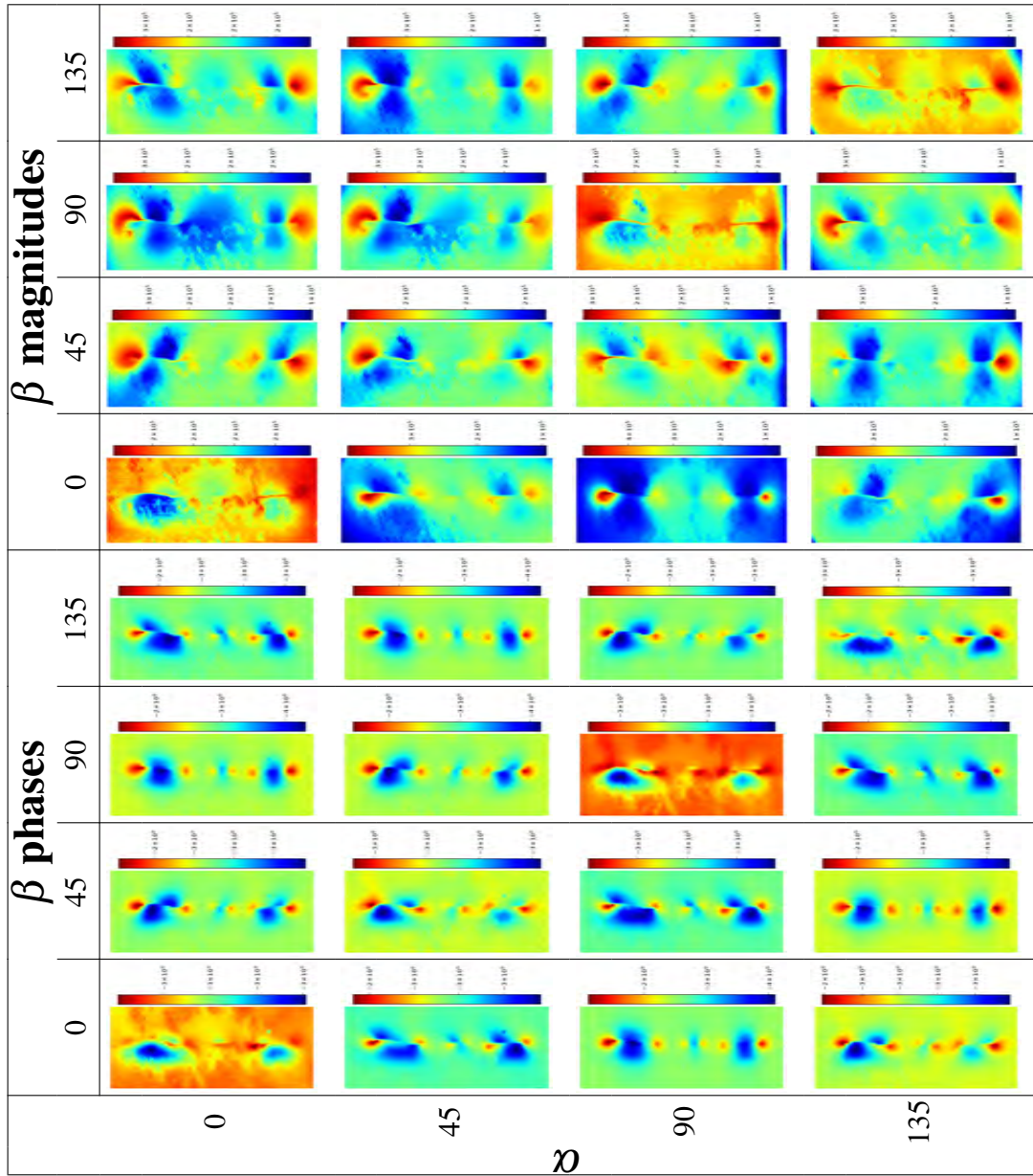


Fig. 3.9 Quadratic inductor on steel mooring chain, depicting different inductor states  $\beta$  on the columns, rotating the inductor on the rows  $\alpha$  and the sample and camera remaining stationary.



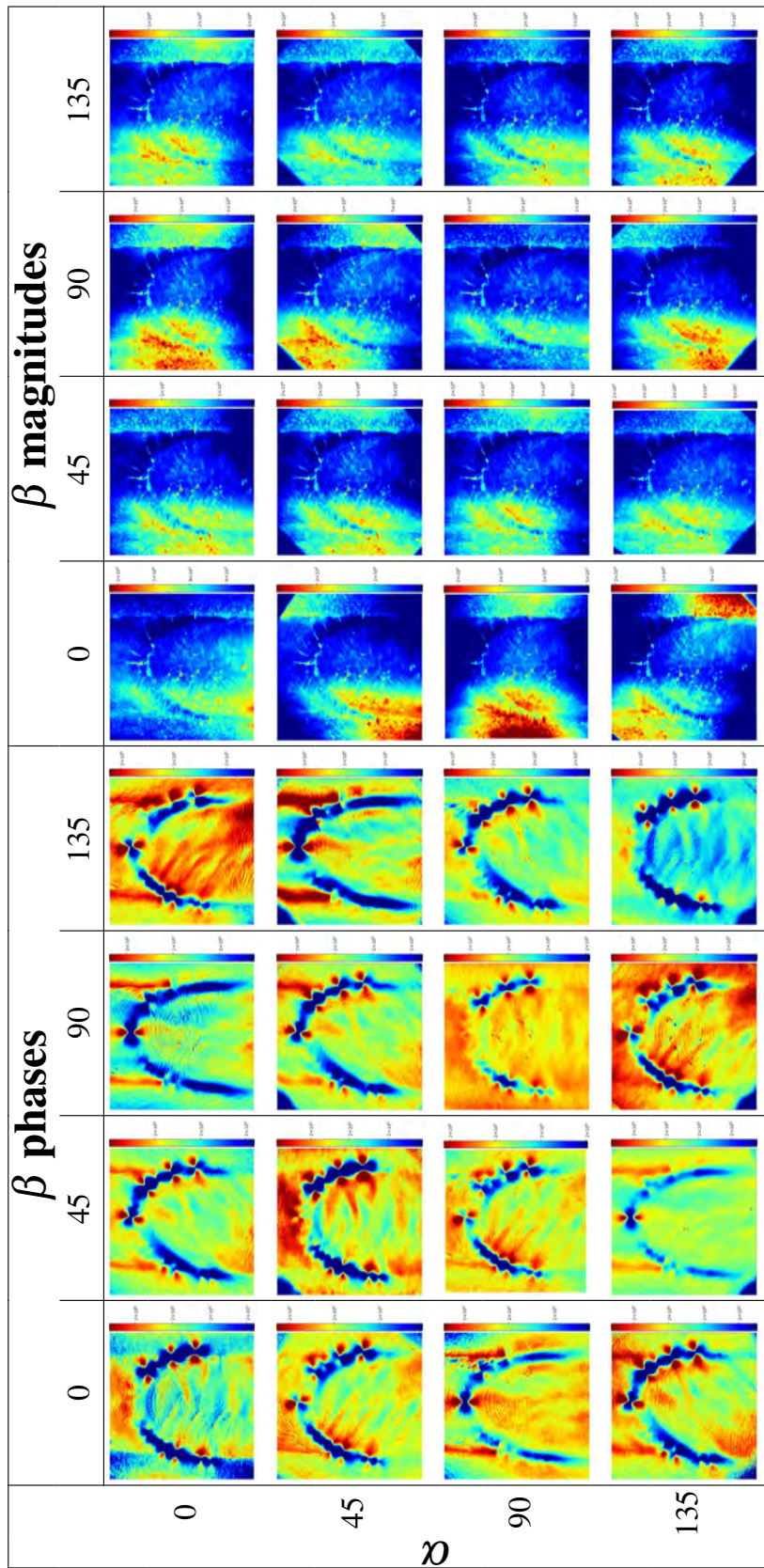


Fig. 3.10 Quadratic inductor on TIG welded hayness sample, depicting different inductor states  $\beta$  on the columns, rotating the inductor on the rows  $\alpha$  and the sample and camera remaining stationary.

Table 3.1 Natural crack recall, hayness sample, considering the maximum signal of each set of induction states with a minimum SNR of 4dB.

	$\alpha_0$	$\alpha_{45}$	$\alpha_{90}$	$\alpha_{135}$
$\beta_0$	0.7	0.8	0.4	0.7
$\max(\beta_0, \beta_{90})$	0.8	1	0.9	0.9
$\max(\beta_0, \beta_{45}, \beta_{90}, \beta_{135})$	1	1	1	1

Fig. 3.11 and fig. 3.12 depicts the SNR and  $\Delta\phi$  of the defects, with multiple rotations of the inductor  $\alpha$ , as well as the combined maximum SNR of single inductor state ( $\beta_0$ ), two orthogonal inductor states ( $\beta_0, \beta_{90}$ ), as well as the 4 states.

The steel chain fragments has 3 cracks which generate a very high signal with a low noise background. These cracks can be detected employing almost any relative direction of the magnetic field. In this scenario, only the smallest crack (n° 2), won't have a significant signal if the relative orientation of the Eddy currents and the crack is orthogonal. The first and third cracks are deeper and the assymetric butterfly pattern indicate that they might be slightly inclined beneath the surface. Note that these thermographies have rotated 90°. . Considering the hayness probe, the small shallow cracks generate a lower phase delta and SNR, which can be associated with smaller heating of the austenitic allow, affected by the varying texture of the weld with a reflective surface finish associated to hayness. To evaluate the performance of this method on the hayness probe considering 3 induction orientation combinations, a simple recall ratio quantification has been performed, as shown in table. 3.1, with a minimum threshold of 4dB for the SNR. Note that recall is defined as  $recall = \frac{TP}{TP+FN}$ , with  $TP$  and  $FN$  being the number of true positives and false negatives respectively.

In this scenario, the mono-directional induction misses multiple cracks with a much lower signal and higher noise, but the employment of two orthogonal direction yields a much better result, ultimately the 4 orientations provide the best result. Note that the total time recording time of each combination is different.

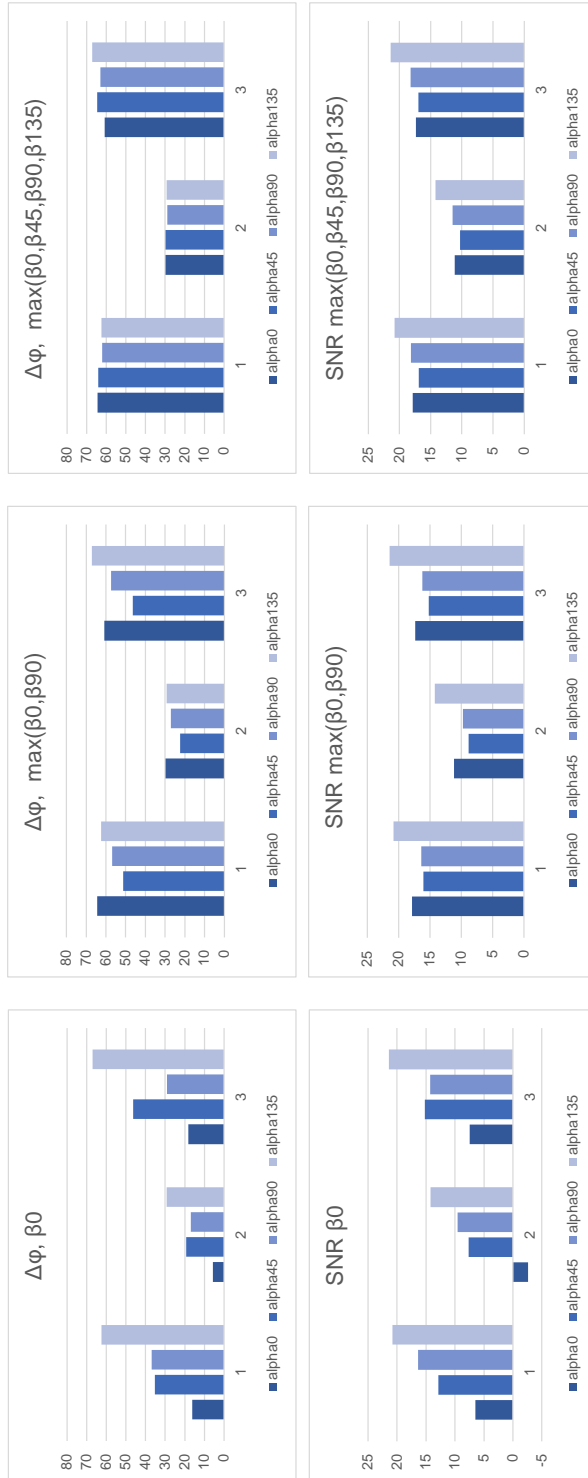


Fig. 3.11 Steel mooring chain,, delta phase (° upper row), SNR (dB lower row) with multiple induction combinations and cracks. Columns with the maximum of different induction combinations, left column 1 state, middle 2 orthogonal states, right, 4 states.



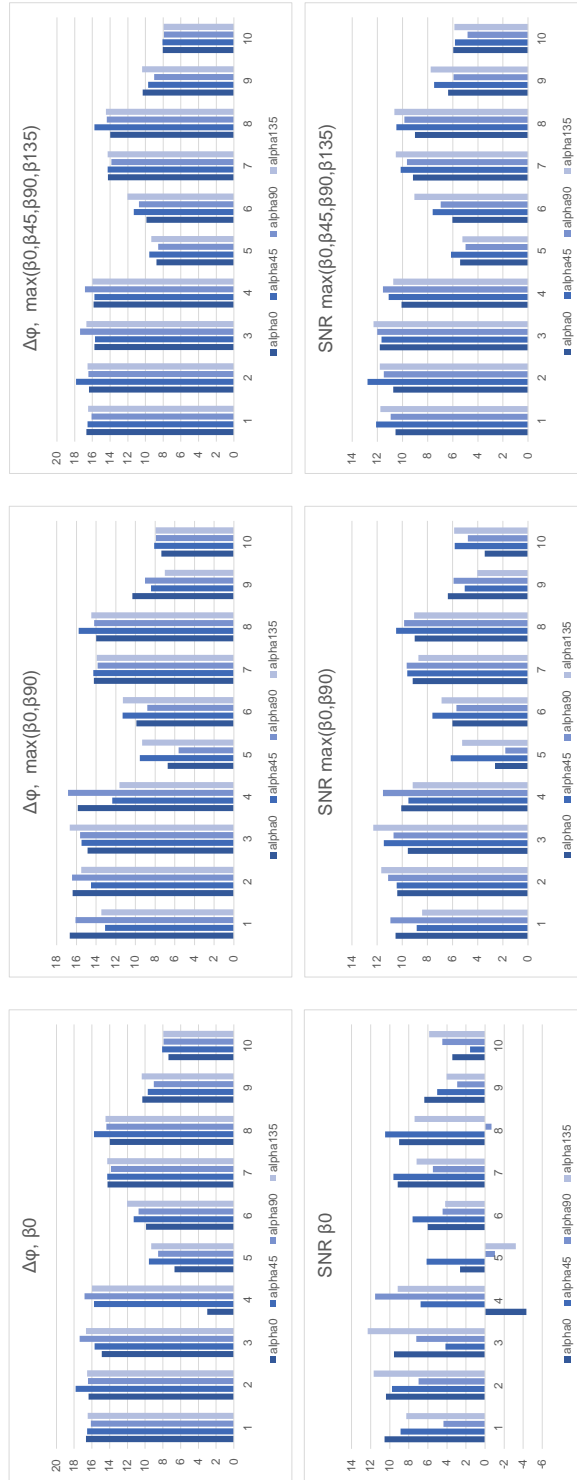


Fig. 3.12 Haynes TIG welded probe, delta phase (° upper row) and SNR (dB lower row) with multiple induction combinations and cracks. Columns with the maximum of different induction combinations, left column 1 state, middle 2 orthogonal states, right, 4 states.

### 3.4 Conclusions

In this chapter a novel inductor for induction thermography has been presented, enabling the generation of thermographies with different thermal patterns associated to the directional magnetic field of the proposed inductor. It is based on a set of two pairs of orthogonal coils, whose winding axes are parallel to the surface. Considering this arrangement, the magnetic field resulting from both pairs can ideally be reduced to the summation of both orthogonal fields. This allows controlling the predominant direction of the magnetic field by altering the phase shift of the alternating current between both pairs of coils.

In this regard, the system has been tested with a set of four current phase shifts between both pairs for non-destructive testing in the directions of the resulting magnetic fields. The obtained results show a variable phase delta depending on the relative orientation of the cracks with respect to the magnetic field. To demonstrate the system's capability, tests have been conducted on samples with real cracks, achieving good results in a steel sample and another one made of the Haynes 282. The results are consistent with the observations of the rotating butterfly pattern previously described in chapter 2.

It provides several industrial advantages compared to traditional inductors: reduction of inspection times, possibility of designing a more robust and simplified inspection system, multidirectional detection, etc.

Future works should focus on the rigorous physical modelization of the system, as well as the extrapolation to a higher number of coils, optimization of design parameters and uniformity of magnetic field. The employment of alternative modulations of the magnetic field should enable an omnidirectional induction with a single thermography using a circular polarization [181], or the excitation with two frequencies at the same time [182]. Another aspect that should a priori improve the thermal response is the combination of these magnetic field orientation modulation methods, with a frequency modulated amplitude resulting in varying thermal diffusion lengths.

# Chapter 4

## Dynamic multi-directional induction thermography

### 4.1 Introduction

The preceding chapters introduced a novel form of induction thermography and an inductor capable of generating magnetic fields in multiple orientations. Both setups produce thermographic images from various directions without requiring movement of the inductor relative to the object. This enhances the system's detection capabilities and simultaneously decreases the overall inspection time. Given that a significant factor extending the overall inspection time in static induction thermography (SIT) is the dead time linked to the camera's movement in relation to the object, this chapter introduces a system aimed at addressing this issue on a multi-directional induction scheme. It integrates the quadratic inductor into a multi-directional induction scan thermography setup, enhancing efficiency and minimizing the impact of dead time on the inspection process. This method allows for continuous scanning of a part through simultaneous multi-directional induction, facilitating defect detection irrespective of the part's orientation during movement.

#### 4.1.1 Motivation

In various scenarios, such as steel hot rolling, metal extrusions, and rail track inspection, the feasibility of employing static induction thermography (SIT) is severely constrained due to the impracticality of using a stationary camera. Additionally, when scanning large components, a considerable volume of recordings is generated, resulting in the dispersion of the detected defects across multiple thermographies. The amalgamation of these thermographies typically occurs post-inspection through the registration of recordings and the mapping of defects

onto a shared reference frame. Moreover, it is important to note that the application of SIT requires an intermittent capture and movement of both the camera and inductor. This operational requirement introduces dead times, thereby effectively prolonging the overall inspection time.

Another factor to consider, is the fact that the detection of the defects is strongly conditioned by the relative orientation of the magnetic field of the inductor regarding defect. Considering that in many scenarios the direction of the defects is not known, the employment of an inductor with a fixed magnetic field might leave some of the defects undetected.

As a result, the combination of the dynamic induction thermography (DIT) with a multi-directional inductor might benefit multiple inspection scenarios.

### **4.1.2 Related works**

Other works have dealt with this problem on an induction thermography scenario focusing on the accurate registration of the dynamic thermal recording employing fiduciary markers to account for the varying scanning velocity [183], or the remapping of the thermographies employing rectification targets on a curved work-piece [184]. The fusion of the thermographies into a common reference yields a pseudo-static thermography which enables the extrapolation of the processing methods employed of the static thermography. Other studies, including the one presented by the author [60], have utilized an optical flow-based registration method to stabilize digitally flash thermography on a wind blade, thereby producing a pseudo-static thermography from a moving camera with a random motion. Multiple works have previously focused in this aspect for the laser excited thermography, such as which are able to successfully build a thermogram for each pixel of the thermography, corresponding to a certain point on the inspected part. The integration of these thermographies into a unified reference produces a pseudo-static thermography, facilitating the application of processing methods akin to those employed in static thermography. Numerous studies have delved into this aspect within the domain of laser-excited thermography, wherein a thermogram is successfully constructed for each pixel of the thermography, corresponding to a specific point on the inspected part. Note that a significant distinction from laser-excited thermography lies in the fact that induced heating often impacts a broad area, leading to accumulated heating on the surface. This accumulation can introduce distortions in the resulting pseudo-static thermogram.

## 4.2 Outline

This chapter focus on a novel system that combines the dynamic thermography with an interleaved rotation of the magnetic field using the previously exposed quadratic inductor in chapter 3. In this context, the capture process involves a linear movement between the workpiece and the camera coupled with the inductor. This is achieved through a simultaneous induction employing a square wave modulation and a consecutive switching sequence of the magnetic field in four distinct states. The resulting process yields a set of 4 thermograms corresponding to each direction of the induced magnetic field, which enables the employment of a fused multi-directional defect detection. Considering that the sequential switching of the magnetic field and simultaneous movement of the camera frame and inductor regarding the inspected part has a compounded effect, the pseudo-static-temporal fusion is not trivial. The spatio-temporal registration of each induction direction yields a set of synchronized pseudo-static thermographies starting at different times and location during the scanning process. The initial fusion exhibits artificial thermal discontinuities which render them useless for any of the SIT processing techniques. To address the variations in starting temperature, a normalized thermal drift compensation is implemented to preserve the oscillating component of the sequence of pulses and a subsequent averaging of the subset of pulses reduces the overall noise. Following this, the application of any of the established SIT processing techniques, including FFT, PCA, TSR and HOS among others, enables the temporal compression of the reconstructed thermographies for data mining and accurate defect detection as it will be exposed in the results with natural defects.

Fig. 4.1 describes the processing of the dynamic multi-directional induction thermography.

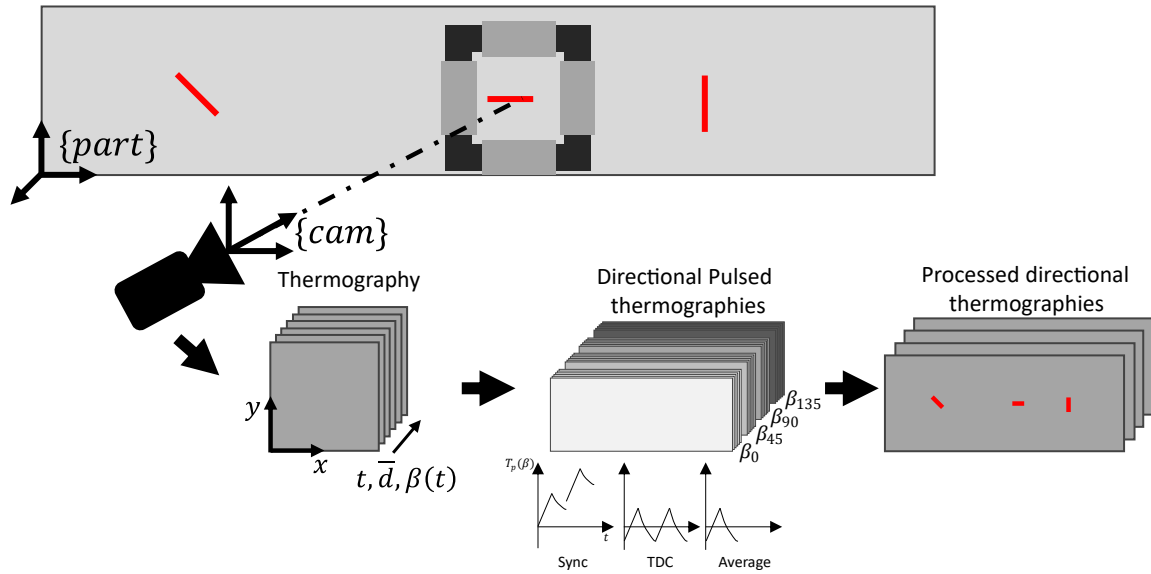


Fig. 4.1 Dynamic multi-directional induction thermography system. Dynamic IR recording with simultaneous multi-directional induction and subsequent pseudo-static directional thermography reconstruction and final processing.

The method consists on the reconstruction of the dynamic thermography to generate a set of directional thermographies. Simultaneously with the recording, a sequence of pulses with a square-wave modulation is induced, alternating the activation of the coils for each pulse sequentially. The process begins with an incremental registration of each frame of the thermogram and continues with the temporal separation and synchronization of each state of the inductor, ensuring that the start of each thermogram aligns with the period of the pulses. Depending on the translation speed, each thermogram might have multiple pulses resulting in discontinuities between the start and the end of consecutive pulses. A thermal drift compensation (TDC) enables the preservation of the oscillating component, yielding a thermogram with multiple pulses with no discontinuities. Afterwards the averaging of the pulses enables the reduction of the noise. These directional pulsed thermographies can be subsequently processed employing most of the temporal compression techniques.

### 4.3 Methods

In this section the proposed method is exposed employing forged steel bolt with a natural crack, as shown in fig. 4.9b. The experimental setup used for this simplified experiment is detailed below, as well as the experimental parameters.

### 4.3.1 Setup

The experimental setup is depicted in fig. 4.2. It features a Flir X6541sc infrared camera equipped with a Stirling-cooled 640x512 InSb sensor capable of achieving a frame rate of 125 Hz at full frame or 4 kHz in windowing mode. A quadratic inductor such as the one exposed in this work, is mounted to a linear axis along with the camera, while the inspected part remains stationary. The induction generator employed is the Edevis ITVis 3000 MHF, which incorporates a full-bridge inverter circuit with pulse-width modulation, enabling an induction frequency range from 10 kHz to 60 kHz. The activation of the inductor coils is handled by another device, enabling the alteration of the magnetic field orientations of the inductor in 4 different states.

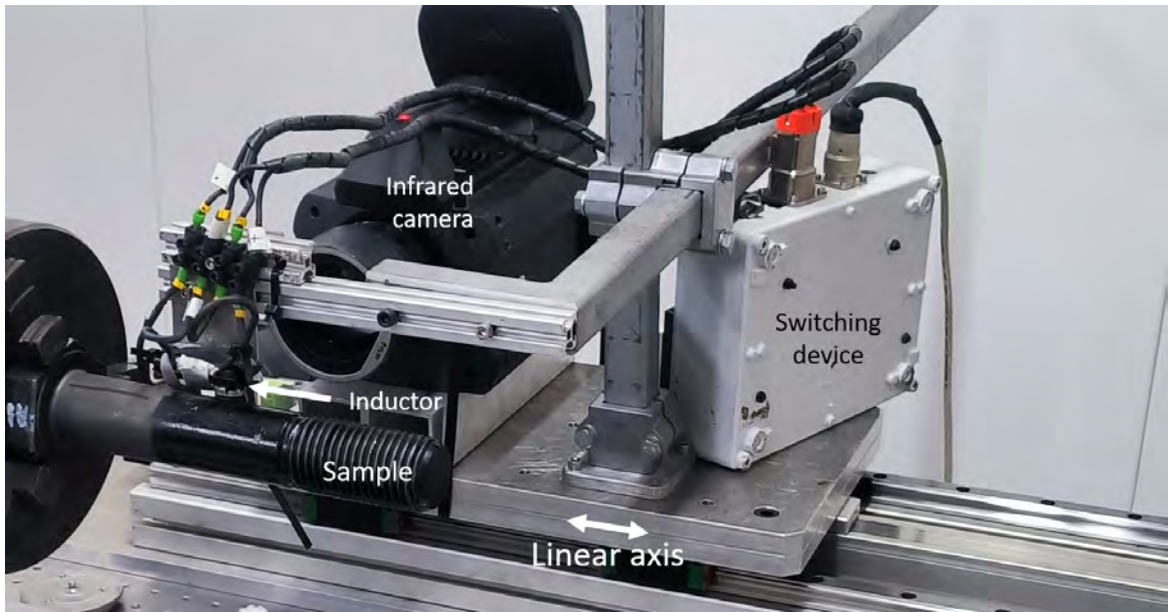


Fig. 4.2 Dynamic multi-directional induction thermography processing setup, with an infrared camera and inductor and switching device mounted on a linear axis scanning a static forged bolt.

### 4.3.2 Synchronized pseudo-static multi-directional thermography

The pulse sequence is modulated with a square wave with a period  $T_l$  and duty ratio  $DT$ , synchronized with a sequential switching sequence,  $\beta = \{0, 45, 90, 135\}$ . For each switching state  $i$  in the sequence, there is a set of  $N$  periods  $j$ , each containing  $O$  instants,  $k$ .

Considering that the main focus of this work consists on the multi-directional aspect of the reconstruction, a fixed translation has been employed to fuse the frames into a common reference for the incremental registration of the thermography. Since the incident angle of the

camera is normal to the surface, the registration is formulated as the translation of each pixel into another frame denoted as  $dst(x,y) = src(x T_x, y T_y)$ , which is interpolated with a bilinear filter. This yields a registered thermography with a common spatial reference starting at the first frame,  $t = 0$ .

The recordings have been carried out with a framerate of 300 Hz, a window resolution of 320x320 on an inductor with a 50x50mm window. The square-wave period is  $T_l = 0.2$  s and  $DT = 50\%$  for the 4-state sequence and a horizontal translation speed of 375m m/min.

Fig. 4.3 displays the different inductor states associated to the activation of the coils, and the corresponding square wave modulation of the generator, as well as the resulting thermogram of a registered point.

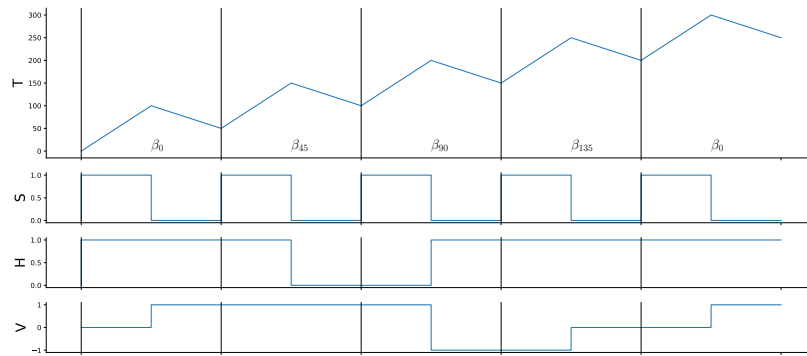


Fig. 4.3 Multi-directional thermo-inductive square wave modulation. The upper graph shows a registered thermogram, the second shows the square wave, and the third and fourth displays the coil activation states of the switching device.

The resulting registered thermograms of 2 points, as well as 3 frames of the sequence are shown in fig. 4.5 and fig. 4.4 respectively. This has allowed the extraction of up to 3 complete pulses per state, as illustrated on fig. 4.6.

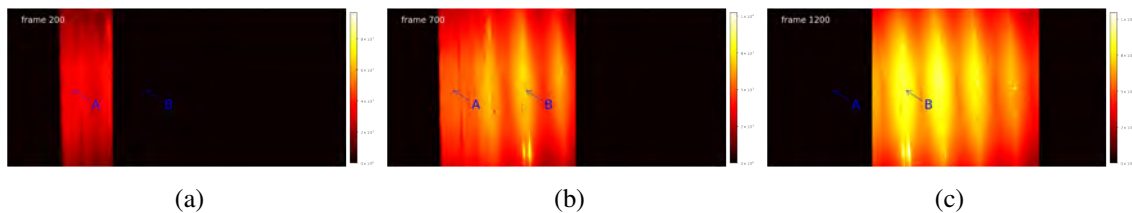


Fig. 4.4 Pseudo-static synchronized thermograms. (a) Frame 200, (b) Frame 700, (c) Frame 1200.



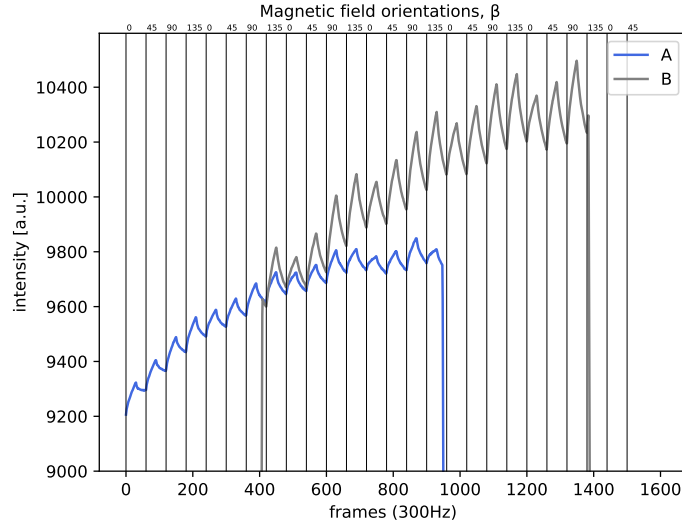


Fig. 4.5 Pseudo-static synchronized thermograms of points A and B from fig. 4.4.

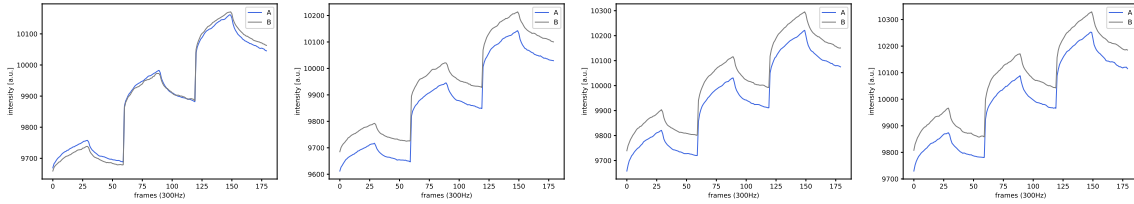


Fig. 4.6 Pseudo-static synchronized thermograms for each state  $\beta$  of the inductor.

### 4.3.3 Thermal drift compensation

The set of four synchronized pseudo-static thermographies contain multiple pulses with a different starting time for each pulse. The associated discontinuities of the thermograms, as shown fig. 4.6 are the result of the thermal drift associated to the accumulated temperature of the surface. This is caused by the overlapping thermal diffusion of the previous pulses with the current one resulting, in different heating and cooling rates for the pulses.

Considering that, in many cases, the thermogram processing occurs in the frequency domain, some authors have proposed a method that preserves its oscillatory component, considering the diffusion of preceding pulses and their initial temperature. The method proposed by [30] involves the decomposition of the raw thermogram into an (1) oscillatory component, (2) a linear component associated with the diffusion of preceding pulses, and (3) the mean value for each pulse. Considering that  $F_{j,k}$  is the temperature of the instant  $k$  and pulse  $j$ , its decomposition is noted as:  $F_{j,k} = F_{d_j} + F_{o_j} + F_{l_{j,k}}$ , with  $F_{d_j}$  being the average of the pulse  $j$  with  $O$  frames,  $F_{l_{j,k}}$  being the linear component associated to the thermal drift,

and  $F_{O_k}$  the oscillating component. Therefore, the decomposition exposed by Breitenstein et al. can be formulated as follows to retain the oscillating component:

$$F_{O_j} = F_{j,k} - \frac{1}{O} \sum_{k=0}^{O-1} F_{j,k} - \left( j - \frac{O}{2} - \frac{1}{2} \right) \frac{\Delta T}{O} \quad (4.1)$$

Oscillating component
mean of pulse  $i$

Temperature pulse  $i$ , instant  $j$ 
linear component with  $\Delta T = F_{j,(O-1)} - F_{j,0}$

The oscillating component of each state for the points A and B of fig. 4.4 is shown in fig. 4.7. Note that it does not exhibit a significant variation of the amplitudes and the previously observed discontinuities. Considering that most of the classical temporal compression techniques are focused on the pulsed thermography, the resulting set of pulses has been averaged to a single pulse, yielding a thermogram with a reduced noise devoid of discontinuities, as shown in fig. 4.8.

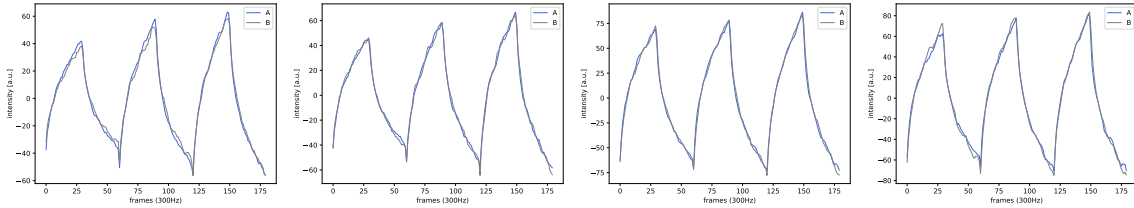


Fig. 4.7 Thermal drift compensation, oscillating component.

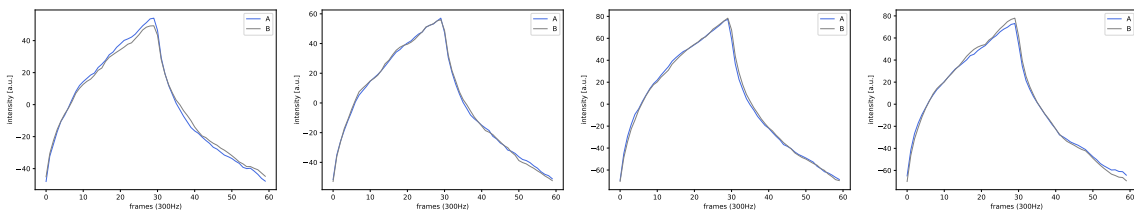


Fig. 4.8 Average oscillating components.

#### 4.3.4 Temporal compression

To assess the extrapolation of the results compared to a SIT, a series temporal compression methods have been chosen.

Firstly by employing the amplitude of the thermogram. Secondly, a FFT, yielding both phase and amplitude images. Afterwards, a PCA [77] and PCT [73] with the first

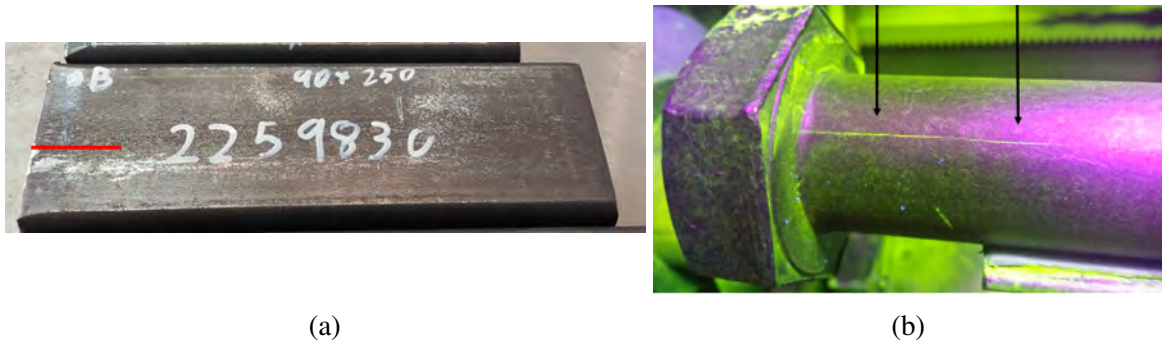


Fig. 4.9 Samples with natural cracks. (a) Steel billet with delamination defect. (b) Forged bolt with longitudinal crack imaged with magnetic particles.

2 components which accounts for 60% of the variance in this scenario. Additionally, the cooling has been temporally compressed employing a TSR [185], which fits the thermogram with a logarithmic polynomial, enabling a robust estimation of the first and second temporal derivatives of thermograms. The fourth method has consisted in the statistical reduction of the cooling, previously exposed by Madruga et al. [186], as Higher Order Statistics (HOS), which comprises the mean, standard deviation, skewness, and kurtosis.

Furthermore, a Robust Principal Component Analysis (RPCA) [79] has been employed, which decomposes the thermography into a low-rank and sparse 3-way tensor associated with potential outliers. Statistically defects can be a priori considered as outliers relative to a homogeneous background. For instance, Liang et al. [78], observed that the signal associated with the sparse component exhibits a significant correlation with the cracks, enabling its usage in scenarios with challenging backgrounds. Results will show the temporal L2 norm of both low-rank and sparse RPCA decomposition.

## 4.4 Results

The assessment of the results, exposed with two samples with natural cracks, the first one being a forged bolt such as the one shown in fig. 4.9a, and the second consists on a steel billet fig. 4.9b, both of which have a longitudinal crack parallel to X axis of the camera, parallel to its motion.

Experimental parameters for the induction, recording and speed of the axis are identical to the previous ones.

#### 4.4.1 Quantitative evaluation criteria

The associated signal of the processing techniques has been analysed considering 4 profiles of 2 samples, with a Signal To Noise ratio described as:  $SNR = 20 \log \frac{|S_{crack} - \mu_{local}|}{\sigma_{sound}}$ , with  $\sigma_{sound}$  being the standard deviation of sound area,  $S_{crack}$  being the absolute value of the signal and  $\mu_{local}$  mean over a 60x60 window centered in each profile. The measurement of the signal,  $S$  has been carried along a set of diagonal profiles A and B traversing sound area and profiles C and D corresponding to crack as shown in registered frame of steel billet in fig. 4.25 and forged bolt in fig. 4.10. For each processing algorithm the SNR have been evaluated using precision and recall, for all profiles and induction orientation combined, with  $recall = TP / (TP + FN)$  and  $precision = TP / (TP + FP)$ , with  $TP$  true positives (profiles C and D),  $FN$  false negatives and  $FP$  false positives (profiles A and B).

#### 4.4.2 Quantitative analysis

The resulting SNRs, precision and recall of steel bolt for each processing algorithm, profile and induction orientation are shown in table 4.1.

Table 4.1 Forged bolt SNR (dB) of profiles of fig. 4.10 highlighting values surpassing 4 dB considering four directions of different processing algorithms and right columns showing precision / recall with 3 minimum thresholds.

Processing Component	Sound profiles												Defect profiles												Recall / Precision					
	A				B				C				D				2dB		4dB		8dB									
	0	45	90	135	0	45	90	135	0	45	90	135	0	45	90	135	R	P	R	P	R	P								
FFT	magnitude	-2.8	<b>5.0</b>	-7.4	-19.1	<b>4.5</b>	<b>6.1</b>	-1.9	2.4	<b>41.3</b>	<b>35.3</b>	-19.4	<b>29.6</b>	<b>47.9</b>	<b>44.4</b>	1.0	<b>38.6</b>	0.8	0.6	0.8	0.7	0.8	1.0							
	phase	<b>9.1</b>	<b>7.9</b>	<b>8.5</b>	<b>9.6</b>	<b>9.6</b>	<b>10.5</b>	<b>8.6</b>	<b>8.7</b>	<b>16.8</b>	<b>17.1</b>	2.5	<b>15.6</b>	<b>14.3</b>	<b>13.8</b>	<b>11.8</b>	<b>12.9</b>	1.0	0.5	0.9	0.5	0.9	0.5							
HOS	kurtosis	<b>7.8</b>	<b>8.9</b>	<b>9.5</b>	<b>12.3</b>	<b>10.6</b>	<b>14.0</b>	<b>10.4</b>	<b>9.8</b>	<b>20.0</b>	<b>19.5</b>	3.6	<b>18.4</b>	<b>4.8</b>	<b>13.0</b>	<b>4.3</b>	<b>11.4</b>	1.0	0.5	0.9	0.5	0.6	0.4							
	skewness	<b>8.9</b>	<b>9.6</b>	<b>10.0</b>	<b>12.0</b>	<b>11.6</b>	<b>14.7</b>	<b>11.9</b>	<b>11.4</b>	<b>20.6</b>	<b>20.7</b>	<b>6.8</b>	<b>19.5</b>	<b>11.8</b>	<b>16.7</b>	1.1	<b>16.1</b>	0.9	0.5	0.9	0.5	0.8	0.4							
PCA	std. dev.	2.8	<b>9.7</b>	0.9	1.0	<b>4.9</b>	<b>9.3</b>	1.0	3.6	<b>58.0</b>	<b>47.3</b>	-17.2	<b>42.7</b>	<b>75.4</b>	<b>68.4</b>	2.6	<b>63.2</b>	0.9	0.6	0.8	0.7	0.8	0.8							
	C0	-3.3	<b>4.6</b>	-7.4	-17.0	<b>5.2</b>	<b>6.5</b>	-1.6	2.7	<b>40.9</b>	<b>34.7</b>	-16.2	<b>29.3</b>	<b>47.7</b>	<b>44.3</b>	2.2	<b>38.6</b>	0.9	0.6	0.8	0.7	0.8	1.0							
PCT	C1	-7.3	-34.7	-1.0	2.2	<b>4.5</b>	<b>4.1</b>	2.2	2.0	<b>36.8</b>	<b>31.7</b>	1.2	<b>28.7</b>	<b>23.8</b>	<b>28.8</b>	<b>4.7</b>	<b>20.4</b>	0.9	0.6	0.9	0.8	0.8	1.0							
	C0	-6.9	1.6	<b>7.1</b>	<b>10.4</b>	<b>18.6</b>	<b>17.2</b>	<b>12.1</b>	<b>16.4</b>	<b>4.3</b>	<b>14.6</b>	<b>6.9</b>	<b>9.6</b>	<b>12.4</b>	<b>13.6</b>	<b>24.6</b>	<b>18.3</b>	1.0	0.6	1.0	0.6	0.8	0.5							
RPCA	C1	-7.4	-9.0	-2.4	-0.1	<b>6.9</b>	<b>6.5</b>	<b>4.0</b>	<b>5.7</b>	-3.1	2.6	-1.5	-3.3	<b>9.1</b>	<b>4.5</b>	<b>7.2</b>	<b>7.4</b>	0.6	0.6	0.5	0.5	0.1	1.0							
	low rank	-3.4	<b>4.7</b>	-8.0	-23.3	<b>4.4</b>	<b>5.9</b>	-1.9	2.3	<b>41.5</b>	<b>35.3</b>	-18.3	<b>29.7</b>	<b>48.0</b>	<b>44.4</b>	0.9	<b>38.6</b>	0.8	0.6	0.8	0.7	0.8	1.0							
Thermo	sparse	-9.3	-14.8	-11.0	-26.1	-5.0	-27.5	-18.3	-14.6	<b>33.8</b>	<b>26.8</b>	-7.9	<b>30.1</b>	<b>43.2</b>	<b>38.4</b>	<b>17.9</b>	<b>39.6</b>	<b>0.9</b>	<b>1.0</b>	<b>0.9</b>	<b>1.0</b>	<b>0.9</b>	<b>1.0</b>							
	delta T	1.2	<b>7.0</b>	-3.3	-5.8	<b>6.9</b>	<b>8.7</b>	0.6	<b>4.8</b>	<b>39.5</b>	<b>33.4</b>	-19.9	<b>28.7</b>	<b>45.9</b>	<b>43.2</b>	0.7	<b>38.0</b>	0.8	0.6	0.8	0.6	0.8	0.9							
TSR	deriv. 1	1.1	<b>6.9</b>	-2.4	-1.0	<b>4.0</b>	<b>6.8</b>	-1.3	2.9	<b>38.3</b>	<b>33.2</b>	-16.1	<b>29.0</b>	<b>49.2</b>	<b>45.8</b>	-5.5	<b>41.0</b>	0.8	0.6	0.8	0.7	0.8	1.0							
	deriv. 2	-3.7	-34.8	-13.5	-1.3	-13.8	-10.2	-24.5	-19.3	<b>43.2</b>	<b>36.6</b>	4.0	<b>34.5</b>	<b>45.2</b>	<b>46.4</b>	1.9	<b>43.1</b>	<b>0.9</b>	<b>1.0</b>	0.8	1.0	0.8	1.0							



Fig. 4.10 Registered forged bolt with a delamination defect overlaid with profiles A and B in sound area corresponding to thread, C and D crack in flat area.

The resulting images of each processing algorithms and induction orientations for the forged bolt are shown in figs 4.11 to 4.24 and sound profiles A and B are displayed on the upper left side of figure each figure, with the bottom left side showing crack profiles C and D. Fig. 4.11 corresponds to magnitude, showing a signal surpassing 30 dB in both defect profiles with the exception of 90° induction orientation. This signal is mainly correlated to the localized heating and, as a result magnitude sound profiles located on the thread are affected by directional component of the emissivity and non-uniform heating. Phase image, fig. 4.12, shows a similar SNR for both sound and crack profiles. Temporal standard deviation of cooling thermogram, fig. 4.13 yields a signal greater than 40 dB for cracks, while skewness, fig. 4.14, and kurtosis, fig. 4.15, do not show the same difference between sound and defect profiles. Delta temperature, fig. 4.16 has a similar signal to magnitude, since they are both correlated. PCA first and second components, shown in figs 4.17 and 4.18, yield a similar signal compared to magnitude image. PCT first and second components, figs 4.19 and 4.20, exhibit reduced SNR difference between sound and defect profiles. RPCA L2 norm of low rank component shown in fig. 4.21, has a similar signal compared to magnitude image but sparse component, fig. 4.22 is able to successfully separate both defect and sound areas, with nearly a total background subtraction of the thread, but it exhibits salt and pepper noise which could be reduced by applying a low pass filter. First and second derivatives of TSR fitted to cooling thermogram, figs 4.23 and 4.24 respectively, both yield a SNR exceeding 40 dB, but the second derivative has a negative SNR in all sound profiles.

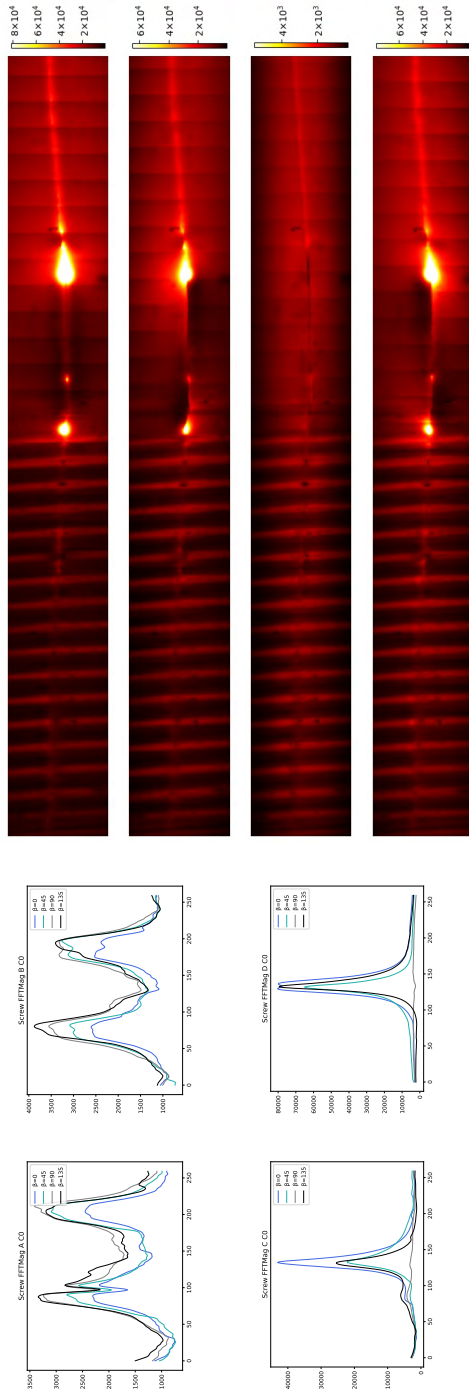


Fig. 4.11 Steel screw FFT Magnitude.

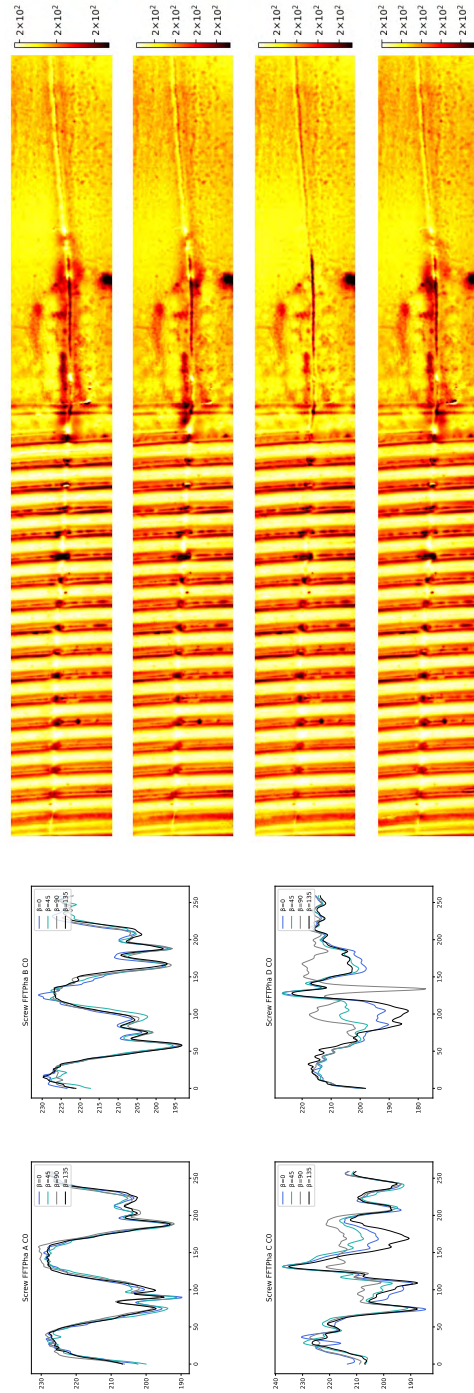


Fig. 4.12 Steel screw FFT Phase.



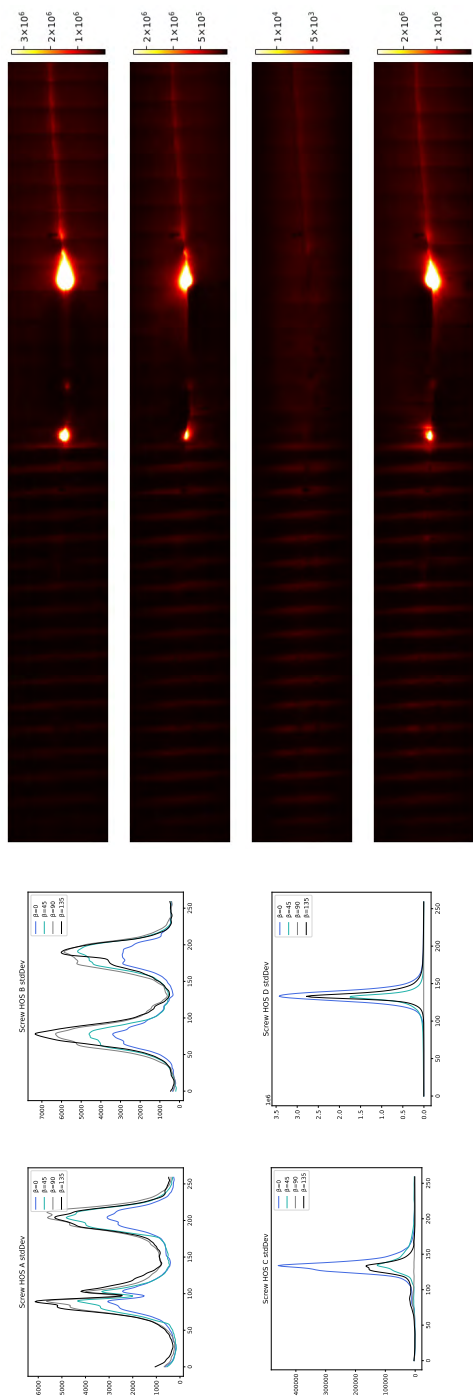


Fig. 4.13 Steel screw Standard deviation, cooling thermogram.

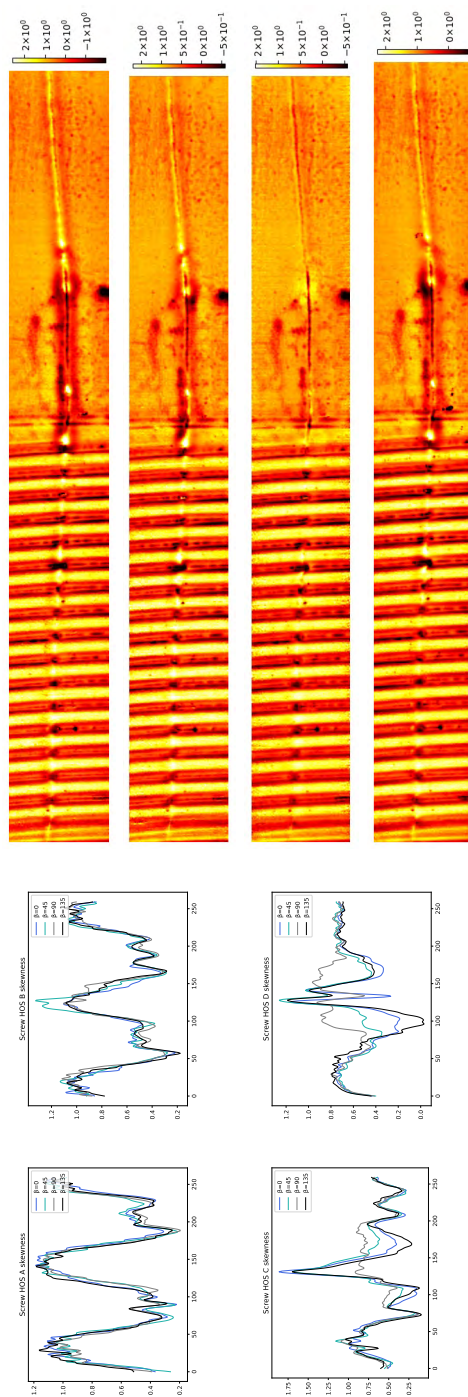


Fig. 4.14 Steel screw Skewness, cooling thermogram.



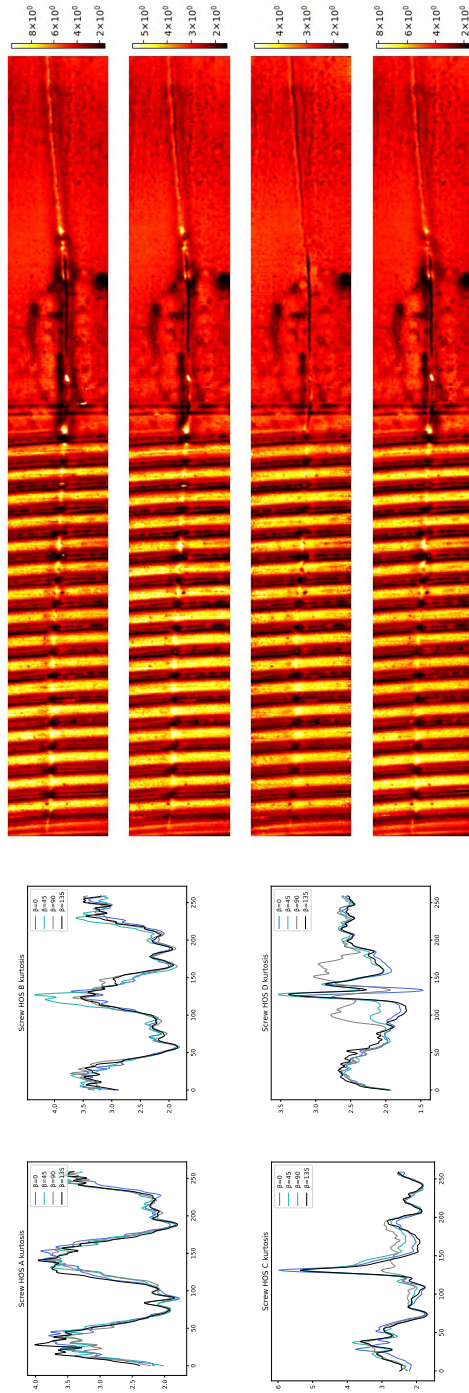


Fig. 4.15 Steel screw Kurtosis, cooling thermogram.

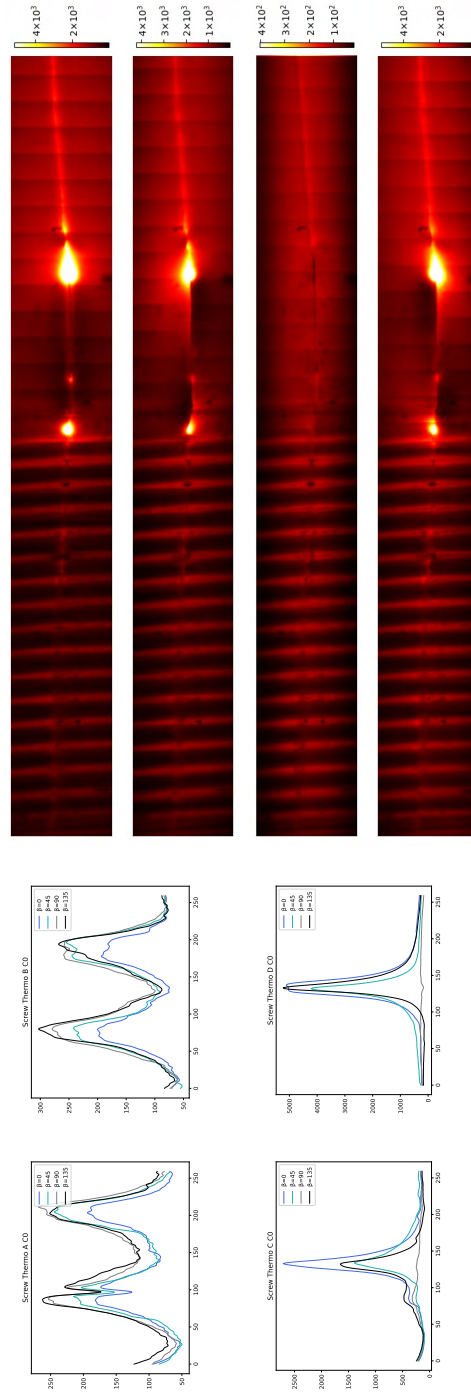


Fig. 4.16 Steel screw Delta temperature.

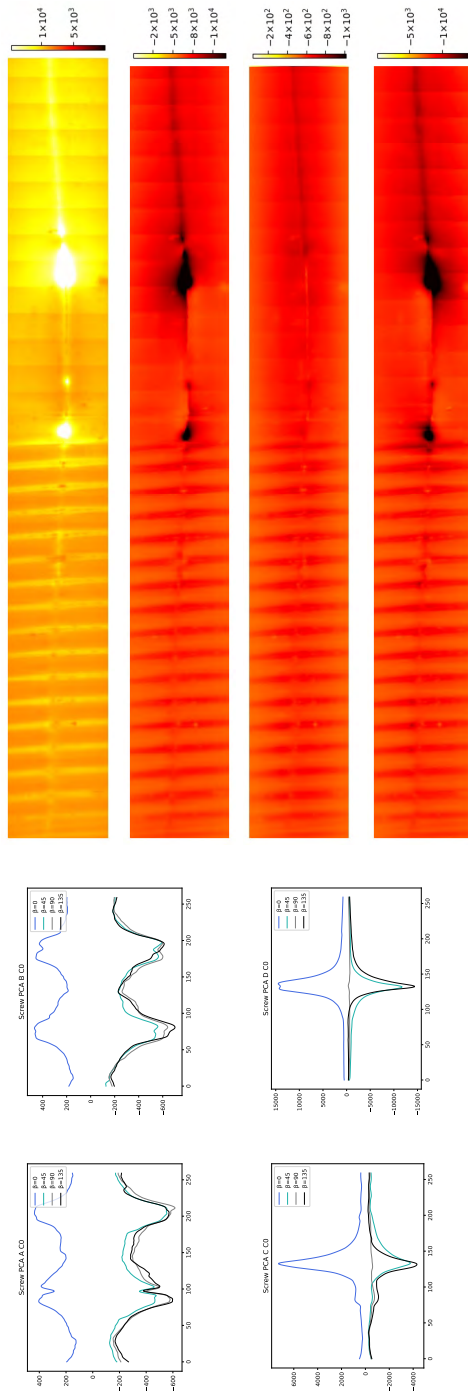


Fig. 4.17 Steel screw PCA component 1.

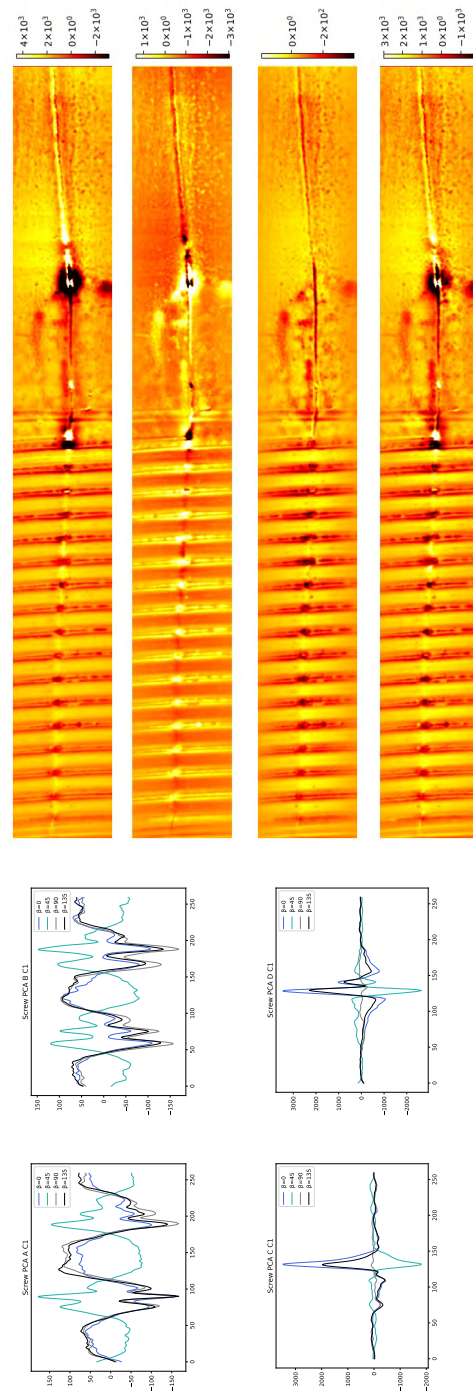


Fig. 4.18 Steel screw PCA component 2.

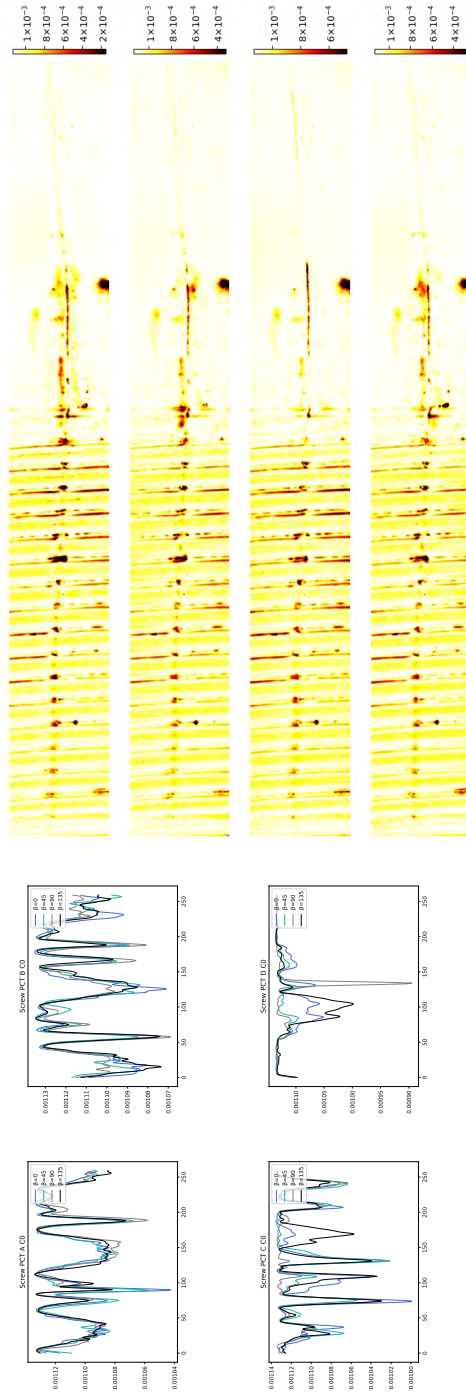


Fig. 4.19 Steel screw PCT component 1.

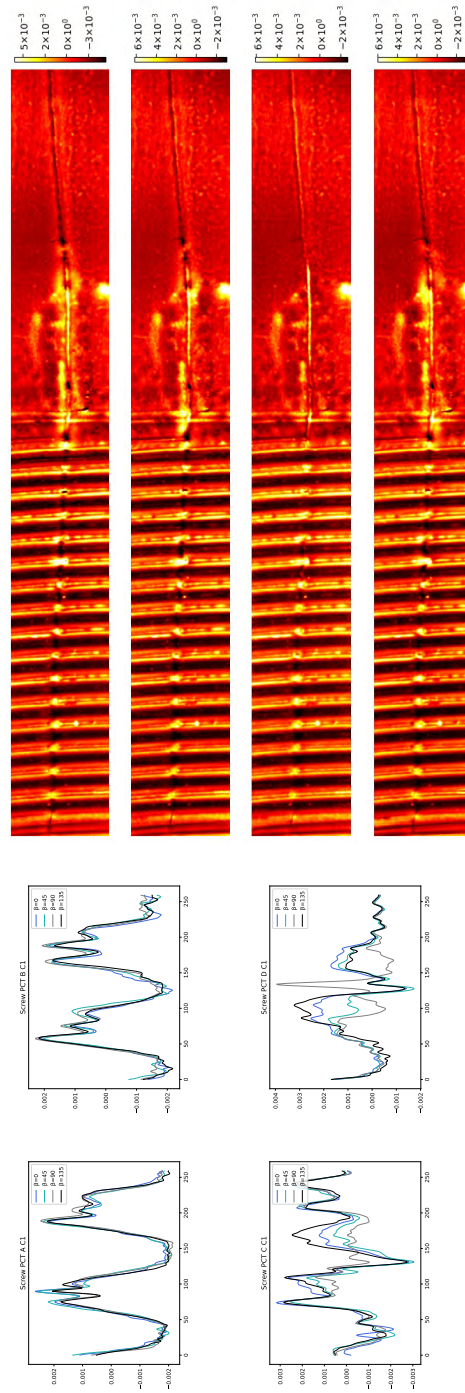


Fig. 4.20 Steel screw PCT component 2.



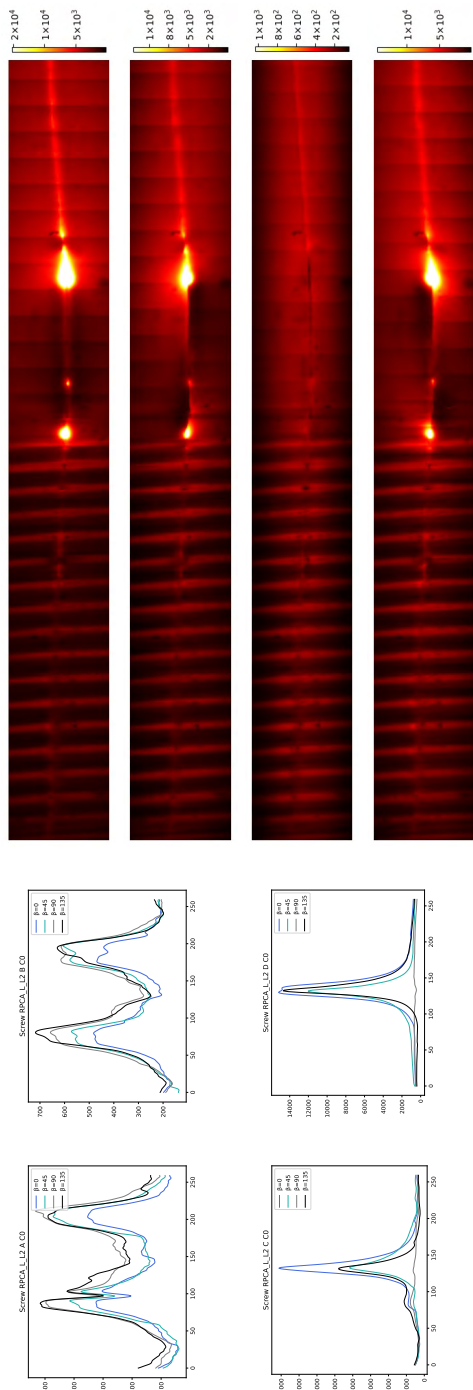


Fig. 4.21 Steel screw RPCA low rank, temporal L2 norm.

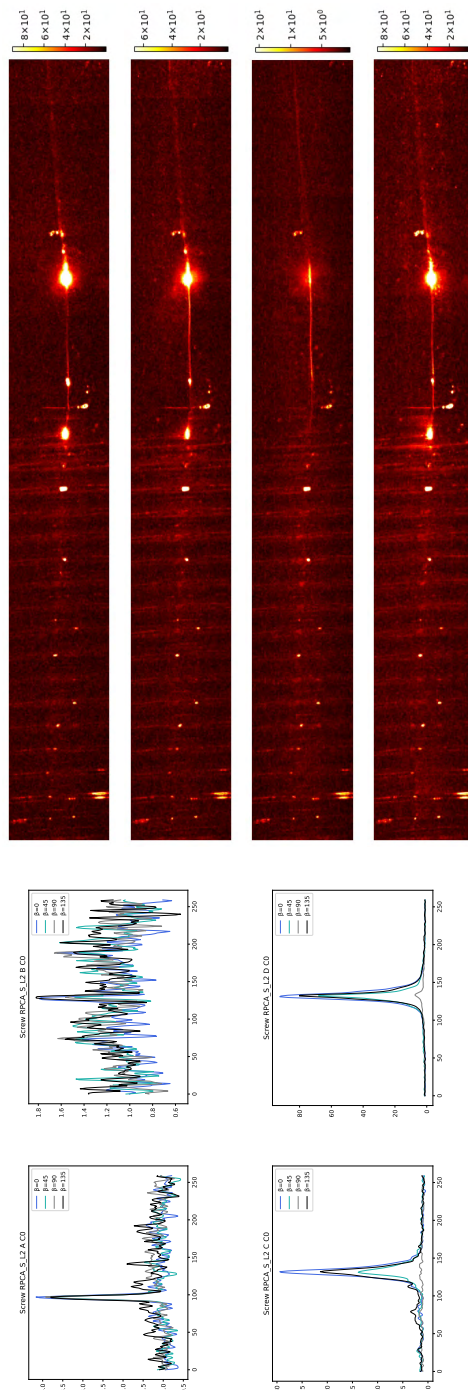


Fig. 4.22 Steel screw RPCA sparse, temporal L2 norm.

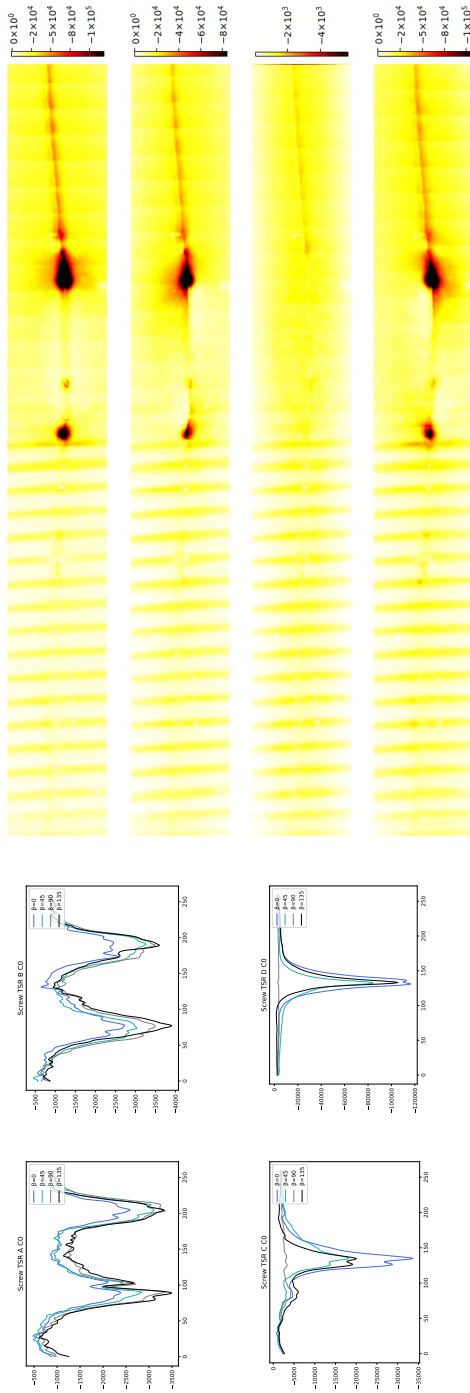


Fig. 4.23 Steel screw TSR first derivative fitted to cooling thermogram, showing frame corresponding to 25% time of cooling frame.

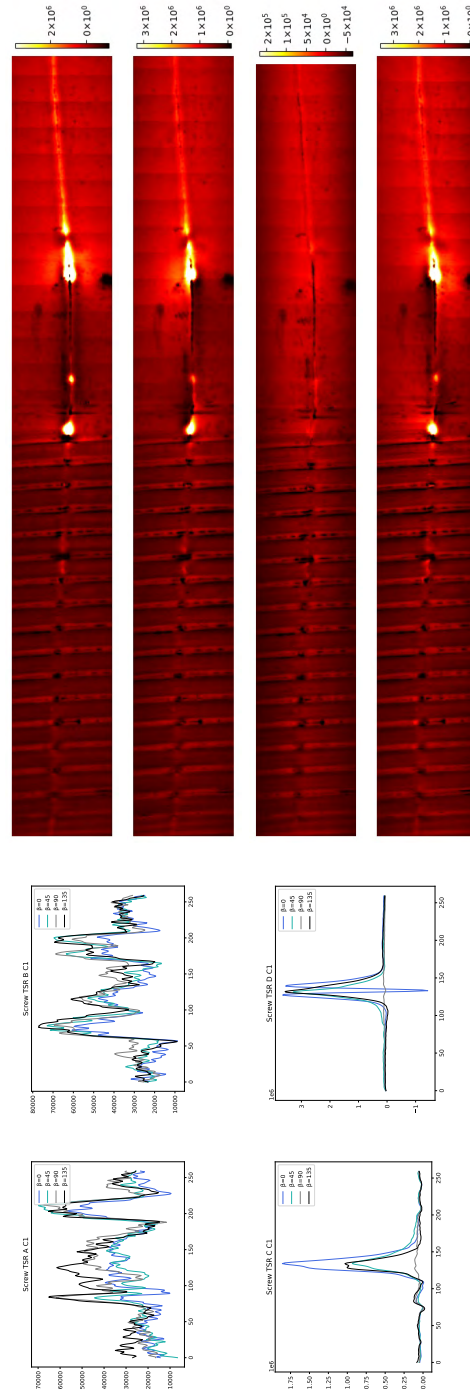


Fig. 4.24 Steel screw TSR second derivative derivative fitted to cooling thermogram, showing frame corresponding to 25% time of cooling frame.

Steel billet SNRs, precision and recall for each processing algorithm, profile and induction orientation are shown in table [4.2](#).

Table 4.2 Steel billet SNR (dB) of profiles of fig. 4.25 highlighting values surpassing 4 dB considering four directions of different processing algorithms and right columns showing precision / recall with 3 minimum thresholds.

Processing Component	Sound profiles												Defect profiles												Recall / Precision					
	A				B				C				D				2dB		4dB		8dB									
	0	45	90	135	0	45	90	135	0	45	90	135	0	45	90	135	R	P	R	P	R	P								
FFT	magnitude	-1.6	-5.3	-18.6	-11.0	-6.6	-5.4	-11.9	-15.4	<b>5.8</b>	<b>13.5</b>	<b>11.8</b>	<b>14.4</b>	<b>12.9</b>	<b>15.3</b>	<b>3.2</b>	<b>5.7</b>	<b>1.0</b>	<b>1.0</b>	<b>0.9</b>	<b>1.0</b>	<b>0.6</b>	<b>1.0</b>							
	phase	-15.2	-5.4	-6.5	-4.4	-8.2	-14.6	-12.6	-11.2	<b>9.9</b>	<b>13.1</b>	<b>7.6</b>	<b>12.5</b>	<b>12.5</b>	<b>14.4</b>	-2.5	<b>11.7</b>	<b>0.9</b>	<b>1.0</b>	<b>0.9</b>	<b>1.0</b>	<b>0.8</b>	<b>1.0</b>							
HOS	kurtosis	-16.0	-12.0	-10.5	-4.3	-19.6	-14.2	-12.9	-15.8	<b>11.1</b>	<b>11.4</b>	<b>7.2</b>	<b>12.7</b>	<b>14.2</b>	<b>14.0</b>	-0.6	<b>12.9</b>	<b>0.9</b>	<b>1.0</b>	<b>0.9</b>	<b>1.0</b>	<b>0.8</b>	<b>1.0</b>							
	skewness	-9.7	-12.8	-8.2	-5.3	-13.7	-11.5	-14.6	-20.0	<b>13.0</b>	<b>12.4</b>	<b>8.8</b>	<b>15.6</b>	<b>15.1</b>	<b>13.9</b>	0.0	<b>14.9</b>	<b>0.9</b>	<b>1.0</b>	<b>0.9</b>	<b>1.0</b>	<b>0.9</b>	<b>1.0</b>							
PCA	std. dev.	0.8	-0.5	-6.9	-19.3	-3.6	-5.3	-13.5	-14.4	<b>5.9</b>	<b>15.3</b>	<b>14.5</b>	<b>16.8</b>	<b>14.9</b>	<b>18.1</b>	<b>6.8</b>	<b>4.7</b>	<b>1.0</b>	<b>1.0</b>	<b>1.0</b>	<b>1.0</b>	<b>0.6</b>	<b>1.0</b>							
	C0	-1.6	-5.5	-19.2	-10.6	-6.7	-5.3	-11.8	-15.4	<b>6.0</b>	<b>13.6</b>	<b>11.8</b>	<b>14.5</b>	<b>13.0</b>	<b>15.4</b>	<b>3.3</b>	<b>5.8</b>	<b>1.0</b>	<b>1.0</b>	<b>0.9</b>	<b>1.0</b>	<b>0.6</b>	<b>1.0</b>							
PCT	C1	-13.6	-23.1	-13.1	-2.0	-14.3	-6.3	-10.9	-10.5	-19.4	<b>11.3</b>	<b>11.2</b>	<b>15.0</b>	<b>12.9</b>	<b>18.6</b>	<b>3.2</b>	<b>11.0</b>	<b>0.9</b>	<b>1.0</b>	<b>0.8</b>	<b>1.0</b>	<b>0.8</b>	<b>1.0</b>							
	C0	-7.6	1.2	-5.3	-5.7	-13.4	-35.7	-12.3	-9.3	1.1	1.1	1.4	2.9	<b>8.9</b>	<b>15.8</b>	-5.3	<b>9.8</b>	0.5	1.0	0.4	1.0	0.4	1.0							
RPCA	C1	-12.8	-3.7	-8.8	-4.0	-8.4	-12.4	-13.8	-13.4	-2.5	-1.6	-15.6	-17.5	-2.7	-6.8	-19.3	-3.6	0.0	0.0	0.0	0.0	0.0	0.0							
	low rank	-1.7	-5.5	-19.0	-10.6	-6.6	-5.3	-11.7	-15.4	<b>5.9</b>	<b>13.5</b>	<b>11.8</b>	<b>14.5</b>	<b>13.0</b>	<b>15.5</b>	<b>3.2</b>	<b>5.9</b>	<b>1.0</b>	<b>1.0</b>	<b>0.9</b>	<b>1.0</b>	<b>0.6</b>	<b>1.0</b>							
Thermo	sparse	-7.0	-1.8	-1.0	-3.5	-2.1	-8.8	-7.1	-6.4	-1.2	-1.7	<b>5.3</b>	<b>6.4</b>	<b>14.0</b>	<b>17.7</b>	<b>14.2</b>	<b>12.9</b>	0.8	1.0	0.8	1.0	0.5	1.0							
	delta T	0.2	-2.8	-9.7	-18.2	-4.2	-7.3	-13.0	-19.1	<b>5.3</b>	<b>12.3</b>	<b>10.7</b>	<b>13.4</b>	<b>12.4</b>	<b>13.9</b>	<b>3.1</b>	<b>4.2</b>	<b>1.0</b>	<b>1.0</b>	<b>0.9</b>	<b>1.0</b>	<b>0.6</b>	<b>1.0</b>							
TSR	deriv. 1	-1.7	-2.9	-13.0	-36.0	-6.8	-6.6	-18.5	-11.8	<b>6.3</b>	<b>12.3</b>	<b>10.9</b>	<b>13.0</b>	<b>11.5</b>	<b>12.8</b>	<b>2.2</b>	<b>2.0</b>	<b>0.9</b>	<b>1.0</b>	<b>0.8</b>	<b>1.0</b>	<b>0.6</b>	<b>1.0</b>							
	deriv. 2	-4.8	-10.1	-22.8	-8.4	-9.0	-4.8	-11.8	-17.9	<b>14.3</b>	<b>16.6</b>	<b>15.1</b>	<b>18.8</b>	<b>17.8</b>	<b>18.7</b>	<b>7.2</b>	<b>13.1</b>	<b>1.0</b>	<b>1.0</b>	<b>1.0</b>	<b>1.0</b>	<b>0.9</b>	<b>1.0</b>							



Fig. 4.25 Registered Steel billet with a delamination defect overlaid with profiles A and B in sound area, C and D crack.

This sample has a uniform flat background which enables an increased SNR difference of sound and defect profiles across all the processing algorithms shown in figures 4.26 to 4.39, resulting in a higher recall and precision ratios compared to the steel bolt. Note that the RPCA L2 norm can effectively identify defects across different profiles and orientations. However, it doesn't offer the same advantage as seen in the TSR second derivative when compared to the steel bolt.



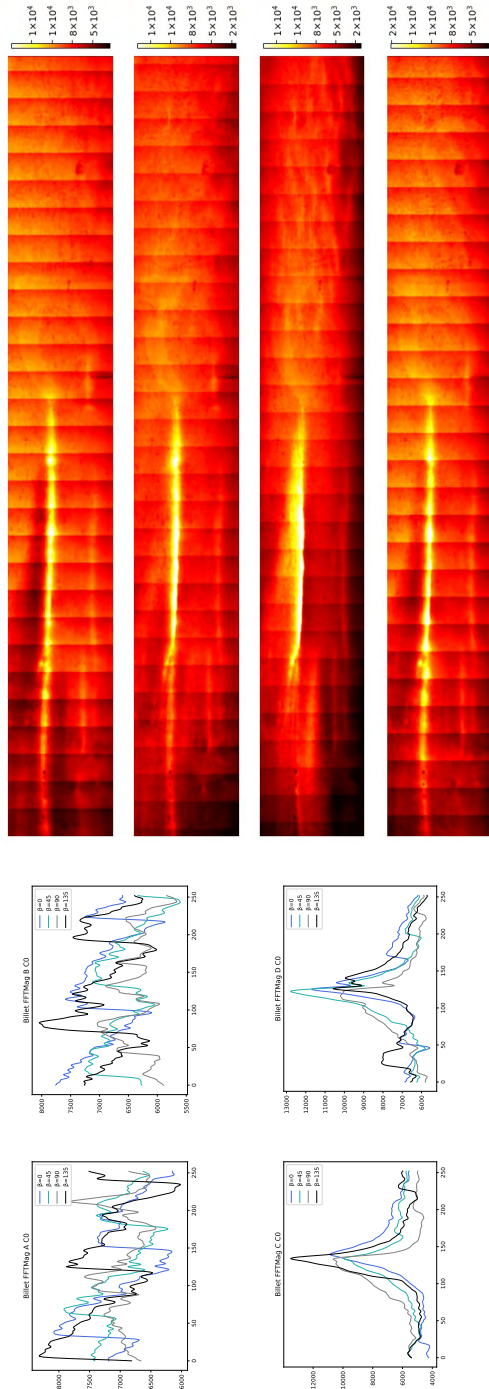


Fig. 4.26 Steel billet FFT Magnitude.

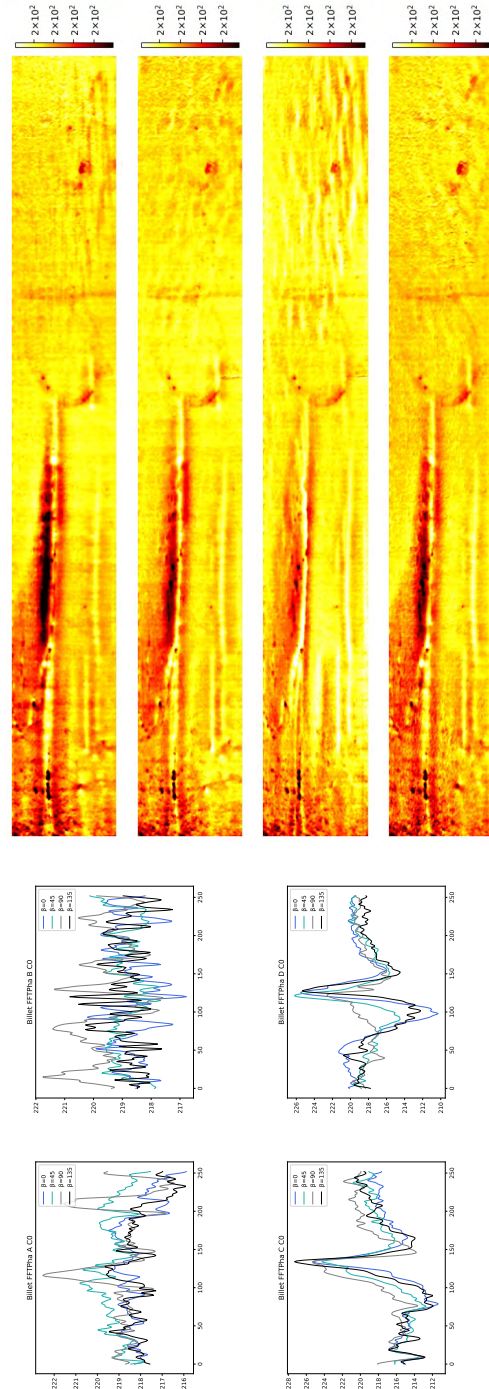


Fig. 4.27 Steel billet FFT Phase.

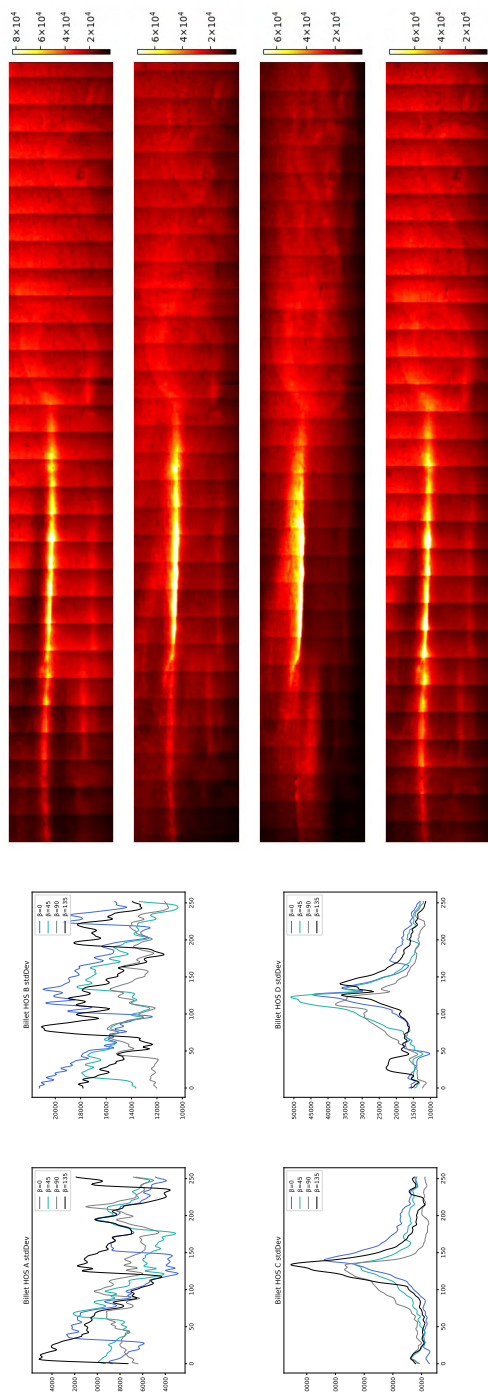


Fig. 4.28 Steel billet Standard deviation, cooling thermogram..

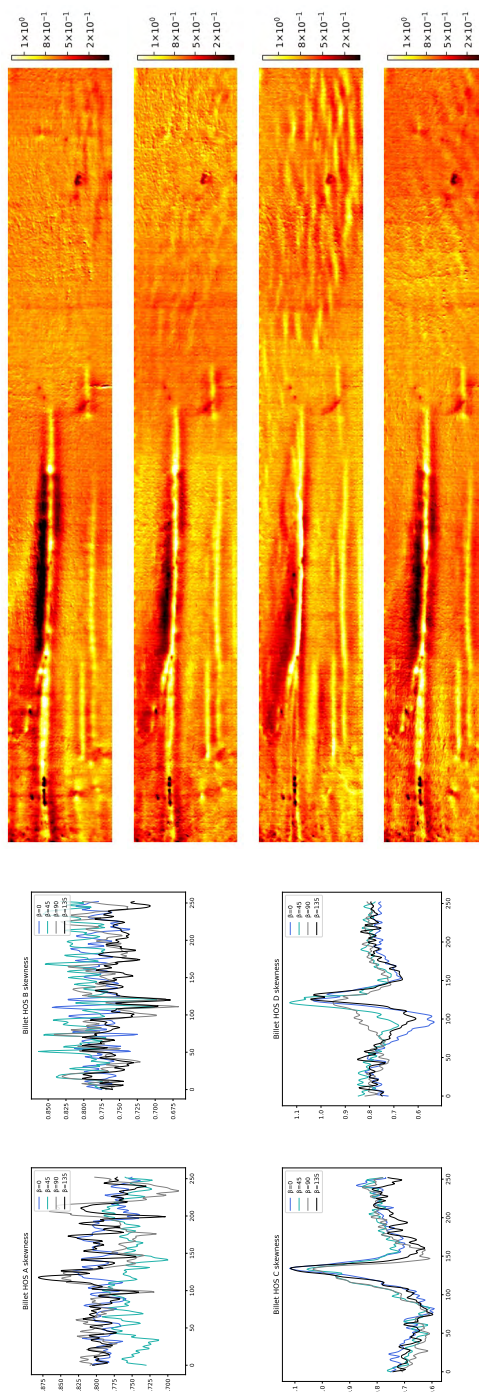


Fig. 4.29 Steel billet Skewness, cooling thermogram..

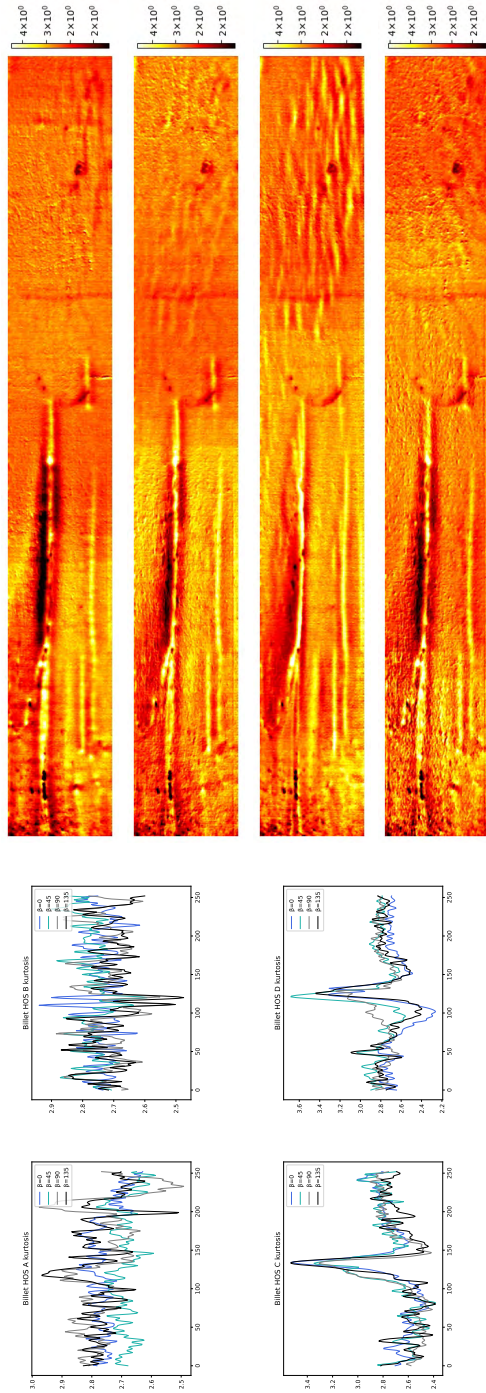


Fig. 4.30 Steel billet Kurtosis, cooling thermogram..

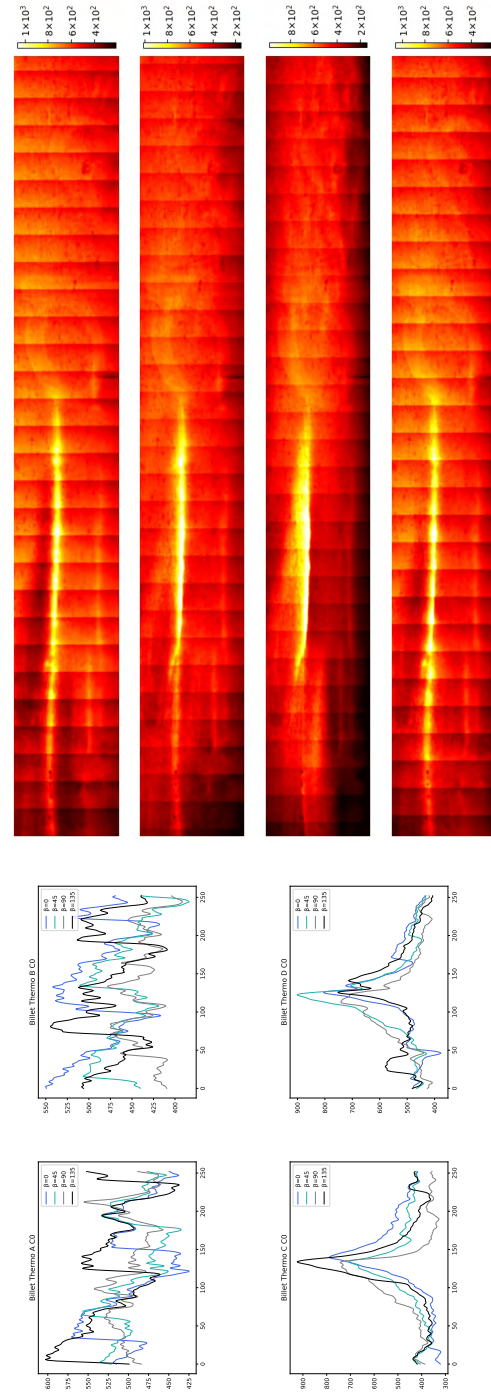


Fig. 4.31 Steel billet Delta temperature.



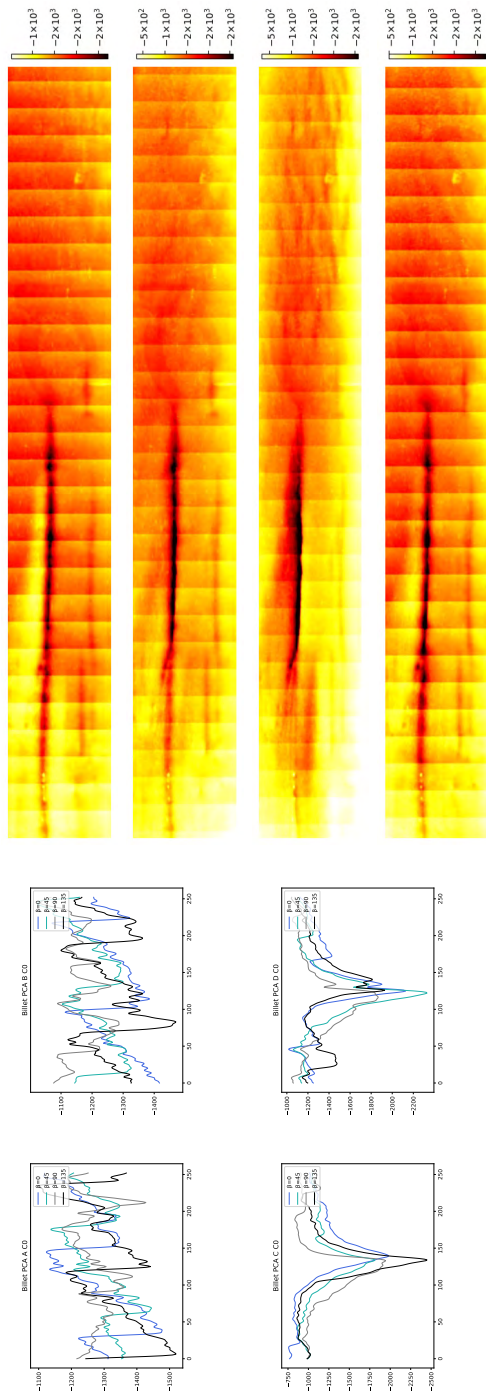


Fig. 4.32 Steel billet PCA component 1.

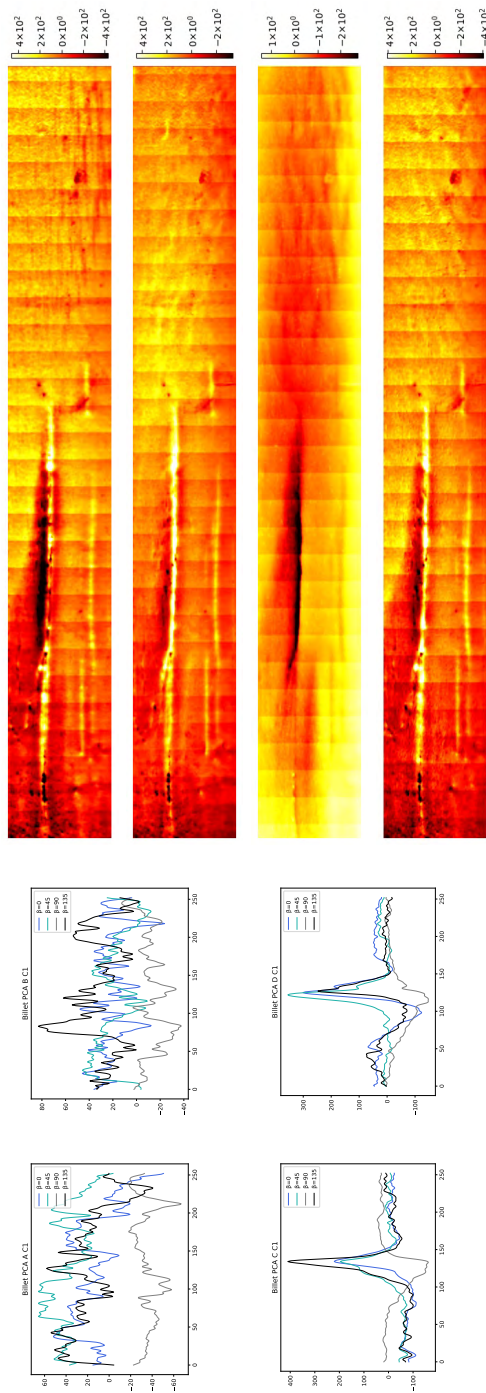


Fig. 4.33 Steel billet PCA component 2.

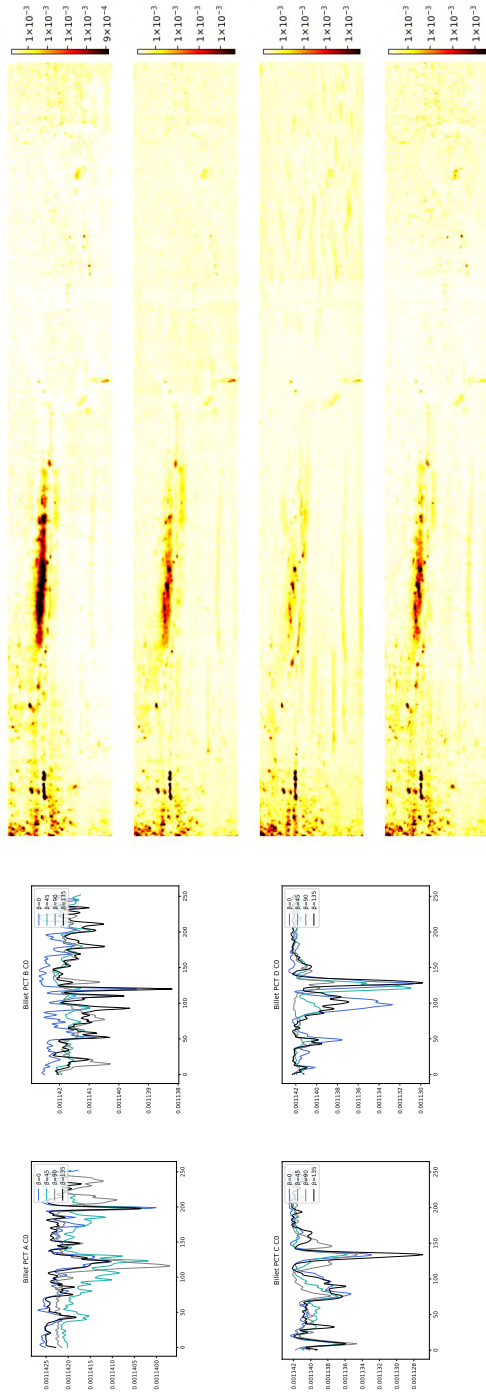


Fig. 4.34 Steel billet PCT component 1.

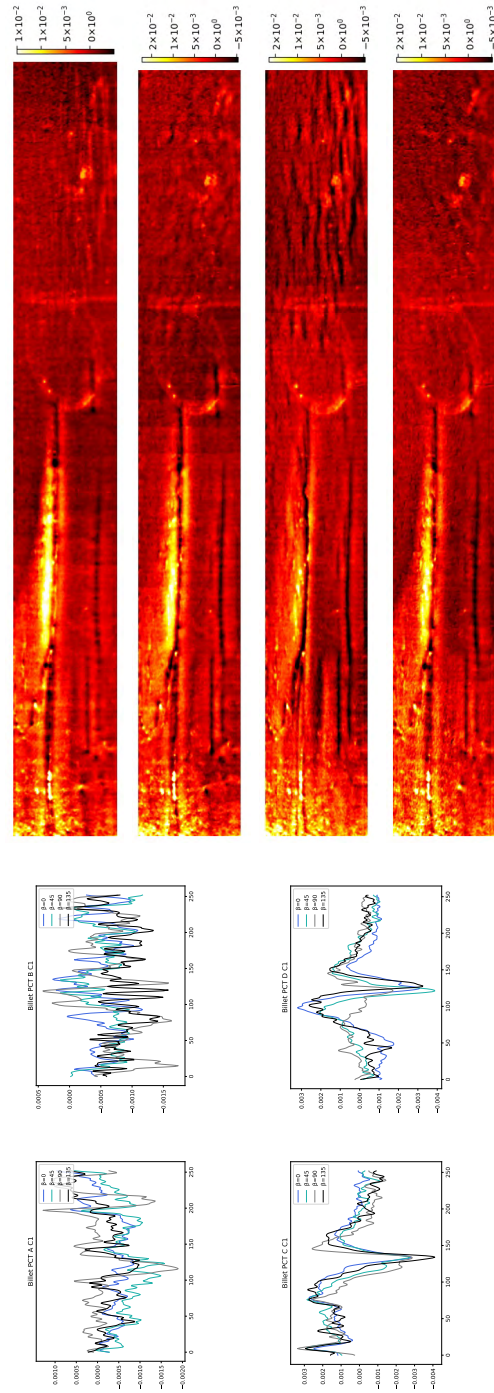


Fig. 4.35 Steel billet PCT component 2.

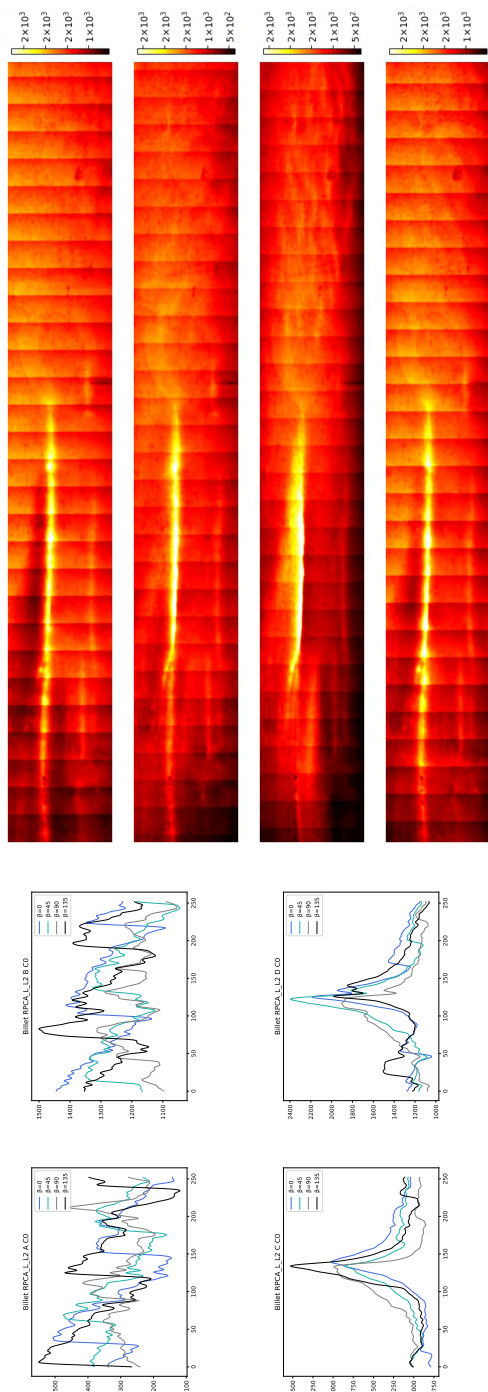


Fig. 4.36 Steel billet RPCA low rank, temporal L2 norm.

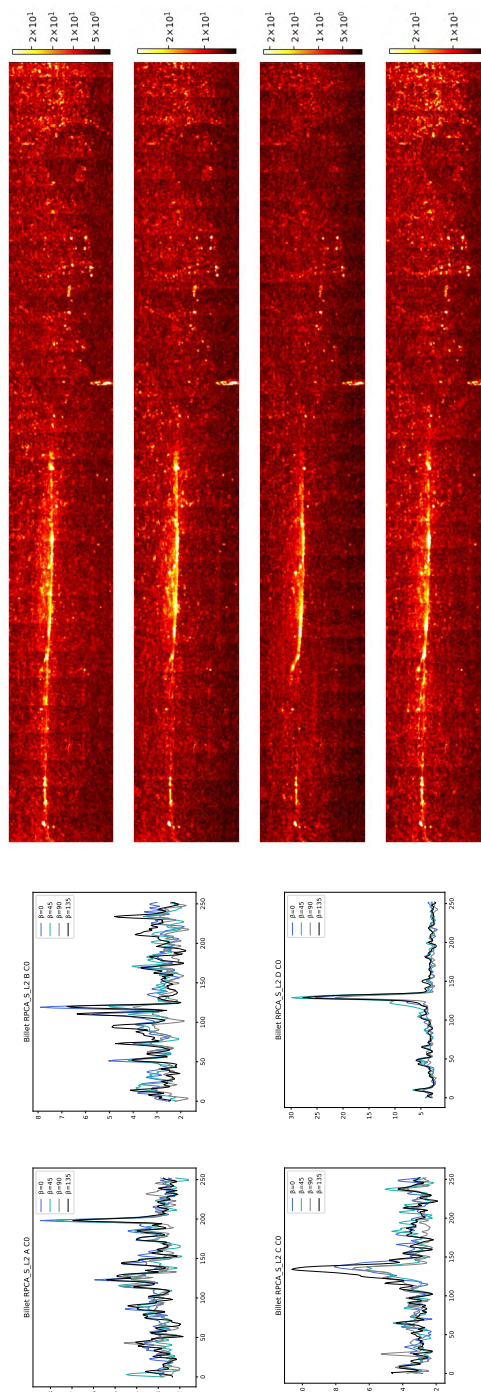


Fig. 4.37 Steel billet RPCA sparse, temporal L2 norm..



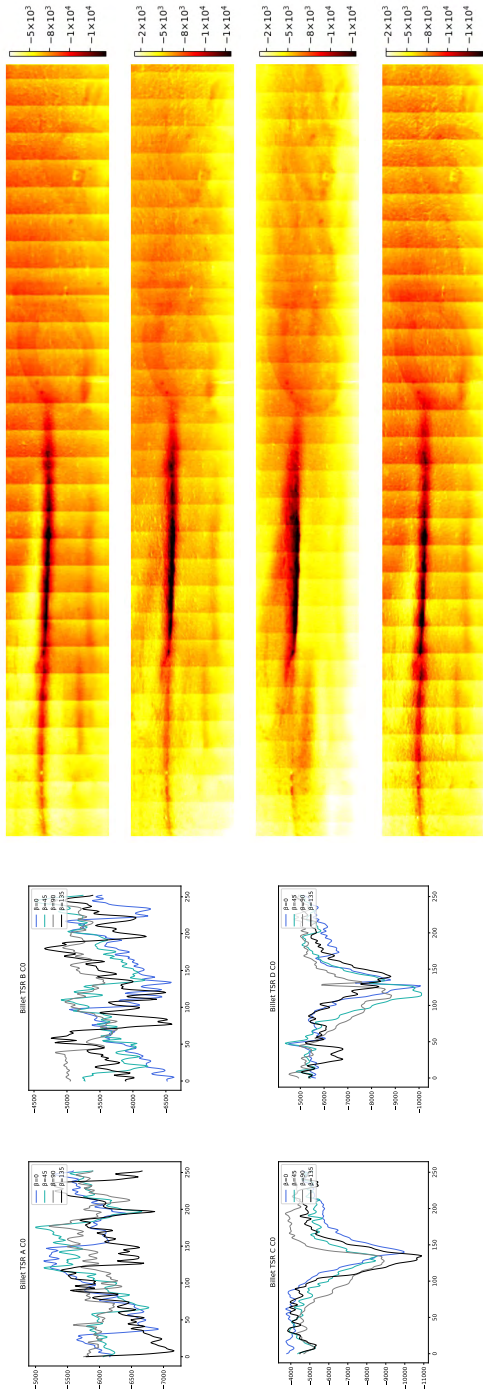


Fig. 4.38 Steel billet TSR first derivative fitted to cooling thermogram, showing frame corresponding to 25% time of cooling frame.

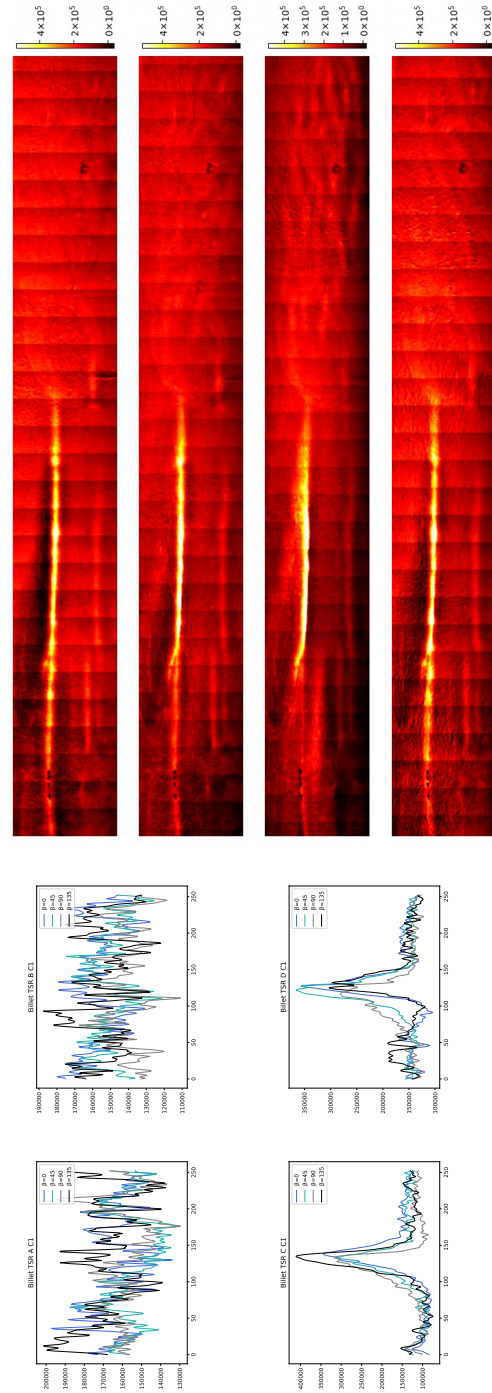


Fig. 4.39 Steel billet TSR second derivative fitted to cooling thermogram, showing frame corresponding to 25% time of cooling frame.

## 4.5 Discussion

The resulting SNR of the proposed method, compared to the static thermography exhibit a reduced SNR associated to the ghosting and other artifacts associated to the reconstruction. Nonetheless, the signal of most of the methods surpass 4 decibel in most of the magnetic field orientations. Note that an ideal signal processing should maximize the SNR on profiles C and D which are centered in hot spots of the cracks and profiles A and B should not yield a significant SNR value.

On the other hand, these types of defects do not necessarily require the 4 orientations to detect the cracks, since most of the evaluated algorithms surpass the minimum SNR threshold of 4 decibels in at least two magnetic field orientations.

At the same time, the thermal drift compensation, along with subsequent averaging, allows for the use of multiple pulses, resulting in lower noise.

Of all the exposed temporal compression methods, the standard deviation of the thermogram consistently produces the highest SNR, although this may be due to the fact that this type of cracks exhibits a very pronounced heating in the cracks.

On the other hand, the  $L$  component of the norm-2 of the RPCA is correlated to the magnitude, as expected, but the  $S$  component does not stand out particularly, due to the higher background noise in the sound area, reducing its SNR.

## 4.6 Conclusions

In this chapter, a novel system has been presented that enables dynamic multi-directional induction thermography on flat and cylindrical parts.

The system involves interleaved induction from various directions of the magnetic field with simultaneous relative motion between the piece and the camera and inductor assembly.

The processing and separation of each direction have been integrated with a thermal drift compensation to preserve the oscillatory component of the pulses, thus normalizing the magnitudes of the mono-directional thermograms. This normalization has allowed for consistent weighting between each pulse in the sequence, enabling the noise reduction of the thermogram with a simple averaging. The resulting system produces consistent multi-directional thermographies in a single scan, allowing the application of conventional processing techniques.

Future instances of the problem could potentially enhance the results by utilizing a local registration of images to cancel out vibrations in the translation system. Additionally, other methods of spatio-temporal fusion based on Machine Learning or neural networks have not



been evaluated yet. The employment of other types of processing techniques, such as the Tucker Decomposition or the canonical polyadic decomposition could potentially be used to process a 4-way tensor adding the orientation of the magnetic field, to the reconstructed video.

The ability to perform dynamic multi-directional thermography has reduced the dead time when the camera is not recording, whether due to the movement required to cover the surface for inspection or the need to rotate the inductor for parts with defects of indeterminate orientation.

The exposed processing algorithms have shown Signal-to-Noise Ratios (SNRs) greater than 4db in most cases considering the four induction orientations, demonstrating the feasibility of this method.



# Chapter 5

## Sparse model-based view planning for complex geometries

Previous sections of this academic paper have presented advancements in induction thermography aimed at refining the technique and while at the same time reducing the total inspection time. In this context, numerous inspection systems require robots to position an inspection head carrying an infrared camera, 3D scanner, or other kinds of sensors. The majority of these systems are integrated into robotic cells, which typically require an offline programming of trajectories to cover a specific inspection surface. Considering that the total inspection time depends significantly on the varying experience of the operators doing the automation, a novel system has been proposed which is able to procedurally automate and optimize the inspection itself on an arbitrary geometry. In this scenario the objective of the inspection is the accurate 3D reconstruction of complex geometries, but this system can be extrapolated to other techniques such as induction thermography.

### 5.1 Introduction

The initial viewpoint sampling method is able to lower the complexity of the algorithm by creating a sparse visibility bipartite graph relating the targeted surface patches, with the potential viewpoints (camera poses defined in  $SE(3)$ ), which are contained in the surroundings of the object. This graph is used to sample and simulate a subset of viewpoints, employing an iterative greedy parallel set cover which weights the coverage of the sparse and simulated visibility. This method prematurely rejects poor candidates and prioritize the viewpoints providing an increased coverage, with no expensive preprocessing of the 3D models. A randomized Greedy Heuristic with local search has been proposed to maximize the coverage,

while minimizing the total inspection time, first with the set cover of the simulated viewpoints, and secondly with the sequencing of the viewpoints and robot positioning with obstacle avoidance. Furthermore, the performance of the system is demonstrated on a set of complex benchmark models from the Stanford and MIT repositories, yielding a higher coverage with a lower computational runtime compared to existing sampling-based methods. The validation of the full system has been carried scanning a Stanford Dragon positioned with a 12 axes kinematic chain composed by two robots.

### 5.1.1 Motivation

Automated inspections have gained significance within the smart manufacturing context as they are necessary for many downstream applications or quality assurance. These systems are commonly required to inspect a surface that will ensure the fulfilment of the required specifications. Usually, the complete coverage of the surface of interest requires a set of captures from different viewpoints. The associated camera network design or the automation of the robotic inspection can be a lengthy process with many delays. The automatic resolution of this aspect is called a view planning problem (VPP).

### 5.1.2 Related work

Typically, the solution to the VPP for an unknown 3D object is handled with a "next best view" (NBV) approach. This method determines iteratively the subsequent position that will reveal the greatest possible portion of the component's surface or its immediate environment for the robot. Some methods recur to octomaps which chart the surroundings of the occupied, empty, and unknown space, to estimate a probabilistic map of the information gain [140], enabling the determination of the upcoming pose. Even if this strategy is useful for reverse-engineering and path finding of robots [187, 188, 122], among other applications, it requires an intermittent online capture and processing, artificially extending the process and incurring in other inefficiencies. Approaching the VPP with an approximate model that enables the simulation of the inspection allows the usage of different heuristics and methods to attain a predictable result.

Depending on the final goal, many specification criteria have been utilized. For instance, in a surface reconstruction problem the minimum sampling density and variance of the point clouds are considered [87], and in a network placement problem, the main objective is to make a complete coverage of the scene [89] with the minimum number of viewpoints.

The classical sampling-based VPP, which employs an approximate model of the targeted surface, such as the one exposed by Scott [87], starts with the sampling of viewpoints, its

subsequent simulation and the final set cover ensuring the maximum coverage. The sampling of the viewpoints starts by decimating [141] or resampling [142] the surface mesh, which yields another mesh with a different distribution and density of the primitives. This mesh is used to sample the surface points by selecting the vertices or the barycenters of the mesh primitives. These points are used to sample a set of a priori ideal viewpoints with a normal incidence angle from a distance corresponding to the maximum optical resolution, which is defined as the center of the depth of field (DOF), as described in alg. 1.

---

**Algorithm 1** Sample Offset DOF [87].
 

---

```

1: function SAMPLEOFFSETDOF(Mesh,  $z_f$ ,  $z_n$ ,  $n_{cams}$ )
2:    $Mesh' \leftarrow ResampleMesh(Mesh, n_{cams})$ 
3:    $P, N \leftarrow SampleBarycenters(Mesh', n_{cams})$ 
4:    $Cams \leftarrow \emptyset$ 
5:   for each  $p_i \in P$  do
6:      $o_i \leftarrow p_i + n_i(z_f + z_n)/2$ 
7:      $Cams \leftarrow Cams \cup ToFrame(o_i, -n_i)$ 
8:   return  $Cams$ 

```

---

Other viewpoint sampling methods such as the one exposed by Jing et al. [103], summarized in alg. 2, generates a volume surrounding the object, computed by calculating the perpendicular at the surface points of the object, and adding the minimum and maximum distance of the DOF. This 3D volume is used to randomly sample the origins of the viewpoints, and their orientations is determined with a potential function of the neighbouring surface normals.

---

**Algorithm 2** Sample Potential Field [103].
 

---

```

1: function SAMPLEPOTENTIALFIELD(Mesh,  $z_f$ ,  $z_n$ ,  $n_{cams}$ )
2:    $Mesh' \leftarrow ResampleMesh(Mesh, n_{cams})$ 
3:    $V \leftarrow dilate(Mesh', z_f) - dilate(Mesh', z_n)$ 
4:    $O_{cams} \leftarrow RandomSampling(V, n_{cams})$ 
5:    $Cams \leftarrow \emptyset$ 
6:   for each  $o_i \in O_{cams}$  do
7:      $v_i \leftarrow potentialField(o_i)$ 
8:      $Cams \leftarrow Cams \cup ToFrame(o_i, v)$ 
9:   return  $Cams$ 

```

---

The resulting set of viewpoints is then simulated considering the visibility, as well as the incident angle  $\theta$ , as illustrated in fig. 5.3a, among other factors, resulting in a visibility vector of the surface points for each viewpoint,  $\vec{A}_i$ . The visibility of the  $N$  viewpoints, regarding  $M$  surface points conforms a visibility matrix,  $\mathbf{A}_{vis} = (\vec{A}_1, \dots, \vec{A}_N)$ , which can be interpreted as a bipartite graph relating both disjoint sets, as formulated by Tarbox et al. [143]. This data

structure, which can be interpreted as a bipartite graph, enables a combinatorial formulation of the VPP as a Set Cover Problem (SCP), to maximize the coverage of the surface with the minimum number of viewpoints.

Considering that the total area to cover is finite, the likelihood of visualizing the same surface patches increases as the number of viewpoints rises. The diminishing returns of this problem is one aspect of its submodularity associated to the total overlap of the visibility [104]. Therefore the coverage and number of viewpoints are two conflicting objectives which must be approximated in a reasonable time scale. The optimization of the problem has been previously solved employing well-established meta-heuristics such as, greedy [144], linear programming [145], Lagrangian relaxation [146], simulated annealing [147], particle swarm optimization [96], and genetic algorithms [148], among others.

The conventional Greedy Set Cover [144], described in alg. 3, repeatedly selects the next column (viewpoint) of  $\mathbf{A}_{\text{vis}}$ , which maximizes the coverage of the remaining uncovered points, until the whole set is covered in  $O(\log n)$ , [149]. Its unweighted cost, as well as the deterministic selection criteria, precludes the exploration of alternative solutions, which can be improved with a randomized selection [150]. Another aspect to consider is that its parallelization is able to reduce the runtime with a similar solution, so long the problem is subdivided in buckets of maximal near-independent sets [151]. The set cover yields a set of unordered inspection frames which might be used to position static cameras or generate an inspection trajectory, minimizing the inspection time and considering the kinematic constraints of the robot and camera attached to the robot wrist, by employing a combinatorial optimization known as the Travelling Salesman Problem (TSP).

---

**Algorithm 3** Greedy Set Cover.

---

```

1: function GREEDYSETCOVER( $A = \{A_1, \dots, A_n\}$ )
2:    $Sol \leftarrow \emptyset$ 
3:   while  $|Uncovered(Sol)| > 0$  do
4:     Select  $j$  that maximizes  $|A_j \cap Uncovered(Sol)|$ 
5:      $Sol \leftarrow Sol \cup j$ 
6:   return  $Sol$ 

```

---

One of the main drawbacks of all these systems is that they do not use complex geometries instances in the exposed results, as well as a typical runtime to solve the problem on the order of minutes [87, 96, 153, 154].

Considering that the simulation of the viewpoints takes a significant share of the total runtime of this problem, the sampling of an optimal subset of viewpoints is an important aspect of the problem. Most of the conventional viewpoint sampling methods are able to restrict its sampling space, but they do not take into account any information from the surrounding geometry, which limits their ability to extrapolate the mutual visibility of the

viewpoints. The occlusion ratio of a point should a priori correlate to the number of incident cameras in a visibility matrix, but it does not retain any spatial information to prioritize the sampling of viewpoints associated with complex surface patches. Some pseudo-illumination models, employed in 3D rendering to shade the surfaces, such as ambient occlusion [189], map a scalar field in the surface, by computing the ratio of occluded local random rays. This yields a scalar field associated to the vertices or faces of the model, with high values related to concave regions, internal geometries, or high curvature regions. But this mapping of the surface is nevertheless unable to determine the best location of the viewpoints for each surface patch.

All the mentioned studies expose different methods to solve the problem, but they typically involve an expensive mesh preprocessing which is prone to alter the original surface and its topology, introducing defects such as normal inversion affecting the visibility and accuracy of the simulation. Another factor to take into account is the extended computational times exposed by these studies, which impose restrictions on the scale and complexity of the inspected part. Furthermore, the minimization of the inspection time focus mainly on the SCP without considering the sequencing of the viewpoints restricted by the axes of the robot positioning the sensor and its workspace. The contributions addressing these shortcomings are enumerated in sec. 5.1.4.

### 5.1.3 VPP combinatorial formulation

The view planning problem (VPP), consists on the determination of a minimum set of scanning viewpoints  $\mathbf{C}_p$  to cover a surface. The surface of the inspected part,  $S$  is composed by a set of vertices in  $\mathbb{R}^3$ , and a collection of polygons, which are defined as an adjacency list of vertices. Another aspect to consider is that the set of viewpoints, must be contained in a space belonging to the Special Euclidean group  $SE(3)$  [190], surrounding  $S$ . The coverage of  $S$  by  $\mathbf{C}_p$ , must also fulfill a set of specification parameters  $\gamma$ , which have been defined in this work as (1) the minimum density, defined as the maximum distance between the points,  $\delta_{\max}[m]$ , and (2) the maximum incident angle of the camera towards a point, noted as  $\theta_{\max}$ .

The combinatorial approach of the VPP requires the discretization of both  $S$  and  $\mathbf{V}_c$  (space of possible camera poses), yielding a set of  $M$  points or polygons  $\mathbf{P} = \{p_1, \dots, p_M\}$ , and  $N$  viewpoints,  $\mathbf{C} = \{c_1, \dots, c_N\}$  with  $\mathbf{C}_p \in \mathbf{C}$ . The determination of the visibility of a point  $p_i$ , regarding a viewpoint  $c_j$ , can be formulated as a binary scalar (0 non-visible, 1 visible),  $a_{ij}$  that takes into consideration the direct line of sight and the specification compliance. Therefore, the computation of the visibility of a viewpoint  $c_j$ , regarding the whole set of points  $\mathbf{P}$ , can be defined as a binary visibility vector,  $\vec{A}_j = (a_{1j}, \dots, a_{Mj})^T$ , with  $a_{ij}$  being the visibility of  $p_i$  regarding  $c_j$ . The combination of all the viewpoint visibility vectors

conforms a binary visibility matrix [143], with the points and the viewpoints corresponding to the rows and columns respectively, noted as  $\mathbf{A}_{\text{vis}} = (\vec{A}_1, \dots, \vec{A}_N)_{|\mathbf{P}| \times |\mathbf{C}|}$ .

Note that  $\mathbf{A}_{\text{vis}}$  can be represented as a bipartite graph of two disjoint sets,  $\mathbf{P}$  and  $\mathbf{C}$ . Fig. 5.1, shows their symbolic relation in (a), as well as its bipartite graph in (b), with the vertices on the top symbolizing the viewpoints, the points below, as well as the edges representing their visibility. The visibility matrix of this figure is shown down below.

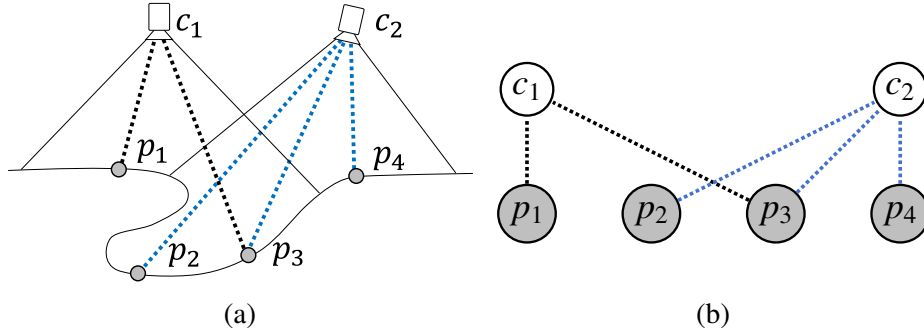


Fig. 5.1 Visibility as a bipartite graph. (a) Symbolic representation of the visibility with 2 cameras covering a surface discretized in 4 points and the dotted line showing the visibility of each point towards the cameras. (b) Bipartite visibility graph corresponding to the left side of the figure

Consequently, we can define the VPP as the joint minimization of (1) the number of viewpoints  $|\mathbf{C}_p|$  with  $\mathbf{C}_p \in \mathbf{V}_c$  and (2) the ratio of uncovered points of  $\mathbf{P}$ , subjected to the visibility and specification compliance  $\gamma$  as follows,

$$\min_{\mathbf{C}_p \in \mathbf{V}_c} \left( f(\mathbf{C}_p), |\mathbf{C}_p| \right) \text{ with } f(\mathbf{C}_p) = 1 - \frac{1}{M} \sum_i \bigcup_j \vec{A}_j \quad (5.1)$$

$\xrightarrow{\text{visibility vector of } j^{\text{th}} \text{ viewpoint}}$   
 $\xrightarrow{\text{uncovered surface}}$   
 $\xleftarrow{\text{subset } \mathbf{C}_p \text{ of positioning space, } \mathbf{V}_c}$

Note that  $f(\mathbf{C}_p)$  represents the ratio of uncovered points considering the union of the visibility vectors of  $\mathbf{C}_p$ .

### 5.1.4 Contributions

A sampling-based view-planning system is exposed with a set of distinct contributions aimed at reducing the runtime of the VPP and the total inspection time of the robot:



- A novel sampling view-planning that employs a sparse representation of the underlying visibility, reducing the sampling space with a clusterization preserving the relation between the space of the viewpoints and the surface.
- A sampling and simulation algorithm that does not require any expensive preprocessing of the 3D model, yielding typical runtimes close to 1 second.
- An improved greedy heuristic for the SCP and Robot Travelling Salesman (RTSP) problem, with a randomized local search, analogous to GRASP [150], to minimize the time to traverse the viewpoints by the robot.
- Results validated with a set of 20 complex benchmark models demonstrating a higher coverage with a lower runtime compared to existing sampling-based methods, as well as the evaluation of the full system scanning a Stanford Dragon with two robots.

## 5.2 Methods

Based on the submodular property of the VPP [104], a set of assumptions can be established to approximate the underlying visibility matrix, which can be used for efficient sampling of the simulated viewpoints.

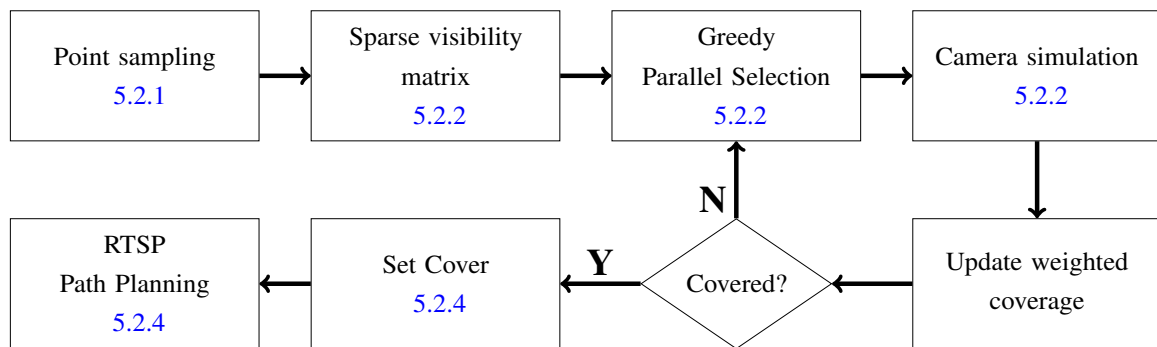


Fig. 5.2 System overview.

Taking into account that this is a sampling-based view-planning, the proposed method estimates a visibility matrix which serves as the basis for the optimization of the objectives to attain the maximum coverage and minimum inspection time. An overview of the system is displayed in fig. 5.2, starting by sampling the surface (sec. 5.2.1), which does not require an expensive pre-processing of the mesh. A subsequent estimation of the visibility yields a sparse visibility matrix (sec. 5.2.2), which is employed to iteratively select a set of viewpoints (sec. 5.2.2), weighing both the sparse and simulated visibility (sec. 5.2.2), taking into account

the accessibility of the robot (sec. 5.2.3). The resulting set of viewpoint vectors links  $\mathbf{P}$  on a dense visibility matrix, which serves as the basis for the minimization of the total inspection time (sec. 5.2.4), first by reducing the set of viewpoints that ensures the coverage by employing a Greedy Randomized SCP (sec. 5.2.4) and a subsequent reordering of the viewpoints, taking into account the robot (sec. 5.2.4), in a problem known as the RTSP.

### 5.2.1 Surface point sampling

As previously stated, depending on the specification parameters of resolution and inherent variable sampling density of most surface reconstruction algorithms employed in the generation of the 3D models, it is necessary to produce a uniform point sampling of the surface,  $S$ . In this system, a modified version of the algorithm exposed by Corsini et al., [191], has been implemented, starting with a Montercarlo point sampling of the surface with a higher resolution of the predefined  $\delta_{\max}$ , typically by a factor of 10. A subsequent subsampling is carried out by iteratively selecting random points and discarding the neighbouring ones at  $\delta_{\max}$  radius. The neighbouring points are typically selected, employing spatial indexers, such as kd-trees [192], or hash tables [193], among others methods. The iterative selection terminates when the projected number of points, based on the area is reached, or no points remain on the uncovered list.

### 5.2.2 Visibility calculation

The determination of the visibility in this scenario starts by the determination of the sparse visibility matrix and the subsequent iterative selection of viewpoints and camera simulation. Note that in this scenario, sec. 5.2.2 is exposed before sec. 5.2.2 to present the view-frustum.

#### Camera simulation employed 3D camera

The employed scanner in this work is a precalibrated Gocator 3520, composed of two 5 MP cameras and a 100 Watt blue light fringe projector, allowing for the 3D measurement, so long the projector has the co-visibility of one camera, enabling the reduction of the shadows and mutual occlusions present in complex geometries. It is based on a structured light phase-shifting scanner, projecting a set of shifted sinusoidal patterns, which ultimately allows the pixel-wise association between the cameras and the projector. This enables the triangulation of the scanned surface points, taking into account the calibrated optics and their relative positions, as illustrated in fig. 5.3b.

As a result, a conservative visibility evaluation of the scanner fuses the visibility of each device as a combination of the visibility of the projector and the cameras. Therefore, the

Table 5.1 Gocator 3520 view-frustum parameters.

$\varphi_x$	$\varphi_y$	$z_n$	$z_f$	$R_x$	$R_y$	$b$	$\theta_v$	$\delta_{\min}$
30°	40°	280mm	430mm	1944	2592	180mm	14°	0.08mm

visibility of a point  $p$  is defined as  $v = v_{proj} \cap (v_{c1} \cup v_{c2})$  with  $v_{proj}$ ,  $v_{c1}$  and  $v_{c2}$ , being the separated visibility of the projector and both cameras respectively.

The visibility of each device towards the surface points has been assessed individually through a three-step process. Firstly, by examining the view-frustum containment of each point [194]; secondly, by evaluating specification compliance; and lastly, by ensuring an unobstructed line of sight.

A pinhole model has been used to describe the view-frustum of each camera, as well as the projector. Fig 5.3a displays the view-frustum as a truncated pyramid in a darker shade, with  $\varphi_x$  and  $\varphi_y$  being the Field of View (FOV) constrained by the sensor rectangular shape in the horizontal and vertical axes respectively. The minimum optical resolution is ensured by constraining the DOF, between  $z_n$  and  $z_f$ . The relative position of the stereo camera with the projector is shown in fig. 5.3b, being  $\theta_v$ , the vergence angle in the XZ plane and  $b$ , the distance between the cameras. Table 5.1 depicts the parameters associated with the Gocator 3520, assuming the same view-frustum for the three devices, with  $R_x$  and  $R_y$  being their resolution.

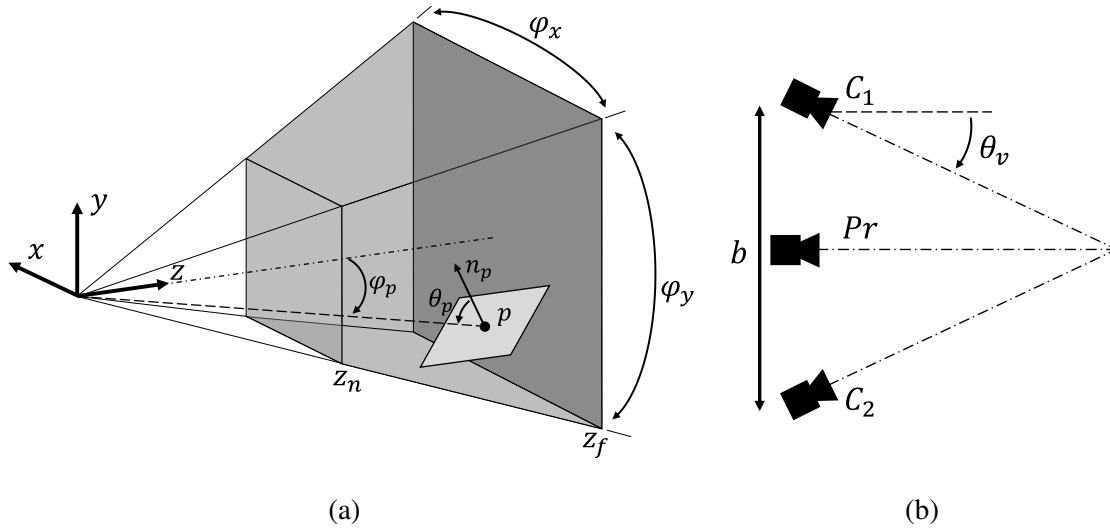


Fig. 5.3 Visibility evaluation. (a) Pinhole view-frustum with a DOF between  $z_n$  and  $z_f$ , FOV with  $\varphi_x$  and  $\varphi_y$ . A ray directed from the focal point towards  $p$  with an incident angle  $\theta_p$  is drawn with a dotted line. (b) Stereo camera and projector relative position with a baseline  $b$  and vergence angle  $\theta_v$ .

Note that the maximum incidence angle depends on the reflectance of the surface, the exposure, and aperture among other factors which has been determined empirically, yielding a value of  $\theta_{\max} = 70^\circ$ .

The specification compliance of the minimum resolution,  $\delta_{\max}$ , has been estimated with a similar approach to the one exposed by Scott, [87], which can be approximated with the following equation:

$$\delta_p = \frac{R_p \Delta\varphi}{H(\theta_p < \theta_{\max}) \cos \theta_p} \quad (5.2)$$

$R_p = \frac{z_p}{\cos \varphi_p}$  is the distance between  $p$  and the focal point,  $\Delta\varphi = \min\left(\frac{\varphi_x}{R_x}, \frac{\varphi_y}{R_y}\right)$  the minimum angular resolution of the sensor,  $H(\theta_p < \theta_{\max})$  being the Heaviside step function with  $\theta_{\max}$  being the maximum incidence angle, and  $(\cos \theta_p)^{-1}$  modelling the Lambertian reflectance associated to the incidence  $\theta_p$ , as shown in fig. 5.3a.

Another aspect to consider is the computation of the direct line of sight of the cameras, which is known to be a complex problem [195], can limit the scale and complexity of the VPP. The two main ways to solve this problem consist on the ray-casting of the optical rays originating from the sensor to the scene, and alternatively the projection of the world into the plane of the sensor.

Using the ray casting to estimate the visibility implies the evaluation of the intersection between each ray with all the geometric primitives of the scene. The alternative, based on the Z-buffer method [196] has an exponential decay [197] in its precision, and the rasterization of the projection implies that the framebuffer resolution must be sufficiently small to visualize the specified surface resolution,  $\delta_{\max}$ .

In this context, a ray-tracing technique, such as Embree [198], has been integrated to project rays from the camera towards the remaining points within the view-frustum. This process adheres to specification compliance and effectively separates the visibility runtime from the sensor's resolution.

### Sparse Visibility matrix

The sparse visibility matrix, is based on the extrapolation of the visibility of the neighbouring viewpoints. The visibility from a point  $pos$ , surrounding the surface is illustrated in fig. 5.4a showing the visible surface points with solid rays, which are restricted by the direct line of sight, DOF and their respective incident angle. Therefore, if two of the remaining rays are contained in the FOV of a viewpoint, both of their respective surface points will be visible. For instance in fig. 5.4a, a  $45^\circ$  FOV camera with its optical axis aligned with the ray of  $p_1$  will also visualize  $p_2$ . The same idea can be extended for the viewpoints located on an Euclidean radius around  $pos$ .

The sparse visibility matrix can be defined as an approximation of the dense visibility matrix described in sec. 5.1.3; however, it exhibits two clear differences. The first one lies in the fact that it relates the visibility towards a random subset of  $\mathbf{P}$  denoted as  $\mathbf{P}_{\text{sp}}$ . The second one is that it has an explicit partition of the viewpoints. This is due to the way the visibility is extrapolated with a spatial indexation of the viewpoints, as it will be explained later. Therefore, the sparse visibility matrix can be denoted as follows:  $\mathbf{A}_{\text{sp}} = (\mathbf{A}_1, \dots, \mathbf{A}_n)$ , where  $\mathbf{A}_{i_{|\mathbf{P}_{\text{sp}}| \times |\mathbf{C}_i|}}$  is the sub-matrix of the extrapolated visibility of a subset of viewpoints  $\mathbf{C}_i$ , regarding  $\mathbf{P}_{\text{sp}}$ .

The sparse visibility matrix is built based on the efficient extrapolation of the local visibility, starting with the sampling of a collection of viewpoint axes from each surface point, and the subsequent extrapolation of the visibility.

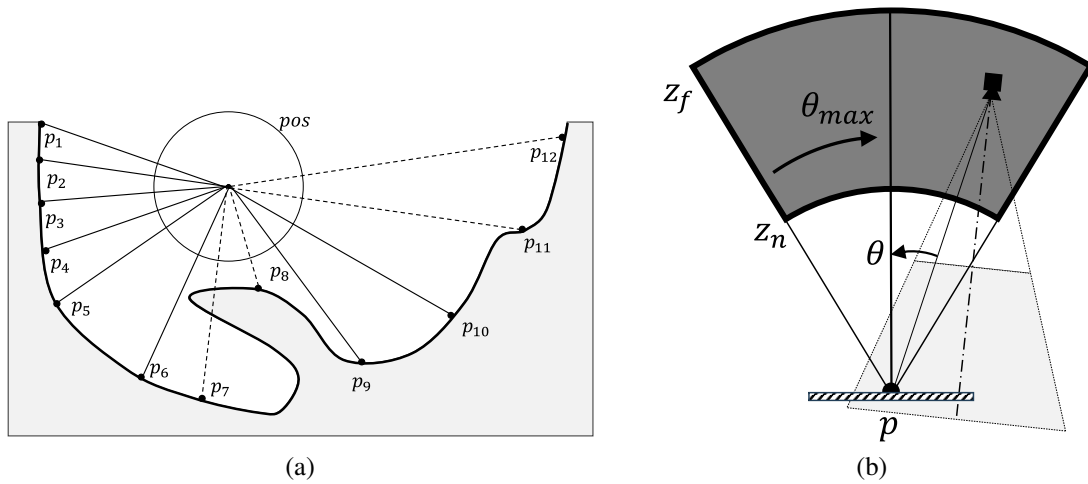


Fig. 5.4 Camera sampling. (a) Symbolic representation of the omnidirectional visibility from a point in space  $pos$ , casting rays to the visible points in solid lines conditioned by the distance, incident angle and the occlusions. (b) Point visibility sampling volume, representing a partial spherical cone, with its vertex and axis coincidental to  $p$  and surface normal,  $n$ , respectively.

**Point visibility sampling** The first phase involves sampling a set of optical axes associated to the points on the surface with a direct visibility. The process starts by selecting a random fraction  $\kappa$  of  $\mathbf{P}$ , denoted as  $\mathbf{P}_{\text{sp}}$ . For each point  $p$  in  $\mathbf{P}_{\text{sp}}$ , a subset of fixed vectors is sampled, representing the optical axes of potential viewpoints directed to  $p$ . To ensure the visibility of an optical axis  $k_p$  towards  $p$  with its normal  $n_p$ , a point visibility space is defined with two equations depending on the pinhole parameters of the camera and  $k_p$ : (1)  $z_n \leq k_p^T n_p \leq z_f$ , (2)  $(\frac{k_p}{|k_p|})^T n_p > \cos \theta_{\text{max}}$ , representing DOF containment and feasible angle of incidence. This volume has the shape of a partial spherical cone, with its vertex and axis coincidental

to the point  $p$  and surface normal,  $n_p$ , respectively. The maximum and minimum radius correspond to the DOF range, and the cone half angle is associated with the maximum incidence angle,  $\theta_{\max}$ , as illustrated in fig. 5.4b. A set of vectors pointing to  $p$  is sampled from this volume with a 3D uniform grid and a  $\Delta d$  resolution. The direct line of sight is evaluated by ray-casting from  $k_p$  towards  $p$ , discarding the occluded ones. Based on the experiments the following grid sampling resolution gives good results:

$$\Delta d = \frac{1}{3} \left( \frac{z_f + z_n}{2} (\tan \varphi_x + \tan \varphi_y) + z_f - z_n \right) \quad (5.3)$$

$\Delta d$  represents an average of the DOF, and the dimensions corresponding to the mid plane cross-section of the view-frustum.

**Visibility extrapolation** The second phase consist on the extrapolation of the visibility of the neighbouring optical axes. Considering that each optical axis is linked to a surface, the extrapolation has been carried out in two steps. The first one consisting on the binning of the optical axes employing a grid which partitions the Euclidean Space  $\mathbb{R}^3$ , and the orientation space with spherical coordinates, as shown in fig. 5.5.

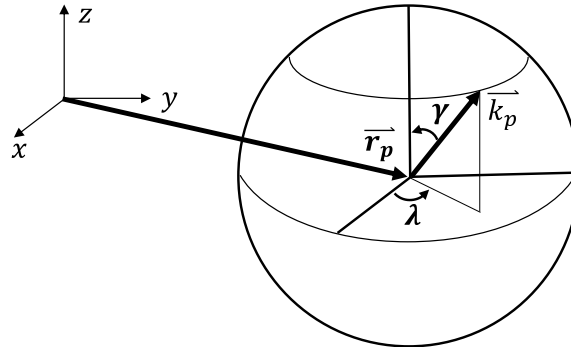


Fig. 5.5 Optical axes grid parameters in  $\mathbb{R}^3$  for  $r_p$  and the latitude  $\gamma$  and longitude  $\lambda$  of  $k_p$  regarding the frame of the object.

The grid is built by indexing the optical axes, assigning 5 integer scalars (3 for position and 2 for orientation) to each optical axis, which are then sorted first by the Euclidean position, and subsequently by the orientation. This effectively groups the optical axes belonging to the same orientation bin, denoted as *ORI*, contained on an Euclidean bin, denoted as *POS*. As a result, all the consecutive elements with the same orientation belong to the same bin. The left side of fig. 5.6 displays the relation of the ordered optical axes, denoted as *CAMS*, contained in the orientation and position bins. So long, the euclidean and angular resolution of the grid,  $\Delta d$  and  $\Delta\beta$  respectively, are sufficiently small, all the optical axes contained

in the same orientation and position, bin will have similar  $r_p$  and  $k_p$  vectors, resulting in a comparable visibility. Therefore, the centroid of the optical axes of each orientation bin inherits the predominant visibility of the bin. The right side of fig. 5.6 displays the centroids of the orientation bin inheriting the visibility of the surface points from the optical axes. Experiments have show that the Euclidean resolution of the grid  $\Delta d$ , described in eq. 5.3 gives good results, as well as the following angular resolution:  $\Delta\beta = \min(\varphi_x, \varphi_y)/4$ . The centroid of the optical axes is determined as follows,  $r_C = \frac{1}{n} \sum_{i=0}^n r_i$  and  $k_C = \frac{\sum_{i=1}^n k_i}{|\sum_{i=1}^n k_i|}$ .

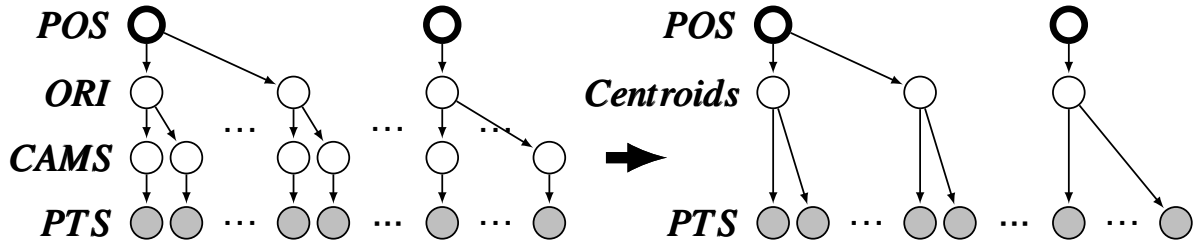


Fig. 5.6 Hierarchical binning is depicted with a two level spatial indexing of the optical axes, with an Euclidean *POS*, and orientation *ORI* partitioning, corresponding to the first and second level respectively. The left side of the figure shows that each orientation bin contains a set of optical axes which are linked to a single point each. The right side displays the *Centroids* of the axes of each bin linked to all incident points of *ORI*.

Note that the ordered list of points of the spatial binning and the strides of the orientation bins associated to the clustered camera centroids can be seamlessly copied to the row and column index buffers of a binary Compressed Row Sparse (CRS) matrix respectively. The resulting CRS matrix conforms an approximation of  $\mathbf{A}_{\text{vis}}$  with a lower density. Considering that the hierarchical binning groups the camera centroids by Euclidean bins, the sparse visibility matrix can be as noted as a set of  $n$  column blocks corresponding to the Euclidean bins *POS*, denoted as  $\mathbf{A}'_{\text{sp}} = (\mathbf{A}_1, \dots, \mathbf{A}_n)$ .

One of the drawbacks of the binning is that the resulting clusterization depends on the origin of the spatial partition. For instance, a cluster of optical axis can be divided, resulting in two contiguous centroids, instead of one that clusters the group. Fig 5.7 shows a set of outgoing rays from *pos* directed to the points shown fig. 5.4b, with an angular partition of  $\Delta\beta = 60^\circ$ , represented with dotted lines, and their respective centroids drawn in blue.

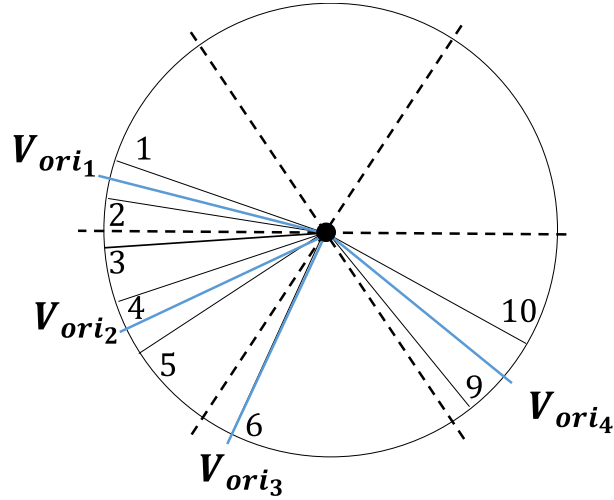


Fig. 5.7 Rays directed to the points illustrated in fig. 5.4a from  $pos$  partitioned in  $60^\circ$  bins with the axes centroids of each bin in blue.

In this example, the viewpoint aligned with  $V_{ori_1}$  will probably see most of the points visualized by  $V_{ori_2}$ , but none of the points corresponding to  $V_{ori_3}$ . Alternatively,  $V_{ori_2}$ , will probably visualize most of their adjacent ones. This redundant co-visibility of the axis centroids can be used to further increase the number of edges in the sparse bipartite graph. Therefore, the co-visibility of the local axes centroids contained in an Euclidean bin,  $K_{bin} = \{k_1, \dots, k_m\}$ , can be formulated as a symmetric adjacency matrix, denoted as:  $\mathbf{A}_{cams} = (\dots e_{ij} \dots)_{m \times m}$ , with  $e_{ij} = k_i^T \cdot k_j > \cos \Delta\beta$ . The extrapolation of the visibility within the Euclidean bin, has been carried out with a graph composition of the sparse visibility matrix,  $\mathbf{A}_{sp}$  and the optical axis orientation adjacency matrix  $\mathbf{A}_{cams}$ , with the following binary matrix multiplication,  $\mathbf{A}_{sp} = \mathbf{A}'_{sp} \times \mathbf{A}_{cams}$ , with  $\mathbf{A}_{sp}$  being the final sparse visibility matrix. Fig. 5.8 shows a visibility graph corresponding to fig. 5.4a, with the upper row corresponding to a set of viewpoint nodes and their mutual adjacency represented by the dotted edges. As a result, the nodes in the bottom are associated to the points  $\mathbf{P}$ , which are connected to the viewpoints  $\mathbf{C}$ , either by the initial binning with gray edges, or the subsequent extrapolation in black.



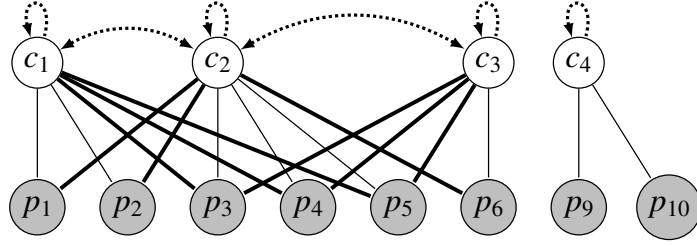


Fig. 5.8 Bipartite graph relating the visibility of the viewpoints on top and the points at the bottom related to fig. 5.4a. The gray edges are associated to the binning, and black ones to the extrapolation. The dotted lines denote the orientation adjacency of the viewpoints.

The following expression shows the graph composition of the visibility extrapolation illustrated in fig. 5.8, corresponding to fig. 5.4a.

$$\begin{pmatrix} 1 & 0 & 0 & 0 \\ 1 & 0 & 0 & 0 \\ 0 & 1 & 0 & 0 \\ 0 & 1 & 0 & 0 \\ 0 & 1 & 0 & 0 \\ 0 & 0 & 1 & 0 \\ 0 & 0 & 0 & 1 \\ 0 & 0 & 0 & 1 \end{pmatrix}_{A'_{sp}} \times \begin{pmatrix} 1 & 1 & 0 & 0 \\ 1 & 1 & 1 & 0 \\ 0 & 1 & 1 & 0 \\ 0 & 0 & 0 & 1 \end{pmatrix}_{A_{cams}} = \begin{pmatrix} 1 & \mathbf{1} & 0 & 0 \\ 1 & \mathbf{1} & 0 & 0 \\ \mathbf{1} & \mathbf{1} & \mathbf{1} & 0 \\ \mathbf{1} & \mathbf{1} & \mathbf{1} & 0 \\ \mathbf{1} & \mathbf{1} & \mathbf{1} & 0 \\ 0 & \mathbf{1} & 1 & 0 \\ 0 & 0 & 0 & 1 \\ 0 & 0 & 0 & 1 \end{pmatrix}_{A_{sp}} \quad (5.4)$$

The generation of the sparse visibility is summarized in alg. 4.

---

**Algorithm 4** Build Sparse Visibility.

---

- 1: **function** BUILDSPARSEVISIBILITY( $\mathbf{P}, \theta_{\max}, \text{CampPars}, \kappa$ )
  - 2:  $\mathbf{P}_{\text{sp}} \leftarrow \text{SubsamplePoints}(\mathbf{P}, \kappa)$   
 $\triangleright$  Sample and ray-cast optical axes for each point (sec. 5.2.2)
  - 3:  $\mathbf{Axes} \leftarrow \text{PointVisibility}(\mathbf{P}_{\text{sp}}, \theta_{\max}, \text{CampPars})$
  - 4:  $\mathbf{Centroids}, \mathbf{A}_{\text{sp}}, \text{Bins} \leftarrow \text{VisibilityExtrapolation}(\mathbf{P}_{\text{sp}}, \mathbf{Axes})$   
 $\triangleright$  Optical axes centroids to viewpoints
  - 5:  $\mathbf{C} \leftarrow \text{ToFrames}(\mathbf{Centroids})$   
 $\triangleright$  Filter invalid Robot viewpoints
  - 6:  $\mathbf{C} \leftarrow \text{FilterInvalidViewpoints}(\mathbf{C})$
  - 7: **return**  $\mathbf{P}_{\text{sp}}, \mathbf{C}, \mathbf{A}_{\text{sp}}$
- 

Note that the viewpoints are calculated from the centroids with a random rotation of the  $z$  axis in line 5 of alg. 4.

### Greedy iterative selection

The sampling and simulation of the viewpoints is based on a greedy set cover (alg. 3), weighting the coverage globally, with a local parallel selection. The selection penalizes the number of covers of each point by weighting both the extrapolated visibility ( $\mathbf{A}_{\text{sp}}$ ), and the simulated viewpoints, up to a minimum number of covers,  $\text{min}_{\text{cov}}$ . Considering that the neighboring viewpoints, contained in the same Euclidean bin ( $\text{POS}$ ), have a higher overlap

of the surface visibility, compared to the farthest ones, it enables its parallel selection in buckets of maximal near-independent sets [151], approximating the sequential greedy set cover solution with a shorter runtime. The proposed method to sample and simulate the viewpoints is exposed in alg. 5.

---

**Algorithm 5** Sparse Iterative Sampling.
 

---

```

1: function SPARSEITERATIVESAMPLING( $\mathbf{P}, \min_{cov}, \text{CamPars}$ )
    ▷ Initialize  $\mathbf{P}$ , Centroids and Sparse visibility, alg. 4
2:  $\mathbf{P}_{sp}, \mathbf{C}, \mathbf{A}_{sp} \leftarrow \text{BuildSparseVisibility}(\mathbf{P}, \theta_{max}, \text{CamPars}, \kappa)$ 
    ▷ Initialize camera viewpoints, visibility matrix and coverage vector
3:  $\text{Cams} \leftarrow \emptyset, \mathbf{A}_{vis} \leftarrow \emptyset, \text{Cov} \leftarrow \emptyset$ 
    ▷ Iterative selection and camera simulation
4: while True do
    ▷ Weighted uncovered points vector
5:  $\overline{Uncov} \leftarrow \max(0, 1 - \frac{\overline{Cov}}{\min_{cov}})$ 
6:  $\text{Cams}' \leftarrow \emptyset$ 
    ▷ Greedy parallel selection
7: for each  $\mathbf{A} \in \mathbf{A}_{sp}$  do
    ▷ Remaining weighted coverage
8:  $\overline{UncovCams} \leftarrow \mathbf{A}^T \times \overline{Uncov}$ 
9: Select  $i$  maximum row of  $\overline{UncovCams}$ 
10: if  $\overline{UncovCams}_i \geq 1$  then
11:   Discard  $i^{th}$  camera in  $\mathbf{A}$ 
12:    $\text{Cams}' \leftarrow \text{Cams}' \cup \mathbf{C}_i$ 
13: if  $\text{Cams}' == \emptyset$  then
14:   break
15:  $\mathbf{A}'_{vis} \leftarrow \text{CameraSimulation}(\mathbf{P}, \text{Cams}', \text{CamPars})$ 
    ▷ Save viewpoints and simulated visibility
16:  $\text{Cams} \leftarrow \text{Cams} \cup \text{Cams}', \mathbf{A}_{vis} \leftarrow \mathbf{A}_{vis} \cup \mathbf{A}'_{vis}$ 
17: Add the dense and sparse coverage of  $\mathbf{P}_{sp}$  to  $\overline{Cov}$ 
18: return  $\text{Cams}, \mathbf{A}_{vis}$ 

```

---

After calculating the sparse visibility matrix with alg. 4 in line 2, the vector  $\overline{Cov}$ , which counts the accumulated covers of each point of  $\mathbf{P}_{sp}$  is initialized, as well as the final set of viewpoints,  $\text{Cams}$  and the simulated visibility matrix  $\mathbf{A}_{vis}$  of  $\mathbf{P}$ . The iterative selection starts by initializing the vector  $\overline{Uncov}$ , which negatively weights the accumulated covers of each point of  $\mathbf{P}_{sp}$ , up to a minimum number of covers,  $\min_{cov}$ , as shown in line 5. The parallel selection within each bin  $POS$ , starts by calculating the weighted new coverage  $\overline{UncovCams}$ , of each viewpoint in line 8, with  $\mathbf{A}$ , being the block of  $\mathbf{A}_{sp}$  corresponding to the viewpoints contained in  $POS$ . Afterwards, the viewpoint with the maximum value, greater or equal to one, is saved. The parallel selection, yields at most a viewpoint for each bin, which are then simulated in line 15 and saved in  $\mathbf{A}_{vis}$ . The accumulated coverage of the points  $\overline{Cov}$ , is updated with the summation of the dense and sparse visibility of  $\text{Cams}'$ . This process is repeated until no viewpoints are selected.

### 5.2.3 Robot accessibility testing

The accessibility of the viewpoints is evaluated based on the existence of a valid robot configuration with no collision. A fast inverse kinematic solver such as IKFAST [199], has been employed returning, the complete set of solutions. The sampling of robot configurations for kinematic chains with more than 6 degrees of freedom has been carried out with two different methods. In the case of external positioning axis, a random or uniform sampling for each redundant axis is sufficient, and for multiple robotic arms, a Cartesian bounding box is defined to randomly sample the possible configurations, as described in the results.

The resulting robot configurations are subsequently tested for any intersection of the robot with the scene. The collision detection is typically handled using a two-phase approach consisting on an initial broad phase and a subsequent narrow phase. The broad phase employs a simplified primitive geometry of the objects to discard the evaluation of distant objects. Some implementations use the sort and sweep algorithm to evaluate the overlap of the projected bounds of the primitives into the three axes. While other approaches recur to a parallel spatial cell subdivisions to evaluate the collision of objects contained in the same cell. The second phase computes the exact contact points of the intersected geometry. A collision detection library, such as FCL [127] has been implemented in this instance with both the broad and narrow phase.

### 5.2.4 Inspection time optimization

After simulating the visibility of the sampled viewpoints, the problem must be able to minimize the total inspection time, maximizing the coverage. The joint optimization of both problems is notoriously hard which has motivated the division of the problem in two steps. The first one consisting on the minimization of the number of selected viewpoints on a SCP, analogous to the greedy set cover alg. 3. And a second phase aims at minimizing the time to visit each viewpoint by simultaneously reordering them considering the robot configurations, which is a variation of the TSP, known as the RTSP. Since the solution of both problems can be formulated as an ordered list, a sequential greedy insertion [144], can be employed in an iterative manner. Some heuristics, such as GRASP [150], add some randomization to the greedy heuristic by choosing among the  $k$  candidates for the solution, instead of the best one. The proposed generic resolution of both problems is displayed in alg. 6, consisting on the generation of an initial solution  $S$ , conformed as an ordered list. This solution is iteratively optimized, by employing a similar scheme to a Variable Neighborhood Search (VNS) [200], first by discarding  $g$  elements and a subsequent randomized insertion of the  $k$  nearest neighbors. The resulting solution  $S'$  is preserved so long it improves  $S$ . The local

search is terminated after  $t_{max}$  seconds, or  $l_{max}$  iterations with no improvements. To enable the adaptation of the generic optimization scheme, to the SCP and RTSP, the following functions must be altered accordingly, *RandomizedGreedyInsertion*, *discardGRandom*, as well as *compareSolution*. The adaptation of the proposed scheme is detailed in the following sections.

---

**Algorithm 6** Greedy Variable Neighborhood Search.
 

---

```

1: function RANDOMIZEDGREEDYVNS( $\mathbf{A} = \{A_1, \dots, A_n\}, k, g$ )
    $\triangleright$  Initial solution
2:  $S' \leftarrow \text{RandomizedGreedyInsertion}(\mathbf{A}, \emptyset, k)$ 
3:  $S \leftarrow S', l \leftarrow 1$ 
4: while  $l \leq l_{max} \cap t < t_{max}$  do
5:    $S' \leftarrow \text{discardGRandom}(S', g)$ 
6:    $S' \leftarrow \text{RandomizedGreedyInsertion}(\mathbf{A}, S', k)$ 
7:   if compareSolution( $S', S$ ) then  $S \leftarrow S', l \leftarrow 1$ 
8:   else  $l \leftarrow l + 1$ 
9: return  $S$ 

```

---

## SCP

Both the initial solution shown in line 2, as well as the insertion of the local search in line 6 from alg. 6, have been implemented with alg. 7, considering the previously calculated visibility matrix,  $\mathbf{A}_{vis} = (\vec{A}_1, \dots, \vec{A}_N)_{|\mathbf{P}| \times |\mathbf{C}|}$ . Note that the insertion of viewpoints stops after reaching a coverage ratio,  $\eta_{vis}$  is reached as shown in line 2. It starts by determining the number of uncovered points of the solution  $S$  of each viewpoint, resulting in the vector  $\vec{Covers}$ . Subsequently, a column among the  $k$  maximums of  $\vec{Covers}$  is chosen. The random removal of  $g$  elements in the unordered solution  $S$ , *discardGRandom* follows a uniform distribution. The iterative local search saves the solution  $S'$ , so long it has a lower cardinality regarding the best  $S$ , or an improved coverage with the same cardinality.

---

**Algorithm 7** Randomized Greedy SCP.
 

---

```

1: function RANDOMIZEDGREEDYINSERTIONSCP( $\mathbf{A}_{vis} = \{A_1, \dots, A_N\}, S, k$ )
2: while  $\frac{1}{M} |Uncovered(S)| > 1 - \eta_{vis}$  do
    $\triangleright$  New covers for each viewpoint
3:  $\vec{Covers} \leftarrow (\dots, |Uncovered(S) \cap A_j|, \dots)_{j \in \{1, \dots, N\}}$ 
4: Pick random  $j$  column within the  $k$  maximums of  $\vec{Covers}$ 
5:  $S \leftarrow S \cup j$ 
6: return  $S$ 

```

---

### Robot travelling salesman problem

The minimum set of viewpoints with a coverage ratio of  $\eta_{vis}$  that complies with the specifications must be sequenced to minimize the time to visit each viewpoint. The scanning space, or task space,  $T$ , is contained in  $SE(3)$ , which is associated with the end-effector of the robot. The projection of the robot space  $R$ , onto  $T$ , known as the forward kinematic (FK), is unique, but its opposite, the inverse kinematic (IK), does not share the same property. Non-holonomic robots, as well as singular points in  $T$ , might even have infinite IK solutions. Consequently, every target  $t_i$  within the set  $T$  forms a cluster of robot configurations denoted as  $R_i = \{r_{ij}\}$ , thereby extending the TSP to a Clustered Traveling Salesman Problem (CTSP).

In most industrial inspections, the start of any robot routine coincides with the end on a “home” configuration,  $r_{home}$ , conforming a Hamiltonian tour traversing all the viewpoints. The RTSP is a particularization of the CTSP, which in some approximations leverages the duality of the robot and task space to reduce the complexity of the problem [201]. Fig. 5.9a displays the Hamiltonian tour on a TSP graph in the task space, and b represents the corresponding RTSP.

The complete set of clusters, including *home*, is defined as  $\mathbf{A} = \{A_0, \dots, A_{N-1}\}$ , with each cluster  $A_i$  composed by a varying number of robot configurations, with  $A(i, j) = a_{ij}$ , being the robot configuration  $j$  of the target  $i$ . A tour  $S$  is defined as an ordered list of  $M$  pairs,  $\{x, y\}$ , with  $x$  and  $y$  being the set point number and its associated configuration respectively.

The time to transition from a robot configuration  $\vec{a}_{ij}$  to  $\vec{a}_{kl}$  is defined as:  $cost(\vec{a}_{ij}, \vec{a}_{kl}) = \max(|\vec{a}_{ij} - \vec{a}_{kl}| \oslash \vec{\omega})$ , with  $\vec{\omega}$  being the axes velocities of the robot and  $\oslash$  the element-wise vector division. As a result, the cost of a tour  $S$  is the summation of all the segments costs. And the function *compareSolution* of line 7 in alg. 6 for the RTSP determines if  $S'$  has a lower cost compared to  $S$ .

Adapting the function *RandomizedGreedyInsertion* for the RTSP has resulted in alg. 8, which assigns a random configuration of  $A$  when the sequence is empty, and then iteratively chooses the configurations that are among the  $k$  minimum costs of the unvisited target configurations.

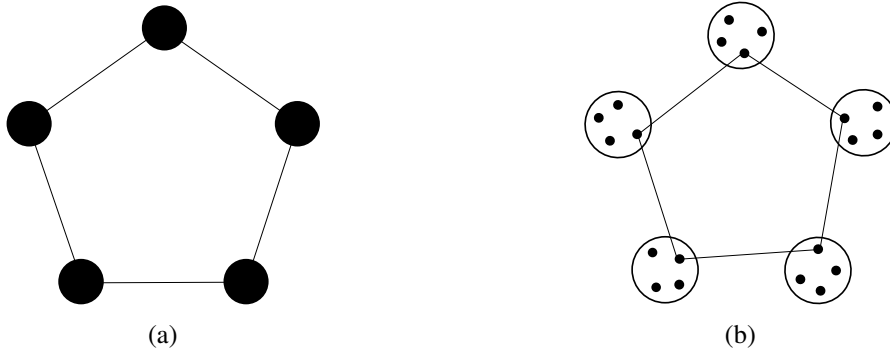


Fig. 5.9 Scan sequencing. (a) Travelling salesman problem. (b) Robot-TSP.

The implementation of *discardGRandom* for the RTSP, defined in line 5 from alg. 6, erases a set of  $g$  contiguous elements of the circular sequence, yielding a unique gap for the subsequent insertions.

---

#### Algorithm 8 Randomized Greedy Insertion RTSP.

---

```

1: function RANDOMIZEDGREEDYINSERTIONRTSP( $\mathbf{A}_{\text{vis}} = \{A_1, \dots, A_N\}, S, k$ )
    $\triangleright$  Hamiltonian cycle enables random start
2: if then  $|S| == \emptyset$ 
3:   pick random  $i \in \{0, \dots, M-1\}$  and  $j \in \{0, \dots, |R_i|-1\}$ 
4:    $S_0 \leftarrow \{i, j\}$ 
    $\triangleright$  Insert in the first gap, next
5:  $curr \leftarrow \text{firstBeforeNull}(S)$ ,  $next \leftarrow (curr + 1) \% M$ 
6: repeat
    $\triangleright$  Costs from  $S_{curr}$  to remaining viewpoint configurations
7:  $Costs = \{ \{ Cost(S_{curr}, \{i, j\}) \}_{\forall i \in (\{0, \dots, M-1\} - S), \forall j \in \{0, \dots, |R_i|-1\}}$ 
8:   Pick random  $\{i, j\}$  among  $k$  minimums in Costs
    $\triangleright$  Add to sequence
9:    $S_{next} \leftarrow \{i, j\}$ 
10:   $curr \leftarrow next$ ,  $next \leftarrow (curr + 1) \% M$ 
11: until  $S_{next} \neq 0$ 
12: return  $S$ 

```

---

## 5.3 Experiments and results

The evaluation of the proposed method has been conducted in two phases. The first one compares the view-planning system without the robot. The second phase benchmarks the full system with two robotic arms and a printed Stanford Dragon.

### 5.3.1 Synthetic view-planning

To evaluate the performance of the contributions, regardless of the employed kinematic chain, a set of 4 models from the Stanford repository and 16, from the MIT CSAIL Textured Models Database has been simulated throughout the pose generation, simulation and the Greedy Set Cover exposed in alg. 3 selecting up to 20 viewpoints. The quantitative evaluation has been carried out by employing the area under the curve (AUC) [159], measuring the accumulated information gain of the final Greedy selection sequence.

The minimum resolution is  $\delta_{\max} = 0.001m$  with a maximum incidence angle,  $\theta_{\max} = 70^\circ$ , employing the camera parameters associated to the Gocator3520, shown in table 5.1.

Two alternative pose generation methods have been compared, the first one proposed by Scott[87], implemented with alg. 1, and a second exposed by Jing [103] following alg. 2. Both methods sample a predetermined number of viewpoints based on the resolution and the area of the mesh as:  $n_{cams} = \frac{1}{20} \frac{area_{model}}{\delta_{\max}^2}$ . Since both methods require a mesh resampling, the method exposed by Schroeder [141] has been used, which is implemented in VTK with the operator `vtkDecimatePro` [202]. Note that the presented method employs the following parameters:  $\kappa = 0.25$  and  $min_{cov} = 15$ .

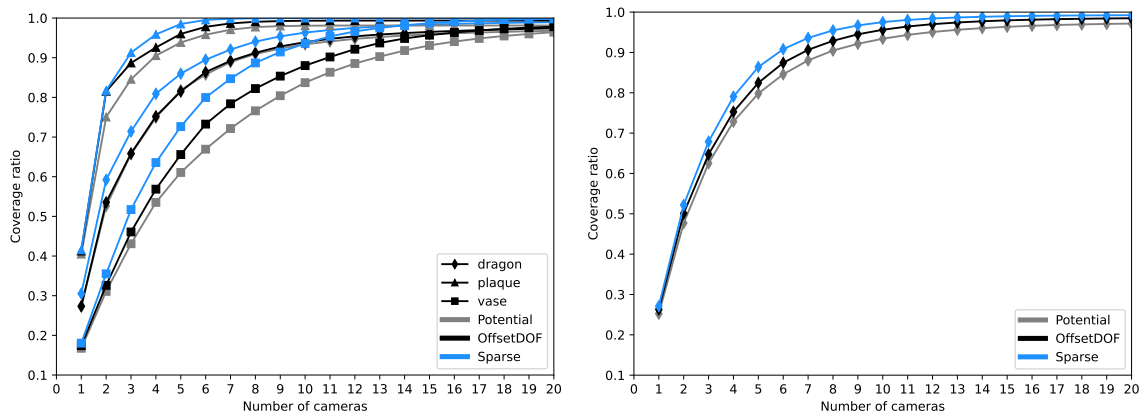


Fig. 5.10 Coverage sequence up to 20 viewpoints comparing the proposed method (sparse) and two alternative methods. (a) Comparison between 3 models of the dataset. (b) Average of the whole dataset.

Table 5.2 Comparison on models from Stanford and MIT repositories, reporting the absolute coverage of 2, 4 and 6 cameras, the AUC up to 20 cameras and the total runtime. All results are averaged with 10 runs.















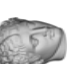





																				
C2	0.524	0.484	0.573	0.526	0.585	0.392	0.508	0.444	0.375	0.539	0.376	0.410	0.448	<b>0.638</b>	0.337	0.492	0.750	0.293	0.533	0.311
C4	0.781	0.717	0.853	0.749	0.878	0.651	0.801	0.713	0.601	0.829	0.582	0.717	0.707	0.849	0.582	0.807	0.905	0.507	0.805	0.535
C6	0.887	0.819	0.960	0.858	0.953	0.819	0.930	0.845	0.740	0.923	0.703	0.881	0.839	0.925	0.742	0.919	0.958	0.633	0.913	0.669
AUC	0.774	0.719	0.832	0.754	0.836	0.705	0.798	0.730	0.642	0.803	0.610	0.744	0.728	0.828	0.641	0.791	0.871	0.554	0.790	0.585
T[s]	2.001	6.988	<b>0.274</b>	5.120	0.723	<b>0.910</b>	2.184	2.454	5.321	1.236	<b>2.184</b>	7.015	3.160	2.992	8.712	<b>0.611</b>	1.248	10.533	1.047	<b>0.867</b>
C2	0.587	0.487	<b>0.627</b>	0.535	0.610	0.488	0.530	0.460	0.390	0.545	0.414	<b>0.424</b>	0.488	0.637	0.308	0.494	0.815	0.289	0.566	0.326
C4	0.851	0.727	0.894	0.752	0.898	0.705	0.822	0.762	0.651	0.844	0.622	<b>0.749</b>	0.747	0.800	0.543	0.804	0.926	0.543	0.848	0.569
C6	0.944	0.833	0.978	0.864	0.975	0.888	0.948	0.927	0.778	0.934	0.764	<b>0.891</b>	0.874	0.909	0.706	0.930	0.978	0.712	0.921	0.733
AUC	0.826	0.728	0.855	0.757	0.851	0.763	0.811	0.778	0.680	0.812	0.659	<b>0.755</b>	0.758	0.813	0.614	0.795	0.894	0.615	0.808	0.626
T[s]	2.088	6.892	0.372	5.708	0.781	1.251	2.279	2.668	6.046	1.335	2.347	7.688	3.373	3.381	9.645	0.847	1.355	11.596	1.150	1.230
C2	<b>0.611</b>	<b>0.516</b>	0.621	<b>0.592</b>	<b>0.642</b>	<b>0.501</b>	<b>0.571</b>	<b>0.510</b>	<b>0.401</b>	<b>0.572</b>	<b>0.426</b>	0.403	<b>0.497</b>	0.624	<b>0.338</b>	<b>0.507</b>	<b>0.817</b>	<b>0.336</b>	<b>0.592</b>	<b>0.355</b>
C4	<b>0.864</b>	<b>0.784</b>	<b>0.908</b>	<b>0.809</b>	<b>0.950</b>	<b>0.751</b>	<b>0.865</b>	<b>0.843</b>	<b>0.703</b>	<b>0.854</b>	<b>0.657</b>	0.711	<b>0.780</b>	<b>0.853</b>	<b>0.605</b>	<b>0.824</b>	<b>0.959</b>	<b>0.611</b>	<b>0.857</b>	<b>0.636</b>
C6	<b>0.967</b>	<b>0.880</b>	<b>0.983</b>	<b>0.895</b>	<b>0.993</b>	<b>0.912</b>	<b>0.975</b>	<b>0.957</b>	<b>0.851</b>	<b>0.943</b>	<b>0.811</b>	0.890	<b>0.899</b>	<b>0.957</b>	<b>0.778</b>	<b>0.939</b>	<b>0.995</b>	<b>0.818</b>	<b>0.941</b>	<b>0.800</b>
AUC	<b>0.842</b>	<b>0.769</b>	<b>0.859</b>	<b>0.795</b>	<b>0.871</b>	<b>0.784</b>	<b>0.837</b>	<b>0.815</b>	<b>0.727</b>	<b>0.823</b>	<b>0.699</b>	0.746	<b>0.776</b>	<b>0.838</b>	<b>0.664</b>	<b>0.804</b>	<b>0.908</b>	<b>0.685</b>	<b>0.826</b>	<b>0.680</b>
T[s]	<b>0.328</b>	<b>1.198</b>	0.356	<b>1.283</b>	<b>0.280</b>	1.510	<b>0.679</b>	<b>0.733</b>	<b>3.575</b>	<b>0.609</b>	6.806	<b>2.074</b>	<b>1.188</b>	<b>0.811</b>	<b>2.214</b>	0.990	<b>0.376</b>	<b>3.885</b>	<b>0.652</b>	2.770



Table 5.2 displays the results of the 20 models and the 3 methods, reporting the coverage of 2, 4 and 6 viewpoints, as well as the AUC and the runtime in seconds. Note that to reduce the randomness, the results are averaged in 10 runs, executed in a laptop with a Ryzen 9 5900HX with 16 parallel threads in 8 cores and 32GB of RAM. Fig. 5.10a illustrates 3 instances of the coverage sequence, and fig. 5.10b displays the average of the whole set.

### 5.3.2 Real tests

#### Setup

The tests have been carried out with a kinematic chain composed of two manipulator with 6 axes, consisting of an ABB IRB 6700 235/2.65 carrying the scanner and an ABB IRB4600 60/2.05 with a printed Stanford Dragon tied to the 6th axis, as illustrated in fig. 5.11. To replicate the real setup in the simulation, the kinematic chain shown in fig. 5.11 has been calibrated employing common methods. The FK of both robots, associated to the frames of their flanges regarding their respective bases,  ${}^{rob}T_{FL}$ , have been determined using the nominal DH parameters of both robots. The relative position of their bases,  ${}^{rob_{cam}}T_{rob_{part}}$  has been calibrated following the default method provided by the robot controller with an error of 2.2mm. As for the hand-eye calibration associated with the relative position of the scanner coordinate system,  ${}^{FL_{cam}}T_{cam}$ , centered in the projector focal point, regarding the flange of its robot, it has been estimated with the quaternion method [203], with a set of 12 captures employing a checkerboard pattern, yielding a square error of 0.278 mm and  $0.012^\circ$ . The frame of the inspected part regarding the flange of the robot,  ${}^{rob_{part}}T_{part}$ , has been determined by averaging the registration of the model with 6 captures yielding an average error of 15.67 mm and  $0.44^\circ$ .

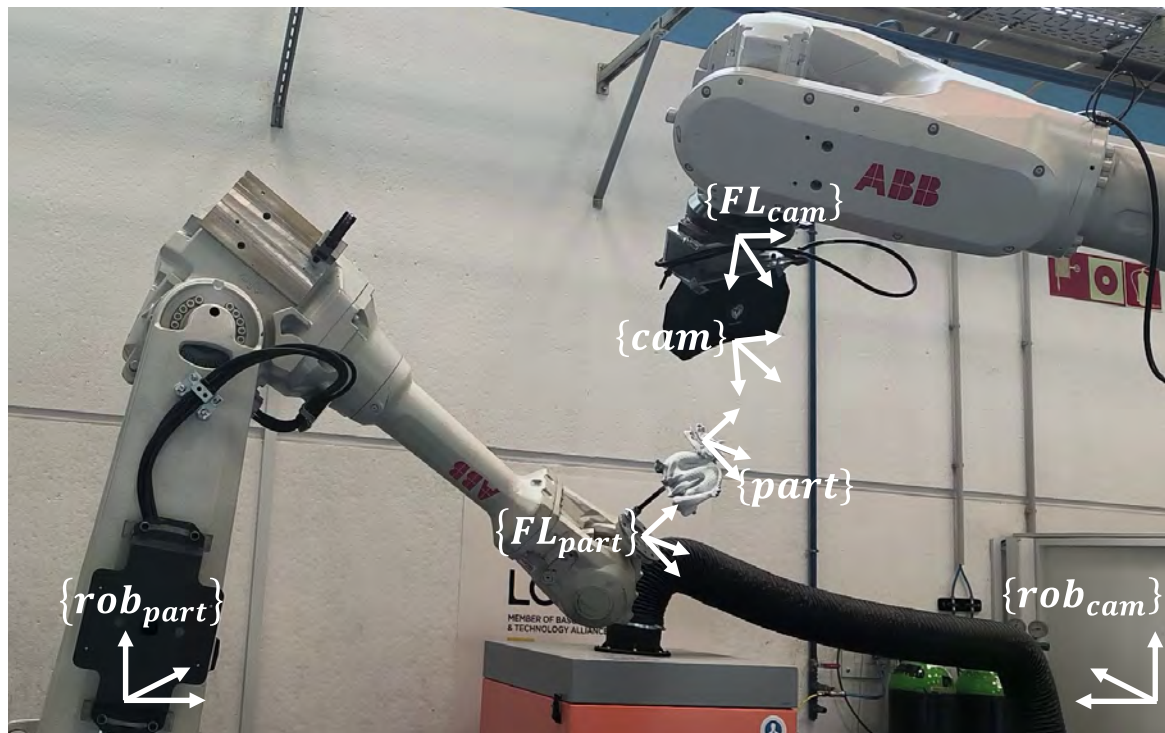


Fig. 5.11 Setup and approximate frames of the kinematic chain carrying the scanner and the part.

### Reconstruction analysis

The employed parameters of the system are presented in table 5.3.

Table 5.3 Robot view-planning parameters.

Specifications		Iterative sparse		SCP				RTSP		
$\delta_{\max}$	$\theta_{\max}$	$min_{cov}$	$\kappa$	$\eta_{vis}$	$t_{scp}$	$g$	$k$	$t_{rtsp}$	$g$	$k$
1mm	70°	35	0.2	90%	10s	2	4	10s	2	4

The resulting sampling has simulated 474 poses for a set of 32671 surface points. The final selection has employed the randomized Greedy SCP with 16 instances in parallel for 10 seconds, selecting the best solution. Fig. 5.13a compares the resulting sequence of the conventional Greedy SCP, as well as the corresponding accumulated visibility of the scanned point clouds. The solution is composed of 7 viewpoints which have been sequenced, employing the RTSP algorithm described in sec. 5.2.4. The 12 axes robot configurations of the capture poses have been sampled, first by selecting a random pose of the viewpoint on a Cartesian bounding box of 0.5x0.5x0.5m to determine the corresponding frame of the

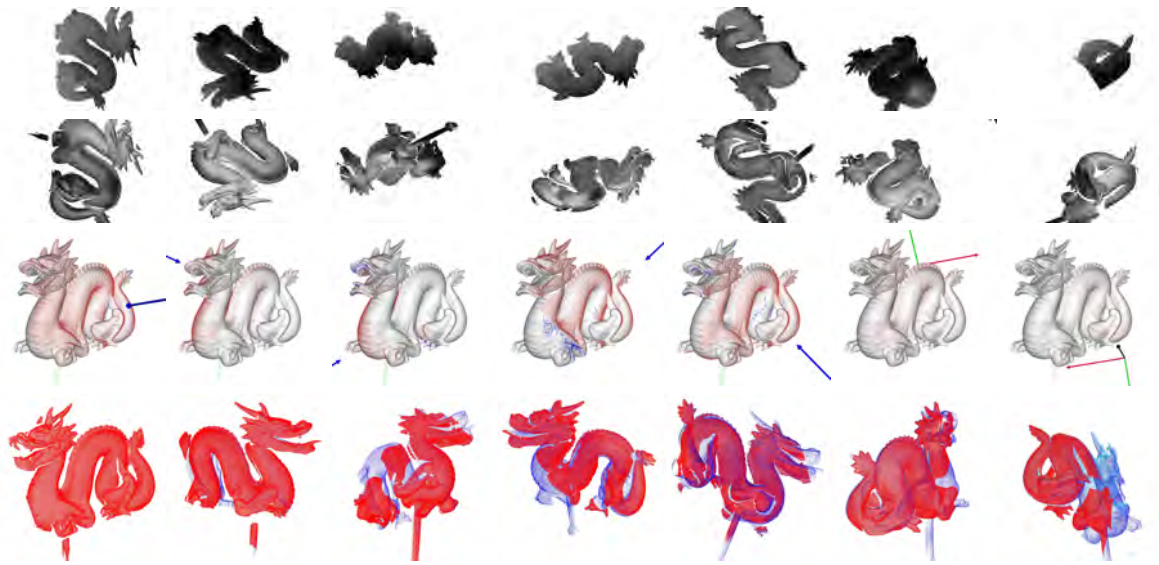


Fig. 5.12 Comparison of the simulated poses and the resulting point clouds with the first and second rows displaying the projected cloud from the viewpoint of the simulated and scanned pose. The third row displays the resulting cloud registered to the model and its corresponding viewpoint. And the last row shows the incremental registration of the clouds with the registered cloud in red and the previous ones in blue.

other robot. The dense path with obstacle avoidance of the resulting sequence of robot configurations has been planned with RRT-Connect [204] implemented in OMPL [205], which has been subsequently post-processed to generate 2 robot programs compatible with the controller enabling a synchronized execution. The accumulated errors of the kinematic chain alter the resulting pose which provokes a deviation from the simulated visibility. The Cartesian deviation of the robot has been measured by registering the point cloud from the theoretical frame of the model, regarding the model itself. The total overlap of the point clouds has been determined, first by discarding the points that do not attain the minimum resolution,  $\delta_{\max}$ , determined by a minimum number of neighbours,  $min_{NN}$ , within a radius,  $r = 2\delta_{\max}$ , employing the following expression:  $min_{NN} = \frac{\pi r^2}{\delta_{\max}^2}$ . And secondly by estimating the number of points of the simulated point cloud within a  $2\delta_{\max}$  distance of the registered capture. Fig. 5.13b shows the registration distance with the resulting overlap. The 7 captures of the inspection are presented in the columns of fig. 5.12, with the top and middle rows displaying the projected point clouds of the simulated and scanned viewpoints. The third row displays the model with the point cloud overlapped to the simulated in red, and the non-overlapping in green, as well as the synthetic points which are not scanned in blue. The surface reconstruction of the model has followed a conventional method consisting on the pre-alignment of the clouds to the frame of the robot flange carrying the scanned

object and a subsequent incremental registration with a modified iterative closest point (ICP) [206]. The ICP has been implemented using the point cloud library [207], employing a different objective function [208], and a correspondence estimation based on a normal shooting coupled with normal rejection. The set of registered clouds is the basis for the surface reconstruction employing the software GOM inspect. Fig. 5.14 shows the resulting surface of the model.

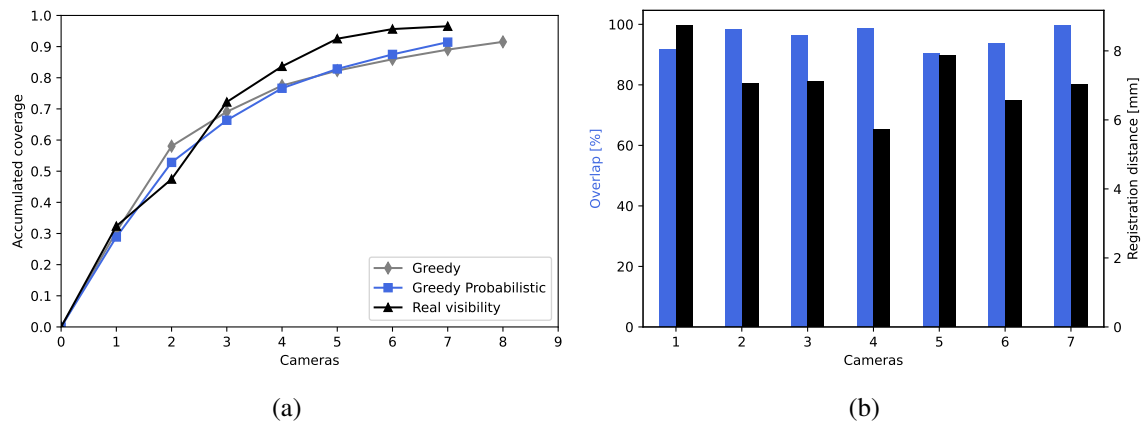


Fig. 5.13 Evaluated coverage sequence and displacement errors. (a) Accumulated visibility of the Greedy Set Cover, and the randomized Greedy with the visibility of the scanner. (b) Overlap ratio of the simulated viewpoints and the registered point cloud, including the registration distance in mm.

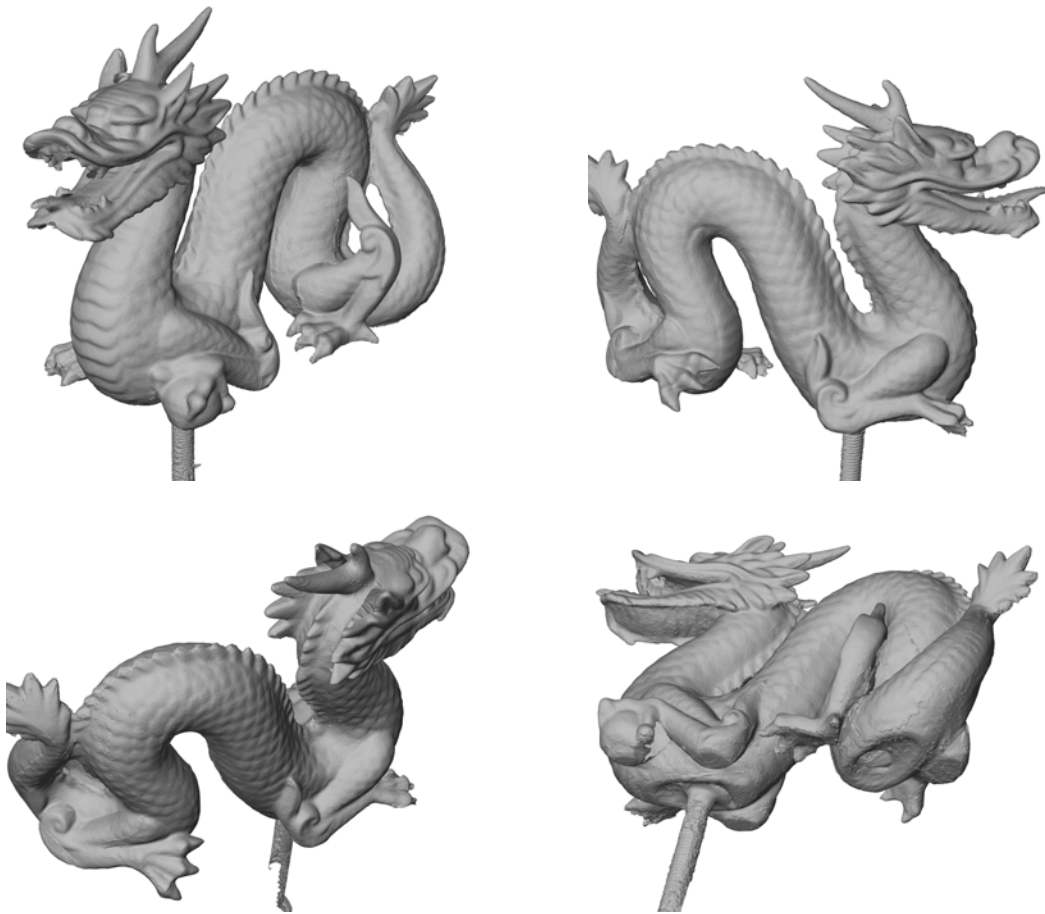


Fig. 5.14 Reconstructed model rendered from 4 perspectives based on the 7 registered point clouds.

## 5.4 Discussion

The outcome presented in section 5.3.1 reveals an enhanced coverage in the majority of instances compared to the analyzed alternatives with a shorter runtime. The employment of expensive mesh preprocessing penalizes the duration of the alternative methods significantly. The results exposed in tab. 5.2 shows that some instances, such as the vase, goblet and bowl improve the coverage by a significant margin, which is likely caused by the deep internal concavity of these containers. Given that the predominant orientation of the faces points to a region where they will not have a direct visibility of the interior, its visibility is restricted to a set of viewpoints with an incidence angle and region of the viewpoint space that is not effectively sampled by these alternative methods. On the contrary, the proposed method samples a subset of cameras that prematurely discards all occluded candidates, ensuring that the subsequent clusterization preserves them by positively weighting their unique visibility.

On the other hand, primarily convex objects with reduced curvature, such as the head and bunny, have an increased co-visibility of the surface, resulting in a comparable coverage. Considering the positive results of the proposed method, future instances of the problem could adapt the sampling and clusterization criteria considering other variables which would a priori enable an improved sampling.

The field test has shown that the full system is able to perform with similar results to the simulated problem, even with an average positioning error of 6mm, yielding an average overlap of 92% of the simulated poses regarding the real captures. The accumulated visibility shown 5.13a is higher than the simulated one, which could be associated with multiple factors such as a conservative maximum incident angle and the mutual compensation of the visibility of the whole set of point clouds.

Another aspect to consider is that only one instance of the randomized set cover has been exposed, which has enabled the reduction of one pose with a higher coverage. Future instances of the problem could integrate other objectives in this SCP algorithm factoring the minimum overlap between the captures and the inclusion of other variables to enable the optimization of secondary objectives. The reduced computational cost of the sparse visibility matrix could serve as the basis for the visibility segmentation which could be employed in the positioning of the parts or the design of tooling factoring the visibility. The greedy RTSP employed with the two robotic arms has not been analyzed but it could be extended to systems with multiple independent scanners.

## 5.5 Conclusions

In this work, a novel method for the view planning has been introduced based on the efficient sampling of a predefined 3D model, by employing a sparse representation of the underlying visibility without any expensive mesh preprocessing.

Experiments on a set of 20 complex models have shown that the presented method is nearly 3 times faster than conventional methods, yielding improved coverage with the same number of viewpoints. This method is able to build a sparse representation of the visibility which enables a premature rejection of poor viewpoint candidates. What is more, at the same time prioritizes the sampling of viewpoints covering complex surface patches, without any expensive mesh preprocessing.

The article on which this chapter is based is currently under review with minor changes.

Finally, a modified randomized greedy heuristic has been proposed to solve separately the Set Cover, as well as the sequencing of the robot scanning poses with satisfactory results. This method has been tested with a stereo-structured light scanner mounted on a robot to

---

scan a complex model positioned by another robot. Despite the significant positioning errors accumulated in the kinematic chain, the resulting coverage of the whole set of captures has produced a higher coverage.





# Chapter 6

## Conclusions

In this thesis, scientific contributions have been presented for non-destructive testing through induction infrared thermography, as well as the procedural generation of 3D inspection trajectories with robots.

The contributions in induction thermography have allowed the inspection and evaluation of various materials and components without affecting their properties. This is achieved using new systems that can detect cracks in all directions without any movement of the induction system. This approach has enabled the generation of thermographies associated with magnetic fields of different orientations. The directional observations facilitate detecting cracks with unknown orientations, and the defect pattern on the phase image reveals a new rotating feature which depends on the magnetic field orientation, inspiring a processing technique based on phase-shifting. This directional thermal response is observed in various samples and crack types. Future work should focus on generalizing this technique using machine learning or neural networks. Rigorous physical modeling is crucial for optimization and potential extrapolation.

Additionally, a new quadratic inductor has been introduced to generate directional magnetic fields with a uniform field distribution, enabling the design of inductors with much larger inspection windows and multidirectional capabilities. Future works should focus on the rigorous physical modelization of the system, employment of circular polarization [181], excitation with two frequencies [182], as well as frequency modulated induction of each coil, among others alternatives.

Furthermore, the previously described directional induction system has been combined with the new quadratic inductor to perform dynamic scanning inspections, where the magnetic field is simultaneously rotated. The system involves interleaved induction from various magnetic field directions while maintaining simultaneous relative motion between the piece and the camera-inductor assembly. The proposed method decompose the thermography in

its directional components including a normalized thermal drift compensation allowing for consistent weighting and noise reduction. This system will benefit in future works with local image registration for vibrations compensation, and the usage of new spatio-temporal fusion methods employed in neural networks, as well as alternative methods to fuse the transient thermographies by incorporating magnetic field orientation into the reconstructed thermographies.

Finally, a system has been developed to address the view planning problem, with contributions aimed at reducing execution time through spatial reduction based on combinatorial clusterization. A novel method for efficient view planning is with a novel sparse visibility representation on a 3D model without costly mesh preprocessing has been exposed. The method prioritizes complex surface patches and employs a modified randomized greedy heuristic for Set Cover and robot scanning pose sequencing, demonstrated demonstrated on complex models with field tests using a 12-axis kinematic chain. Future works could focus on the extrapolation of the sparse visibility employing neural networks to enable VPP with no model, as well as the adaptation to inspections with surface contact, such as induction thermography.

# References

- [1] HX Yuan, YQ Wang, YJ Shi, and L Gardner. Residual stress distributions in welded stainless steel sections. *Thin-Walled Structures*, 79:38–51, 2014.
- [2] DongYue Li and Yong Zhang. The ultrahigh charpy impact toughness of forged alxcoerfeni high entropy alloys at room and cryogenic temperatures. *Intermetallics*, 70:24–28, 2016.
- [3] SA McKelvey and A Fatemi. Surface finish effect on fatigue behavior of forged steel. *International Journal of Fatigue*, 36(1):130–145, 2012.
- [4] Ying Han, Hua Wu, Wei Zhang, Dening Zou, Guiwu Liu, and Guanjun Qiao. Constitutive equation and dynamic recrystallization behavior of as-cast 254smo super-austenitic stainless steel. *Materials & Design*, 69:230–240, 2015.
- [5] MD Banea and Lucas FM da Silva. The effect of temperature on the mechanical properties of adhesives for the automotive industry. *Proceedings of the Institution of Mechanical Engineers, Part L: Journal of Materials: Design and Applications*, 224(2):51–62, 2010.
- [6] A Mondon, MN Jawaid, J Bartsch, M Glatthaar, and SW Glunz. Microstructure analysis of the interface situation and adhesion of thermally formed nickel silicide for plated nickel–copper contacts on silicon solar cells. *Solar energy materials and solar cells*, 117:209–213, 2013.
- [7] Louis Cartz. *Nondestructive testing*. ASM International, Materials Park, OH (United States), 1995.
- [8] J Vetterlein, H Klümper-Westkamp, T Hirsch, and P Mayr. Eddy current testing at high temperatures for controlling heat treatment processes. In *Proceedings of the International Symposium of Non Destructive Testing in Civil Engineering (NDT-CE 2003), Berlin, Germany*, pages 16–19, 2003.
- [9] F Honarvar and A Varvani-Farahani. A review of ultrasonic testing applications in additive manufacturing: Defect evaluation, material characterization, and process control. *Ultrasonics*, 108:106227, 2020.
- [10] Xavier Maldague. *Theory and practice of infrared technology for nondestructive testing*. a, 2001.
- [11] G Raymond Peacock. Thermal imaging of liquid steel and slag in a pouring stream. In *Thermosense XXII*, volume 4020, pages 50–60. SPIE, 2000.

- [12] Peter Meinschmidt and Jochen Aderhold. Thermographic inspection of rotor blades. In *Proceedings of the 9th European Conference on NDT*, 2006.
- [13] NY Utami, Y Tamsir, A Pharmatrisanti, H Gumilang, B Cahyono, and R Siregar. Evaluation condition of transformer based on infrared thermography results. In *2009 IEEE 9th International Conference on the Properties and Applications of Dielectric Materials*, pages 1055–1058. IEEE, 2009.
- [14] B Lehmann, K Ghazi Wakili, Th Frank, B Vera Collado, and Ch Tanner. Effects of individual climatic parameters on the infrared thermography of buildings. *Applied Energy*, 110:29–43, 2013.
- [15] U Sreedhar, CV Krishnamurthy, Krishnan Balasubramaniam, VD Raghupathy, and S Ravisankar. Automatic defect identification using thermal image analysis for online weld quality monitoring. *Journal of Materials Processing Technology*, 212(7):1557–1566, 2012.
- [16] LM Serio, D Palumbo, U Galietti, LAC De Filippis, and AD Ludovico. Monitoring of the friction stir welding process by means of thermography. *Nondestructive Testing and Evaluation*, 31(4):371–383, 2016.
- [17] RK Bhan and Vikram Dhar. Recent infrared detector technologies, applications, trends and development of hgcdte based cooled infrared focal plane arrays and their characterization. *Opto-Electronics Review*, 27(2):174–193, 2019.
- [18] C Besikci. Extended short wavelength infrared fpa technology: status and trends. *Quantum Sensing and Nano Electronics and Photonics XV*, 10540:110–125, 2018.
- [19] Samuel Pierpont Langley. The bolometer and radiant energy. In *Proceedings of the American Academy of Arts and Sciences*, volume 16, pages 342–358. JSTOR, 1880.
- [20] PV Karthik Yadav, Isha Yadav, B Ajitha, Abraham Rajasekar, Sudha Gupta, and Y Ashok Kumar Reddy. Advancements of uncooled infrared microbolometer materials: A review. *Sensors and Actuators A: Physical*, 342:113611, 2022.
- [21] Muhammad A Butt, Nikolay L Kazanskiy, Svetlana N Khonina, Grigory S Voronkov, Elizaveta P Grakhova, and Ruslan V Kutluyarov. A review on photonic sensing technologies: Status and outlook. *Biosensors*, 13(5):568, 2023.
- [22] Antoni Rogalski. History of infrared detectors. *Opto-Electronics Review*, 20:279–308, 2012.
- [23] Jeroen Peeters, Simon Verspeek, Seppe Sels, Boris Bogaerts, and Gunther Steenackers. Optimized dynamic line scanning thermography for aircraft structures. *Quantitative InfraRed Thermography Journal*, 16(3-4):260–275, 2019.
- [24] Jaeger Carslaw. *Conduction of heat in solids*, volume 7299. a, 1959.
- [25] Adel A Badghaish and David C Fleming. Non-destructive inspection of composites using step heating thermography. *Journal of composite materials*, 42(13):1337–1357, 2008.

- [26] Deonna F Woolard and K Elliott Cramer. Line scan versus flash thermography: Comparative study on reinforced carbon-carbon. In *Thermosense XXVII*, volume 5782, pages 315–323. SPIE, 2005.
- [27] GM Carlomagno and Pier Giorgio Berardi. Unsteady thermotopography in non-destructive testing. In *Proc. 3rd Biannual Exchange, St. Louis/USA*, volume 24, page 26, 1976.
- [28] Gerd Busse. Optoacoustic and photothermal material inspection techniques. *Applied optics*, 21(1):107–110, 1982.
- [29] Jean Baptiste Joseph Fourier. *Théorie analytique de la chaleur*. Gauthier-Villars et fils, 1888.
- [30] Otwin Breitenstein and Martin Langenkamp. Lock-in thermography. *Basics and Use for Functional Diagnostics of Electronics Components*, 2003.
- [31] Vanita Arora, Juned A Siddiqui, Ravibabu Mulaveesala, and Amarnath Muniyappa. Pulse compression approach to nonstationary infrared thermal wave imaging for nondestructive testing of carbon fiber reinforced polymers. *IEEE Sensors Journal*, 15(2):663–664, 2014.
- [32] Ravibabu Mulaveesala and Suneet Tuli. Theory of frequency modulated thermal wave imaging for nondestructive subsurface defect detection. *Applied Physics Letters*, 89(19), 2006.
- [33] Ester D’Accardi, Davide Palumbo, and Umberto Galietti. A comparison among different ways to investigate composite materials with lock-in thermography: the multi-frequency approach. *Materials*, 14(10):2525, 2021.
- [34] Giovanni Betta, Luigi Ferrigno, Marco Laracca, Pietro Burrascano, Marco Ricci, and Giuseppe Silipigni. An experimental comparison of multi-frequency and chirp excitations for eddy current testing on thin defects. *Measurement*, 63:207–220, 2015.
- [35] A Rashed, Darryl P Almond, DAS Rees, S Burrows, and S Dixon. Crack detection by laser spot imaging thermography. In *AIP Conference Proceedings*, volume 894, pages 500–506. American Institute of Physics, 2007.
- [36] Teng Li, Darryl P Almond, and D Andrew S Rees. Crack imaging by scanning pulsed laser spot thermography. *Ndt & E International*, 44(2):216–225, 2011.
- [37] Christine Boué and S Holé. Open crack depth sizing by multi-speed continuous laser stimulated lock-in thermography. *Measurement Science and Technology*, 28(6):065901, 2017.
- [38] Pablo López de Uralde, Eider Gorostegui-Colinas, Ander Muniategui, Izaskun Gorostegui, Borja Hériz, Mikel Ayuso, and Xabier Sabalza. A new method for surface crack detection by laser thermography based on thermal barrier effect. In *14th Quantitative InfraRed Thermography Conference*, 2018.

- [39] Fariba Khodayar, Fernando Lopez, Clemente Ibarra-Castanedo, and Xavier Maldague. Optimization of the inspection of large composite materials using robotized line scan thermography. *Journal of Nondestructive Evaluation*, 36:1–15, 2017.
- [40] Jiacheng Wei, Fei Wang, Junyan Liu, Yang Wang, and Lin He. A laser arrays scan thermography (lasst) for the rapid inspection of cfrp composite with subsurface defects. *Composite Structures*, 226:111201, 2019.
- [41] Yun-Kyu An, Jinyeol Yang, Soonkyu Hwang, and Hoon Sohn. Line laser lock-in thermography for instantaneous imaging of cracks in semiconductor chips. *Optics and Lasers in Engineering*, 73:128–136, 2015.
- [42] K Mandal and DL Atherton. A study of magnetic flux-leakage signals. *Journal of Physics D: Applied Physics*, 31(22):3211, 1998.
- [43] Ping Wang, Yunlai Gao, GuiYun Tian, and Haitao Wang. Velocity effect analysis of dynamic magnetization in high speed magnetic flux leakage inspection. *Ndt & E International*, 64:7–12, 2014.
- [44] Beate Oswald-Tranta. Detection and characterisation of short fatigue cracks by inductive thermography. *Quantitative InfraRed Thermography Journal*, pages 1–22, 2021.
- [45] Bin Gao, Wai Lok Woo, and Gui Yun Tian. Electromagnetic thermography nondestructive evaluation: Physics-based modeling and pattern mining. *Scientific Reports*, 6(1):1–12, 2016.
- [46] Beata Oswald-Tranta. Thermoinductive investigations of magnetic materials for surface cracks. *Quantitative InfraRed Thermography Journal*, 1(1):33–46, 2004.
- [47] John Wilson, Gui Yun Tian, Ilham Zainal Abidin, Suixian Yang, and Darryl Almond. Modelling and evaluation of eddy current stimulated thermography. *Nondestructive Testing and Evaluation*, 25(3):205–218, 2010.
- [48] Yunlai Gao, Gui Yun Tian, Ping Wang, Haitao Wang, Juan Ji, and Song Ding. Ferrite-yoke based pulsed induction thermography for cracks quantitative evaluation. In *2015 IEEE Far East NDT New Technology & Application Forum (FENDT)*, pages 197–201. IEEE, 2015.
- [49] John R Reitz. *Foundations of electromagnetic theory*. Pearson Education India, 2009.
- [50] Beate Oswald-Tranta and Mario Sorger. Localizing surface cracks with inductive thermographical inspection: from measurement to image processing. *Quantitative InfraRed Thermography Journal*, 8(2):149–164, 2011.
- [51] Beate Oswald-Tranta. Induction thermography for surface crack detection and depth determination. *Applied Sciences*, 8(2):257, 2018.
- [52] Eider Gorostegui-Colinas, Ander Muniategui, Pablo López de Uralde, Izaskun Gorostegui, Borja Hériz, and Xabier Sabalza. A novel automatic defect detection method for electron beam welded inconel 718 components using inductive thermography. In *14th Quantitative InfraRed Thermography Conference*, volume 1, pages 2–2, 2018.

- [53] Oscar Lucía, Pascal Maussion, Enrique J Dede, and José M Burdío. Induction heating technology and its applications: past developments, current technology, and future challenges. *IEEE Transactions on industrial electronics*, 61(5):2509–2520, 2013.
- [54] Anahi Pereira da Costa, Edson Cocchieri Botelho, Michelle Leali Costa, Nilson Eiji Narita, and José Ricardo Tarpani. A review of welding technologies for thermo-plastic composites in aerospace applications. *Journal of Aerospace Technology and Management*, 4:255–265, 2012.
- [55] B. Tang, D. Hou, T. Hong, and S. Ye. Influence of the external magnetic field on crack detection in pulsed eddy current thermography. *Insight: Non-Destructive Testing and Condition Monitoring*, 60(5):240–246, 2018. cited By 1.
- [56] Yanfeng Li, Xiangdong Gao, Yanxi Zhang, Deyong You, Nanfeng Zhang, Congyi Wang, and Chuncao Wang. Detection model of invisible weld defects by magneto-optical imaging at rotating magnetic field directions. *Optics and Laser Technology*, 121, 2020. Cited by: 10.
- [57] P Levesque, A Deom, and D Balageas. Non destructive evaluation of absorbing materials using microwave stimulated infrared thermography. In *Review of Progress in Quantitative Nondestructive Evaluation: Volumes 12A and 12B*, pages 649–654. Springer, 1993.
- [58] Takahide Sakagami, Shiro Kubo, Tatsuhito Komiyama, and Hironobu Suzuki. Proposal for a new thermographic nondestructive testing technique using microwave heating. In *Thermosense XXI*, volume 3700, pages 99–103. SPIE, 1999.
- [59] Nasser N Qaddoumi, Wael M Saleh, and Mohamed Abou-Khousa. Innovative near-field microwave nondestructive testing of corroded metallic structures utilizing open-ended rectangular waveguide probes. *IEEE Transactions on Instrumentation and Measurement*, 56(5):1961–1966, 2007.
- [60] Beñat Urtasun, Pablo López de Uralde, Karlos Velar, Eider Gorostegui-Colinas, Joonas Neelov, Steve Wright, Matthew Studley, Pedro Lima, Alberto Vale, and Meysam Basiri. Pulsed thermography digital motion stabilization for the unmanned vehicle inspection of solar farms and grfp wind blades through uavs and ugvs. In *Thermosense: Thermal Infrared Applications XLIII*, volume 11743, pages 42–57. SPIE, 2021.
- [61] M. Z. Umar, V. Vavilov, H. Abdullah, and A. K. Ariffin. Ultrasonic infrared thermography in non-destructive testing: A review. *Russian Journal of Nondestructive Testing*, 52(4):212–219, Apr 2016.
- [62] A Scott Mercer, P Klinkhachorn, Udaya B Halabe, and Hota VS GangaRao. The effects of heating methods on infrared thermography. In *AIP Conference Proceedings*, volume 894, pages 1593–1599. American Institute of Physics, 2007.
- [63] Herman van Dyk and Richard L Lemaster. An investigation of the use of active infrared thermography to detect localized surface anomalies in lumber. *Scanning*, 32(4):219–223, 2010.

- [64] Takahide Sakagami and Keiji Ogura. New flaw inspection technique based on infrared thermal images under joule effect heating. *JSME international journal. Ser. A, Mechanics and material engineering*, 37(4):380–388, 1994.
- [65] Roberto Guzman De Villoria, Namiko Yamamoto, Antonio Miravete, and Brian L Wardle. Multi-physics damage sensing in nano-engineered structural composites. *Nanotechnology*, 22(18):185502, 2011.
- [66] JC Krapez and D Balageas. Early detection of thermal contrast in pulsed stimulated infrared thermography. In *Proc. Conf. QIRT*, volume 94, pages 1994–039, 1994.
- [67] Darryl P Almond and SK Lau. Defect sizing by transient thermography. i. an analytical treatment. *Journal of Physics D: Applied Physics*, 27(5):1063, 1994.
- [68] JC Krapez, X Maldague, and P Cielo. Thermographic nde: Data inversion procedure (part ii: 2d analysis and experimental results).-res. *NDE.(2)*, pages 101–124, 1991.
- [69] Xavier Maldague and Sergio Marinetti. Pulse phase infrared thermography. *Journal of applied physics*, 79(5):2694–2698, 1996.
- [70] CF Gauss. Theoria interpolationis methodo nova tractata werke band 3, 265–327. *Göttingen: Königliche Gesellschaft der Wissenschaften*, 1886.
- [71] Steven M Shepard, James R Lhota, Bruce A Rubadeux, David Wang, and Tasdiq Ahmed. Reconstruction and enhancement of active thermographic image sequences. *Optical Engineering*, 42(5):1337–1342, 2003.
- [72] FJ Madruga, C Ibarra-Castanedo, O Conde, JM Lopez-Higuera, and X Maldague. Automatic data processing based on the skewness statistic parameter for subsurface defect detection by active infrared thermography. In *Proc. QIRT*, volume 9. Citeseer, 2008.
- [73] Nikolas Rajic. Principal component thermography for flaw contrast enhancement and flaw depth characterisation in composite structures. *Composite structures*, 58(4):521–528, 2002.
- [74] D Griefahn, Jörg Wollnack, and Wolfgang Hintze. Principal component analysis for fast and automated thermographic inspection of internal structures in sandwich parts. *Journal of Sensors and Sensor Systems*, 3(1):105–111, 2014.
- [75] Ruslee Sutthaweekul, GuiYun Tian, Zijun Wang, and Francesco Ciampa. Microwave open-ended waveguide for detection and characterisation of fbhs in coated gfrp pipes. *Composite Structures*, 225:111080, 2019.
- [76] Karl Pearson. Liii. on lines and planes of closest fit to systems of points in space. *The London, Edinburgh, and Dublin philosophical magazine and journal of science*, 2(11):559–572, 1901.
- [77] Sergio Marinetti, Ermanno Grinzato, Paolo G Bison, Edoardo Bozzi, Massimo Chimenti, Gabriele Pieri, and Ovidio Salvetti. Statistical analysis of ir thermographic sequences by pca. *Infrared Physics & Technology*, 46(1-2):85–91, 2004.



- [78] Yiping Liang, Libing Bai, Jinliang Shao, and Yuhua Cheng. Application of tensor decomposition methods in eddy current pulsed thermography sequences processing. In *2020 International Conference on Sensing, Measurement & Data Analytics in the era of Artificial Intelligence (ICSMD)*, pages 401–406. IEEE, 2020.
- [79] Emmanuel J Candès, Xiaodong Li, Yi Ma, and John Wright. Robust principal component analysis? *Journal of the ACM (JACM)*, 58(3):1–37, 2011.
- [80] MIL HDBK. Nondestructive evaluation system reliability assessment. *Department of Defense Handbook*, 7, 2009.
- [81] Luca Gandossi and Kaisa Simola. Derivation and use of probability of detection curves in the nuclear industry. *Insight-Non-Destructive Testing and Condition Monitoring*, 52(12):657–663, 2010.
- [82] Charles Annis. Statistical best-practices for building probability of detection (pod) models. *R package mh1823, Version 5.4.5*, 2(4.4):650, 2010.
- [83] David L Olson and Dursun Delen. *Advanced data mining techniques*. Springer Science & Business Media, 2008.
- [84] George A Georgiou. Pod curves, their derivation, applications and limitations. *Insight-Non-Destructive Testing and Condition Monitoring*, 49(7):409–414, 2007.
- [85] Charles Annis and Jeremy Knopp. Comparing the effectiveness of a90/95 calculations. In *AIP Conference Proceedings*, volume 894, pages 1767–1774. American Institute of Physics, 2007.
- [86] William Meeker, Dennis Roach, and Seth Kessler. Statistical methods for probability of detection in structural health monitoring. -, 2019.
- [87] William R. Scott. Model-based view planning. *Machine Vision and Applications*, 20(1):47–69, Jan 2009.
- [88] Cl Connolly. The determination of next best views. In *Proceedings. 1985 IEEE international conference on robotics and automation*, volume 2, pages 432–435. IEEE, 1985.
- [89] Yi-Chun Xu, Bangjun Lei, and Emile A Hendriks. Camera network coverage improving by particle swarm optimization. *EURASIP Journal on Image and Video Processing*, 2011:1–10, 2011.
- [90] Ali Hosseinaveh and Fabio Remondino. An imaging network design for ugv-based 3d reconstruction of buildings. *Remote Sensing*, 13(10), 2021. Cited by: 7; All Open Access, Gold Open Access.
- [91] Kento Yamazaki, Kohei Okahara, and Akira Minezawa. View planning using geospatial information for 3d reconstruction with unmanned aerial vehicles. In *IGARSS 2023-2023 IEEE International Geoscience and Remote Sensing Symposium*, pages 4760–4763. IEEE, 2023.

- [92] Yuxiang Li, Jiancheng Wang, Haoyao Chen, Xin Jiang, and Yunhui Liu. Object-aware view planning for autonomous 3d model reconstruction of buildings using a mobile robot. *IEEE Transactions on Instrumentation and Measurement*, 2023.
- [93] Jun Yang, Dong Li, and Steven L Waslander. Probabilistic multi-view fusion of active stereo depth maps for robotic bin-picking. *IEEE Robotics and Automation Letters*, 6(3):4472–4479, 2021.
- [94] Nathaniel Merrill, Yuliang Guo, Xingxing Zuo, Xinyu Huang, Stefan Leutenegger, Xi Peng, Liu Ren, and Guoquan Huang. Symmetry and uncertainty-aware object slam for 6dof object pose estimation. In *Proceedings of the IEEE/CVF Conference on Computer Vision and Pattern Recognition*, pages 14901–14910, 2022.
- [95] Cregg K. Cowan and Peter D Kovesi. Automatic sensor placement from vision task requirements. *IEEE Transactions on Pattern Analysis and machine intelligence*, 10(3):407–416, 1988.
- [96] Aaron Mavrincac, Xiang Chen, and Jose Luis Alarcon-Herrera. Semiautomatic model-based view planning for active triangulation 3-d inspection systems. *IEEE/ASME Transactions on Mechatronics*, 20(2):799–811, 2014.
- [97] Sho Kobayashi, Weiwei Wan, Takuya Kiyokawa, Keisuke Koyama, and Kensuke Harada. Obtaining an object’s 3d model using dual-arm robotic manipulation and stationary depth sensing. *IEEE Transactions on Automation Science and Engineering*, 2022.
- [98] J. Peeters, B. Bogaerts, S. Sels, B. Ribbens, J. J. J. Dirckx, and G. Steenackers. Optimized robotic setup for automated active thermography using advanced path planning and visibility study. *Appl. Opt.*, 57(18):D123–D129, Jun 2018.
- [99] Marc Gronle and Wolfgang Osten. View and sensor planning for multi-sensor surface inspection. *Surface Topography: Metrology and Properties*, 4(2):024009, 04 2016.
- [100] S.Y. Chen and Youfu Li. Automatic sensor placement for model-based robot vision. *IEEE transactions on systems, man, and cybernetics. Part B, Cybernetics : a publication of the IEEE Systems, Man, and Cybernetics Society*, 34:393–408, 03 2004.
- [101] Minwoo Na, HyunJun Jo, and Jae-Bok Song. Cad-based view planning with globally consistent registration for robotic inspection. *International Journal of Precision Engineering and Manufacturing*, 22(8):1391 – 1399, 2021. Cited by: 2.
- [102] Stephan Irgenfried, Heinz Wörn, Stephan Bergmann, Mahsa Mohammadikajii, Jürgen Beyerer, and Carsten Dachsbacher. A versatile hardware and software toolset for computer aided inspection planning of machine vision applications. In Leszek Borzemski, Jerzy Świątek, and Zofia Wilimowska, editors, *Information Systems Architecture and Technology: Proceedings of 38th International Conference on Information Systems Architecture and Technology – ISAT 2017*, pages 326–335, Cham, 2018. Springer International Publishing.

- [103] Wei Jing, Joseph Polden, Wei Lin, and Kenji Shimada. Sampling-based view planning for 3d visual coverage task with unmanned aerial vehicle. In *2016 IEEE/RSJ International Conference on Intelligent Robots and Systems (IROS)*, pages 1808–1815. IEEE, 2016.
- [104] Mike Roberts, Debadeepta Dey, Anh Truong, Sudipta Sinha, Shital Shah, Ashish Kapoor, Pat Hanrahan, and Neel Joshi. Submodular trajectory optimization for aerial 3d scanning. In *Proceedings of the IEEE International Conference on Computer Vision*, pages 5324–5333, 2017.
- [105] Samuel Arce, Cory A. Vernon, Joshua Hammond, Valerie Newell, Joseph Janson, Kevin W. Franke, and John D. Hedengren. Automated 3d reconstruction using optimized view-planning algorithms for iterative development of structure-from-motion models. *Remote Sensing*, 12(13), 2020. Cited by: 16; All Open Access, Gold Open Access, Green Open Access.
- [106] Guillaume Hardouin, Julien Moras, Fabio Morbidi, Julien Marzat, and El Mustapha Mouaddib. Next-best-view planning for surface reconstruction of large-scale 3d environments with multiple uavs. In *2020 IEEE/RSJ International Conference on Intelligent Robots and Systems (IROS)*, pages 1567–1574. IEEE, 2020.
- [107] Abdulrahman Goian, Reem Ashour, Ubaid Ahmad, Tarek Taha, Nawaf Almoosa, and Lakmal Seneviratne. Victim localization in usar scenario exploiting multi-layer mapping structure. *Remote Sensing*, 11(22):2704, 2019.
- [108] Geoffrey A Hollinger, Brendan Englot, Franz Hover, Urbashi Mitra, and Gaurav S Sukhatme. Uncertainty-driven view planning for underwater inspection. In *2012 IEEE International Conference on Robotics and Automation*, pages 4884–4891. IEEE, 2012.
- [109] Narcís Palomeras, Natalia Hurtós, Marc Carreras, and Pere Ridao. Autonomous mapping of underwater 3-d structures: From view planning to execution. *IEEE Robotics and Automation Letters*, 3(3):1965–1971, 2018.
- [110] Marc Carreras, Juan David Hernández, Eduard Vidal, Narcís Palomeras, and Pere Ridao. Online motion planning for underwater inspection. In *2016 IEEE/OES Autonomous Underwater Vehicles (AUV)*, pages 336–341. IEEE, 2016.
- [111] Eduard Vidal, Juan David Hernández, Klemen Istenič, and Marc Carreras. Online view planning for inspecting unexplored underwater structures. *IEEE Robotics and Automation Letters*, 2(3):1436–1443, 2017.
- [112] Eduard Vidal, Narcís Palomeras, Klemen Istenič, Nuno Gracias, and Marc Carreras. Multisensor online 3d view planning for autonomous underwater exploration. *Journal of Field Robotics*, 37(6):1123–1147, 2020.
- [113] Leonardo Zacchini, Matteo Franchi, and Alessandro Ridolfi. Sensor-driven autonomous underwater inspections: A receding-horizon rrt-based view planning solution for auvs. *Journal of Field Robotics*, 39(5):499–527, 2022.
- [114] Hartmut Surmann, Andreas Nüchter, and Joachim Hertzberg. An autonomous mobile robot with a 3d laser range finder for 3d exploration and digitalization of indoor environments. *Robotics and Autonomous Systems*, 45(3-4):181–198, 2003.

- [115] Dorit Borrmann, Andreas Nüchter, Marija Đakulović, Ivan Maurović, Ivan Petrović, Dinko Osmanković, and Jasmin Velagić. A mobile robot based system for fully automated thermal 3d mapping. *Advanced Engineering Informatics*, 28(4):425–440, 2014.
- [116] Zehui Meng, Hao Sun, Hailong Qin, Ziyue Chen, Cihang Zhou, and Marcelo H Ang. Intelligent robotic system for autonomous exploration and active slam in unknown environments. In *2017 IEEE/SICE International Symposium on System Integration (SII)*, pages 651–656. IEEE, 2017.
- [117] Rui Zeng, Yuhui Wen, Wang Zhao, and Yong-Jin Liu. View planning in robot active vision: A survey of systems, algorithms, and applications. *Computational Visual Media*, 6:225–245, 2020.
- [118] Sumantra Dutta Roy, Santanu Chaudhury, and Subhashis Banerjee. Recognizing large 3-d objects through next view planning using an uncalibrated camera. In *Proceedings Eighth IEEE International Conference on Computer Vision. ICCV 2001*, volume 2, pages 276–281. IEEE, 2001.
- [119] Merrill Edmonds, Jingang Yi, Naveen Kumar Singa, and Lingyun Max Wang. Generation of high-density hyperspectral point clouds of crops with robotic multi-camera planning. In *2019 IEEE 15th International Conference on Automation Science and Engineering (CASE)*, pages 1475–1480. IEEE, 2019.
- [120] Albrecht Meydenbauer. Die photometrographie. *Wochenblatt des Architektenvereins zu Berlin*, 1(14):125–126, 1867.
- [121] Javad Baqersad, Peyman Poozesh, Christopher Niezrecki, and Peter Avitabile. Photogrammetry and optical methods in structural dynamics—a review. *Mechanical Systems and Signal Processing*, 86:17–34, 2017.
- [122] Yuxiang Li, Jiancheng Wang, Haoyao Chen, Xin Jiang, and Yunhui Liu. Object-aware view planning for autonomous 3d model reconstruction of buildings using a mobile robot. *IEEE Transactions on Instrumentation and Measurement*, 2023.
- [123] Dinh Van Nam and Kim Gon-Woo. Solid-state lidar based-slam: A concise review and application. In *2021 IEEE International Conference on Big Data and Smart Computing (BigComp)*, pages 302–305. IEEE, 2021.
- [124] Josep Forest Collado et al. *New methods for triangulation-based shape acquisition using laser scanners*. Universitat de Girona, 2004.
- [125] Morgan Quigley, Ken Conley, Brian Gerkey, Josh Faust, Tully Foote, Jeremy Leibs, Rob Wheeler, Andrew Y Ng, et al. Ros: an open-source robot operating system. In *ICRA workshop on open source software*, volume 3, page 5. Kobe, Japan, 2009.
- [126] Nathan Koenig and Andrew Howard. Design and use paradigms for gazebo, an open-source multi-robot simulator. In *2004 IEEE/RSJ international conference on intelligent robots and systems (IROS)(IEEE Cat. No. 04CH37566)*, volume 3, pages 2149–2154. IEEE, 2004.

- [127] Jia Pan, Sachin Chitta, and Dinesh Manocha. Fcl: A general purpose library for collision and proximity queries. In *2012 IEEE International Conference on Robotics and Automation*, pages 3859–3866. IEEE, 2012.
- [128] Erwin Coumans et al. Bullet physics library. *Open source: bulletphysics.org*, 15(49):5, 2013.
- [129] Tomas Möller and Ben Trumbore. Fast, minimum storage ray-triangle intersection. *Journal of Graphics Tools*, 2(1):21–28, 1997.
- [130] Chen Shen, James F O’Brien, and Jonathan R Shewchuk. Interpolating and approximating implicit surfaces from polygon soup. In *ACM SIGGRAPH 2004 Papers*, pages 896–904. -, 2004.
- [131] Jonathan C Carr, Richard K Beatson, Jon B Cherrie, Tim J Mitchell, W Richard Fright, Bruce C McCallum, and Tim R Evans. Reconstruction and representation of 3d objects with radial basis functions. In *Proceedings of the 28th annual conference on Computer graphics and interactive techniques*, pages 67–76, 2001.
- [132] Hugues Hoppe, Tony DeRose, Tom Duchamp, John McDonald, and Werner Stuetzle. Surface reconstruction from unorganized points. In *Proceedings of the 19th annual conference on computer graphics and interactive techniques*, pages 71–78, 1992.
- [133] Jonathan D Cohen, Ming C Lin, Dinesh Manocha, and Madhav Ponamgi. I-collide: An interactive and exact collision detection system for large-scale environments. In *Proceedings of the 1995 symposium on Interactive 3D graphics*, pages 189–ff, 1995.
- [134] Steven M Rubin and Turner Whitted. A 3-dimensional representation for fast rendering of complex scenes. In *Proceedings of the 7th annual conference on Computer graphics and interactive techniques*, pages 110–116, 1980.
- [135] Stéphane Redon, Abderrahmane Kheddar, and Sabine Coquillart. Fast continuous collision detection between rigid bodies. In *Computer graphics forum*, volume 21, pages 279–287. Wiley Online Library, 2002.
- [136] Jon Louis Bentley. Multidimensional binary search trees used for associative searching. *Communications of the ACM*, 18(9):509–517, 1975.
- [137] Henry Fuchs, Zvi M Kedem, and Bruce F Naylor. On visible surface generation by a priori tree structures. In *Proceedings of the 7th annual conference on Computer graphics and interactive techniques*, pages 124–133, 1980.
- [138] Raphael A Finkel and Jon Louis Bentley. Quad trees a data structure for retrieval on composite keys. *Acta informatica*, 4:1–9, 1974.
- [139] Donald Meagher. Geometric modeling using octree encoding. *Computer graphics and image processing*, 19(2):129–147, 1982.
- [140] Armin Hornung, Kai M. Wurm, Maren Bennewitz, Cyrill Stachniss, and Wolfram Burgard. Octomap: an efficient probabilistic 3d mapping framework based on octrees. *Autonomous Robots*, 34(3):189–206, Apr 2013.

- [141] William J Schroeder, Jonathan A Zarge, and William E Lorenson. Decimation of triangle meshes. In *Proceedings of the 19th annual conference on Computer graphics and interactive techniques*, pages 65–70, 1992.
- [142] Kenji Shimada and David C Gossard. Bubble mesh: automated triangular meshing of non-manifold geometry by sphere packing. In *Proceedings of the third ACM symposium on Solid modeling and applications*, pages 409–419, 1995.
- [143] G.H. Tarbox and S.N. Gottschlich. Planning for complete sensor coverage in inspection. *Computer Vision and Image Understanding*, 61(1):84–111, jan 1995.
- [144] Vasek Chvatal. A greedy heuristic for the set-covering problem. *Mathematics of operations research*, 4(3):233–235, 1979.
- [145] Carlton E Lemke, Harvey M Salkin, and Kurt Spielberg. Set covering by single-branch enumeration with linear-programming subproblems. *Operations Research*, 19(4):998–1022, 1971.
- [146] Alberto Caprara, Paolo Toth, and Matteo Fischetti. Algorithms for the set covering problem. *Annals of Operations Research*, 98(1-4):353–371, 2000.
- [147] Sandip Sen. Minimal cost set covering using probabilistic methods. In *Proceedings of the 1993 ACM/SIGAPP symposium on Applied computing: states of the art and practice*, pages 157–164, 1993.
- [148] Wen-Chih Huang, Cheng-Yan Kao, and Jorng-Tzong Horng. A genetic algorithm approach for set covering problems. In *Proceedings of the first IEEE conference on evolutionary computation. IEEE world congress on computational intelligence*, pages 569–574. IEEE, 1994.
- [149] Thomas H Cormen, Charles E Leiserson, Ronald L Rivest, and Clifford Stein. *Introduction to algorithms*. MIT press, 2022.
- [150] Thomas A Feo and Mauricio GC Resende. Greedy randomized adaptive search procedures. *Journal of global optimization*, 6:109–133, 1995.
- [151] Guy E Blelloch, Harsha Vardhan Simhadri, and Kanat Tangwongsan. Parallel and i/o efficient set covering algorithms. In *Proceedings of the twenty-fourth annual ACM symposium on Parallelism in algorithms and architectures*, pages 82–90, 2012.
- [152] Mustafa Devrim Kaba, Mustafa Gokhan Uzunbas, and Ser Nam Lim. A reinforcement learning approach to the view planning problem. In *Proceedings of the IEEE Conference on Computer Vision and Pattern Recognition*, pages 6933–6941, 2017.
- [153] Qian Wu, Wei Zou, and De Xu. Viewpoint planning for freeform surface inspection using plane structured light scanners. *International Journal of Automation and Computing*, 13(1):42–52, Feb 2016.
- [154] Juan Vasquez-Gomez, Luis Sucar, and Rafael Murrieta-Cid. View/state planning for three-dimensional object reconstruction under uncertainty. *Autonomous Robots*, 12 2015.

- [155] Joseph E Banta, LR Wong, Christophe Dumont, and Mongi A Abidi. A next-best-view system for autonomous 3-d object reconstruction. *IEEE Transactions on Systems, Man, and Cybernetics-Part A: Systems and Humans*, 30(5):589–598, 2000.
- [156] Simon Kriegel, Christian Rink, Tim Bodenmüller, and Michael Suppa. Efficient next-best-scan planning for autonomous 3d surface reconstruction of unknown objects. *Journal of Real-Time Image Processing*, 10:611–631, 2015.
- [157] Souhail Khalfaooui, Ralph Seulin, Yohan Fougerolle, and David Fofi. An efficient method for fully automatic 3d digitization of unknown objects. *Computers in Industry*, 64(9):1152–1160, 2013.
- [158] J Irving Vasquez-Gomez, L Enrique Sucar, Rafael Murrieta-Cid, and Efrain Lopez-Damian. Volumetric next-best-view planning for 3d object reconstruction with positioning error. *International Journal of Advanced Robotic Systems*, 11(10):159, 2014.
- [159] Jeffrey Delmerico, Stefan Isler, Reza Sabzevari, and Davide Scaramuzza. A comparison of volumetric information gain metrics for active 3d object reconstruction. *Autonomous Robots*, 42(2):197–208, 2018.
- [160] Michael Krainin, Brian Curless, and Dieter Fox. Autonomous generation of complete 3d object models using next best view manipulation planning. In *2011 IEEE international conference on robotics and automation*, pages 5031–5037. IEEE, 2011.
- [161] Zhirong Wu, Shuran Song, Aditya Khosla, Fisher Yu, Linguang Zhang, Xiaoou Tang, and Jianxiong Xiao. 3d shapenets: A deep representation for volumetric shapes. In *Proceedings of the IEEE conference on computer vision and pattern recognition*, pages 1912–1920, 2015.
- [162] Geoffrey E Hinton, Simon Osindero, and Yee-Whye Teh. A fast learning algorithm for deep belief nets. *Neural computation*, 18(7):1527–1554, 2006.
- [163] Wentao Yuan, Tejas Khot, David Held, Christoph Mertz, and Martial Hebert. Pcn: Point completion network. In *2018 international conference on 3D vision (3DV)*, pages 728–737. IEEE, 2018.
- [164] Chenming Wu, Rui Zeng, Jia Pan, Charlie CL Wang, and Yong-Jin Liu. Plant phenotyping by deep-learning-based planner for multi-robots. *IEEE Robotics and Automation Letters*, 4(4):3113–3120, 2019.
- [165] Rui Zeng, Wang Zhao, and Yong-Jin Liu. Pc-nbv: A point cloud based deep network for efficient next best view planning. In *2020 IEEE/RSJ International Conference on Intelligent Robots and Systems (IROS)*, pages 7050–7057. IEEE, 2020.
- [166] Han Zhang, Ian Goodfellow, Dimitris Metaxas, and Augustus Odena. Self-attention generative adversarial networks. In *International conference on machine learning*, pages 7354–7363. PMLR, 2019.
- [167] J Irving Vasquez-Gomez, David Troncoso, Israel Becerra, Enrique Sucar, and Rafael Murrieta-Cid. Next-best-view regression using a 3d convolutional neural network. *Machine Vision and Applications*, 32:1–14, 2021.

- [168] Benat Urtasun, Imanol Andonegui, and Eider Gorostegui-Colinas. Phase-shifted imaging on multi-directional induction thermography. *Scientific Reports*, 13(1), 2023. Cited by: 0; All Open Access, Gold Open Access, Green Open Access.
- [169] Christian Srajbr. Induction excited thermography in industrial applications. In *Proceedings of the 19th World Conference on Non-Destructive Testing, Munich, Germany*, pages 13–17, 2016.
- [170] Joseph N Zalameda, Nikolas Rajic, and William P Winfree. A comparison of image processing algorithms for thermal nondestructive evaluation. In *Thermosense XXV*, volume 5073, pages 374–385. SPIE, 2003.
- [171] Henrik O Saldner and Jonathan M Huntley. Temporal phase unwrapping: application to surface profiling of discontinuous objects. *Applied optics*, 36(13):2770–2775, 1997.
- [172] Daniel Scharstein and Richard Szeliski. High-accuracy stereo depth maps using structured light. In *2003 IEEE Computer Society Conference on Computer Vision and Pattern Recognition, 2003. Proceedings.*, volume 1, pages I–I. IEEE, 2003.
- [173] Guanming Lai and Toyohiko Yatagai. Generalized phase-shifting interferometry. *JOSA A*, 8(5):822–827, 1991.
- [174] Berthold KP Horn and Brian G Schunck. Determining optical flow. *Artificial intelligence*, 17(1-3):185–203, 1981.
- [175] Bruce D Lucas, Takeo Kanade, et al. *An iterative image registration technique with an application to stereo vision*, volume 81. Vancouver, 1981.
- [176] Alexey Dosovitskiy, Philipp Fischer, Eddy Ilg, Philip Hausser, Caner Hazirbas, Vladimir Golkov, Patrick Van Der Smagt, Daniel Cremers, and Thomas Brox. FlowNet: Learning optical flow with convolutional networks. In *Proceedings of the IEEE international conference on computer vision*, pages 2758–2766, 2015.
- [177] Yizhe Wang, Bin Gao, Wai lok Woo, Guiyun Tian, Xavier Maldague, Li Zheng, Zheyu Guo, and Yuyu Zhu. Thermal pattern contrast diagnostic of microcracks with induction thermography for aircraft braking components. *IEEE Transactions on Industrial Informatics*, 14(12):5563–5574, 2018.
- [178] Gunnar Farneback. Two-frame motion estimation based on polynomial expansion. In *Scandinavian conference on Image analysis*, pages 363–370. Springer, 2003.
- [179] Takahide Sakagami and Shiro Kubo. Development of a new crack identification technique based on near-tip singular electrothermal field measured by lock-in infrared thermography. *JSME International Journal Series A Solid Mechanics and Material Engineering*, 44(4):528–534, 2001.
- [180] Charles Annis, Luca Gandossi, and Oliver Martin. Optimal sample size for probability of detection curves. *Nuclear Engineering and Design*, 262:98–105, 2013.
- [181] Ruizhen Yang, Yunze He, Andreas Mandelis, Nichen Wang, Xuan Wu, and Shoudao Huang. Induction infrared thermography and thermal-wave-radar analysis for imaging inspection and diagnosis of blade composites. *IEEE Transactions on Industrial Informatics*, 14(12):5637–5647, 2018.



- [182] Beate Oswald-Tranta and Mario Sorger. Localizing surface cracks with inductive thermographical inspection: from measurement to image processing. *Quantitative InfraRed Thermography Journal*, 8(2):149–164, 2011.
- [183] Christoph Tuschl, Beate Oswald-Tranta, Timotheos Agathocleous, and Sven Eck. Scanning inductive pulse phase thermography with changing scanning speed for non-destructive testing. *Quantitative InfraRed Thermography Journal*, pages 1–16, 2023.
- [184] Christoph Tuschl, Beate Oswald-Tranta, and Sven Eck. Scanning inductive thermographic surface defect inspection of long flat or curved work-pieces using rectification targets. *Applied Sciences*, 12(12):5851, 2022.
- [185] S.M. Shepard, J.R. Lhota, B.A. Rubadeux, D. Wang, and T. Ahmed. Reconstruction and enhancement of active thermographic image sequences. *Optical Engineering*, 42(5):1337–1342, 2003. cited By 348.
- [186] Francisco J Madruga, Clemente Ibarra-Castanedo, Olga M Conde, José M López-Higuera, and Xavier Maldague. Infrared thermography processing based on higher-order statistics. *NDT & E International*, 43(8):661–666, 2010.
- [187] Andreas Bircher, Mina Kamel, Kostas Alexis, Helen Oleynikova, and Roland Siegwart. "Receding horizon" next-best-view" planner for 3d exploration. In *2016 IEEE international conference on robotics and automation (ICRA)*, pages 1462–1468. IEEE, 2016.
- [188] Manikandasriram Ramanagopal, Andre Nguyen, and Jerome Le Ny. A motion planning strategy for the active vision-based mapping of ground-level structures. *IEEE Transactions on Automation Science and Engineering*, PP:1–13, 11 2017.
- [189] Michael S Langer and Heinrich H Bülthoff. Depth discrimination from shading under diffuse lighting. *Perception*, 29(6):649–660, 2000.
- [190] Eduardo Gallo. The so (3) and se (3) lie algebras of rigid body rotations and motions and their application to discrete integration, gradient descent optimization, and state estimation. *arXiv preprint arXiv:2205.12572*, 2022.
- [191] Massimiliano Corsini, Paolo Cignoni, and Roberto Scopigno. Efficient and flexible sampling with blue noise properties of triangular meshes. *IEEE transactions on visualization and computer graphics*, 18(6):914–924, 2012.
- [192] Jon Louis Bentley. Multidimensional binary search trees used for associative searching. *Communications of the ACM*, 18(9):509–517, 1975.
- [193] Ward Douglas Maurer and Ted G Lewis. Hash table methods. *ACM Computing Surveys (CSUR)*, 7(1):5–19, 1975.
- [194] James D Foley. *Computer graphics: principles and practice*, volume 12110. Addison-Wesley Professional, 1996.

- [195] Jiri Bittner, Vlastimil Havran, and Pavel Slavik. Hierarchical visibility culling with occlusion trees. In *Proceedings. Computer Graphics International (Cat. No. 98EX149)*, pages 207–219. IEEE, 1998.
- [196] Edwin Earl Catmull. *A subdivision algorithm for computer display of curved surfaces*. The University of Utah, 1974.
- [197] Eugene Lapidous and Guofang Jiao. Optimal depth buffer for low-cost graphics hardware. In *Proceedings of the ACM SIGGRAPH/EUROGRAPHICS workshop on Graphics hardware*, pages 67–73, 1999.
- [198] Ingo Wald, Sven Woop, Carsten Benthin, Gregory S Johnson, and Manfred Ernst. Embree: a kernel framework for efficient cpu ray tracing. *ACM Transactions on Graphics (TOG)*, 33(4):1–8, 2014.
- [199] Rosen Diankov. *Automated construction of robotic manipulation programs*. PhD thesis, Carnegie Mellon University, The Robotics Institute Pittsburgh, 2010.
- [200] Nenad Mladenović and Pierre Hansen. Variable neighborhood search. *Computers & operations research*, 24(11):1097–1100, 1997.
- [201] Sergey Alatarsev, Sebastian Stellmacher, and Frank Ortmeier. Robotic task sequencing problem: A survey. *Journal of intelligent & robotic systems*, 80:279–298, 2015.
- [202] Will Schroeder, Ken Martin, and Bill Lorensen. *The Visualization Toolkit (4th ed.)*. Kitware, 2006.
- [203] Jack CK Chou and M Kamel. Finding the position and orientation of a sensor on a robot manipulator using quaternions. *The international journal of robotics research*, 10(3):240–254, 1991.
- [204] James J Kuffner and Steven M LaValle. Rrt-connect: An efficient approach to single-query path planning. In *Proceedings 2000 ICRA. Millennium Conference. IEEE International Conference on Robotics and Automation. Symposia Proceedings (Cat. No. 00CH37065)*, volume 2, pages 995–1001. IEEE, 2000.
- [205] Ioan A Sucas, Mark Moll, and Lydia E Kavraki. The open motion planning library. *IEEE Robotics & Automation Magazine*, 19(4):72–82, 2012.
- [206] Paul J Besl and Neil D McKay. Method for registration of 3-d shapes. In *Sensor fusion IV: control paradigms and data structures*, volume 1611, pages 586–606. Spie, 1992.
- [207] Radu Bogdan Rusu and Steve Cousins. 3d is here: Point cloud library (pcl). In *2011 IEEE international conference on robotics and automation*, pages 1–4. IEEE, 2011.
- [208] Szymon Rusinkiewicz. A symmetric objective function for icp. *ACM Transactions on Graphics (TOG)*, 38(4):1–7, 2019.